

Search for Supersymmetry in States with Large Missing Transverse Momentum and Three Leptons including a Z -Boson

A Dissertation Presented

by

Jeremiah Jet Goodson

to

The Graduate School

in Partial Fulfillment of the Requirements

for the Degree of

Doctor of Philosophy

in

Physics

Stony Brook University

May 2012



Stony Brook University

The Graduate School

Jeremiah Jet Goodson

We, the dissertation committee for the above candidate for the Doctor of Philosophy degree, hereby recommend acceptance of this dissertation.

Professor Robert McCarthy – Dissertation Advisor
Department of Physics

Professor Paul Grannis – Chairman of the Defense
Department of Physics

Professor Thomas Hemmick
Department of Physics

Professor Patrick Meade
C.N. Yang Institute of Theoretical Physics

Doctor George Redlinger — Outside Member
Particle Physicist
Brookhaven National Laboratory

This dissertation is accepted by the Graduate School.

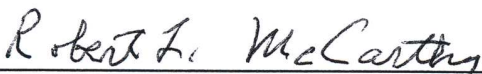
Charles Taber
Interim Dean of the Graduate
School

Stony Brook University

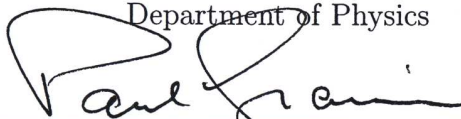
The Graduate School

Jeremiah Jet Goodson

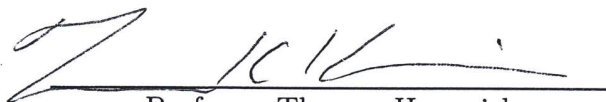
We, the dissertation committee for the above candidate for the Doctor of Philosophy degree, hereby recommend acceptance of this dissertation.



Professor Robert McCarthy – Dissertation Advisor
Department of Physics



Professor Paul Grannis – Chairman of the Defense
Department of Physics



Professor Thomas Hemmick
Department of Physics



Professor Patrick Meade
C.N. Yang Institute of Theoretical Physics



Doctor George Redlinger — Outside Member
Particle Physicist
Brookhaven National Laboratory

This dissertation is accepted by the Graduate School.

Charles Taber

Interim Dean of the Graduate School

Abstract of the Dissertation

**Search for Supersymmetry in States with
Large Missing Transverse Momentum and
Three Leptons including a Z -Boson**

by

Jeremiah Jet Goodson

Doctor of Philosophy

in

Physics

Stony Brook University

2012

I present a search for supersymmetric particle production requiring 3 leptons (e or μ) and missing transverse momentum greater than 50 GeV. Two of the leptons are required to have the same flavor but opposite charge with an invariant mass within 10 GeV of the Z -boson mass. The dataset consists of $\sqrt{s} = 7$ TeV proton-proton collisions with an integrated luminosity of 2.06 fb^{-1} collected at the ATLAS detector of the Large Hadron Collider during the 2011 operations. There were 95 events observed in data and 72 ± 12 were expected. An upper limit of 23.8 fb is set on the visible cross section for processes beyond the standard model at 95% confidence level. Exclusion intervals are set on the parameter space of General Gauge Mediated supersymmetry.



To the memory of

my brother from another mother,
Matt Geary
12 June, 1982 — 27 September, 2008

and my favorite Bronco fan,
Grandma Dia
16 March, 1934 — 28 February, 2012

...I was away when they went their way...



Contents

List of Figures	viii
List of Tables	xii
Preface	xiv
Acknowledgements	xv
1 Theoretical Background & Motivation	1
1.1 The Standard Model of Particle Physics	1
1.1.1 Quantum Electrodynamics	3
1.1.2 Quantum Chromodynamics	4
1.1.3 The Electroweak Model	6
1.1.4 The Hierarchy Problem and Quadratic Divergence . . .	8
1.2 Supersymmetry	9
1.2.1 Hierarchy and Quadratic Divergence under Supersymmetry	10
1.2.2 R-Parity and the Lightest Supersymmetric Particle . .	11
1.2.3 Minimal Supersymmetric Standard Model	13
1.2.4 Paving the Road to Unification with Supersymmetry .	15
1.2.5 Gauge Mediation	16
1.2.6 General Gauge Mediation	19
2 The CERN Accelerator Complex	22
3 The ATLAS Experiment	26
3.1 Inner Tracker	27
3.1.1 The Pixel Tracker	28
3.1.2 The SemiConductor Tracker	28
3.1.3 The Transition Radiation Tracker	29
3.2 Calorimetry	30

3.2.1	Liquid Argon Calorimeter	31
3.2.2	Tile Calorimeter	35
3.3	Muon Spectrometry	37
3.3.1	Monitored Drift Tube Chambers	37
3.3.2	Cathode Strip Chambers	40
3.3.3	Resistive Plate Chambers	41
3.3.4	Thin Gap Chambers	43
3.4	Luminosity and Forward Detectors	44
3.4.1	Beam Conditions Monitor	46
3.4.2	Minimum Bias Trigger Scintillators	46
3.4.3	LUCID	46
3.4.4	ZDC	47
3.4.5	ALFA	48
3.5	Magnet System	48
3.5.1	Central Solenoid Magnet	49
3.5.2	Barrel Toroid Magnets	49
3.5.3	End-cap Toroid Magnets	50
3.6	Trigger, Data Acquisition, and Detector Control	50
4	Data Sample	55
5	Monte Carlo	57
5.1	Standard Model Monte Carlo	57
5.2	GGM SUSY Signal Grids	63
6	Analysis	67
6.1	Physics Objects	
	Reconstruction & Selection	67
6.1.1	Particle Selection	67
6.1.2	Overlap Removal	70
6.1.3	Further Object Selection Criteria	71
6.1.4	E_T^{miss} Definition	71
6.2	Event Handling	74
6.2.1	Trigger	74
6.2.2	Data Quality & Cleaning	75
6.2.3	Data & Monte Carlo Corrections	77
6.3	Definition of the Signal Region	80
6.4	Sensitivity	80
6.5	Data-Driven Background Estimation	81
6.6	E_T^{miss} -Performance	90
6.7	Systematic Uncertainties	91

6.7.1	Irreducible Backgrounds	94
6.7.2	Reducible Backgrounds	96
6.7.3	Systematic Uncertainties on the Signal Grids	97
6.8	Observed Data in the Signal Region	99
7	Interpretations of Results	109
8	Future Studies	113
8.1	Alternative Analysis Scenarios	113
8.2	Outstanding Issues	114
9	Conclusion	117
	Bibliography	118
	Appendices	133
A	Displays of Selected Events	133
B	Acceptance and Efficiency of the GGM Grids	146
C	Monitoring of the Liquid Argon Read-Out Drivers	153
D	Muons in MET	158
E	Offline Software Development	165
E.1	MissingETD3PDMaker	166
E.2	SUSYD3PDMaker	168
E.3	METUtility	171
F	Miscellaneous	174
F.1	Coordinate Frame	174
F.2	Calorimeter Resolution	175
F.3	Sagitta	175
F.4	Anti- k_T Jet Clustering Algorithm	177
F.5	Missing Transverse Momentum	178
F.6	Tag-and-Probe	179
F.7	Glossary	179

List of Figures

1.1	An example of conservation of lepton number in muon decay. .	3
1.2	Feynman diagrams demonstrating the conservation of baryon number.	4
1.3	The loop corrections for the Higgs boson.	9
1.4	A potential decay chain for the proton if L - and B -number is violated.	11
1.5	Example Feynman diagrams showing the conservation of R-Parity.	12
1.6	The gauge-coupling constants evolution from the experimentally measured values at the Z -pole.	17
1.7	A potential $\tilde{g}\tilde{g}$ production process which could produce three leptons.	21
2.1	The LHC accelerator complex at CERN.	23
2.2	The luminosity delivered by the LHC for the 2011 data-taking period.	25
3.1	The ATLAS detector.	26
3.2	A cross-section of one quadrant of the ATLAS inner detector.	27
3.3	A half-shell of the pixel.	28
3.4	A completed SCT barrel with all modules.	29
3.5	An end-cap of the TRT during assembly.	30
3.6	The layout of the ATLAS calorimeter.	31
3.7	The hardware architectures used in the segments of the LAr calorimeter.	32
3.8	Schematic of a LAr barrel module.	33
3.9	The flow of data in the ATLAS LAr detector.	34
3.10	The triangular signal pulse of the ATLAS LAr calorimeter under various conditions.	35
3.11	A schematic of a Tile Calorimeter module.	36
3.12	The layout of the ATLAS muon spectrometer.	38

3.13	Diagrams of an MDT and an MDT chamber.	39
3.14	The layout of the CSC end-cap wheel.	41
3.15	The layout of a CSC layer and the read-out scheme a CSC. . .	42
3.16	Cross-section of an RPC.	43
3.17	Cross-section of a TGC layer.	44
3.18	The forward detectors of ATLAS.	45
3.19	The layout of the ATLAS magnet systems.	49
3.20	Diagram of the ATLAS TDAQ system.	51
6.1	The ATLAS clustering algorithm.	72
6.2	The flow of the E_T^{miss} -algorithm.	73
6.3	The effect of the re-weighting of MC in order to match the μ seen in data	79
6.4	The E_T^{miss} distribution after the three-lepton event selection. .	82
6.5	The invariant mass, $m_{\ell+\ell-}$, after the three-lepton event selection.	83
6.6	The E_T^{miss} distribution after the $ m_{\ell+\ell-} - m_Z < 10$ GeV event selection.	84
6.7	The signal significance, Z_{LLR} , for the two GGM grids.	85
6.8	The E_T^{miss} linearity after the three lepton event selection. . . .	90
6.9	The E_T^{miss} resolution versus $\sum E_T^{\text{EM}}$ after the three lepton event selection.	91
6.10	The distribution of $E_{x(y)}^{\text{miss,e}}$	92
6.11	The distribution of $E_{x(y)}^{\text{miss,jets}}$	92
6.12	The distribution of $E_{x(y)}^{\text{miss,clusters}}$	93
6.13	The distribution of $E_{x(y)}^{\text{miss},\mu}$	93
6.14	The E_T^e (p_T^μ) distribution for the leading lepton in the signal region.	100
6.15	The E_T^e (p_T^μ) distribution for the second leading lepton in the signal region.	100
6.16	The E_T^e (p_T^μ) distribution for the third leading lepton in the signal region.	101
6.17	The E_T^{miss} distribution in the signal region.	101
6.18	The jet multiplicity after the E_T^{miss} selection.	102
6.19	The jet p_T distribution after the E_T^{miss} selection.	102
6.20	The effective mass distribution in the signal region.	103
6.21	The distribution of the invariant mass calculated from all three leptons in the signal region.	108
7.1	The 95% CL exclusion limit for the GGM Higgsino grid. . . .	111
7.2	The 95% CL exclusion limit for the GGM Wino grid.	112

8.1	The exclusion potential for possible future analyses of the Higgsino grid.	115
8.2	The exclusion potential for possible future analyses of the Wino grid.	116
A.1	Event display for Event 1649049 from run 180400.	133
A.2	Event display for Event 4702311 from run 182454.	134
A.3	Event display for Event 16677615 from run 182486.	134
A.4	Event display for Event 21528951 from run 182486.	135
A.5	Event display for Event 103600363 from run 182787.	135
A.6	Event display for Event 117824417 from run 182787.	136
A.7	Event display for Event 25255214 from run 183054.	136
A.8	Event display for Event 160821752 from run 183081.	137
A.9	Event display for Event 16288174 from run 183129.	137
A.10	Event display for Event 2242543 from run 183412.	138
A.11	Event display for Event 35750750 from run 184169.	138
A.12	Event display for Event 25257494 from run 185644.	139
A.13	Event display for Event 5228295 from run 186179.	139
A.14	Event display for Event 7407118 from run 186182.	140
A.15	Event display for Event 18855850 from run 186361.	140
A.16	Event display for Event 30840259 from run 186721.	141
A.17	Event display for Event 81190803 from run 186729.	141
A.18	Event display for Event 243498369 from run 186729.	142
A.19	Event display for Event 126711223 from run 186877.	142
A.20	Event display for Event 120508399 from run 186965.	143
A.21	Event display for Event 180209937 from run 186965.	143
A.22	Event display for Event 28815719 from run 186965.	144
A.23	Event display for Event 68267656 from run 187219.	144
A.24	Event display for Event 61044675 from run 187763.	145
B.1	The acceptance of the higgsino grid	147
B.2	The efficiency of the higgsino grid	148
B.3	The acceptance \times efficiency of the higgsino grid	149
B.4	The acceptance of the wino grid	150
B.5	The efficiency of the wino grid	151
B.6	The acceptance \times efficiency of the wino grid	152
C.1	The Run Manager panel showing a LAr ROD busy signal. . .	154
C.2	The Run Manager panel showing busy DSPs.	155
C.3	An example of the ROD busy plot in OHP.	156
C.4	An example of the ROD busy fraction plot provided in OHP. .	157

D.1	The muon η distribution for various muon collections.	159
D.2	The muon isolation versus p_T for CaloTrkMuID and MuTag muons.	161
D.3	A comparison of the $E_{x(y)}^{\text{miss,truth}} - E_{x(y)}^{\text{miss,reco}}$ distribution after var- ious changes to the muons used in the E_T^{miss} -algorithm.	163
D.4	A comparison of $\sigma_{E_{x(y)}^{\text{miss}}} = k \cdot \sqrt{\Sigma E_T}$ after various changes to the muons used in the E_T^{miss} -algorithm.	164
E.1	Block diagram showing the flow of data to the MissingETD3PDMaker.	167
E.2	Block diagram showing the flow of data to the SUSYD3PDMaker.	170
E.3	Block diagram showing the functionality of the METUtility software.	172
F.1	The sagitta, S, and chord, L, of a circle.	176
F.2	The method used to measure the sagitta in the ATLAS muon spectrometer.	176
F.3	The relationship of E_T^{miss} to physics objects and the beam in collisions.	178

List of Tables

1.1	The leptons of the standard model.	2
1.2	The quarks of the standard model.	2
1.3	The gauge bosons of the standard model.	2
1.4	Examples of hadrons demonstrating quark composition.	5
1.5	The supersymmetric particle and sparticle spectrum	15
3.1	The key trigger objects and their L1 thresholds at $\mathcal{L} = 10^{32} \text{ cm}^{-2}\text{s}^{-1}$	54
4.1	The data periods used in this analysis with integrated luminosity and μ	56
5.1	The background MC samples produced using PYTHIA.	58
5.2	The background MC samples produced using HERWIG.	58
5.3	The background MC samples produced using MADGRAPH.	59
5.4	The background MC samples produced using MC@NLO.	60
5.5	The W -background MC samples produced using ALPGEN.	61
5.6	The background MC samples produced using ALPGEN.	62
5.7	The cross sections for $\tilde{g}\tilde{g}$ -production in the GGM grids.	64
5.8	σ_{NLO} for gaugino-production processes in the Higgsino grid.	65
5.9	σ_{NLO} for gaugino-production processes in the Wino grid.	66
6.1	The triggers used for each data taking period.	75
6.2	The cut flow of the Standard Model backgrounds for the signal selections.	81
6.3	The cut flow of the Higgsino model points for the signal selections.	87
6.4	The cut flow of the Wino model points for the signal selections.	88
6.5	The result of the background estimate test.	89
6.6	The effect of the systematics on the irreducible backgrounds.	96
6.7	The expected number of events for each SM background MC and the observed number of data events.	99

6.8	The $e^+e^-e^\pm$ events found in data.	104
6.9	The $e^+e^-\mu^\pm$ events found in data.	105
6.10	The $\mu^+\mu^-e^\pm$ events found in data.	106
6.11	The $\mu^+\mu^-\mu^\pm$ events found in data.	107
D.1	The result of the isolation- p_T selection on CaloTrkMuID muons in selected samples.	160
D.2	The result of the isolation- p_T selection on MuTag muons in selected samples.	162

Preface

The first chapter of this thesis is a general introduction to the theory that underlies the search performed. After that are chapters providing information on the Large Hadron Collider and the ATLAS detector. The remaining chapters are devoted to the analysis, followed by appendices which provide additional information that may aid the reader's understanding, as well as documentation on other projects developed by the author for the ATLAS experiment.

The data and Monte Carlo used in this analysis was pocessed with Release 16 of ATHENA, the ATLAS reconstruction framework.

The framework used to perform this analysis can be found in the ATLAS SVN repository:

<https://svnweb.cern.ch/trac/atlasgrp/browser/Institutes/StonyBrook/Autolykus>.

Additional tools used for analysis are also found at:

<https://svnweb.cern.ch/trac/atlasusr/browser/jgoodson/analysis>.

Acknowledgements

Thanks to my advisor, Dr. Robert McCarthy, for his guidance.

Thanks to Adam for letting me be his $E_{\text{T}}^{\text{miss}}$ -sidekick.
Thanks to Tina for being a multilepton M.V.P.

Thanks to Moustapha for showing me the ropes.
Thanks to Julia for being my coffee-time BFF.
Thanks to Burton, Stephanie, and Katy for letting me bounce ideas off of them.

Thanks to Kira for being a muse in technicolor.
Thanks to *¡El Chupacabra!* for keeping me entertained.
Thanks to Jim, Kevin, and Steve for being awesome office mates.
Thanks to Jim & Megan for being gracious hosts.

Thanks to all of my collaborators on ATLAS.
Thanks to the people who make the LHC run, for giving us beam.
Thanks to the National Science Foundation for underwriting this research.

Thanks to my mother and father for rearing me.
Thanks to my brothers for making me look golden.

*I suppose the process of acceptance will pass through the usual four stages:
1. This is worthless nonsense, 2. This is an interesting, but perverse, point of
view, 3. This is true, but quite unimportant, 4. I always said so.*

J.B.S. Haldane [1]

1

Theoretical Background & Motivation

1.1 The Standard Model of Particle Physics

In particle physics, the standard model is the currently accepted theory for explaining the phenomena observed at the smallest scales and highest energy densities, and thus governed by the most fundamental physical laws. The standard model is a non-Abelian Yang-Mills relativistic quantum field theory of the topological group $SU(3)_C \otimes SU(2)_L \otimes U(1)_Y$. The $SU(3)_C$ group corresponds to quantum chromodynamics (the strong-nuclear force). The $SU(2)_L \otimes U(1)_Y$ spontaneously breaks, leaving only the $U(1)_{em}$ portion unbroken; this broken $SU(2)_L \otimes U(1)_Y$ corresponds to the electroweak model (the unification of the weak-nuclear force and electromagnetism) [2]. The standard model has been repeatedly shown to be the best representation of fundamental physics, owing to the high precision to which its predictions agree with results, but it is recognized as an incomplete theory, as it fails to include gravity and has outstanding problems related to the yet unobserved Higgs boson required for electroweak unification (see Section 1.1.4 for further details).

In the standard model, matter is composed of fermions, divided into two types, quarks and leptons. The forces that exist between fermions, and give matter much of its substance, are mediated by gauge bosons. The physical characteristics of the leptons can be seen in Table 1.1, the quarks in Table 1.2, and the gauge bosons in Table 1.3. For each of the fermions there is also an anti-particle with certain quantum numbers, such as charge, having the opposite value. In the gauge bosons, the W^\pm -bosons are each other's anti-particle.

In the standard model, there are several fundamentally conserved quan-

Leptons						
Flavor		Electric Charge	Mass [MeV/c ²]	L_e	L_μ	L_τ
1 st Generation	e (electron)	-1	0.511	1	0	0
	ν_e (electron neutrino)	0	$<3 \times 10^{-9}$	1	0	0
2 nd Generation	μ (muon)	-1	105.7	0	1	0
	ν_μ (muon neutrino)	0	$<1.9 \times 10^{-4}$	0	1	0
3 rd Generation	τ (tau)	-1	1776.8	0	0	1
	ν_τ (tau neutrino)	0	$<1.8 \times 10^{-2}$	0	0	1

Table 1.1: The leptons of the standard model [3].

Quarks				
Flavor		Electric Charge	Mass [MeV/c ²]	Baryon Number
1 st Generation	u (up)	+2/3	1.5—3.3	1/3
	d (down)	-1/3	3.5—6.0	1/3
2 nd Generation	c (charm)	+2/3	1270	1/3
	s (strange)	-1/3	78—138	1/3
3 rd Generation	t (top)	+2/3	171200	1/3
	b (bottom)	-1/3	4200	1/3

Table 1.2: The quarks of the standard model [3].

Gauge Bosons					
Force		Boson	Spin	Charge	Mass [GeV/c ²]
Electroweak	Electromagnetic	γ (photon)	1	0	$< 10^{-27}$
	Charged Weak	W^\pm	1	± 1	80.399
	Neutral Weak	Z^0	1	0	91.1876
	Strong	g_i (gluons, i=1,...8)	1	0	$< \mathcal{O}(10^{-3})$
	Gravitation	g (graviton)	2	0	$< 7 \cdot 10^{-41}$

Table 1.3: The gauge bosons of the standard model. The graviton is included for completeness [3].

tites, such as electric charge or energy, which are the consequence of certain symmetries in the standard model. Other quantities are only conserved partially, such as flavor. Flavor is the type of a particle, such as it being a muon or an up-quark. The electromagnetic and strong-nuclear forces are not capable of changing flavor, but the weak-nuclear force can, such as when a muon decays into an electron mediated by a W -boson.

Additionally, there are quantities that are empirically believed to be conserved, but for which we have no theoretical underpinning to support the conservation law. This is the case with lepton number, L , for which all leptons have $L = 1$ and all anti-leptons have $L = -1$. This can be further subdivided by flavor, so that there is a lepton number L_i for $i = e, \mu, \tau$, with each lepton number conserved. This conservation can be seen in Figure 1.1, where $L_\mu = 1$ and $L_e = 1 + (-1) = 0$. Another empirically conserved quantity is baryon number, B , for which all baryons receive $B = 1$ and all anti-baryons receive $B = -1$. Mesons have $B = 0$. Baryon number was introduced as a reason for why proton decay was never observed, but it is observed to be conserved beyond that scope. An example of baryon decay can be seen in Figure 1.2(a) where the baryon value of $B = 1$ is conserved and Figure 1.2(b), where the $B = 0$ is conserved and the meson decays into leptons [4].

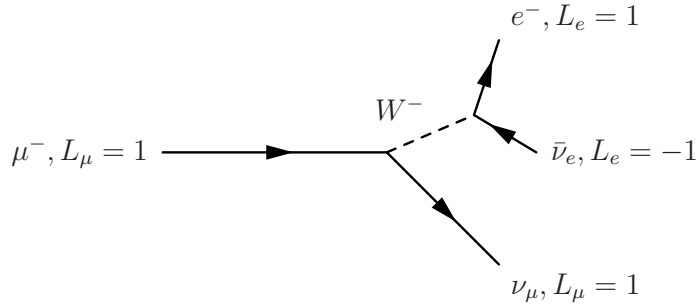


Figure 1.1: Shown here is an example of the conservation of lepton number in the decay of a muon, with $L_\mu = 1$ and $L_e = 1 + (-1) = 0$.

1.1.1 Quantum Electrodynamics

Quantum Electrodynamics (QED) is the relativistic field theory concerning the interaction of charged particles with electromagnetic fields. It is a relativistic quantum field theory, in that it satisfies $E = mc^2$ and properly allows for particle/anti-particle pairs created *ex nihilo*. QED was the first successful quantum field theory and later theories follow in form from it. In quantum

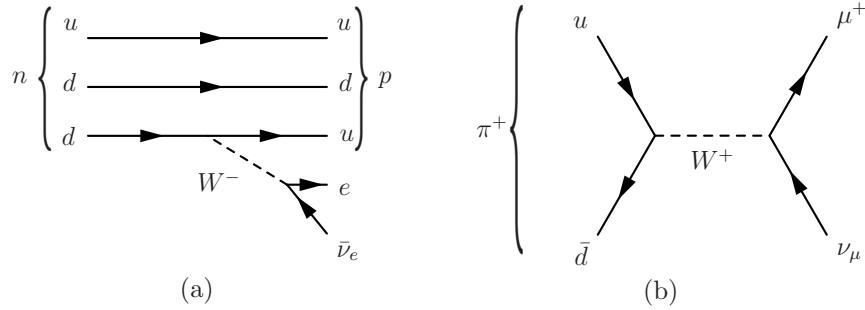


Figure 1.2: (a) shows the conservation of baryon number in the decay of a neutron ($B = 1$) to a proton ($B = 1$), an electron ($B = 0$), and a neutrino ($B = 0$). (b) shows the decay of a pion to a muon and neutrino, all with $B = 0$.

field theory, the various particles we observe are excitations of an associated field, or flavor, such as for electrons or muons [5, 6].

The interaction field of QED is the electromagnetic field and the photon is the excitation of that field. A fundamental feature of the electromagnetic field is that of gauge invariance; that a continuous local transformation does not change the electromagnetic Lagrangian. Photons do not possess an electric charge and thus do not self-interact. This is reflective of the fact that QED is an abelian field theory with symmetry group $U(1)$, which has generators that are commutative with each other [7, 8]. The coupling-constant of the electromagnetic field is the fine-structure constant, $\alpha = e^2/\hbar c = 7.2973525376(50) \cdot 10^{-3}$.

QED was the first successful relativistic quantum field theory and is still the most precisely verified theory in physics, providing results with an accuracy of eight significant figures. With this success in mind, the other theoretical developments of the standard model are modeled from QED, or built upon it, including the extension of Feynman diagrams [9].

1.1.2 Quantum Chromodynamics

One of the narratives of 20th-century physics is the evolution in our understanding of the strong-nuclear force, culminating in the Theory of Quantum Chromodynamics. Prior to 1950s the strong-nuclear force was theorized to consist of a Yukawa interaction via pi-mesons between protons and neutrons. The discovery of the K^0 in 1947 and the Λ^0 in 1950 ushered in the “strange” particles which forced a reconsideration of strong-nuclear theory that resulted in the Quark Model in 1964. The Quark Model proposed that baryons, such

as the proton or neutron, are composed of three quarks (or anti-quarks) and mesons, such as $\pi^{\pm,0}$, are composed of a quark and an anti-quark. Objects made of quarks are referred to as hadrons in general. Originally the theory contained the up (u), down (d), and strange (s) quarks. These can combine to produce hadrons as shown in Table 1.4. Experiments probing the structure of the proton are in agreement with a three valence parton structure. The probes also display evidence of asymptotic freedom, that at large energies or small scales, the quarks behave as if they are unbound. Due to the lack of observation of unpaired quarks, which would be notable for their fractional charge, the quark model also requires “quark confinement”, requiring that unbound quarks are disallowed [10, 11].

(a)			(b)		
Mesons			Baryons		
qq	Charge	Name	qqq	Charge	Name
$(u\bar{u} - d\bar{d})\sqrt{2}$	0	π^0	uuu	2	Δ^{++}
$u\bar{d}$	+1	π^+	uud	1	p
$d\bar{s}$	0	K^0	udd	0	n
			uds	0	Λ^0
			sss	-1	Ω^-

Table 1.4: Examples of hadrons demonstrating quark composition [3]

The interactions of the quarks are governed by the Theory of Quantum Chromodynamics (QCD). QCD is a non-abelian Yang-Mills theory, meaning that it contains non-commutative elements and is based on a $SU(N)$ special unitary group, namely $SU(3)$. QCD introduces a “color” charge, which can have values red (R), green (G), and blue (B), as well anti-colors in the case of anti-particles. QCD describes the behavior of color fields, the gauge boson of those fields, the gluon (g), and their interaction with quarks. The non-abelian nature provides for the gluon possessing a color charge resulting in the gluons undergoing self-interactions. Each gluon exists as a superposition combining both color and anti-color states (such as $(r\bar{b} + b\bar{r})/\sqrt{2}$) and the set of different possible combinations form an octet, because for a special unitary group $SU(N)$ there are $N^2 - 1$ generators. The strong coupling constant, α_s , is the characteristic parameter of the strong-nuclear force, but is known to be modulated with the scale of the interaction. At small distances the gluons provide an anti-screening effect and cancel out the strength of the strong

interaction, providing for the asymptotic freedom of the quark model while still strongly confining the quarks. Additionally, QCD requires that all free particles must be colorless, thus precluding any unbound quarks [10, 12, 13].

After the discovery of the predicted J/Ψ in 1974 and the introduction of the charm (c) quark, the quark model gained widespread acceptance and eventually expanded to include the bottom (b) and top (t) quarks [10].

1.1.3 The Electroweak Model

The Electroweak theory is the culmination in the understanding of the weak-nuclear theory and its unification with QED. The electro-weak force has long been known to be extremely short ranged, leading to the hypothesis that the mediator of the force is a massive charged-particle with an exponentially-decaying Yukawa interaction.

The result of intense effort culminated in the Glashow-Weinberg-Salam (GWS) model of the electroweak interaction. The model begins with conserved quantities weak isospin, I_3 (only the third component is important), and weak hypercharge, Y . The relation between these quantities and electric charge, Q , is:

$$Q = I_3 + \frac{1}{2}Y \quad (1.1)$$

This conservation leads to the $SU(2)_L \otimes U(1)_Y$ symmetry, where L denotes the left-handed nature of the weak-nuclear force and Y represents the hypercharge dependence of $U(1)$. For the $SU(2)_L$ symmetry $N^2 - 1 = 3$ gauge bosons are required, $b_\mu^{1,2,3}$, and for $U(1)_Y$ one is required, \mathcal{A}_μ . At this point in the formulation, all four gauge bosons are massless. This is clearly at odds with the observable world, where only one massless gauge boson is observed, the photon. Additionally, the nature of the weak-nuclear force requires a massive mediator and the $SU(2)_L$ symmetry requires massless fermions, much as QCD requires massless quarks. The solution to this is the introduction of a mechanism to break the $SU(2)_L \otimes U(1)_Y$ and leave one massless gauge boson corresponding to conserved electric charge, and provide for fermion masses [14, 15].

To break the symmetry and introduce mass, the GWS model introduces a complex scalar field with the potential:

$$V(\phi) = \mu^2|\phi|^2 + \lambda|\phi|^4 \quad (1.2)$$

with the expectation value $\langle \phi \rangle = \sqrt{-\mu^2/2\lambda}$. If $\mu^2 < 0$ and $\lambda > 0$ this results in a non-invariant vacuum for the operators of $SU(2)_L \otimes U(1)_Y$, which results in Goldstone-bosons satisfying Goldstone's Theorem that every broken

symmetry is accompanied by a massless vector boson [16]. The combination of the operators that corresponds to electric charge does leave the vacuum invariant, allowing for a massless gauge boson, which must correspond to the photon, and preserves the $U(1)_{\text{EM}}$ symmetry of QED [14, 15, 17].

The scalar field that breaks the symmetry also provides a Yukawa-coupling term to the Lagrangian that gives mass to the electron, as well as the high-generation leptons and the quarks in QCD. The gauge bosons of $SU(2)_L \otimes U(1)_Y$ can be combined to give:

$$W_\mu^\pm = \frac{b_\mu^1 \mp ib_\mu^2}{\sqrt{2}}, \quad Z_\mu^0 = \frac{-g\mathcal{A}_\mu + g'b_\mu^3}{\sqrt{g^2 + g'^2}}, \quad A_\mu = \frac{g\mathcal{A}_\mu + g'b_\mu^3}{\sqrt{g^2 + g'^2}} \quad (1.3)$$

where W_μ^\pm and Z_μ^0 are weak-nuclear force mediators and A_μ corresponds to the photon, with b_μ^3 and \mathcal{A}_μ combined such that the photon is massless and satisfies $U(1)_{\text{EM}}$ invariance while Z_μ^0 is massive. The Goldstone-bosons that were a consequence of the symmetry breaking are absorbed into the W_μ^\pm and Z_μ^0 , providing the longitudinal components to the corresponding fields and providing their mass [18]. At the time GWS model was formulated, the masses were predicted to be $M_W = 82 \pm 2 \text{ GeV}/c^2$ and $M_Z = 92 \pm 2 \text{ GeV}/c^2$ [19, 20].

When the GWS model was derived, the existence of a pair of charged gauge bosons, W^\pm , was expected, due to the nature of the weak-nuclear force. However, it remained unobserved. The predicted Z that would produce a weak neutral-current interaction was also unobserved and surprising. This prediction and the narrow mass predictions provided an avenue for potentially falsifying the GWS model. To this end a proton-anti-proton collider was built at CERN which could reach the collision energies necessary to produce W s and Z s and the predictions of the GWS model were soon verified [20]. The most recent results gives masses of $M_W = 80.385 \pm 0.015 \text{ GeV}/c^2$ [21] and $M_Z = 91.1876 \pm 0.0021 \text{ GeV}/c^2$ [3].

The field introduced in Equation 1.2 in order to break the $SU(2)_L \otimes U(1)_Y$ symmetry also results in an excitation of that field, the Higgs Boson, a scalar boson with an expected mass of

$$M_H = -\mu^2 > 0 \quad (1.4)$$

and a spin of 0 [19]. The Higgs boson is as-of-yet unobserved and has been a Holy Grail of particle physics for the last 30 years, since the confirmation of the weak gauge bosons. As of January 2012, experiments by numerous detectors have narrowed the search for the standard model Higgs boson to approximately $115 < m_H < 130 \text{ GeV}/c^2$, though other masses may be possible if accompanied by other new particles beyond the weak-scale [3, 22–24]. It is also possible that

the Higgs boson simply does not exist and another mechanism is responsible for the symmetry breaking in the GWS model.

1.1.4 The Hierarchy Problem and Quadratic Divergence

While the standard model is a successful theory due to the accuracy with which its predictions have been tested, it is still an incomplete theory owing to its failure to include phenomena such as gravity or the matter-antimatter asymmetry of the observed universe. There is a vast gulf between the strength of the standard model forces and the strength of gravity, with the electromagnetic force having a strength 10^{40} times greater than gravity [25]. A rough idea of the energy scale at which gravity is unified with the standard model forces can be determined by examining when the gravitational constant, G_N , approaches unity. This is approximately $M_{Planck} = (\hbar c/G_N)^{1/2} \sim 10^{19} \text{ GeV}/c^2$, though gravity becomes comparable to standard forces at closer to $10^{18} \text{ GeV}/c^2$ [26].

The question then is why there is this hierarchy of scales in physics? The Higgs Boson mass is necessarily at the electroweak scale, $M_{EW} \sim 100 \text{ GeV}/c^2$, in order to produce Z and W masses in agreement with observation, but gravity becomes important 16 orders of magnitude beyond this. Additionally, the Higgs mechanism mass term $-\mu^2 \sim -M_{EW}^2$ is sensitive to the scale of physics beyond the weak-scale. Quantum loop fluctuations of the type seen in Figure 1.3 lead to corrections of the Higgs mass with the cutoff, $f^2\Lambda^2$, for renormalization determined by the scale of whatever lies beyond M_{EW} , Λ :

$$-M_H^2 \sim -\mu_0^2 + f^2\Lambda^2 \sim -M_{EW}^2 \quad (1.5)$$

Here f represents other factors in the calculation. If there is a particle desert extending to the Planck scale, then the quadratic divergence $f^2\Lambda^2$ will scale to M_{Planck}^2 . Nonetheless, the GWS model requires a Higgs mass on the electroweak scale, requiring that the initial Higgs mass before the loop corrections also be of $\mathcal{O}(M_{Planck})$ and that two quadratic terms on the order of $(10^{19} \text{ GeV})^2$ cancel to within $(100 \text{ GeV})^2$. This level of exactitude in fine-tuning is not considered natural without a well-motivated physical mechanism to provide for it, and argues in favor of new particles and fields between the electroweak and Planck scales [26–28].

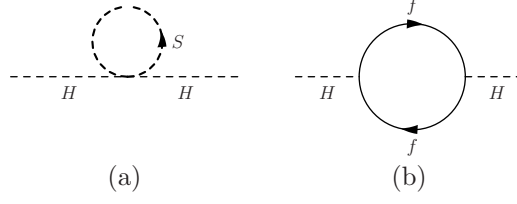


Figure 1.3: The loop corrections for the Higgs boson.

1.2 Supersymmetry

Supersymmetry is a theory positing a symmetry between fermions and bosons, such that for each fermion (boson) there is a corresponding boson (fermion) with the same quantum numbers except the spin is changed by $1/2$. This is the symmetry that gives the theory its name. In general these particles can be referred to as “sparticles”. More specifically, the partner sparticles of fermions have an *s*- prefix (sfermions, sleptons, squarks) and the partners of bosons have *-ino* suffix (gauginos, photinos, winos). Supersymmetric particles are also labeled with a tilde, e.g. $\mu \rightarrow \tilde{\mu}$. Supersymmetry is considered a particularly promising extension beyond the standard model, providing solutions to outstanding issues with the standard model.

Supersymmetry is built around operators (Q, Q^\dagger) that change the spin of the particle being operated on by a value of $1/2$, such that [17]:

$$\begin{aligned} Q|fermion\rangle &= |boson\rangle \\ Q|boson\rangle &= |fermion\rangle \end{aligned} \quad (1.6)$$

The fundamental anticommutation relationship for these operators is (ignoring spin labels):

$$\{Q, Q^\dagger\} \propto P^\mu \quad (1.7)$$

P_μ is the generator in the Poincaré group for space-time, the inclusion of which forces the operator Q to act on every field of the Lagrangian, thus making supersymmetry a symmetry that acts on every member of the standard model [29].

Supersymmetry makes every gauge boson a member of a vector superfield that links the fields of the gauge bosons to a two component fermion field which produces a gaugino, the sparticle-partner of gauge bosons. Every left-handed fermion and its right-handed charge conjugate become members of a chiral superfield that includes a complex scalar field that produces the corresponding

sfermion, as does the right handed component. Because the left-handed and right-handed fermions are transformed in the gauge group differently, they must be treated as separate particles in supersymmetry and each receives its own sparticle-partner. Thus the partners of the electron are \tilde{e}_L, \tilde{e}_R . It should be noted that the chiral notation refers to the standard model particle, as the superpartners are spin-0 particles. The Higgs field also becomes part of a chiral superfield, linked to 2-component fermion field [17, 30].

From the very beginning it is known that supersymmetry, like the electroweak symmetry, must be a broken symmetry. No one has observed a scalar boson with the mass of an electron, or any other potential sparticles matching standard model particles. How supersymmetry could be broken is not known *a priori* and the details of which can significantly affect the character of supersymmetric models. In general the symmetry breaking is expected to be spontaneous and to originate with phenomena higher than the weak-scale. It is also preferred that the symmetry breaking be *soft*, which means that it does not introduce quadratic divergences to the scalar particles. Lacking an strong motivation for a process, the Lagrangian terms necessary to break the symmetry as desired are introduced by hand [17].

1.2.1 Hierarchy and Quadratic Divergence under Supersymmetry

A primary motivation for supersymmetry is to introduce particles near the electroweak scale in such a way as to cut off the quadratic divergence of the Higgs boson. Equation 1.5 can be expanded to show the important terms (ignoring logarithmic divergences and higher order terms):

$$M_H^2 \sim \mu_0^2 + \sum_{SM\text{fermions}} g_f^2(\Lambda^2 + m_f^2) - \sum_{SM\text{scalars}} g_s^2(\Lambda^2 + m_s^2) \quad (1.8)$$

where g_f (g_s) represents the coupling constant for fermions (scalars) and m_f (m_s) is the mass of the fermion (scalar). With supersymmetry, a fermion is introduced for every scalar and vice versa and additional terms are introduced into Equation 1.8:

$$\begin{aligned} M_H^2 \sim \mu_0^2 + \sum_{SM\text{fermions}} \left(g_f^2(\Lambda^2 + m_f^2) - g_{\tilde{f}}^2(\Lambda^2 + m_{\tilde{f}}^2) \right) \\ + \sum_{SM\text{scalars}} \left(-g_s^2(\Lambda^2 + m_s^2) + g_{\tilde{s}}^2(\Lambda^2 + m_{\tilde{s}}^2) \right) \end{aligned} \quad (1.9)$$

Since the sparticles have identical quantum numbers except for spin and mass, the supersymmetric contributions will have $g_f = g_{\tilde{f}}$ and $g_s = g_{\tilde{s}}$ so that Equation 1.9 simplifies to:

$$M_H^2 \sim \mu_0^2 + \sum_{\text{fermions}} g_f^2 (m_f^2 - m_{\tilde{f}}^2) + \sum_{\text{SM scalars}} g_s^2 (m_s^2 - m_{\tilde{s}}^2) \quad (1.10)$$

This will lead to a tractable contribution to the Higgs boson mass, depending on how great the differences in masses between the sparticles and their standard model partners are. As long as the differences in mass are $\mathcal{O}(1 \text{ TeV})$ the cancellation can be considered natural [30, 31].

1.2.2 R-Parity and the Lightest Supersymmetric Particle

It is possible to construct a supersymmetric Lagrangian with terms that do not conserve baryon-number or lepton-number, though no process which violates baryon-number or lepton-number has been observed. If such terms are allowed in the supersymmetric Lagrangian, they would allow for proton decay via a meson-lepton channel, such as the channel shown in Figure 1.4. The result of this would be a proton lifetime much less than the observed limit of greater than 10^{32} s. Thus these decays are rare or non-existent [17, 32].

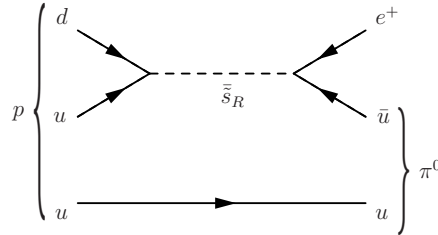


Figure 1.4: A potential decay chain for the proton into a positron and a pion in the case that L -number and B -number is not conserved [17].

However, both baryon and lepton conservation are known to be individually violated by non-perturbative electroweak effects which may be important in the early universe for baryogenesis and leptogenesis, but occur too rarely to be reliably observed at the energy densities of current colliders [33–35]. The desire to keep these processes available precludes imposing baryon-number or lepton-number conservation by hand. Instead, it is common in supersymmetric

models to introduce a conserved quantity called R-Parity, defined as:

$$R = (-1)^{3 \cdot (B-L) + 2s} \quad (1.11)$$

where B is baryon number, L is lepton number, and s is the spin. The known standard model particles have an R-Parity of 1, while the supersymmetric partners have an R-Parity of -1. R-Parity is a multiplicative quantity and such that when a supersymmetric particle decays, it must include another supersymmetric particle as a decay product. The consequence of this is that there will be a Lightest Supersymmetric Particle (LSP), which will not decay because there is no lighter sparticle to decay to while conserving R-Parity. Since supersymmetry is also broken and the sparticle masses are pushed above the electroweak scale, the sparticles are unavailable for proton decay channels and the lepton and baryon-symmetry violating terms are not permitted in a supersymmetric Lagrangian. See Figure 1.5 to see two examples of the conservation of R-Parity in interactions [36].

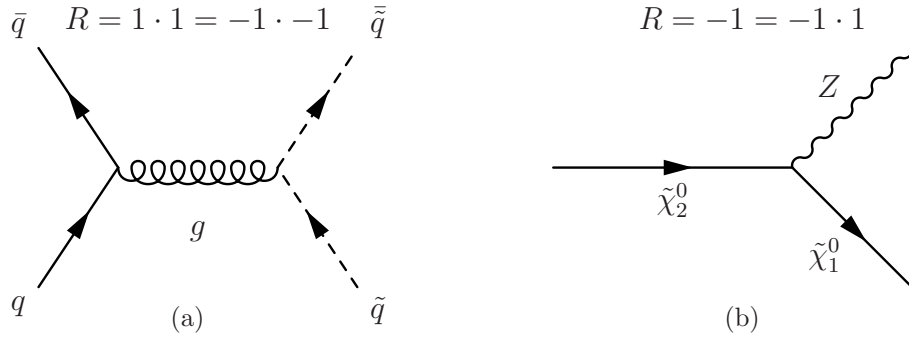


Figure 1.5: An example of R-Parity conservation in $\tilde{q}\tilde{q}^*$ -production, showing how supersymmetric particles must be produced in pairs in order for the multiplicative R-Parity to match the initial state. (b) an example of a supersymmetric decay of a $\tilde{\chi}_2^0$ into a Z and $\tilde{\chi}_1^0$, showing how supersymmetric particles must include lighter supersymmetric particles in their decay.

While the exact nature of the LSP is dependent on the particular supersymmetric model, some restrictions on its nature are determined by physical observation. It cannot possess charge or color, because that would allow it to form bound states that have not been observed; searches for anomalously heavy charged particles have ruled out any such particles with masses less than 10000 atomic mass units (~ 9 TeV) [37]. Thus, in order for the LSP to be produced at currently attainable energy scales, it must be composed of either the

$\tilde{\nu}$, a combination of neutral, colorless gauginos (neutralinos), or the gravitino. The $\tilde{\nu}$ is excluded by observations made by astrophysics experiments and the Large Electron-Positron collider [36].

An additional motivation for R-Parity is that the presence of a neutral, colorless LSP at the end of sparticle decay chains makes the LSP an ideal candidate for the composition of dark matter, which is required due to astrophysical observations. Evidence for dark matter was first observed by Swiss astronomer Fritz Zwicky [38], who noticed a disparity in the mass estimated from the luminosity of galaxies in the Coma cluster compared to the mass estimate from their orbital velocities using the virial theorem. The luminosity measured for the Coma cluster galaxy is $5.5 \cdot 10^{12}$ solar luminosities (L_{\odot}), which suggests an estimate of $5.5 \cdot 10^{12}$ solar masses (M_{\odot}), assuming stars make up the bulk of the mass. The virial theorem for an r^{-1} potential states that $2 \langle K \rangle + \langle U \rangle = 0$ for kinetic energy, K , and potential energy U . Using Newtonian gravity and assuming the cluster is uniform and that the galaxies have isotropic velocity dispersion ($\sigma_r^2 = \sigma_{\theta}^2 = \sigma_{\phi}^2$), an estimate for the total mass can be made:

$$M_{total} = \frac{5R\sigma_r^2}{G} \quad (1.12)$$

for cluster radius R , gravitational constant G , and radial velocity dispersion, σ_r . Modern measurements of the Coma cluster find $\sigma_r = 977$ km/s and $R = 9.3 \cdot 10^{19}$ km, resulting in a mass estimate for the Coma cluster of $3.3 \cdot 10^{15} M_{\odot}$. This gives a factor of ~ 670 disparity in the mass estimated via the virial theorem and that estimated by luminosity [39, 40]. One explanation proposed by Zwicky for the disparity was the presence of large amounts of non-luminous matter: “dark matter”. The dark matter hypothesis has since been bolstered by measurements of galactic rotation curves [41], observations of gravitational lensing [42], and observations of the Cosmic Microwave Background (CMB) [43]. The combination of these and numerous other observations point to the existence of a Weakly-Interacting Massive Particle (WIMP) with an average density of $\rho_{WIMP} \approx 1.2 \times 10^{-6}$ GeV/cm³ [17]. Supersymmetric models with R-Parity and an LSP as a consequence offer the tantalizing possibility of providing solutions to both standard model problems and cosmology problems.

1.2.3 Minimal Supersymmetric Standard Model

While there are numerous supersymmetric models, the most straightforward is the Minimal Supersymmetric Standard Model (MSSM), which is

a softly broken general supersymmetry which aims to introduce the fewest changes to the standard model.

The first change made is a modification of the Higgs sector of the standard model. In the standard model the Higgs field gives mass via Yukawa interactions to the $I_3 = 1/2$ fermions, while the charge-conjugate Higgs field gives mass to the $I_3 = -1/2$ fermions. However, supersymmetry prevents Yukawa interactions that involve a scalar field and its hermitian conjugate due to right-chiral superfields being excluded from the superpotential of supersymmetry. Instead, a second left-chiral Higgs field is introduced that couples with $I_3 = -1/2$ fermions to give them mass. The Higgs doublets are:

$$H_u = \begin{pmatrix} H_u^+ \\ H_u^0 \end{pmatrix}, \quad H_d = \begin{pmatrix} H_d^0 \\ H_d^- \end{pmatrix} \quad (1.13)$$

where the labeling u, d reflects that H_u acts on $I_3 = 1/2$ fermions, which include up-type quarks and neutrinos, while H_d acts on $I_3 = -1/2$ fermions, down-type quarks and the massive leptons. Additionally, the pair of doublets allows for their sparticle partners to cancel their respective contributions to quadratic divergences. This gives eight degrees of freedom for the two Higgs doublets, of which three become incorporated into the W and Z . This results in five observable Higgs particles, h^0 , H^0 , A^0 , and two charged-Higgs, H^\pm . The h^0 particle corresponds most closely to the standard model Higgs [44, 45].

Much like the components of the electroweak theory mix to form γ , Z , and W , certain sparticles also undergo mixing. The gauginos, \tilde{B} and \tilde{W}^0 , and the neutral Higgs components, $\tilde{H}_{u,d}^0$, mix to become four *neutralinos*, denoted as $\tilde{\chi}_{i=1,2,3,4}^0$. The sparticles corresponding to the W and the charged components of the Higgs doublets, \tilde{H}_u^+ and \tilde{H}_d^- , mix to produce two *charginos*, denoted as $\tilde{\chi}_{i=1,2}^\pm$. The sfermions also are capable of mixing. No principle prevents all of the sleptons from mixing together to form new states, as well as the squarks with themselves. However, the gulf in mass between the second and third fermion generations results in degenerate states for the lighter two generations and only the $\tilde{\tau}_{l,r}$, $\tilde{b}_{l,r}$, and $\tilde{t}_{l,r}$ undergo mixing, producing new states $\tilde{\tau}_{1,2}$, $\tilde{b}_{1,2}$, and $\tilde{t}_{1,2}$. The resulting spectrum of the supersymmetric standard model can be seen in Table 1.5 [17, 30].

One notable fact of the MSSM is the sheer number of parameters it introduces. In addition to the 19 parameters of the standard model (including the Higgs sector), the MSSM introduces 105 new parameters. Of those, three are additions to the Higgs sector from the extra Higgs doublet, five reflect the gaugino masses, and the other 97 are concerned with the sfermions. With 124 independent parameters, the MSSM provides a considerable challenge to

Particles	Sparticles
$\gamma, Z^0, h^0, H^0, A^0$	$\chi_1^0, \chi_2^0, \chi_3^0, \chi_4^0$
W^\pm, H^\pm	χ_1^\pm, χ_2^\pm
G	\tilde{G}
$e^-, \nu_e, \mu^-, \nu_\mu, \nu_\tau$	$\tilde{e}_r^-, \tilde{e}_l^-, \tilde{\nu}_e, \tilde{\mu}_r^-, \tilde{\mu}_l^-, \tilde{\nu}_\mu, \tilde{\nu}_\tau$
τ^-	$\tilde{\tau}_1, \tilde{\tau}_2$
u, d, s, c	$\tilde{u}_r, \tilde{u}_l, \tilde{d}_r, \tilde{d}_l, \tilde{s}_r, \tilde{s}_l, \tilde{c}_r, \tilde{c}_l$
b	\tilde{b}_1, \tilde{b}_2
t	\tilde{t}_1, \tilde{t}_2

Table 1.5: The particles and sparticles of the supersymmetric standard model [17, 30]

modeling its processes to make predictions. Fortunately, much of the parameter space is ruled out where it comes into conflict with observation. Should supersymmetry be found to be a feature of the universe, it is hoped that measurements will lead to an understanding of the symmetry-breaking process and allow a simplification of the parameter space. Models based on the MSSM are usually simplified via assumptions about the nature of symmetry breaking [46, 47].

1.2.4 Paving the Road to Unification with Supersymmetry

The running of the coupling constants in a gauge theory can be extrapolated from an initial energy scale, Q_0 , to a higher energy scale, Q , via the relationship:

$$\frac{1}{\alpha_i(Q)} = \frac{1}{\alpha_i(Q_0)} + \frac{b_i}{2\pi} \ln \frac{Q_0}{Q} \quad (1.14)$$

where $\alpha_{i=1,2,3}$ is the coupling constant for (1) the electromagnetic force, (2) the weak-nuclear force, and (3) the strong-nuclear force. The parameter b_i is dictated by the number of fermion generations, N_g , and the number of Higgs doublets, N_H , according to the equation:

$$\begin{pmatrix} b_1 \\ b_2 \\ b_3 \end{pmatrix} = \begin{pmatrix} 0 \\ -\frac{22}{3} \\ -11 \end{pmatrix} + \frac{4}{3} N_g + \begin{pmatrix} \frac{1}{10} \\ \frac{1}{6} \\ 0 \end{pmatrix} N_H \quad (1.15)$$

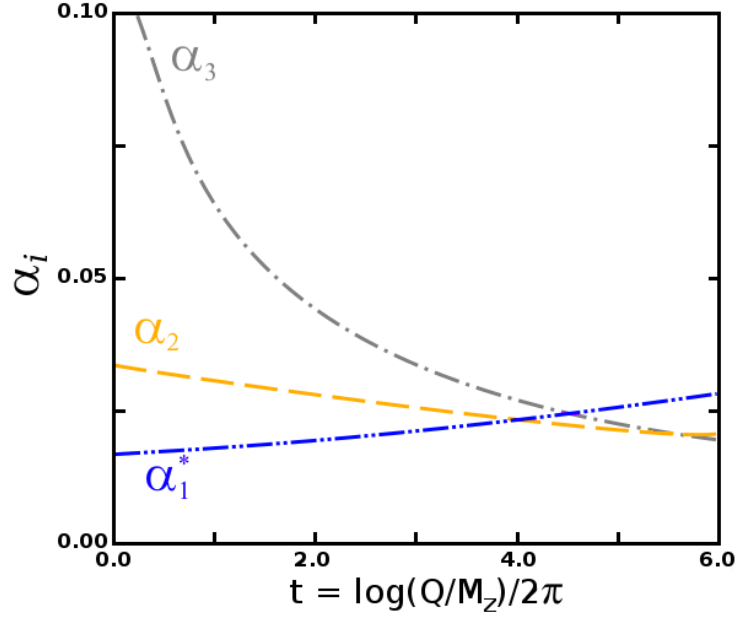
For the standard model $N_g = 3$ and $N_H = 1$. Running Equation 1.14 from $Q_0 = M_Z$ up to the expected unification scale of $\sim 10^{18}$ GeV gives the result shown in Figure 1.6(a). Note that the plotted coupling constant is $\alpha_1^* \equiv 5\alpha/3$, which is the value appropriate for Grand Unification Theories. One can see that while the coupling constants converge at approximately 10^{14} GeV, there is no true unification of the coupling constants. However, if the standard model is supplemented by weak-scale supersymmetry, the relation in Equation 1.15 changes due to the inclusion of the particles and becomes:

$$\begin{pmatrix} b_1 \\ b_2 \\ b_3 \end{pmatrix} = \begin{pmatrix} 0 \\ -6 \\ -9 \end{pmatrix} + 2N_g + \begin{pmatrix} \frac{3}{10} \\ \frac{1}{2} \\ 0 \end{pmatrix} N_H \quad (1.16)$$

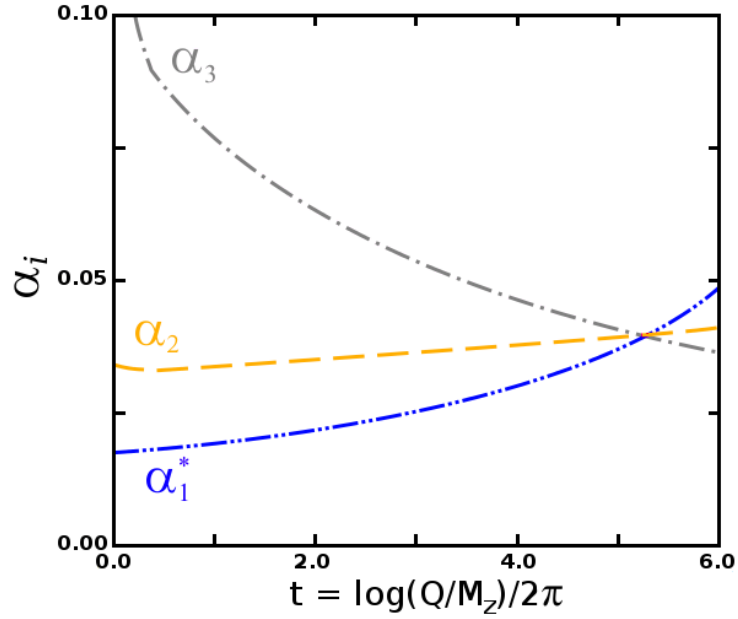
Additionally, supersymmetry requires that there be at least two Higgs doublets, $N_H = 2$. The resulting evolution of the coupling constants then comes to look like Figure 1.6(b), where the constants converge at 10^{16} GeV and results in a more convincing unification. This unification is often taken to be indirect evidence for weak-scale supersymmetry and motivates searches for supersymmetry. Note that the elbow at approximately 10^3 GeV is an artifact due to the couplings for the standard model being used instead of the supersymmetric ones up to that point. It should also be stated that supersymmetry is not a silver bullet for unification and the quality of the unification is entirely dependent upon the model used. If the number of Higgs doublets is increased to $N_H = 4$, the couplings again come to converge like the standard model case, without true unification [30, 48].

1.2.5 Gauge Mediation

One of the fundamental elements of a complete supersymmetric theory is the manner in which supersymmetry is broken. The MSSM sidesteps this question by parameterizing a generic Lagrangian consistent with the standard model and introducing the minimum number of terms. There is an advantage to speculating on the nature of the symmetry breaking though, since in certain models the number of parameters can be reduced from the 105 of the MSSM and other theoretical problems with the MSSM can be reduced or eliminated [49]. It is common to further refine the MSSM by pre-supposing that SUSY is broken in a “hidden sector” by non-SM fields that have been unobserved and are unlikely to be observed prior to the SUSY sector; the effects of this hidden sector are then transmitted to the SUSY sector [50]. One framework for this process is Gauge-Mediated Supersymmetry Breaking (GMSB).



(a) The evolution of the gauge-coupling constants under the standard model.



(b) The evolution of the gauge-coupling constants in a weak-scale SUSY model, with thresholds at 1 TeV.

Figure 1.6: The gauge-coupling constants evolution from the experimentally measured values at the Z -pole. $\alpha_1^* \equiv 5\alpha/3$, the relevant value in Grand Unified Theories. α_1 corresponds to the electromagnetic force, α_2 corresponds to the weak-nuclear force, and α_3 corresponds to the strong force [30].

In GMSB, the hidden sector where supersymmetry is broken communicates the SUSY breaking through a messenger sector to the MSSM superfields. The messenger sector couples to the hidden sector but also has $SU(3) \times SU(2) \times U(1)$ quantum numbers coupling it to the MSSM sector via SM gauge interactions [47, 49, 51]. The coupling of the messenger fields to the hidden sector produces in the fields a supersymmetric mass of order M with mass-squared splittings of order F , with \sqrt{F} being the scale of supersymmetry breaking in the messenger sector. The actual framework of messenger sector is unknown and produces a model-dependence in GMSB; the hidden sector is also unknown, but more insulated from influencing the model [52].

Because the MSSM does not couple directly to the hidden sector and only couples to the messenger sector through gauge interactions, masses arise in loop corrections and the SM gauge bosons are protected from further mass corrections by gauge invariance. The gaugino masses are generated in one loop since they can couple directly to messengers and thus their masses are dictated by the scale of supersymmetry breaking and their gauge coupling strength [17, 52, 53]. Taking $F/M = \Lambda$, the gaugino masses are predicted to be:

$$M_i = \frac{\alpha_i}{4\pi} \cdot \Lambda, \quad i = 1, 2, 3. \quad (1.17)$$

for the respective gauge interactions. The sfermions cannot couple directly to the messenger sector and thus receive a two-loop contribution to their squared masses. Each sfermion squared mass is determined by the supersymmetric mass scale, Λ , and the gauge couplings, resulting in contributions to the squared masses of order $(\alpha_i \Lambda)^2$ for each gauge interaction. Note that in many gauge mediation models the mass scale is shared by sfermion and gaugino mass terms; this results in a hierarchy of masses that makes the color-state sparticles more massive than other sparticles [54, 55]. This results in gaugino and sfermion masses of the same order in the MSSM [17, 52, 53]. In order to produce a relatively natural closure of the quadratic divergence of the Higgs boson, we expect $\Lambda \sim \mathcal{O}(100 \text{ TeV})$, resulting in sparticle masses of less than 1 TeV [47].

A cause for concern in SUSY is the flavor problem, whereby the existence of sparticles can cause new channels for flavor-changing neutral currents (FCNCs) to occur. SM limits on FCNCs have been set through measurements of $K^0 - \bar{K}^0$ and $B^0 - \bar{B}^0$ mixing and searches for flavor-changing decays such as $\mu \rightarrow \gamma e$ and $b \rightarrow \gamma s$. These measurements set strong bounds on FCNCs in supersymmetry and it is necessary for a mechanism to exist to suppress FCNCs and solve the flavor problem. The strength of FCNCs are dependent on the mass splitting of the sfermions generations, thus mechanisms which induce

sfermion degeneracy solve the flavor problem. That this mass degeneracy is intrinsic to the character of GMSB models is seen as a virtue [17, 56].

Paralleling Goldstone’s Theorem [16], the spontaneous breaking of supersymmetry results in a massless fermion, the goldstino. As opposed to the generators of the electroweak model, the generators of SUSY must carry spin $\frac{1}{2}$ in order to achieve the basic operations seen in Equation 1.6, which produces a massless fermion instead of a massless boson when the symmetry is broken [57]. However, much like the Higgs Mechanism which gives mass to electroweak mediators, a super-Higgs mechanism sees the goldstino being absorbed by the gravitino and giving it mass:

$$m_{3/2} = \frac{F}{\sqrt{3}M_P}, \quad (1.18)$$

where M_P is the reduced Planck mass, $M_{Planck}/\sqrt{8\pi}$. Note that the gravitino mass is proportional to F/M_P as opposed to the other sparticle masses, which are proportional to $\Lambda = F/M$. In the realm of low-energy SUSY breaking, $M \ll M_P$, the gravitino is very likely to be the LSP [51, 52, 58]. The goldstino component has a large effect on the coupling of other sparticles to the gravitino, allowing the very weak gravitational couplings to be ignored in favor of the stronger goldstino couplings and possibly allowing for prompt decays observable in a collider detector experiment [17].

1.2.6 General Gauge Mediation

General gauge mediation (GGM) is an effort to provide a generic framework for the diverse GMSB models. The fundamental feature of GGM is the requirement that as the running of the gauge interaction coupling constants approach the weak scale ($\alpha_i \rightarrow 0$), the theory decouples into the MSSM and the isolated hidden sector responsible for supersymmetry breaking. Strongly coupled theories are included in the framework via correlation functions which parameterize the hidden sector contribution on the MSSM. This framework reproduces the standard characteristics of gauge-mediation, including degenerate sfermion masses and the LSP being a gravitino, although the mass predictions are modified by the correlation function [59, 60]. This modification contains no restriction preventing color-state sparticles from being at the same or lower mass than other sparticles, which is markedly different from the prediction of previous gauge mediation models or models in which gravity is responsible for supersymmetry breaking [54].

The GGM parameter space spans regions where almost any sparticle is a possible NLSP [61]. In ATLAS, the parameters used to define GGM are:

- m_1 , the U(1) gaugino mass,
- m_2 , the SU(2) gaugino mass,
- $m_{\tilde{g}}$, the gluino mass,
- μ , the SUSY Higgs mass parameter,
- $\tan\beta$, the ratio of the SUSY Higgs vacuum-expectation values,
- $c\tau_{\text{NLSP}}$, the characteristic range of the NLSP before it decays, which is determined by the scale of supersymmetry breaking, F ,

as well as the soft parameters from the correlation functions. The interesting feature of the various GGM models is the identity of the NLSP. For the analysis present herein, there are two NLSP cases which are considered:

Higgsino NLSP: In this case, $|\mu| \ll |m_1|, |m_2|$, and the NLSP is the neutral higgsino, \tilde{h} . Specifically, this analysis is interested in the models whereby the branching ratios favor a Z -boson rich decay, $\tilde{\chi}_1^0 \rightarrow Z\tilde{G}$. Figure 1.7 provides an example of a three lepton decay for this case when the $\tilde{\chi}_1^\pm$ decays to an off-shell W^\pm and $\tilde{\chi}_1^0$. The W^\pm may then decay leptonically while the $\tilde{\chi}_1^0$ decays non-leptonically to a \tilde{G} and SM particles [61, 62].

Wino co-NLSPs: This case occurs when $|m_2| \ll \mu$ and $|m_2| < |m_1|$ and the lightest neutralino is wino-like (i.e., \tilde{W}^0). The difference in mass between the neutral and charged wino will be approximately m_Z^4/μ^3 and be almost degenerate for $\mu > \mathcal{O}(100 \text{ GeV})$. The neutral NLSP will then decay to $Z\tilde{G}$ or $\gamma\tilde{G}$ and the charged NLSP will decay to $W^\pm\tilde{G}$. In Figure 1.7 this produces three leptons for the case where the $\tilde{\chi}_1^\pm$ decays to $W^\pm\tilde{G}$ [61, 62].

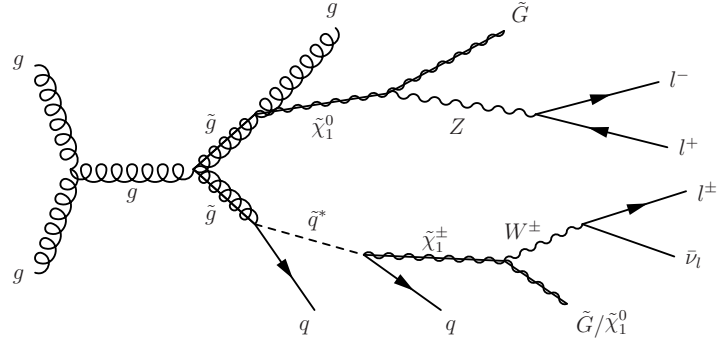


Figure 1.7: A potential supersymmetric process via $\tilde{g}\tilde{g}$ production which could produce three leptons and $E_{\text{T}}^{\text{miss}}$ from the gravitino and neutrino. $\tilde{\chi}_1^\pm$ is expected to decay to $W^\pm\tilde{\chi}_1^0$ ($W^\pm\tilde{G}$) in the higgsino NLSP (wino co-NLSP) case.

*Now witness the firepower of this fully **armed** and **operational** battle station!*

George Lucas [63]

2

The CERN Accelerator Complex

The Accelerator Complex at CERN is composed of a chain of accelerators that provide protons of increasingly higher energy which are eventually injected into the Large Hadron Collider (LHC), the accelerator which provides proton-proton collisions to the ATLAS detector.

Protons are provided by Linac2 with an energy of 50 MeV and current of 180 mA. Pulses of protons from Linac2 are injected into the Proton Synchrotron Booster (PSB). The PSB is composed of four parallel accelerator rings that raise the energy of the protons to 1.4 GeV before they are injected into the Proton Synchrotron (PS). The PS then accelerates the protons to 25 GeV. The protons are then transferred to the Super Proton Synchrotron (SPS), where they are brought to an energy of 450 GeV and injected into the LHC [64, 65]. During operations involving the collisions of heavy-ions, the accelerator chain starts with 3.2 MeV/nucleon lead ions from Linac3 are injected into the Low Energy Ion Ring (LEIR) and accelerated to 72.2 MeV/nucleon before being injected into the PS [66].

The LHC is composed of two counter accelerating rings housed in a 26.7 km circumference tunnel 45 to 175 m beneath the Franco-Swiss border. Bunches of protons are injected into each of the two rings where they are then accelerated to collision energy. The LHC was designed toward a collision energy of 7 TeV per beam and a center of mass energy of 14 TeV. However, it is currently operated at 3.5 TeV per beam with a center of mass energy of 7 TeV. This is a precautionary measure in response to an incident involving the LHC magnets which occurred in September of 2008 during the initial testing of the LHC [67].

The LHC is designed for a peak instantaneous luminosity of $L = 10^{34}$ cm⁻²s⁻¹ [68]. At the end of the pp collision data taking in 2011, the record

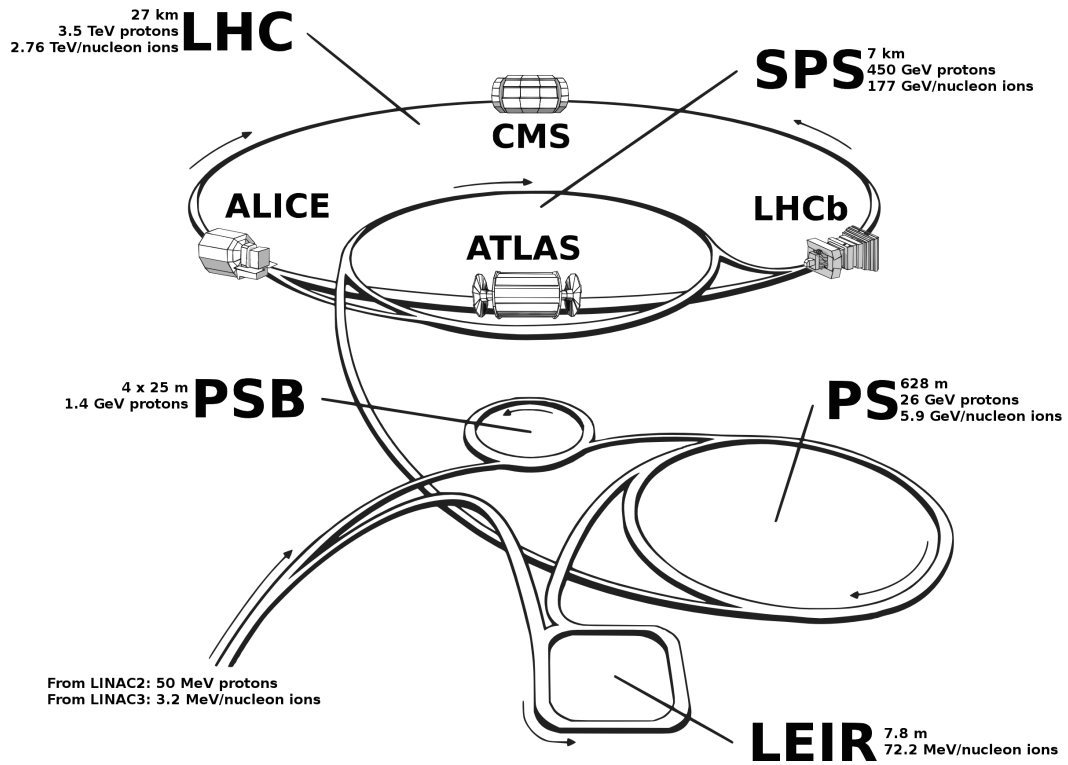
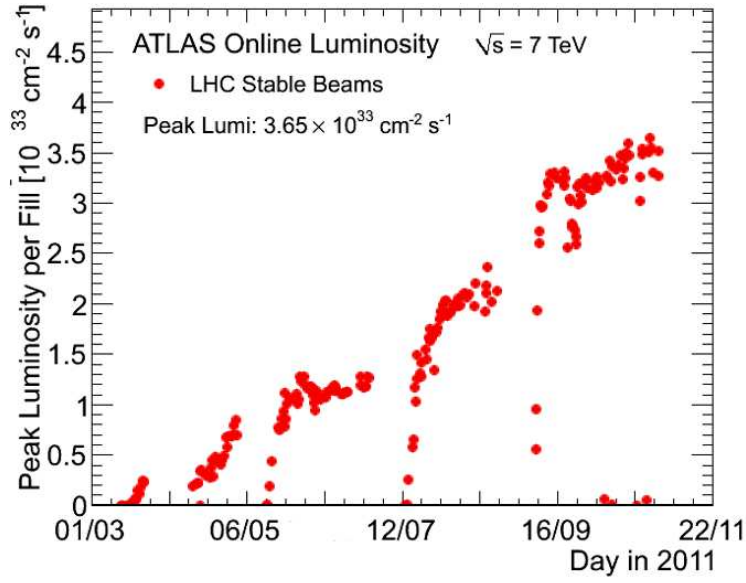
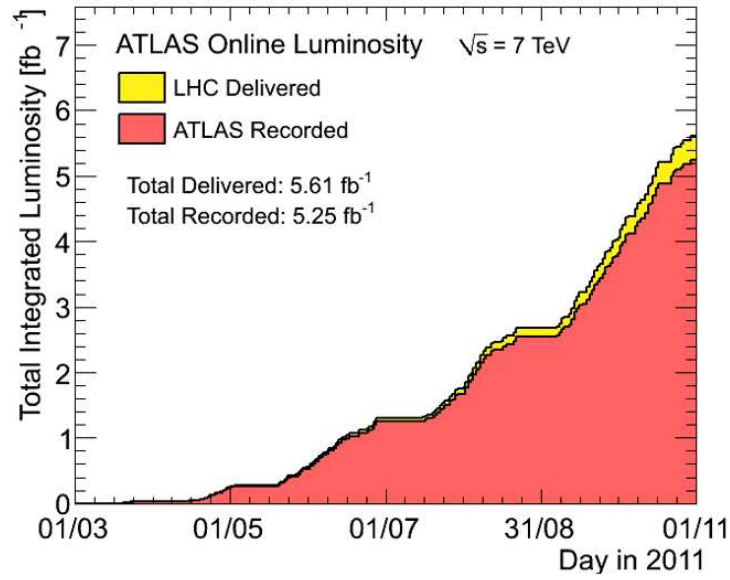


Figure 2.1: The accelerator complex at CERN, including the LHC and the various accelerators used to supply protons and heavy ions to the LHC.

peak instantaneous luminosity achieved was $3.65 \cdot 10^{33} \text{ cm}^{-2}\text{s}^{-1}$. Over the course of the 2011 collisions running, the LHC delivered 5.61 fb^{-1} of integrated luminosity. Of which, ATLAS recorded 5.25 fb^{-1} of stable data. Plots of the instantaneous luminosity and the integrated luminosity can be seen in Figure 2.2.



(a)



(b)

Figure 2.2: (a) The peak instantaneous luminosity achieved each fill by the LHC for the 2011 data taking period, (b) The integrated luminosity delivered by the LHC and recorded by ATLAS per day for the 2011 data taking period.

A process cannot be understood by stopping it. Understanding must move with the flow of the process, must join it and flow with it.

Frank Herbert [69]

3

The ATLAS Experiment

The ATLAS Detector is a multi-purpose particle detector. The detector consists of multiple sub-detectors combined into one apparatus in order to allow ATLAS to make measurements on multiple types of particles and over a large solid angle. The sub-detectors of ATLAS are detailed in the following sections.

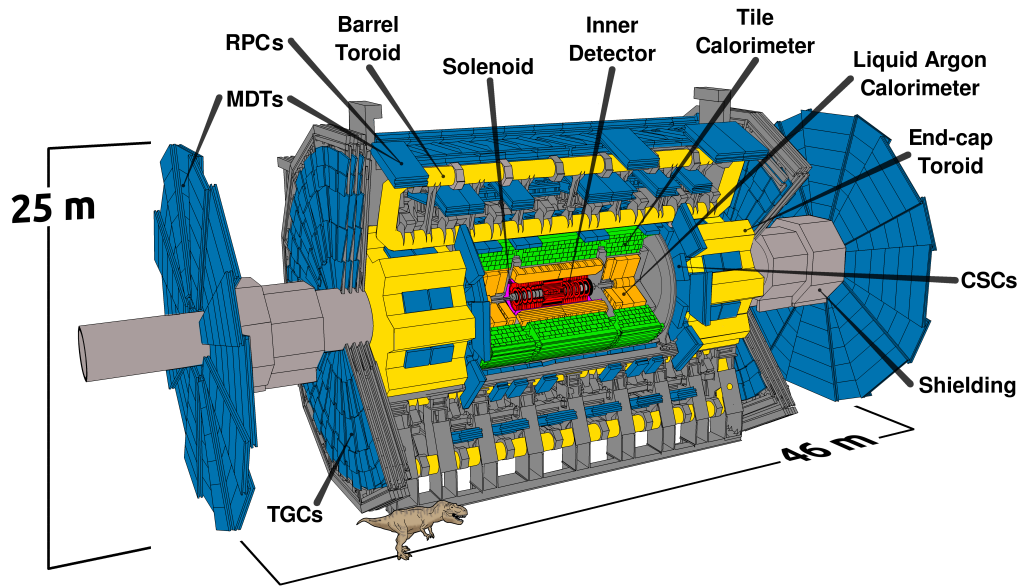


Figure 3.1: The ATLAS Detector, showing the overall size and the relative positions of the various sub-detectors.

3.1 Inner Tracker

The design of the ATLAS inner detector systems is intended to provide for efficient and robust measurement of tracks in the high-radiation region near the interaction point. Hits recorded in the inner detector are used to make high-resolution measurements of the position and momentum of each track and provide for measurements of the primary and secondary vertices, and in turn allow for more involved analysis techniques, such as flavor-tagging. At the accelerator design luminosity of $10^{34} \text{ cm}^{-2}\text{s}^{-1}$ the inner detector will be required to measure on the order of 1000 charged particle tracks every 25 ns with dozens of hits recorded for each track, down to a p_T threshold of 0.5 GeV [70, 71]. Consequently, the inner detector must be capable of functioning in this high-radiation environment for the duration of the ATLAS experiment and provide sufficient granularity of measurement to allow for accurate pattern recognition, and balance these objectives against affordability. The inner detector makes use of three sub-detectors to meet these needs. The pixel and Semiconductor Tracker (SCT) are silicon sensor based detectors which provide high-precision measurement near the beam line, while the Transition Radiation Tracker (TRT) makes use of gas-filled straws and provides a less precise measurement of hit positions that is balanced by the greater number of hits in the sub-detector [70, 72]. The entire inner detector is provided with a 2 T magnetic field by the ATLAS central solenoid (see Section 3.5.1).

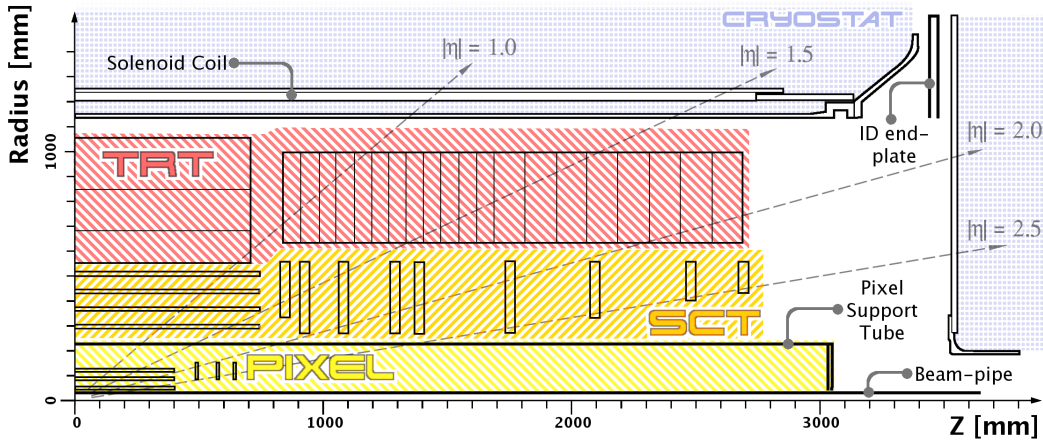


Figure 3.2: The layout of the ATLAS inner tracker, shown as the cross-section of one quarter of the detector.

3.1.1 The Pixel Tracker

The innermost component of the ATLAS Experiment is the pixel tracker. The pixel tracker provides a highly granular measurement of particle tracks using 80.4 million silicon pixel sensors, each with a sensitive area of $50 \times 400 \mu\text{m}^2$. The pixel detector is sub-divided into three layers (and thus, likely to provide three points to measure track trajectories) in both its barrel and endcap, extending from 50.5 mm from the beam pipe to 122.5 mm. The innermost layer is referred to as the vertexing layer, due to its importance in identifying vertices (and in turn, heavy flavor jets). The pixel tracker covers the range $|\eta| < 2.5$ in pseudo-rapidity. The pixel tracker has a designed spatial accuracy of $10 \mu\text{m}$ in $R-\phi$ for both barrel and endcap sections. The barrel has an accuracy of $115 \mu\text{m}$ in z and the endcaps have an accuracy of $115 \mu\text{m}$ in R [70].

Of critical importance to the pixel tracker is radiation-hardness. The vertexing layer is expected to receive 158000 Gy/y and the outer pixel layer is expected to receive 25400 Gy/y for a luminosity of $10^{34} \text{ cm}^{-2}\text{s}^{-1}$ and year of 10^7 s [71]. The sensors are composed of an n-bulk substrate with n+ implants oxygenated to help increase radiation-hardness, although radiation exposure will eventually convert the substrate into a p-type [71, 73]. Due to the high fluxes at the vertexing layer it is scheduled for replacement after an integrated luminosity of 300 fb^{-1} , with a new pixel layer called the Insertable B-Layer to be inserted at 31 mm, between the vertexing layer and a narrower replacement beam pipe [74, 75].

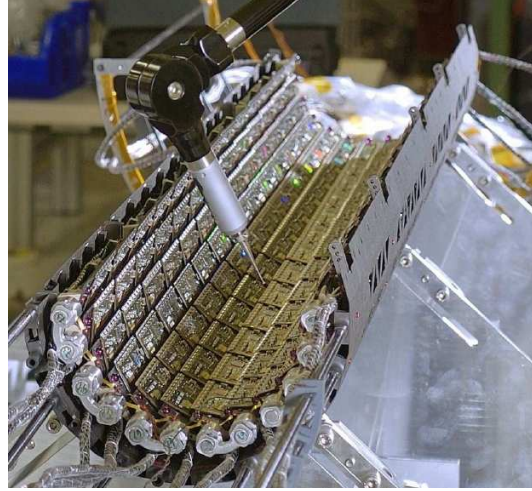


Figure 3.3: A half-shell of the pixel barrel being loaded with rows of pixel modules [71].

3.1.2 The SemiConductor Tracker

The Semi-Conductor Tracker (SCT) is composed of 4088 silicon sensor modules with a total of 6.3 million read-outs, divided into a barrel region extending up to $|\eta| < 1.1$ and two end-caps which extend the coverage to $|\eta| < 2.5$.

Each module consists of two sensors glued back-to-back with an angular offset of 40 mrad in order to provide 2D spatial resolution. Each sensor has 768 active silicon strips [76]. In the barrel region the modules are divided between four layers extending from a sensitive radius of 299 mm to 514 mm. Each endcap has 9 layers which extend from $839 < |z| < 2735$ mm with a radius from 275 mm to 560 mm. In both the barrel and endcap, the SCT provides a resolution of $17 \mu\text{m}$ in $R - \phi$. In the barrel the z -resolution is $580 \mu\text{m}$ and the endcap provides a resolution of $580 \mu\text{m}$ in R [70, 71]. The SCT sees considerably less radiation flux than the pixel tracker, receiving an ionization dose of 7590 Gy/y in the innermost SCT layer [71].

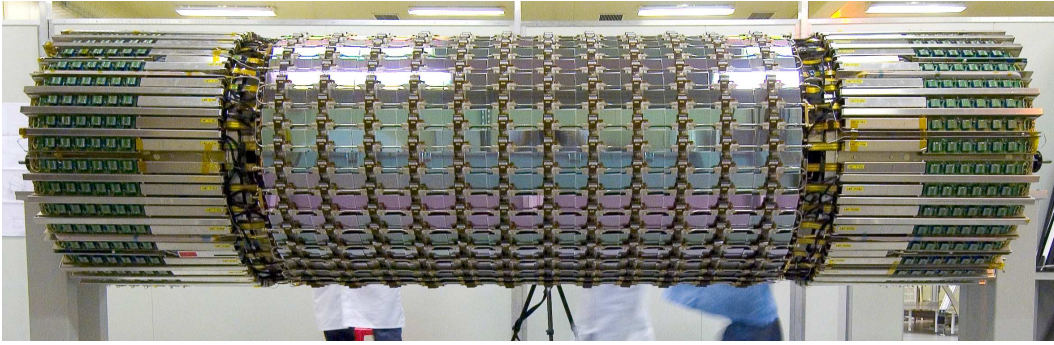


Figure 3.4: A completed SCT barrel after all of the individual modules have been mounted [77].

3.1.3 The Transition Radiation Tracker

The Transition Radiation Tracker (TRT) is the outermost sub-component in the inner tracker. The TRT is composed of 4 mm diameter drift tubes composed of a carbon reinforced polyimide tubes coated internally with $0.2 \mu\text{m}$ of aluminum to form a cathode and containing a $31 \mu\text{m}$ gold-plated tungsten wire anode. The gas mixture used in the drift tubes is 70% Xe, 27% CO_2 , and 3% O_2 . This configuration gives a spatial resolution of $130 \mu\text{m}$ in $R - \phi$ [71]. While the TRT does not provide particularly fine spatial resolution compared to the pixel detector or SCT, it complements these detectors with providing a large number of hits, typically 30 hits per track [70]. Surrounding the drift tubes in the TRT modules is a matrix of $19 \mu\text{m}$ -diameter polypropylene-polyethylene fibers. These fibers aid in particle identification through transition radiation X-ray photons produced as charged-particles cross between materials with different dielectric constants. The TRT can aid in the identification of electrons

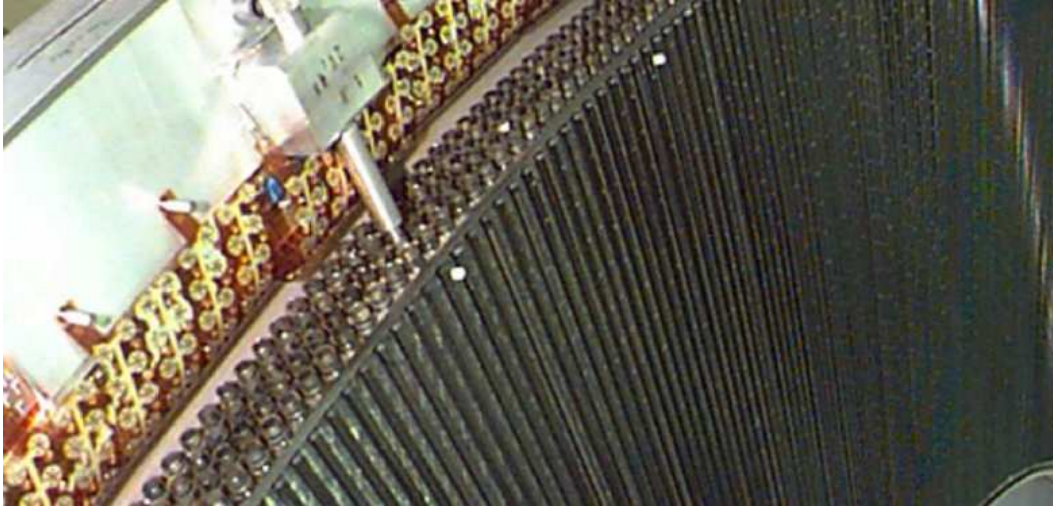


Figure 3.5: An end-cap of the TRT during assembly. Clearly visible is the first layer of drift tubes resting on the polypropylene-polyethylene transition radiation fibers. The ends of an additional three layers of drift tubers are visible at the rim of the drift tube section [71].

based on the signature of the transition radiation photons entering the drift tube [78].

The TRT provides bulk charged track measurements to a pseudo-rapidity of $|\eta| < 2.0$ [78]. There are 52544 drift tubes in the barrel region, each 144 cm long and running parallel to the beam pipe. The barrel drift tubes are split into two active regions at $\eta = 0$ by a plastic support and fused glass capillary in order to decrease occupancy. In the innermost nine layers of the barrel (out of 73), the drift tubes are split into three sections, with the middle 80 cm section not read out to decrease occupancy. Each end-cap contains 122880 drift tubes that are 37 cm long and aligned perpendicular to the beam pipe. In total there are 350848 channels to be read out in the TRT [70, 79].

3.2 Calorimetry

The ATLAS Detector makes use of two calorimeter technologies for its energy measurements. The inner calorimeter is the Liquid Argon calorimeter, which is a sampling calorimeter using cryogenically liquified noble gas as the active medium. The other system used for calorimetry is the Tile Calorimeter, a scintillating-tile sampling calorimeter. The LAr calorimeter is used for electromagnetic measurements, forward calorimetry, and also for the hadronic

measurements in the endcap regions where high radiation levels exclude a scintillating tile system. The tile system performs hadronic measurements in the barrel region and the extended barrel region [80].

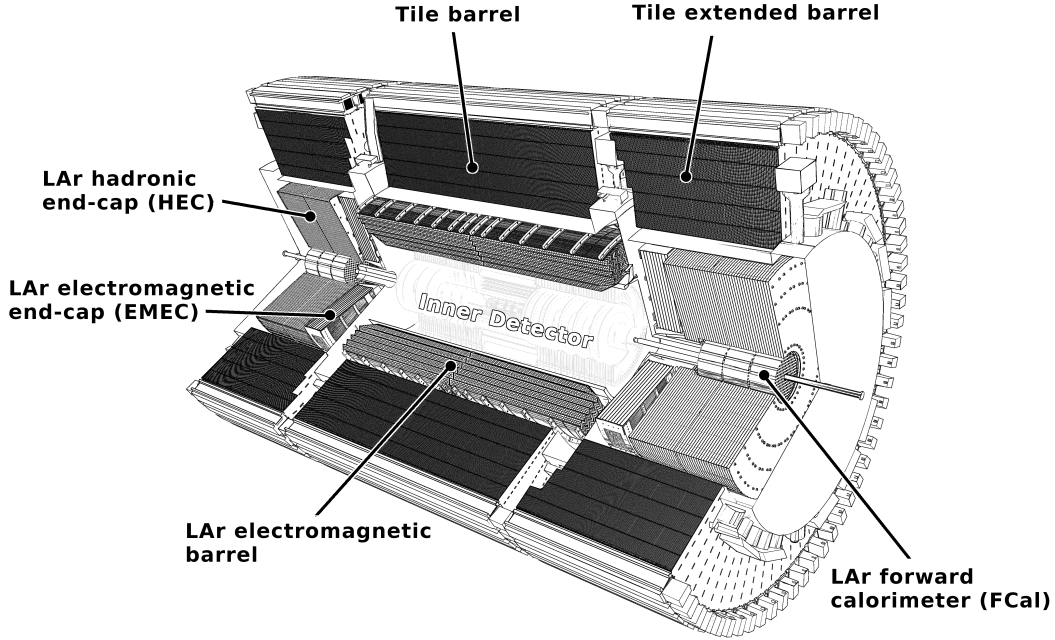


Figure 3.6: The layout of the ATLAS calorimeter.

3.2.1 Liquid Argon Calorimeter

The use of a Liquid Argon (LAr) sampling calorimeter in ATLAS was driven by the necessity to have a radiation hard calorimeter, while also providing a linear behavior and stable response, all of which are provided by the use of ionizing cryogenic argon [80]. The LAr calorimeter is divided into multiple partitions with differing designs to match diverse measurement requirements and limitations. See Fig. 3.7 for examples of each sub-detector's architecture. These partitions are:

Electromagnetic (EM) Barrel & End-caps: The EM partition is notable for a unique accordion geometry that aids hermetic coverage in ϕ by minimizing cracks, as well as providing a single read-out at the either end of a module, instead of the interrupting read-outs in a traditional parallel

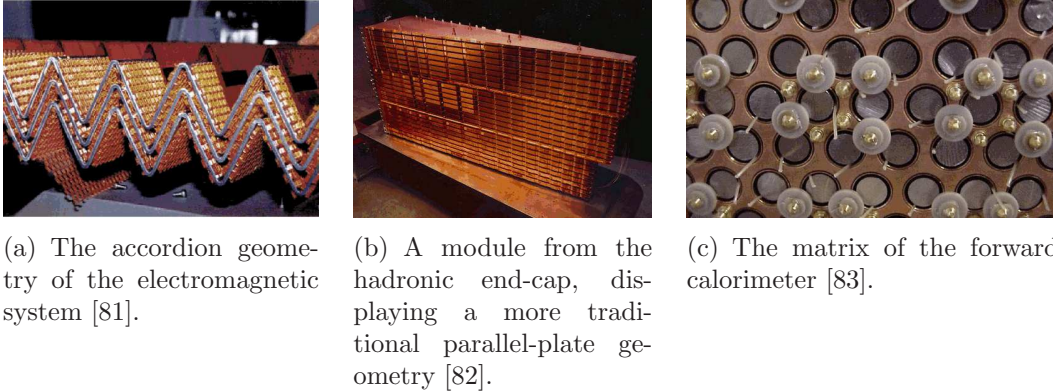


Figure 3.7: The hardware architectures used in the segments of the LAr calorimeter.

plate geometry. The absorber in this partition is composed of lead laminated with steel support plates and provides for a minimum 22 radiation lengths. The gap between the absorbers contains three copper layers separated by honeycombed polyimide sheets that are immersed in the active medium. The outer two layers provide the high-voltage potential with the inner layer acting as a read-out by capacitive coupling [71, 84]. The read-out is etched to provide for η granularity [85]. The EM barrel region contains 109568 read-out channels, while the end-caps contain 63744 read-out channels [86]. The EM partition extends to $|\eta| < 3.2$, with the barrel covering up to $|\eta| < 1.475$ and the end-caps covering $1.5 < |\eta| < 3.2$ [80]. Up to $|\eta| < 1.8$, barrel and end-cap are equipped with a pre-sampler inside of the first layer which is used to estimate energy losses due to dead material. The design energy resolution of the EM partition is $\sigma(E)/E \sim 10\%/\sqrt{E} \oplus 0.7\%$ [87]. A schematic of a Liquid Argon barrel module can be seen in Figure 3.8

Hadronic End-cap The hadronic end-cap partition makes use of a more traditional flat-plate geometry with copper as the passive material, providing a depth equivalent of 10 interaction lengths. As in the EM partition, the active gap is filled with copper electrodes, honeycombed polyimide sheets filled with the active medium, and a central copper read-out channel. The hadronic end-caps contain 5632 read-out channels [71]. In the case of the hadronic end-cap the copper read-out channel is etched with pads to provide semi-pointing geometry aligned on the interaction region. The hadronic end-cap covers the pseudo-rapidity range from

$1.5 < |\eta| < 3.2$ [71, 84]. The design energy resolution of the hadronic end-cap is $\sigma(E)/E \sim 50\%/\sqrt{E} \oplus 3\%$ [87]

Forward Calorimeter The forward calorimeter partition is constructed from a matrix of 12260 narrow, cylindrical channels filled with liquid argon surrounding copper electrode cores [71]. The forward calorimeter is divided into three modules. The innermost modules uses a matrix of copper, while the outermost two modules use a tungsten matrix with respective gaps between matrix and electrode of 0.250, 0.375, and 0.5 mm. This configuration reduced ion drift time and space-charge build-up, a design that reflects the high-radiation environment of the forward region, $3.2 < |\eta| < 4.9$. The combined modules provide an absorption length of $10\lambda_I$ [80, 84] and account for 3524 read-out channels [86]. The design energy resolution of the forward calorimeter is $\sigma(E)/E \sim 100\%/\sqrt{E} \oplus 10\%$ [87]

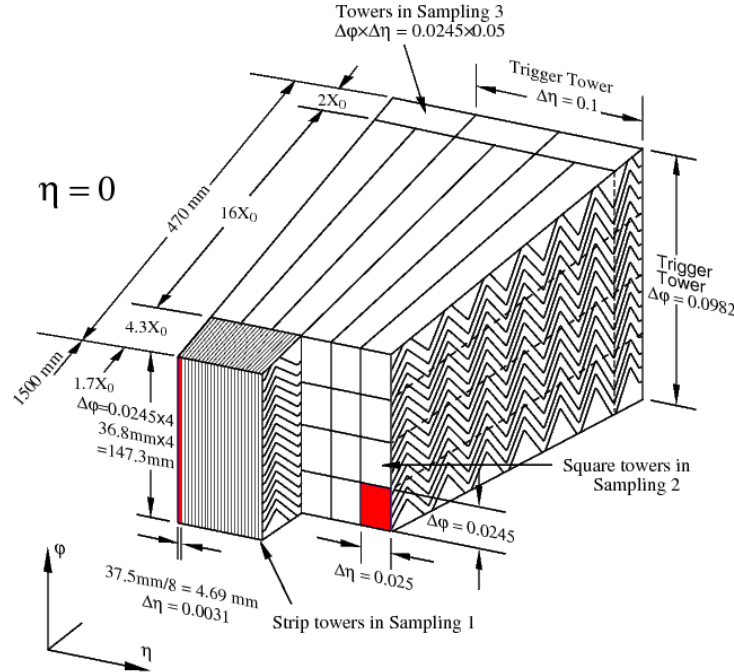


Figure 3.8: Schematic of a barrel module showing the η - ϕ granularity of the cells [71].

In total, the LAr calorimeter has 182,468 channels to be read-out and a collision frequency of 40 MHz, posing a considerable challenge to monitoring, read-out, and data storage [84].

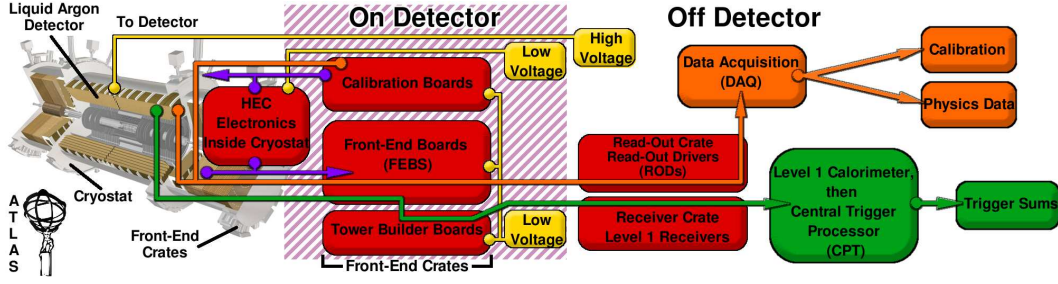


Figure 3.9: The flow of data in the ATLAS LAr detector [88].

Like all sampling calorimeters, the signal measurements in the LAr calorimeter begin with ionization pulses in the individual cells of the calorimeter due to particle tracks. These pulses are sent (see Fig. 3.9) from the detector to the Front-End Boards (FEBs), where the analog signals are amplified and shaped. The FEBs sum the signals from the calorimeter cells into towers of size $\Delta\eta \times \Delta\phi = 0.1 \times 0.1$ for each layer in preparation for input to the Tower Builder Boards. The FEBs store the signals in on-board memory until the Level-1 trigger decides whether to keep or reject the event. If the event passes the Level-1 trigger the FEBs digitize the signals and pass them on to the Read-Out Drivers (RODs), while the analog signals are passed to the Tower Builder Boards [89].

In the electromagnetic segment Tower Builder Boards complete the analog sum of cells in order to construct trigger towers. These towers are transmitted to the Level-1 off-detector electronics for digitization. In the Hadronic End-Cap, Tower Driver Boards produce differential signals and pass them on to Level-1 trigger [89].

The RODs receive the digitized signal from the FEBs and proceed to compute the energy for each channel, as well as the timing and a pulse shape quality measurement (χ^2). As shown in Fig. 3.10, the pulses produced in the calorimeter are triangular, but are shaped by the FEBs into a bipolar shape that is sent to the RODs. The bipolar pulse is sampled by the FEBs at intervals of 25 ns. Digital Signal Processors (DSPs) on the RODs reconstruct the signal and use the amplitude of the shaped pulse to calculate the energy. Due to the timing restrictions (Level-1 operates at 75 kHz) usually only 5 samples are taken of the pulse, timed to capture the region of the peak of the signal pulse, but as many as 32 samples can be taken. The samples from signals with energy greater than a threshold are stored in the event stream for later checks by monitoring algorithms. The RODs also monitor operations and parameters, such as the temperature of the electronics and busy signals. The resulting

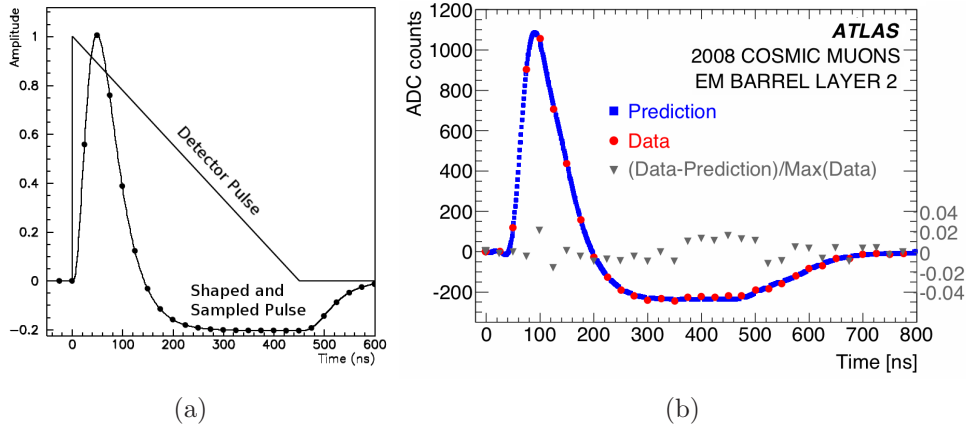


Figure 3.10: (a) The triangular signal pulse produced inside the LAr calorimeter and the pulse used by the RODs after re-shaping by the FEBs. The peak in the re-shaped pulse is used to calculate the energy in each channel [81]. (b) A typical measurement in 32-sample calibration mode of a pulse shape from a 15 GeV cosmic-ray in the second layer of an EM barrel module (\bullet), compared to the predicted ionization pulse (\blacksquare). Also plotted is the fractional difference between measured and predicted (\blacktriangledown).

signal data are passed to the Level-2 trigger [84, 89]. The Level-2 trigger and the succeeding event filter construct more complicated physics objects from the signals.

The LAr calorimeter is also equipped with calibration boards used for testing the detector. During calibration, an electronic pulser is used to inject current into the calorimeter cells and provide a well-defined proxy for the actual physics signal. These benchmark pulses can then be used to calibrate the signal gain, as well as guarantee timing measurements with a resolution on the order of 1 ns, both of which are vital for producing precision energy measurements. Pedestals are also taken for the calorimeter cells during calibration, providing a benchmark for how the calorimeter responds when no signal pulses are present [84, 90].

3.2.2 Tile Calorimeter

The ATLAS Tile Calorimeter is a sampling calorimeter that uses steel plates for its absorbers and scintillating plastic tile for its active medium. The Tile Calorimeter covers the pseudo-rapidity $|\eta| < 1.7$ and provides at least $7.4\lambda_I$ of material [71]. The Tile Calorimeter is divided into a central barrel

(5.8 m) and two extended end-caps (2.6 m). Each is constructed from 64 azimuthal modules covering $\Delta\phi = 0.1$ (see Figure 3.11). The plates composing the modules are perpendicular to the beam axis and radially staggered. The tiles are read-out from each end using wave-length shifting fibers into two different photomultipliers and provide 4672 read-out channels. Grouping of the tiles and photomultipliers allows segmentation in pseudo-rapidity, resulting in a typical cell dimension of $\Delta\eta \times \Delta\phi = 0.1 \times 0.1$ [91, 92].

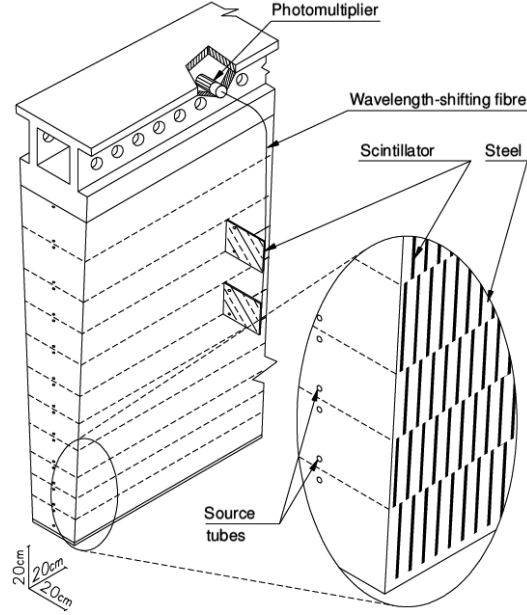


Figure 3.11: An example schematic of a Tile Calorimeter module [71].

The Tile Calorimeter is calibrated in three different ways. First, the front-end electronics are calibrated via a charge-injection system that maintains the electronics calibration to a 1% accuracy over a timescale of months [71]. The response of the photomultipliers used is calibrated using a 532 nm wavelength neodymium yttrium-vanadate crystal (Nd:YVO4) laser providing light pulses of ~ 10 ns duration. The targeted accuracy is less than 1% [71, 93]. The entire system, including the scintillators, is calibrated with a ~ 10 mCi ^{137}Cs γ -source. The source transits the detector through hydraulic tubes distributed throughout the Tile Calorimeter (note source tubes in Figure 3.11). This system allows for single tile response to be calibrated to less than $\pm 2\%$ [71].

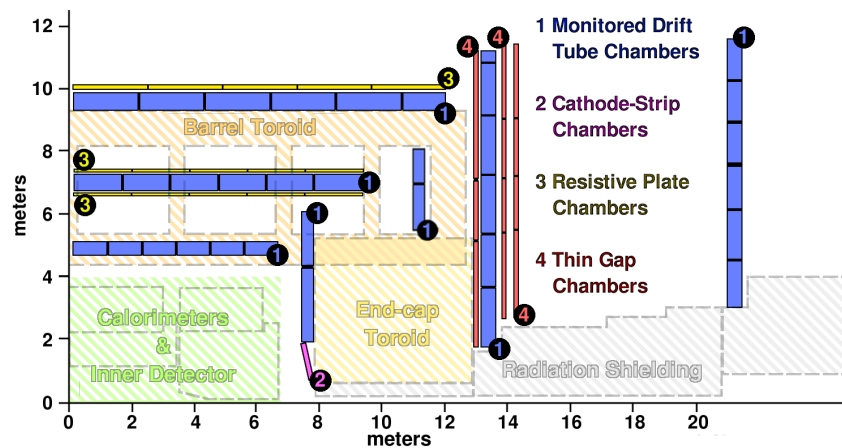
Test beam analysis of the Tile Calorimeter found an energy resolution for isolated pions of $\sigma(E)/E \sim 56\%/\sqrt{E} \oplus 5.5\%$ at $\eta = 0.35$, however this value is known to depend on η due to the changes in depth as η increases [71].

3.3 Muon Spectrometry

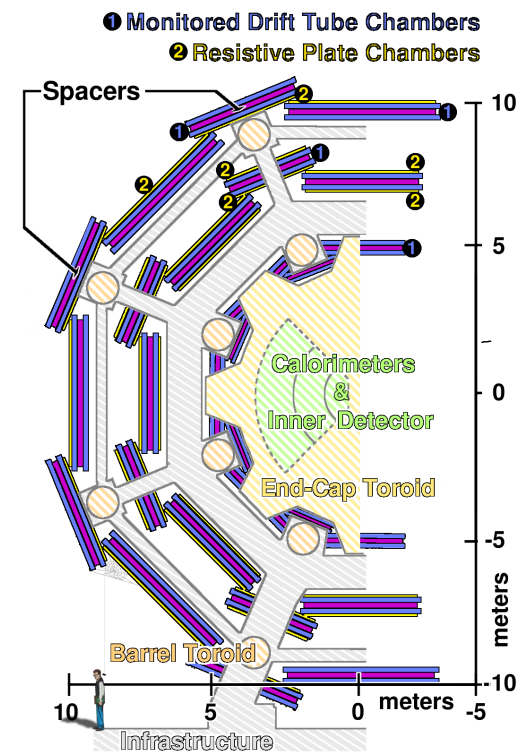
The muon spectrometer detectors are the outermost sub-detectors of the ATLAS detector. The spectrometer measures the momenta of charged particles that exit the calorimeters. The spectrometer systems extend to a pseudorapidity of $|\eta| < 2.7$. The muon spectrometer was designed to measure muon momenta over the range 3 GeV/c to 1000 GeV/c and to provide a resolution of less than 10% on a 1000 GeV/c muon track [70, 71]. The muon spectrometer is composed of four types of detectors. The Muon Drift Tubes (MDTs) and Cathode Strip Chambers (CSCs) provide precise spatial measurements for determining a particle’s position, momentum, and charge. The Resistive Plate Chambers (RPCs) and Thin Gap Chambers (TGCs) are used for triggering, as they are designed to give more prompt — but less spatially accurate — measurements of muons for use in triggering, which requires that signals be returned within $\mathcal{O}(10\text{ ns})$ [71]. The muon spectrometer detectors interspersed with the magnetic toroids of the ATLAS detector, which provide the magnetic fields which enable momentum measurements in the muon spectrometer. The toroids are discussed in Section 3.5. The measurement of muon momenta is highly dependent on uncertainty in the position of the muon spectrometer components. A 1000 GeV/c muon has a sagitta of 500 μm , thus requiring an 50 μm sagitta resolution in order to achieve 10% resolution on the momentum, in turn requiring that the positions of the detector components be known to 30 μm . To achieve this, the muon spectrometer is outfitted with a sophisticated alignment measuring system. Detailed information about the system can be found in [71].

3.3.1 Monitored Drift Tube Chambers

The Monitored Drift Tube Chambers (MDTs) are composed of numerous drift-tubes. The drift-tubes in each module are arranged in two “multi-layers” on each side of the chamber support structure. Each multi-layer is composed of 6 to 8 layers of drift-tubes depending on the size of the chamber and their distance from the interaction point [95], though there are additional special chambers with as few as 3 layers in a single multi-layer. This is due to the muon spectrometer sharing space with the ATLAS toroidal magnetic system, thus requiring special chambers to provide coverage in spaces with inconvenient size. The MDTs are placed in the barrel and the end-caps, covering the range $|\eta| < 2.0$, beyond which cathod-strip chambers are used. There are 1150 MDT chambers in the spectrometer, providing ~ 354000 read-out channels. The many MDT chambers are grouped in three concentric layers referred to as stations (see Figure 3.12) [71].



(a) The layout of the ATLAS muon spectrometer [70].



(b) The layout of the ATLAS muon spectrometer in the $r - \phi$ -plane [94].

Figure 3.12:

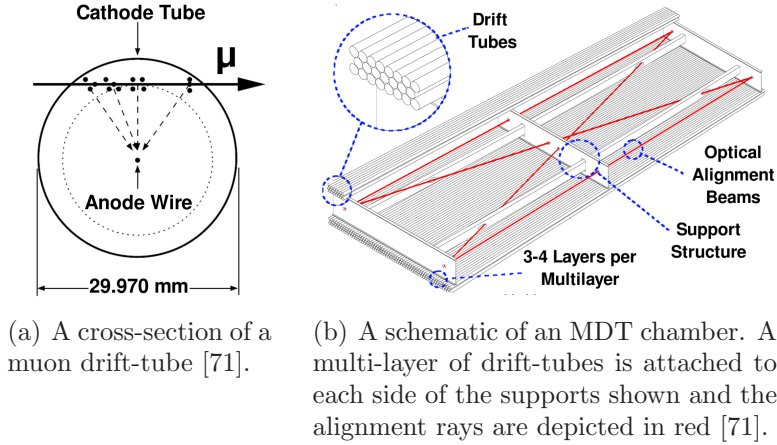


Figure 3.13:

Each drift-tube is 29.970 mm in diameter, while the length of the tube varies based on its position in the detector. The tubes are pressurized to 3 bar with a mixture of 93% Ar and 3% CO₂, selected for good aging properties and the absence of deposits forming on the wire. As much as 300 ppm of H₂O is added to improve HV stability. Suspended in the center of each tube is a 50 μ m gold-plated tungsten-rhenium wire that acts as the anode. Support plugs at either end of the tube maintain the concentricity of the wire to less than 10 μ m [71]. The tube itself is made of an aluminum-manganese alloy and acts as the cathode [95]. The construction of the chambers using individual tubes, as opposed to a multi-wire proportion chamber (MWPC), was motivated by the separate, stiff tubes providing high mechanical precision. The chambers are also more robust than an MWPC due to the fact that MDT chambers may continue to operate if they lose a single tube. Additionally, the usage of individual, cylindrical tubes leads to greater precision by simplifying the electric-field geometry compared to a multi-wire chamber (with wire anode suspended between parallel-plate cathodes). The radial drift geometry lessens the dependence of the measurement accuracy on incidence angle compared to a multi-wire chamber, where drift-time can vary based on the location of the track relative to the anode and cathode. However, the radial drift geometry also causes the signal to consist of a long pulse train, as electrons produced near the cathode-wall have a drift-time of ~ 700 ns and a track produced near the anode will have a signal length of that magnitude, though only the earliest part of the signal is needed to measure the track coordinate. To prevent this long train from being interpreted as multiple track hits, the front-end electronics

for the MDTs include an adjustable dead time [71].

While the utmost care was given during construction of the chambers to measure and maintain the alignment of the various components, it is expected that differences in location and temperature will cause deformations in the chambers. Consequently, the chambers are designed with an internal alignment system in order to constantly monitor the chamber so that muon reconstruction can compensate for deformations. The alignment system consists of four optical rays as shown in Figure 3.13(b). Light-emitting diodes and CCDs are located in each end, with lenses in the middle. The system can measure deformations on the order of a few μm . The MDT chambers are also fitted with thermal sensors to monitor thermal deformations. The local magnetic field is monitored by multiple B-field sensors in each chamber [71].

Careful measurements of the alignment allow an MDT chamber to measure the central point of a track segment with a resolution of 35(30) μm for a chamber with 3(4) layers per multi-layer. The relative positions of radially-neighboring stations are accurate to 30 μm . In a typical track reconstruction with 3 chamber crossings, the sagitta resolution will be $\sim 45 \mu\text{m}$, giving just slightly better than 10% resolution of momentum (see Section F.3 for an explanation of the sagitta) [71].

3.3.2 Cathode Strip Chambers

In the forward direction the flux of particles and density of tracks is much higher than in the central regions. Due to the increased multiplicity of tracks and the need for increased radiation-hardness, cathode-strip chambers (CSCs) are used in the range $2.0 < |\eta| < 2.7$. While MDTs are considered safe to operate up to counting rates of 150 Hz/cm², CSCs are safe to 1000 Hz/cm². In addition CSCs have high time and double-track resolution. In each end-cap are two disks of CSCs, a disk composed of 8 small chambers and a disk composed of 8 large chambers, as shown in Figure 3.14. Each chamber contains 4 CSC-planes, allowing for 4 independent measurements of η and ϕ for each track passing through the CSC [71].

The CSCs are designed as multi-wire proportion chambers operating with a gas mixture of 80% Ar and 20% CO₂. The layout of the CSC sensors and electronics can be seen in Figure 3.15(a). The central wire in each CSC is oriented radially with the other wires parallel to it. The wire pitch is 2.5 mm. Each plane of wires has two segmented cathode planes separated from the anode by 2.5 mm. The position of the track is determined by interpolating from the charge induced on the cathode. One cathode is segmented perpendicularly to the anodes to provide the precision coordinate in the bending plane with a resolution of 60 μm (see Figure 3.15(b)). The other cathode is segmented par-

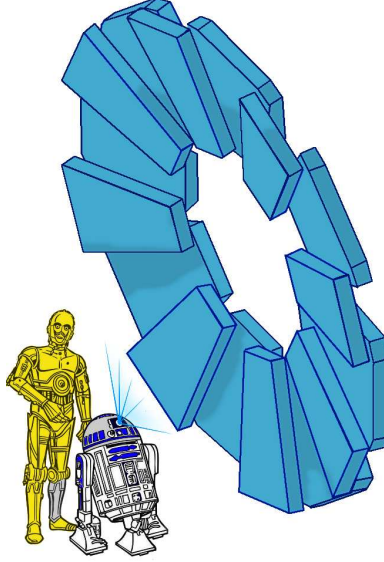


Figure 3.14: The layout of the CSC end-cap wheel, with pop culture icons C-3PO and R2-D2 for scale [96].

allel to the anodes to provide a courser transverse coordinate with a resolution of 5 mm. This geometry and method of read-out provide for the ability to distinguish more than one track at a time. Additionally the geometry allows for electron drift times of less than 40 ns, resultings in a timing resolution of 7 ns for each CSC plane. The CSC-plane also has the advantage that its read-out is based on the relative charge distributed on the anode, thus making it resistant to changes in the whole chamber, such as changes in temperature and pressure [71].

3.3.3 Resistive Plate Chambers

In the barrel region, $|\eta| < 1.05$, muon triggering is provided by the Resistive Plate Chambers (RPCs). Each RPC is made of two overlapping RPC units (see Figure 3.16); each unit contains two detection layers, each layer composed of two phenolic-melaminic plastic laminate resistive plates separated by 2 mm plastic spacers. The outer faces of the plates are painted with a thin layer of graphite to provide for the high-voltage and ground connection. The space between the plates is filled with a gaseous mixture of 94.7% tetrafluoroethane ($\text{C}_2\text{H}_2\text{F}_4$), 5.0% isobutane (Iso- C_4H_{10}), and 0.3% sulfur hexafluoride (SF_6) [71].

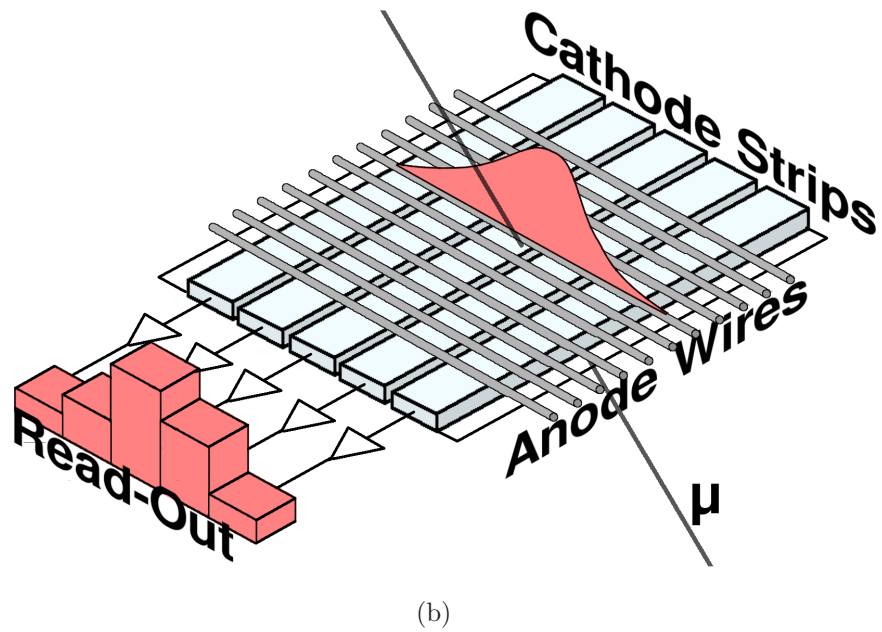
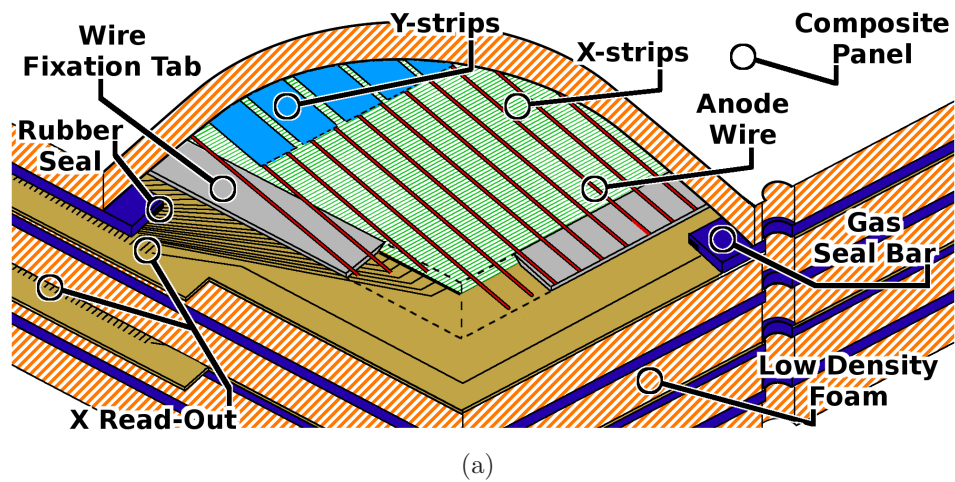


Figure 3.15: (a) A cut-out schematic of a single layer of a CSC [96], (b) the read-out scheme of the CSC electrodes [71].

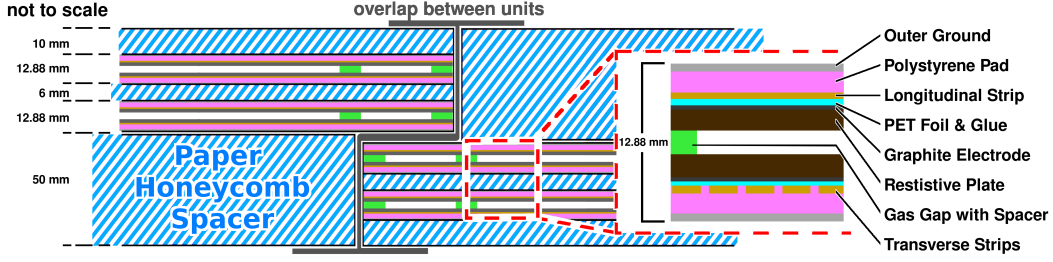


Figure 3.16: Cross-section of an RPC, showing the two overlapping units, each composed of two detection layers [71].

An electric field between the plates of ~ 4.9 kV/mm allows the ionizing track of a muon to trigger avalanches and the signal is read out via capacitive-coupled copper strips on the outer faces of the plates. The strips on each face are orthogonal to each other, to provide for stereo readout. The copper strips are insulated from the graphite layer with a polyethylene terephthalate film. An additional polystyrene pad is bonded to each read out plane, insulating it from the copper grounding sheet which forms the outermost layer of the unit. The RPCs are operated in avalanche mode, whereby the electric field is not strong enough to create a discharge. This is to avoid the increased charge-depletion deadtime that discharges create, allowing an RPC unit to operate at rates of approximately ~ 1 KHz/cm². However, the signal amplitude in avalanche mode is orders of magnitude less than in streamer mode and requires amplification in the read-out electronics [71, 97]. RPCs allow for a time resolution of ~ 1.5 ns [98].

3.3.4 Thin Gap Chambers

Muon triggering in the end-cap regions is provided by Thin Gap Chambers (TGCs), with an inner wheel covering the pseudo-rapidity range $1.05 < |\eta| < 2.4$ and an outer wheel covering the pseudo-rapidity region $1.05 < |\eta| < 1.92$. The time resolution of the TGCs at 4 ns is inferior to the RPCs, but provide sufficient resolution to identify the 25 ns beam-crossing window. TGCs are also capable of a higher rate of operation than RPCs, greater than 20 kHz/cm². The TGCs complement the MDTs in the end-cap by providing the azimuthal coordinate with a resolution on the less than 10 mm [71, 99].

TGCs are multi-wire proportional chambers with an anode-wire-to-cathode distance smaller than the wire-to-wire distance, 1.4 mm to 1.8 mm, which provides for high time resolution when combined with a high electric field. The high electric field is balanced by a quenching gas mixture, 55% CO₂ and 45%

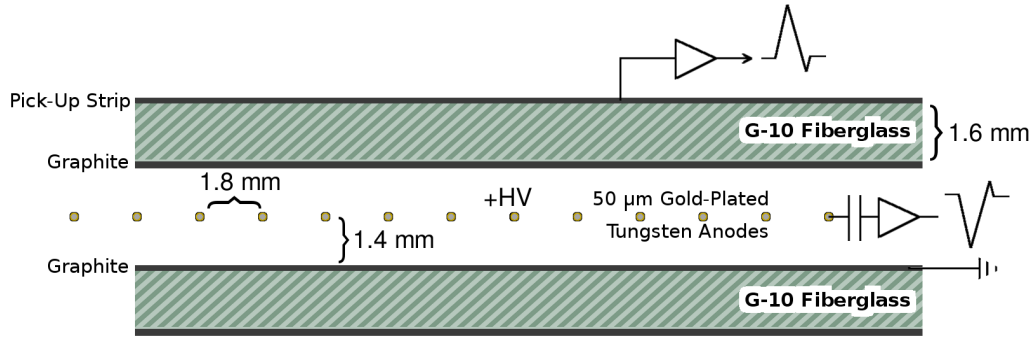


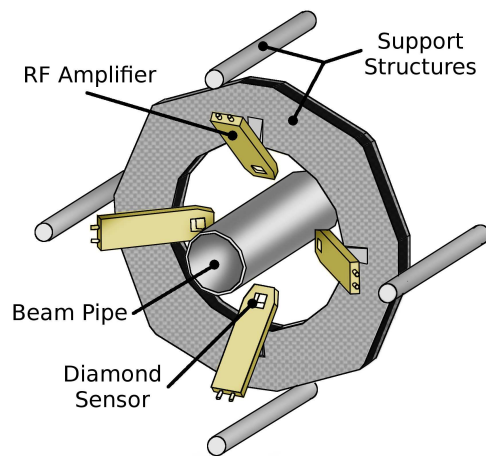
Figure 3.17: Cross-section of a TGC layer [71].

n-pentane ($n\text{-C}_5\text{H}_{12}$). Because of the high voltage of the electric field, the signal tails are chiefly populated by orthogonal tracks passing equidistant between wires, due to the field approaching zero strength. This allows for the signal from the TGCs, including propagation time, to fall in a 25 ns window 99% of the time. The anodes are gold-plated tungsten wires. The cathodes are composed of sheets of fiberglass with flame retardant epoxy binding, coated with graphite on the inside face, opposite the wires. The opposing face is clad in copper. Solid cladding serves as a ground. Segmented copper cladding provides read-out strips, oriented radially and perpendicular to the anode wires, which are perpendicular to the beam line [71, 100].

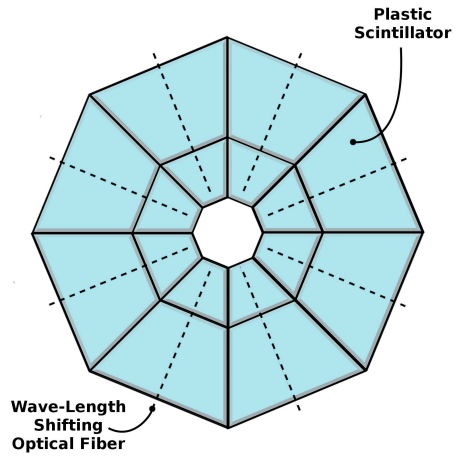
Each plane of anodes and two cathode-planes forms a single TGC. TGCs are combined into doublets or triplets to form a unit. The inner wheel is composed of doublet units, while the outer wheel is composed of two doublets and a triplet. Each unit is enclosed in a gas tight envelope flushed with CO_2 . The composition of this CO_2 flushing system is monitored against flammable $n\text{-C}_5\text{H}_{12}$ leaking from a chamber and into the high voltage system [71].

3.4 Luminosity and Forward Detectors

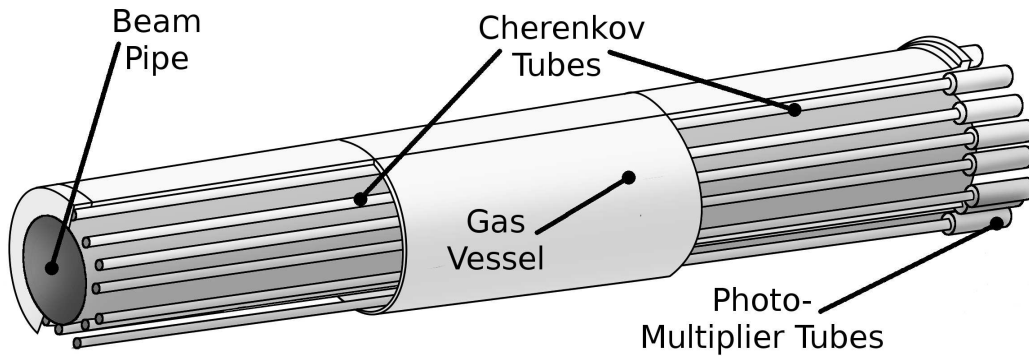
In addition to the previously outlined detector systems in ATLAS, there are sub-components specialized for making measurements in the far forward region.



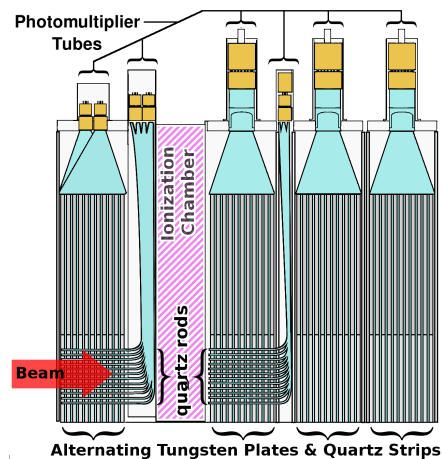
(a) The ATLAS Beam Conditions Monitor [101].



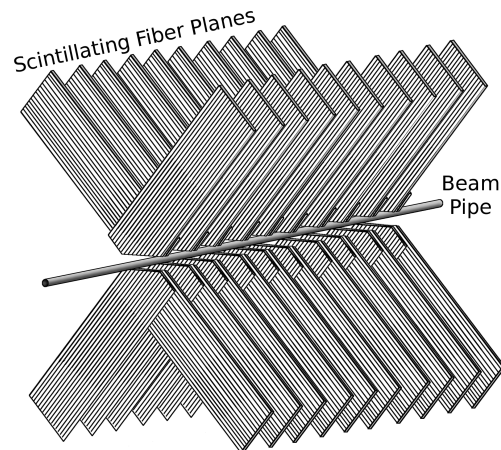
(b) The layout of the scintillators in the MBTS [102].



(c) The design of LUCID [103].



(d) The design of the ZDC [104].



(e) The layout of scintillating fibers in the ALFA detector [105].

Figure 3.18: The forward detectors and luminosity monitors of ATLAS.

3.4.1 Beam Conditions Monitor

The Beam Conditions Monitor (BCM) provides information about the instantaneous collision rate and the background rate, as well as providing the accelerator operators with information about conditions near the interaction point, such as instabilities that may potentially damage LHC and ATLAS infrastructure. Two BCM monitors are installed along the beam line, bracketing the interaction point at a distance of 1.84 m. Each detector element is composed of an active material of polycrystalline Chemical-Vapor-Deposition (pCVD) diamond, a material chosen for its radiation hardness. The proximity to the interaction point requires a material that can withstand 10^{15} pions/cm², which the pCVD exceeds. Each BCM has four detectors composed of two back-to-back sensors with an acceptance area of 0.5 cm² placed 7 cm from the beamline with a tilt of 45° from the beam axis. The detector provides a signal rise time of 1 ns with a frequency of ≥ 100 MHz [101]. To fulfill a primary design goal, the BCM system uses time-of-flight measurements to determine whether particles are from a beam-on-beam collision or a bi-product particle spray due to a beam incident. In the latter case the information is used by the LHC to determine whether a beam dump is required. While particles from a collision should arrive at the opposing BCMs almost instantaneously (< 1 ns), particles from a beam incident will display a time-of-flight of 12-13 ns [106].

3.4.2 Minimum Bias Trigger Scintillators

The Minimum-Bias Trigger Scintillators (MBTS) are designed to provide for a minimum-bias trigger during the early data taken period. An MBTS is placed on the two inner faces of the calorimeter cryostat, 3.56 m from the interaction point. Each MBTS is divided into two regions by pseudo-rapidity, covering $2.09 < |\eta| < 2.82$ and $2.82 < |\eta| < 3.84$, and eight regions by azimuth. Each region is composed of a plastic scintillating tile feeding into a photomultiplier tube. The units are operated as simple counters. In early data taking the MBTS played a crucial role in providing a minimum bias trigger and was used primarily to form triggers based on one or two hits in one side of the MBTS, or a coincidence between both sides of the MBTS [107, 108]; this system is no longer usable due to high-radiation exposure.

3.4.3 LUCID

LUCID is the *L*uminosity measurement using *C*erenkov *I*ntegrating *D*etector. A LUCID module is located 17 m ($|\eta| \approx 5.8$) to either side of the interaction point. LUCID measures forward, inelastic p-p scattering. A LU-

CID module is a series of tubes. Each module consists of 20 polished tubes (1.5 m×15 mm) surrounding the beam pipe at a radius of 10 cm. The tubes are contained in an aluminum gas vessel filled with perfluorobutane (C_4F_{10}) at ~ 1.3 bar, which results in a Cerenkov threshold of 10 MeV for electrons and 2.8 GeV for pions. The Cerenkov light produced by a particle entering the gas is reflected off the polished tube and read-out by photomultiplier tubes at the end of each tube and of equal radius. By design it is possible to count the number of particles entering each tube using the pulse height from the photomultiplier tube, but in practice the probability of multiple particles entering one tube is only a few percent at a luminosity of $\sim 10^{33}\text{cm}^{-2}\text{s}^{-1}$. Consequently, LUCID is usually run by counting the number of tubes exhibiting a signal about a set threshold. Measuring p-p scattering allows the detector to measure integrated luminosity and allow for online monitoring of beam status and instantaneous luminosity. Initially, the detector will be calibrated using LHC design parameters and achieve a luminosity precision of $\sim 20\text{--}30\%$. Calibration with physics processes and against the other forward luminosity detector, ALFA, will allow the precision to become better than 5% [71].

3.4.4 ZDC

ZDC is the *Zero-Degree Calorimeter*. Each ZDC is located 140 m from the interaction point, just beyond the point where the beam pipe splits. The ZDCs sit between the two pipes. The ZDCs are primarily used to detect $|\eta| > 8.3$ neutrons resulting from heavy-ion collisions, which can help determine the centrality of such events. During initial, low-luminosity p-p collisions ($10^{33}\text{cm}^{-2}\text{s}^{-1}$) the ZDCs improve forward acceptance of the calorimeters and assist with minimum-bias triggering. Coincidence triggering off the ZDCs can also significantly reduce backgrounds from beam-gas and beam-halo effects.

Each ZDC consists of one electromagnetic module (29 radiation lengths) and three hadronic modules (each 1.14 interaction lengths). Each module consists of 11 tungsten plates arranged perpendicular to the beam pipe. Parallel to the plates are 1.5 mm quartz strips that guide Cerenkov light into photomultiplier tubes in order to measure energy. Penetrating the tungsten plates parallel to the beam pipe are 96 quartz rods that also feed Cerenkov light into photomultipliers. These rods allow for position measurements of traversing particles to be measured. The photomultipliers are calibrated to an accuracy of $\sim 1\%$ using a system of a blue, light-emitting diodes [71].

3.4.5 ALFA

ALFA is the *Absolute Luminosity for ATLAS* detector, which measures the absolute luminosity through small angle elastic-scattering, making use of the connection between forward elastic-scattering amplitude to total cross-section dictated by the optical theorem [109],

$$\sigma_{tot} = \frac{4\pi}{k} \text{Im}(f(0)) \quad (3.1)$$

where f_0 is the normalized scattering amplitude in the forward direction and k is the wave-number. These measurements require very small scattering angles, $\sim 3 \mu\text{rad}$, which is smaller than the beam divergence in regular operation. Consequently, the luminosity measurements must be performed with specifically prepared beam conditions and the detectors must be far removed from the interaction point and kept close to the beam. In order to achieve this, ALFA consists of Roman pot detectors which can be moved to 1 mm from the beam from above and below (but not the sides, due to the dual pipes). There will be two ALFA detectors on each side of the interaction point, at 240 m and 244 m. The detector in each Roman pot is a scintillating-fiber tracker. The fibers are 0.5 mm wide and aluminized to reduce losses and cross-talk. The fibers are arranged in ten double-sided planes with 64 fibers each, arranged in a perpendicular cross-hatched $u - v$ stereo geometry, which allows for a spatial resolution of $25 \pm 3 \mu\text{m}$ for high-energy hadron beams. However, at low energies multiple-scattering can reduce this resolution to $36 \mu\text{m}$. The fibers have a pitch of $700 \mu\text{m}$ and the 10 modules are staggered at $70 \mu\text{m}$ to maintain coverage. Each module covers just under $32 \times 32 \text{ mm}^2$ and the fibers are cut so that the sensitive area forms a shield-shaped pentagon [71].

3.5 Magnet System

The ATLAS magnet system is comprised of four systems. Surrounding the inner detector is a solenoid. Interspaced with the muon spectrometer is a barrel toroid system and two end-cap toroid systems. In each system the design varies, but all are composed of Al-stabilized NbTi/Cu conductor cable [110]. The four systems have a stored energy of 1600 MJ and provides a field of at least 50 mT over a volume of $12,000 \text{ m}^3$ [71].

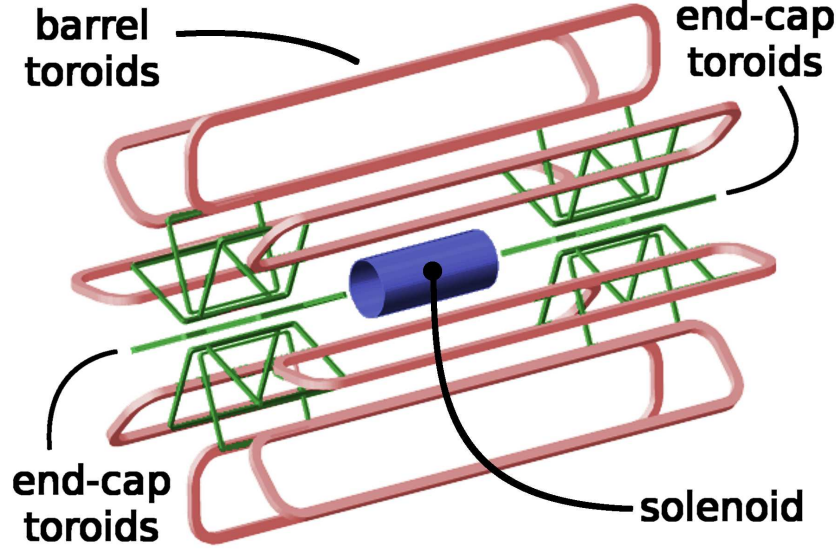


Figure 3.19: The layout of the ATLAS magnet systems[111]

3.5.1 Central Solenoid Magnet

The central solenoid is located between the inner tracking detector and the Liquid Argon calorimeter, sharing a cryostat with the calorimeter. The solenoid is designed to minimize the amount of material placed in front of the calorimeter, with the final extension being ~ 0.66 radiation lengths [71]. The solenoid is a single layer of $30 \text{ mm} \times 4.25 \text{ mm}$ conductor cable in 1154 turns, supported by an aluminum support cylinder [110]. At the nominal current of 7.730 kA the solenoid provides a magnetic field of 2 T for the inner tracker. The solenoid can be charged and discharged in ~ 30 minutes, however in the case of a quench, the energy of the solenoid is dumped into the cryostat cold mass and safely raising the temperature as high as 120 K. In this instance the return to regular operation occurs in less than a day as the cold mass is cooled back down to 4.5 K [112].

3.5.2 Barrel Toroid Magnets

The ATLAS barrel toroid magnets provide the magnetic field in the volume outside the barrel region outside the calorimeters and end-caps [71]. The system includes eight racetrack-shaped toroids composed of two coils contained in stainless-steel vacuum vessels. Each coil is made from $57 \text{ mm} \times 12 \text{ mm}$ conductor cable wound into a flattened, pancake-shaped coil of 120 turns.

The system is 25.3 m in length and extends from a radius of 4.7 m to 10.05 m. The nominal current in the coils is 20.5 kA, which produces a field of strength in its bore of between 0.2 and 2.5 T (including the azimuthal angle between toroids), which is affected by the geometry of the coils and the presence of nearby magnetic materials [110, 113].

3.5.3 End-cap Toroid Magnets

The end-cap toroid magnets provide the magnetic field in the end-cap region, ensuring proper bending power for the muon spectrometer in that region [71]. Each end-cap toroid is 5.0 m along the Z-axis and extends from 0.825 m to 5.35 m in radius. Each end-cap is composed of a gear-shaped aluminum vacuum vessel containing a rigid support structure to counter Lorentz forces and eight coil pairs. Each coil in a pair is a pancake-shaped bundle wound in 116 turns of 41 mm \times 12 mm conductor cable. The current in the end-cap toroid is nominally 20.5 kA and provides 0.2—3.5 T field strength in its bore. The vacuum vessel is gear-shaped such that it slots into the barrel toroid system with a 22.5° angle between the end-cap toroid and its neighboring barrel toroid. This twist allows for the bending power of the transition region between the systems to be optimized, as well as allowing overlap between the two systems radially [71, 110].

3.6 Trigger, Data Acquisition, and Detector Control

The trigger and data acquisition (TDAQ) system of ATLAS functions much like the detector’s brain, deciding whether data is interesting enough to merit recording. The trigger system can be divided into Level-1 (L1), Level-2 (L2), and the Event Filter (EF), with the latter two making up the High-Level Trigger (HLT). The data acquisition (DAQ) system is responsible for read-out of the detector, provides information to the HLT, and ultimately records the raw data to local storage. The DAQ system is also used to configure the detector, determining which sub-detectors and components will be included in any given run. A block diagram of the TDAQ can be seen in Figure 3.20. The Detector Control System (DCS) is used to monitor the infrastructure of the detector, such as power-supplies.

The L1 trigger decision is based on coarse information from the muon spectrometer (L1Muon) and calorimeter (L1Calo) systems and has a maximum rate of 75 kHz (upgradable to 100 kHz). The L1Muon trigger is built from

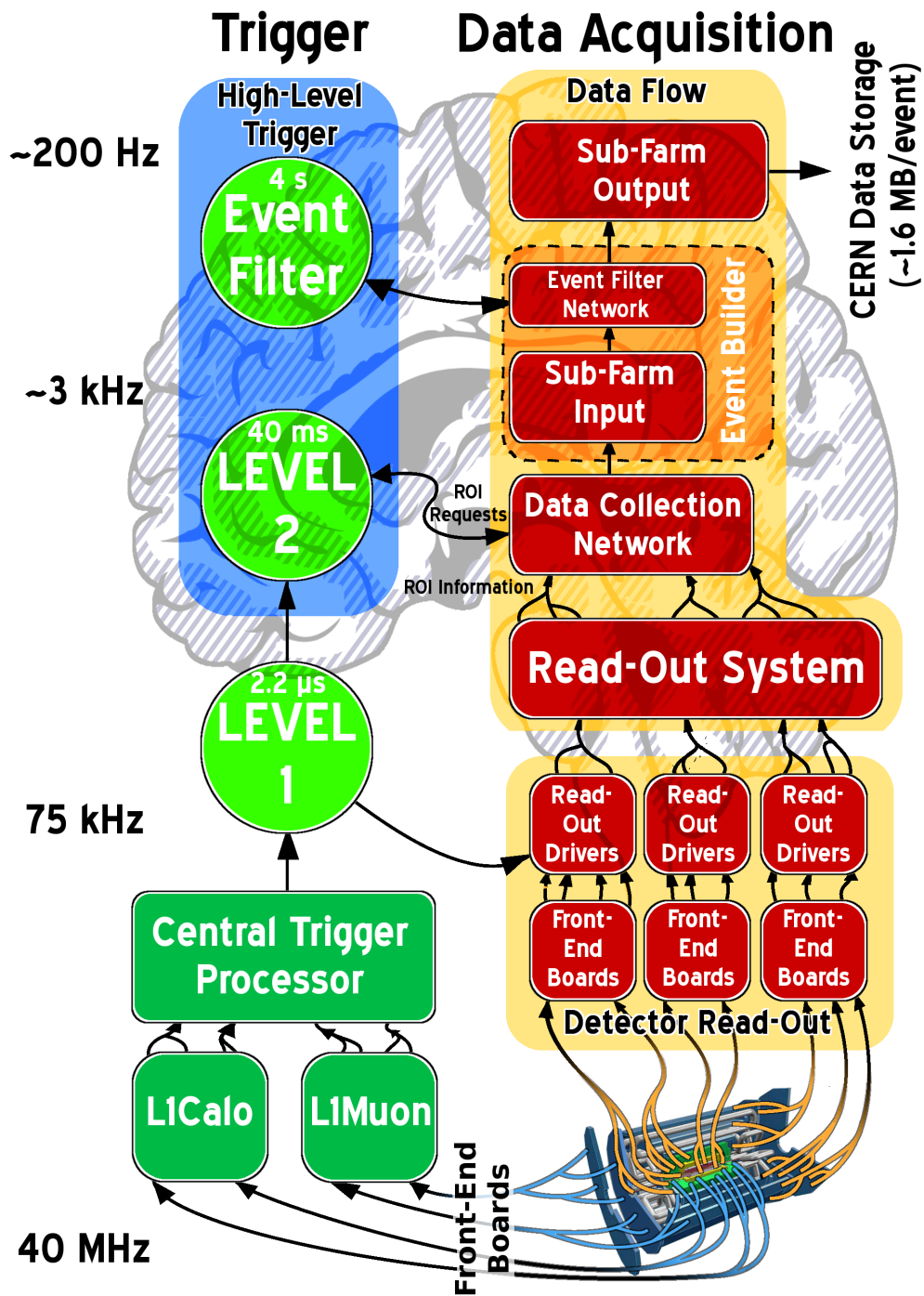


Figure 3.20: Block diagram of the ATLAS TDAQ system [114].

signals from the RPCs in the barrel and TGCs in the end-cap, described in Sections 3.3.3 and 3.3.4. The L1Muon trigger requires hits in at least three muon trigger stations and provides logic for six p_T thresholds. Its temporal resolution is sufficient to correctly identify the bunch crossing of muon-candidates. The L1Calo trigger divides the ATLAS calorimeters into ~ 7000 trigger towers ($\eta \times \phi \approx 0.1 \times 0.1$, but of increased size at high η ; see Figure 3.8 for example). These towers are used to identify electrons, photons, taus, and jets, as well as event level variables such as E_T^{miss} and ΣE_T . The electrons, photons, and taus can include isolation as a selection in triggering, based on angular separation of towers. The latency of the L1Calo trigger is $\sim 2.1 \mu\text{s}$, well within the $2.5 \mu\text{s}$ target latency for the L1 trigger.

Decisions from L1Muon and L1Calo are passed to the Central Trigger Processor (CTP) in the form of trigger object multiplicities or threshold flags for event level variables; additional information, such as the 40.08 MHz clock is also processed in the CTP. The CTP allows for a trigger menu containing up to 256 distinct triggers based on L1Calo and L1Muon information. While the L1 trigger decisions are processed, detector read-out is stored in on-detector pipeline memories, a necessity as the calorimeter signal width is equivalent to at least four bunch crossings and the time-of-flight for muons in the muon spectrometer is also greater than the bunch crossing interval. Once the trigger decisions have been processed the detector data is read-out from the pipeline memories into the DAQ system. The position of the L1 trigger objects is passed on to both the L2 trigger system and the DAQ system in the form of Regions of Interest (ROIs) [71].

Once the L1 decision permits the read-out of the detector, the pipeline memories are passed to the on detector read-out drivers, which allow for pre-processing for sub-detector specific monitoring. The detector information is passed to the DAQ's Read-Out System (ROS) via 1574 Read-Out Links and into an equal number of Read-Out Buffers (ROBs) where they are stored for use by the DAQ/HLT systems. Communication between processors and storage is provided by the DAQ's DataCollection Network (DCN), a system of gigabit-Ethernet connections). Resident on the DCN is the DataFlow Manager which handles data requests and forwarding [71, 115].

L1 ROIs are used by the L2 trigger to determine which data is pertinent to the L1 triggers which fired. The L1 ROIs are matched to additional detector data, such as inner detector tracks or finer calorimeter clusters. This allows for trigger decisions of increased complexity over the L1 trigger, using variables such as shower shape and track-cluster matches, in addition to E_T -thresholds. Processing time for L2 trigger decisions averages ~ 40 ms, keeping the rate below 3.5 kHz. Decisions from the L2 trigger are passed to the DataFlow

Manager (DFM). Events not passing L2 selection criteria are cleared from the ROS [71].

Selected events are passed to the SubFarm Inputs (SFIs) of the DAQ, which acts as an event-building node. Once the SFI has built a full event-structure the event is passed to the event filter network and the event is expunged from the ROS. The event is piped to the event filter, which applies standard ATLAS reconstruction tools to the event and processes the event in a manner similar to L2 by calling on data from the event filter network and applying algorithms of further increased complexity. Events in the event filter are classified into physics streams, the main streams being Egamma, Muons, and JetTauEtmis. The event filter latency is ~ 4 s. However, the total system frequency to this point is 200 Hz, due to the parallel processing of events in multiple SFIs. Decisions by the event filter and the fully constructed event are transferred by the event filter network to the SubFarm Outputs (SFOs). The SFOs transmit the full event from DAQ to the CERN data storage at a maximum rate of ~ 400 Hz. Each event has a data-size of approximately 1.6 MB [71].

Examples of common trigger objects can be found in Table 3.1 [116].

Monitoring of the infrastructure and hardware of ATLAS is provided by the Detector Control System. The DCS monitors the hardware, power supplies, gas systems, cryogenics, and magnetic systems of ATLAS. DCS provides alerts concerning important variables, such as current in hardware and power supplies, straying outside of accepted ranges. It also provides for turning hardware on and off. In addition to specific sub-detector and infrastructure monitoring, the system also monitors cavern temperature and radiation levels and includes motion sensors to track personnel in the cavern [71].

Trigger Signature	Short Name		Threshold [GeV]							
	L1	HLT								
Electron	EM	e	2	3	5	10	10i	14	14i	85
Photon	EM	g	2	3	5	10	10i	14	14i	85
Muon	MU	mu	0	6	10	15	20			
Jet	J	j	5	10	15	30	55	75	95	115
Tau	TAU	tau	5	6	6i	11	11i	20	30	50
E_T^{miss}	XE	xe	10	15	20	25	30	35	40	50
$\sum E_T$	TE	te	20	50	100	180				

Table 3.1: The key physics trigger objects, their L1 and HLT short names, and the available L1 thresholds at $\mathcal{L} = 10^{32} \text{ cm}^{-2}\text{s}^{-1}$. For muons the threshold refers to p_T , for all other objects the threshold is E_T (or E_T^{miss}). Thresholds marked with an i indicate that they further require isolation from other energy deposits [116].

There might as well be [an infinite amount of money out there], but most of it gets spent on pornography, sugar water, and bombs. There is only so much that can be scraped together for particle accelerators.

Neal Stephenson [117]

4

Data Sample

The data used in this analysis was recorded from 22 March, 2011 to 22 August, 2011. During the operation of the ATLAS detector, each run over a stable fill provided by the LHC is divided into luminosity blocks of approximately two minutes. This is an amount of time for which we expect beam conditions to be stable. During a run the various sub-components of the detector are monitored and problems are logged, including which components were inactive or exhibited noisy channels. Infrastructure problems, such as unstable beams are also noted. These conditions are compiled into a Good Runs List (GRL) by each working group or analysis, depending on what their tolerances for sub-detector failure are [118, 119]. In this analysis the GRL is strict, requiring that there be no major failures in the detector or large scale noise. Certain long-term problems, such as lost cells in the LAr calorimeter, are ignored by the GRL in favor of kinematic corrections or particle specific vetoes. However, any data event failing the GRL is not processed in the analysis. The total integrated luminosity for the dataset is 2.06 fb^{-1} calculated using only those luminosity blocks passing the GRL veto.

ATLAS data taking is broken into periods based on the conditions of the accelerator and detector. The integrated luminosity and average number of pp interactions per bunch crossing (μ , a measure of pile-up) are detailed for each period in Table 4.1.

Period	μ ($pp/\text{crossing}$)	$\int \mathcal{L} dt$ [pb $^{-1}$]	Dates
B,D	5.9 ± 1.3	175	22 March — 28 April
E-H	5.6 ± 1.2	863	30 April — 28 June
I	6.1 ± 1.5	307	13 July — 29 July
J	7.2 ± 1.8	214	30 July — 4 August
K	7.3 ± 1.9	503	4 August — 22 August

Table 4.1: The data periods used in this analysis and the integrated luminosity calculated from unscaled triggers. Also shown is the value of μ , the number of interactions per crossing, which is used as a measure of pile-up. Note that Periods A and C are not used because of the paucity of good runs available.

Certainly the game is rigged. Don't let that stop you; if you don't bet, you can't win.

Robert A. Heinlein [120]

5

Monte Carlo

The ATLAS Monte Carlo (MC) samples used in this analysis use the parameter tune given in [121]. The detector is simulated using GEANT4 [122]. Details on the MC used are provided in the following sections.

5.1 Standard Model Monte Carlo

The MC background for the three lepton signal consists of numerous possible channels. Multiple event generators have been used depending on the relative performance and specialization of the generator. These generators and their respective background channels are:

PYTHIA [123] is used to generate the multi-jet QCD background at LO. The individual samples with LO cross section and integrated luminosity are shown in Table 5.1. Note that while these samples are included for completeness, none of these events survive to the three-lepton event selection.

HERWIG [124] is used for the ZZ , WZ , and $W^\pm W^\mp$ samples. These events are filtered to require at least one lepton with $p_T > 10$ GeV and $|\eta| < 2.8$. The off-shell mass of the Z/W must be above 20 GeV. A k-factor is applied to correct to the next-to-leading order (NLO) cross section from leading order (LO). This k-factor is calculated using MCFM [125] and following [126]. The individual samples with cross section, k-factor, filter efficiency and integrated luminosity are shown in Table 5.2. The ZZ and WZ samples are labeled as such in plots; however, the WW samples are paired with $V\gamma$ (for $V = W, Z$) samples and labeled $V\gamma + WW$.

Process (ID)	σ_{LO} [pb]	$\int \mathcal{L} dt$ [fb $^{-1}$]
J0 (105009)	986080×10^4	1.7×10^{-6}
J1 (105010)	67818×10^4	1.1×10^{-5}
J2 (105011)	40922000	6.8×10^{-5}
J3 (105012)	2192900	1.3×10^{-3}
J4 (105013)	87701	3.2×10^{-2}
J5 (105014)	2350	1.2
J6 (105015)	33	83
J7 (105016)	0.14	1.0×10^4

Table 5.1: The background MC produced by PYTHIA used in this analysis. Shown are the LO cross sections and integrated luminosity corresponding to the number of events generated. Also shown is the ATLAS process ID.

Process (ID)	σ_{LO} [pb]	k-factor	filter efficiency	$\int \mathcal{L} dt$ [fb $^{-1}$]
ZZ (105986)	4.60	1.35	0.212	190.4
ZW (105987)	11.23	1.70	0.31	42.4
W^+W^- (105985)	29.60	1.48	0.388	146.6

Table 5.2: The background MC produced by HERWIG used in this analysis. Shown are the LO cross sections, k-factors, and filter efficiencies, as well as the integrated luminosity corresponding to the number of events generated. Also shown is the ATLAS process ID.

MADGRAPH [127] is used for the $Z\gamma$, $W\gamma$, W^+W^+/W^-W^- +jets, and $t\bar{t}Z/tW + jets$ channels. The individual samples with cross section, k-factor, filter efficiency and integrated luminosity are shown in Table 5.3. The k-factor for the $t\bar{t}V$ samples are taken from [128]. Hadronic showers in these events are modeled using PYTHIA. The samples with $t\bar{t}V$ -production are labeled as such in plots. As previously mentioned, the $V\gamma$ samples are labeled $V\gamma + WW$.

MC@NLO [129] is used to generate the samples for the production of $t\bar{t}$ and single t , using $M_t = 172.5$ GeV. The $t\bar{t}$ samples are produced without full hadronization. The samples are generated with a branching ratio of 0.111 for $W \rightarrow \ell\nu$ but the k-factors are adjusted to match the branching ratio of 0.1080 given in the 2010 PDG [3]. A next-to-next-to-leading-order (NNLO) approximate [130] k-factor of 1.082 is applied to the $t\bar{t}$ sample. The fragmentation and hadronization for these events is

Process (ID)	σ_{LO} [pb]	k-factor	filter efficiency	$\int \mathcal{L} dt$ [fb ⁻¹]
$W^\pm W^\pm + jet$ (119357)	0.22	1		433.0
$W^+ \gamma (e\nu)$ (106001)	27.97	1	1	1.8
$W^+ \gamma (\mu\nu)$ (106002)	27.94	1	1	1.8
$W^+ \gamma (\tau\nu)$ (106003)	25.42	1	0.17 (1)	11.0
$W^- \gamma (e\nu)$ (108288)	18.59	1	1	2.7
$W^- \gamma (\mu\nu)$ (108289)	18.59	1	1	2.7
$W^- \gamma (\tau\nu)$ (108290)	16.86	1	0.17	17.1
$Z\gamma (ee)$ (108323)	10.02	1	1	5.0
$Z\gamma (\mu\mu)$ (108324)	10.02	1	1	5.0
$Z\gamma (\tau\tau)$ (108325)	9.76	1	0.17	29.6
$t\bar{t} W$ (119353)	0.12	1.39	1	577.7
$t\bar{t} W + jet$ (119354)	0.08	1.39	1	861.1
$t\bar{t} Z$ (119355)	0.10	1.39	1	752.0
$t\bar{t} Z + jet$ (119356)	0.08	1.39	1	880.6
$t\bar{t} WW$ (119583)	0.001	1.39	1	57541.3

Table 5.3: The background MC produced by MADGRAPH used in this analysis. Shown are the LO cross sections, k-factors, and filter efficiencies, as well as the integrated luminosity corresponding to the number of events generated. Also shown is the ATLAS process ID.

simulated using HERWIG and the underlying event is simulated using JIMMY [131]. The individual samples with cross section \times k-factor \times filter efficiency and integrated luminosity are shown in Table 5.4. Both t and $t\bar{t}$ are combined in plots and labeled $t + t\bar{t}$.

ALPGEN [132] is used to model the W and Z/γ^* in association with jets production. The fragmentation and hadronization for these events is simulated using HERWIG and the underlying event is simulated using JIMMY. The ALPGEN LO cross sections are scaled to NNLO with a k-factor calculated in [126]. Samples with W and heavy-flavor quarks (c, b) are also used. For all W samples a k-factor of 1.2 is applied to reach the NNLO cross section. The Z/γ^* samples come in three different types, representing different kinematic regions or channels:

Light Flavor samples are produced with $40 < M_{\ell+\ell^-} < 2000$ GeV. These samples do not specifically exclude processes with b -quarks. This is corrected by vetoing such events during later analysis. A k-factor of 1.25 is applied to these samples. Heavy flavor contributions

Process	$\sigma_{LO} \times \text{k-factor} \times \text{filter efficiency [pb]}$	$\int \mathcal{L} dt [\text{fb}^{-1}]$
$t\bar{t}$ (105200)	89.36	129.49
t-channel $e\nu$ (108340)	7.12	24.95
t-channel $\mu\nu$ (108341)	7.12	24.93
t-channel $\tau\nu$ (108342)	7.10	24.97
s-channel $e\nu$ (108343)	0.47	540.04
s-channel $\mu\nu$ (108344)	0.47	539.50
s-channel $\tau\nu$ (108345)	0.47	539.67
Wt (108346)	14.59	54.65

Table 5.4: The t -quark samples produced using MC@NLO, with the total integrated luminosity represented by the number of events and the cross section \times k-factor \times filter efficiency. Also shown is the ATLAS process ID.

from these events are discarded during analysis to avoid overlap with the following heavy flavor MC samples.

Heavy Flavor samples are produced with $30 < M_{\ell^+\ell^-} < 2000$ GeV and specifically model $Z + b\bar{b} \rightarrow \ell^+\ell^- + \text{partons}$. A k-factor of 1.75 is applied to these samples.

Low Mass Z/γ^* are produced with $10 < M_{\ell^+\ell^-} < 40$ GeV. A k-factor of 1.25 is applied to these samples.

The individual samples with NLO cross section and integrated luminosity are shown in Table 5.5 for W backgrounds and Table 5.6 for Z backgrounds. All $W + \text{jets}$ and $Z/\gamma^* + \text{jets}$ are combined in plots and labeled $V + \text{jets}$.

The Standard Model MC makes use of three particle distribution function (PDF) sets. The MC@NLO samples make use of the next-to-leading order CTEQ6.6 [133] PDF set. ALPGEN and MADGRAPH use the CTEQ6L1 [134] PDF set. All other Standard Model MC samples make use of MRST2007LO* [135].

Process			σ_{NNLO} [pb]	$\int \mathcal{L} dt$ [fb ⁻¹]	Process			σ_{NNLO} [pb]	$\int \mathcal{L} dt$ [fb ⁻¹]
<i>W</i> +jets	(<i>eν</i> +Np0) (107680)		8305.9	0.4	<i>W_c</i>	Np0 (117288)		518	1.6
	(<i>eν</i> +Np1) (107681)		1565.2	0.4		Np1 (117289)		192	1.7
	(<i>eν</i> +Np2) (107682)		454.0	8.3		Np2 (117290)		51	1.7
	(<i>eν</i> +Np3) (107683)		121.7	8.3		Np3 (117291)		12	1.7
	(<i>eν</i> +Np4) (107684)		31.0	8.1	<i>W_{cc}</i>	Np0 (117284)		153	1.7
	(<i>eν</i> +Np5) (107685)		8.4	8.3		Np1 (117285)		124	1.6
	(<i>μν</i> +Np0) (107690)		8303.5	0.4		Np2 (117286)		62	1.7
	(<i>μν</i> +Np1) (107691)		1565.0	0.4		Np3 (117287)		20	1.7
	(<i>μν</i> +Np2) (107692)		453.4	8.3	<i>W_{bb}</i>	Np0 (106280)		4.0	1.6
	(<i>μν</i> +Np3) (107693)		122.3	8.3		Np1 (106281)		3.2	1.7
	(<i>μν</i> +Np4) (107694)		30.9	8.3		Np2 (106282)		1.7	1.8
	(<i>μν</i> +Np5) (107695)		8.3	8.4		Np3 (106283)		0.8	1.9
	(<i>τν</i> +Np0) (107700)		8302.3	0.4					
	(<i>τν</i> +Np1) (107701)		1563.8	0.4					
	(<i>τν</i> +Np2) (107702)		453.8	8.3					
	(<i>τν</i> +Np3) (107703)		121.8	8.3					
	(<i>τν</i> +Np4) (107704)		30.8	8.1					
	(<i>τν</i> +Np5) (107705)		8.5	7.5					

Table 5.5: The *W*-background MC produced by ALPGEN used in this analysis. Shown are the NNLO cross sections and integrated luminosity corresponding to the number of events generated. Also shown is the ATLAS process ID. Note that the Np# indicates the number of generated partons.

Process			σ_{NNLO} [pb]	$\int \mathcal{L} dt$ [fb ⁻¹]	Process			σ_{NNLO} [pb]	$\int \mathcal{L} dt$ [fb ⁻¹]
Z+jets	(<i>ee</i> +Np0) (107650)	835.4	7.9	Drell-Yan	(<i>ee</i> +Np0) (116250)	3819.0	0.3		
	(<i>ee</i> +Np1) (107651)	168.0	7.9		(<i>ee</i> +Np1) (116251)	106.2	2.8		
	(<i>ee</i> +Np2) (107652)	50.7	8.0		(<i>ee</i> +Np2) (116252)	51.8	9.7		
	(<i>ee</i> +Np3) (107653)	14.0	7.9		(<i>ee</i> +Np3) (116253)	10.5	14.3		
	(<i>ee</i> +Np4) (107654)	3.6	8.3		(<i>ee</i> +Np4) (116254)	2.3	17.3		
	(<i>ee</i> +Np5) (107655)	1.0	8.7		(<i>ee</i> +Np5) (116255)	0.6	17.4		
	($\mu\mu$ +Np0) (107660)	835.9	7.9		($\mu\mu$ +Np0) (116260)	3818.6	0.3		
	($\mu\mu$ +Np1) (107661)	167.7	8.0		($\mu\mu$ +Np1) (116261)	106.1	2.8		
	($\mu\mu$ +Np2) (107662)	50.4	8.0		($\mu\mu$ +Np2) (116262)	51.8	9.7		
	($\mu\mu$ +Np3) (107663)	14.0	7.9		($\mu\mu$ +Np3) (116263)	10.5	14.3		
	($\mu\mu$ +Np4) (107664)	3.4	8.7		($\mu\mu$ +Np4) (116264)	2.3	17.3		
	($\mu\mu$ +Np5) (107665)	1.0	10.4		($\mu\mu$ +Np5) (116265)	0.6	17.4		
	($\tau\tau$ +Np0) (107670)	835.5	7.9		($\tau\tau$ +Np0) (116270)	3818.9	0.3		
	($\tau\tau$ +Np1) (107671)	168.5	7.9		($\tau\tau$ +Np1) (116271)	106.2	2.8		
	($\tau\tau$ +Np2) (107672)	50.5	8.0		($\tau\tau$ +Np2) (116272)	51.8	9.6		
	($\tau\tau$ +Np3) (107673)	14.1	7.8		($\tau\tau$ +Np3) (116273)	10.5	14.4		
	($\tau\tau$ +Np4) (107674)	3.5	8.6		($\tau\tau$ +Np4) (116274)	2.3	17.3		
	($\tau\tau$ +Np5) (107675)	1.0	10.4		($\tau\tau$ +Np5) (116275)	0.6	17.4		
<i>Zbb</i>	(<i>ee</i> +Np0) (109300)	11.5	13.0	<i>Zbb</i>	($\mu\mu$ +Np0) (109305)	11.5	13.1		
	(<i>ee</i> +Np1) (109301)	4.3	23.0		($\mu\mu$ +Np1) (109306)	4.3	23.1		
	(<i>ee</i> +Np2) (109302)	1.5	25.0		($\mu\mu$ +Np2) (109307)	1.5	25.7		
	(<i>ee</i> +Np3) (109303)	0.7	14.6		($\mu\mu$ +Np3) (109308)	0.7	14.6		
<i>Zbb</i>	($\tau\tau$ +Np0) (109310)	11.5	13.0						
	($\tau\tau$ +Np1) (109311)	4.3	22.9						
	($\tau\tau$ +Np2) (109312)	1.5	25.7						
	($\tau\tau$ +Np3) (109313)	0.7	13.2						

Table 5.6: The background MC produced by ALPGEN used in this analysis. Shown are the NNLO cross sections and integrated luminosity corresponding to the number of events generated. Also shown is the ATLAS process ID. Note that the Np# indicates the number of generated partons.

5.2 GGM SUSY Signal Grids

The Z -rich higgsino grid requires $\mu \ll m_{1,2}$, which produces an NLSP corresponding to the higgsino which then decays into $\gamma\tilde{G}$ or $Z\tilde{G}$. The parameters are set to $m_1 = m_2 = 1$ TeV, $\tan\beta = 1.5$, and $c\tau_{NLSP} = 0.1$ mm. Soft supersymmetry-breaking parameters are set to 1.5 TeV. The μ term is required to be positive, but is within the bounds required for a higgsino NLSP. The grid is parameterised over $300 < m_{\tilde{g}} < 1000$ GeV and $120 < m_{\tilde{H}} < 990$ GeV.

The wino co-NLSPs model requires $m_2 \ll \mu$ and $m_2 < m_1$ in order to produce a wino-like chargino and neutralino that are degenerate in mass and act as co-NLSPs. The NLSPs then decay into $\gamma\tilde{G}$, $Z\tilde{G}$, and $W\tilde{G}$. The parameters are set to $m_1 = \mu = 1.5$ TeV, $\tan\beta = 2$, $c\tau_{NLSP} = 0.1$ mm. m_2 is varied as required to produce the wino co-NLSP. The grid is parameterised in terms of $300 < m_{\tilde{g}} < 1000$ GeV and $120 < m_{\tilde{W}} < 990$ GeV.

The GGM grids were produced with PYTHIA 6.423 [123] with the MRST2007LO* used for the PDFs. with mass spectra calculated using SUSPECT 2.41 [136] and SDECAY 1.3 [137]. The Higgsino signal grid was optimized for leptonic searches by applying a $Z \rightarrow \ell^+\ell^-$ filter to the MC generation. For the wino signal grid, a two-lepton filter was applied, except in the case of points with $m_{\tilde{W}} = 120$ GeV, where the $Z \rightarrow \ell^+\ell^-$ filter was applied. NLO production cross sections for the signal points of the GGM grids were calculated using Prospino 2.1 [138–140]. For samples with gluino and light squark masses in the range of 200 GeV to 2 TeV, NLLFAST [141] was used for $\tilde{g}\tilde{g}$ -production to provide next-to-leading-logarithmic (NLL) corrected calculations of the cross section. For the Higgsino grid the important gaugino processes are $\tilde{\chi}_1^0\tilde{\chi}_2^0$, $\tilde{\chi}_1^0\tilde{\chi}_1^+$, $\tilde{\chi}_1^0\tilde{\chi}_1^-$, $\tilde{\chi}_2^0\tilde{\chi}_1^+$, $\tilde{\chi}_2^0\tilde{\chi}_1^-$, and $\tilde{\chi}_1^\pm\tilde{\chi}_1^\mp$. For the Wino grid the important processes are $\tilde{\chi}_1^0\tilde{\chi}_1^+$, $\tilde{\chi}_1^0\tilde{\chi}_1^-$, and $\tilde{\chi}_1^\pm\tilde{\chi}_1^\mp$.

Two points are used as a signal reference for plots in this analysis, one from each grid. The parameters of the points used are $m_{\tilde{g}} = 300$ GeV and $m_{\tilde{H}} = 200$ GeV ($m_{\tilde{W}} = 200$ GeV) for the higgsino (wino) grid point. The reference signal points are labeled “Ref \tilde{H} ” (“Ref \tilde{W} ”) for the higgsino (wino) grid point. If they have had the SM prediction added to them, they appear as “MC + Ref \tilde{H} ” (“MC + Ref \tilde{W} ”).

$m_{\tilde{g}}$ [GeV]	σ_{NLO} [pb]
300	66 ± 10
400	10.7 ± 1.7
500	2.4 ± 0.4
600	0.63 ± 0.13
700	0.18 ± 0.05
800	0.06 ± 0.02
900	0.020 ± 0.007
1000	0.007 ± 0.003

Table 5.7: The NLL cross sections for $\tilde{g}\tilde{g}$ -production in the Higgsino and Wino GGM grids. The $\tilde{g}\tilde{g}$ -production is solely dependent on $m_{\tilde{g}}$. The uncertainty on the cross section includes uncertainties on the PDF, factorization and normalization scale, and α_S .

$m_{\tilde{H}}$ [GeV]	σ_{NLO} [pb]					
	$\tilde{\chi}_1^0 \tilde{\chi}_2^0$	$\tilde{\chi}_1^0 \tilde{\chi}_1^+$	$\tilde{\chi}_1^0 \tilde{\chi}_1^-$	$\tilde{\chi}_2^0 \tilde{\chi}_1^+$	$\tilde{\chi}_2^0 \tilde{\chi}_1^-$	$\tilde{\chi}_1^\pm \tilde{\chi}_1^\mp$
110	1.08 ± 0.07	1.43 ± 0.09	0.79 ± 0.07	1.18 ± 0.08	0.65 ± 0.05	1.13 ± 0.09
115	0.89 ± 0.06	1.19 ± 0.08	0.65 ± 0.05	0.99 ± 0.06	0.54 ± 0.05	0.94 ± 0.07
120	0.75 ± 0.05	1.00 ± 0.06	0.55 ± 0.05	0.85 ± 0.05	0.45 ± 0.04	0.79 ± 0.06
150	0.30 ± 0.02	0.41 ± 0.03	0.21 ± 0.02	0.36 ± 0.02	0.18 ± 0.01	0.33 ± 0.02
200	0.090 ± 0.006	0.130 ± 0.007	0.060 ± 0.005	0.115 ± 0.007	0.053 ± 0.004	0.102 ± 0.007
290	0.017 ± 0.001	0.027 ± 0.002	0.0109 ± 0.0009	0.024 ± 0.002	0.0096 ± 0.0007	0.020 ± 0.001
300	0.015 ± 0.001	0.023 ± 0.002	0.0092 ± 0.0007	0.021 ± 0.001	0.0082 ± 0.0007	0.017 ± 0.001
390	0.0041 ± 0.0003	0.0068 ± 0.0005	0.0024 ± 0.0002	0.0060 ± 0.0005	0.0022 ± 0.0002	0.0049 ± 0.0004
400	0.0036 ± 0.0003	0.0059 ± 0.0005	0.0021 ± 0.0002	0.0053 ± 0.0004	0.0019 ± 0.0002	0.0042 ± 0.0003
490	0.0012 ± 0.0001	0.0020 ± 0.0002	$(6.8 \pm 0.7) \cdot 10^{-4}$	0.0018 ± 0.0001	$(6.0 \pm 0.6) \cdot 10^{-4}$	0.0014 ± 0.0001
500	0.0011 ± 0.0001	0.0018 ± 0.0001	$(6.1 \pm 0.6) \cdot 10^{-4}$	0.0016 ± 0.0001	$(5.3 \pm 0.6) \cdot 10^{-4}$	0.0013 ± 0.0001
590	$(3.9 \pm 0.3) \cdot 10^{-4}$	$(6.9 \pm 0.6) \cdot 10^{-4}$	$(2.2 \pm 0.3) \cdot 10^{-4}$	$(5.9 \pm 0.5) \cdot 10^{-4}$	$(1.9 \pm 0.2) \cdot 10^{-4}$	$(4.9 \pm 0.5) \cdot 10^{-4}$
600	$(3.5 \pm 0.3) \cdot 10^{-4}$	$(6.2 \pm 0.5) \cdot 10^{-4}$	$(2.0 \pm 0.2) \cdot 10^{-4}$	$(5.3 \pm 0.4) \cdot 10^{-4}$	$(1.7 \pm 0.2) \cdot 10^{-4}$	$(4.4 \pm 0.4) \cdot 10^{-4}$
690	$(1.4 \pm 0.1) \cdot 10^{-4}$	$(2.5 \pm 0.2) \cdot 10^{-4}$	$(7.9 \pm 1.0) \cdot 10^{-5}$	$(2.1 \pm 0.2) \cdot 10^{-4}$	$(6.6 \pm 0.9) \cdot 10^{-5}$	$(1.8 \pm 0.2) \cdot 10^{-4}$
700	$(1.2 \pm 0.1) \cdot 10^{-4}$	$(2.2 \pm 0.2) \cdot 10^{-4}$	$(7.2 \pm 0.9) \cdot 10^{-5}$	$(1.9 \pm 0.2) \cdot 10^{-4}$	$(6.0 \pm 0.8) \cdot 10^{-5}$	$(1.6 \pm 0.2) \cdot 10^{-4}$
790	$(4.9 \pm 0.5) \cdot 10^{-5}$	$(9.5 \pm 0.8) \cdot 10^{-5}$	$(3.1 \pm 0.4) \cdot 10^{-5}$	$(7.4 \pm 0.7) \cdot 10^{-5}$	$(2.4 \pm 0.3) \cdot 10^{-5}$	$(7.2 \pm 0.8) \cdot 10^{-5}$
800	$(4.5 \pm 0.4) \cdot 10^{-5}$	$(8.6 \pm 0.8) \cdot 10^{-5}$	$(2.8 \pm 0.4) \cdot 10^{-5}$	$(6.7 \pm 0.6) \cdot 10^{-5}$	$(2.2 \pm 0.3) \cdot 10^{-5}$	$(6.5 \pm 0.7) \cdot 10^{-5}$
890	$(1.8 \pm 0.2) \cdot 10^{-5}$	$(3.8 \pm 0.4) \cdot 10^{-5}$	$(1.2 \pm 0.2) \cdot 10^{-5}$	$(2.6 \pm 0.3) \cdot 10^{-5}$	$(8.6 \pm 0.1) \cdot 10^{-5}$	$(3.0 \pm 0.3) \cdot 10^{-5}$

Table 5.8: The NLO cross sections for gaugino-production processes in the Higgsino grid. Gaugino-production cross sections are only dependent on $m_{\tilde{H}}$. The uncertainty on the cross section includes uncertainties on the PDF, factorization and normalization scale, and α_S .

$m_{\tilde{H}}$ [GeV]	σ_{NLO} [pb]		
	$\tilde{\chi}_1^0 \tilde{\chi}_1^+$	$\tilde{\chi}_1^0 \tilde{\chi}_1^-$	$\tilde{\chi}_1^\pm \tilde{\chi}_1^\mp$
120	3.3 ± 0.2	1.8 ± 0.2	2.5 ± 0.2
150	1.35 ± 0.08	0.68 ± 0.05	1.00 ± 0.07
200	0.41 ± 0.02	0.19 ± 0.01	0.29 ± 0.02
290	0.076 ± 0.005	0.031 ± 0.002	0.051 ± 0.004
300	0.064 ± 0.004	0.026 ± 0.002	0.043 ± 0.003
390	0.016 ± 0.001	0.0058 ± 0.0005	0.0104 ± 0.0008
400	0.014 ± 0.001	0.0050 ± 0.0005	0.0090 ± 0.0007
490	0.0040 ± 0.0003	0.0013 ± 0.0001	0.0025 ± 0.0002
500	0.0035 ± 0.0003	0.0012 ± 0.0001	0.0022 ± 0.0002
590	$(1.06 \pm 0.09) \cdot 10^{-3}$	$(3.4 \pm 0.4) \cdot 10^{-4}$	$(6.8 \pm 0.6) \cdot 10^{-4}$
600	$(9.3 \pm 0.8) \cdot 10^{-4}$	$(3.0 \pm 0.3) \cdot 10^{-4}$	$(6.0 \pm 0.5) \cdot 10^{-4}$
690	$(2.9 \pm 0.2) \cdot 10^{-4}$	$(9.2 \pm 0.1) \cdot 10^{-5}$	$(1.9 \pm 0.2) \cdot 10^{-4}$
700	$(2.5 \pm 0.2) \cdot 10^{-4}$	$(8.0 \pm 1.0) \cdot 10^{-5}$	$(1.7 \pm 0.2) \cdot 10^{-4}$
790	$(7.9 \pm 0.7) \cdot 10^{-5}$	$(2.5 \pm 0.3) \cdot 10^{-5}$	$(5.8 \pm 0.6) \cdot 10^{-5}$
800	$(6.9 \pm 0.6) \cdot 10^{-5}$	$(2.2 \pm 0.3) \cdot 10^{-5}$	$(5.1 \pm 0.5) \cdot 10^{-5}$
890	$(2.1 \pm 0.2) \cdot 10^{-5}$	$(7.0 \pm 1.0) \cdot 10^{-6}$	$(1.7 \pm 0.2) \cdot 10^{-5}$

Table 5.9: The NLO cross sections for gaugino-production processes in the Wino grid. Gaugino-production cross sections are only dependent on $m_{\tilde{H}}$. The uncertainty on the cross section includes uncertainties on the PDF, factorization and normalization scale, and α_S .

Mother Nature doesn't care if you're having fun.

Larry Niven [142]

6

Analysis

6.1 Physics Objects Reconstruction & Selection

6.1.1 Particle Selection

Electrons are reconstructed using the “medium” level selections developed in [143] as a baseline. Electron clusters are created in the middle sampling layer of the LAr calorimeter using a 3×5 cell sliding window to identify clusters with energy greater than 2.5 GeV (the dimension in ϕ is larger to account for bremsstrahlung losses as the track bends in the ID). Each cell is 0.025×0.0245 in $\eta \times \phi$. Clusters are then matched to an ID track, taking the nearest track in ΔR from the cluster barycenter as the electron track. After track matching the cluster is re-calculated into a 3×7 (5×5) cell cluster in the barrel (end-caps). The medium selections include requirements on the hadronic leakage and shower shape, as well as requiring at least one hit in the pixel detector, at least seven hits in the SCT, and a transverse impact parameter of less than 5 mm. It is also required that a medium electron have no more than $\Delta\eta < 0.01$ distance between the cluster barycenter and the track that comprise the electron. After these preliminary selections, addition selections are applied to the electrons:

- The energy of electrons in data is rescaled in order to accurately match the observed energy scale of the ATLAS detector, based on measurements using the decay of the Z -boson and J/Ψ -meson to electron-pairs [144].

- MC electrons are subject to smearing in order to match the energy resolution observed in data.
- $E_T > 10$ GeV.
- $|\eta_{cluster}| < 2.47$, specifically using the cluster η measurement instead of the track measurement.
- Electrons traversing inactive regions in the EM calorimeter due to dead optical transmitters (OTX) are discarded.
- Electrons in the calorimeter crack, $1.37 < |\eta_{cl}| < 1.52$, are required to have $E_T > 15$ GeV.

Electrons passing these selections are subjected to an overlap removal scheme explained in Section 6.1.2. The corrections to electron energy scale and resolution are implemented using tools supplied by the egamma performance group [144].

Finally, *signal electrons* passing these selections and overlap are required to be isolated such that for all tracks with $p_T^{track} > 1$ GeV [145]:

$$\frac{\sum_{\Delta R_{e,track} \leq 0.2} p_T^{track}}{E_T^e} < 0.1 \quad (6.1)$$

and it is further required that signal electrons pass the “tight” level selections [143]. In addition to the medium requirements, tight electrons are required to have at least one hit in the pixel detector b-layer. In the TRT the difference between the number of hits and the expected average number of hits must be ≤ 15 . Tight electrons must have no more than $\Delta\phi < 0.02$ distance between the cluster and the track that correspond to the electron and the $\Delta\eta$ selection is tightened to be less than 0.005. The transverse impact parameter is also tightened to $d_0 < 1$ mm and a veto is applied to electrons that reconstruct a photon conversion. Additional selections are made on the fraction of high-threshold TRT hits and the E/p ratio for the electron track.

Prior to the isolation and tight-electron requirements, an electron is considered a *tagged electron*.

Muons are reconstructed with the STACO (**ST**Atistical **CO**mbination) algorithm. STACO combines a reconstructed muon spectrometer track with a matched inner detector track to form a combined muon. This is supplemented with muons constructed with an inner detector track

then matched to a hit or segments of hits in the muon spectrometer or deposits in the calorimeter [70]. Additional cuts are applied as follows:

- The p_T of the MC combined and segment-tagged muons are smeared in order to match the momentum resolution observed in data, using tools provided by the muon combined performance group [146]
- $p_T > 10$ GeV
- $|\eta| < 2.40$
- Segment-tagged muons are muons constructed from an ID track and hits or segments in the MS without a full track; they are required to meet one of the following criteria:
 - One hit in the endcap region ($|\eta| > 1.05$) of the muon spectrometer, but no TGC end-cap hits.
 - At least two tagged segments.
 - At least three TGC end-cap hits in the tagged segments.
- The muon track must have at least one hit in the pixel tracker and at least six SCT hits.
- The muon track must satisfy the following TRT requirements where $n = n_{TRT}^{hits} + n_{TRT}^{outliers}$ (a TRT outlier is a hit not associated with a track or a track in which the TRT component does not form a smooth trajectory with the pixel and SCT components [147]):
 - if $|\eta| < 1.9$, require $n > 5$ and $n_{TRT}^{outliers} < 0.9n$.
 - if $|\eta| \geq 1.9$ and $n > 5$ require $n_{TRT}^{outliers} < 0.9n$.

After passing these selections the muons are subjected to an overlap removal scheme explained in Section 6.1.2.

Signal muons are also subject to a further isolation requirement, such that for all tracks with $p_T^{track} > 1$ GeV :

$$\sum_{\Delta R_{\mu, track} \leq 0.2} p_T^{track} < 1.8 \text{ GeV} \quad (6.2)$$

Prior to the isolation requirement, a muon is considered a *tagged muon*.

Jets are reconstructed with an anti- k_T jet algorithm [148] with four-momentum recombination using characteristic radius $R_c = 0.4$ (see Appendix F.4 for further details of the anti- k_T algorithm). These jets are reconstructed using topological clusters [149]. See Section 6.1.4 for how

topological clusters are constructed. The topological clusters used for this reconstruction are initially scaled to the electromagnetic energy scale that is optimized for electron and photon showers. This scale systematically underestimates the energy in hadronic objects because the non-compensating calorimeters have a lower response to hadronic objects, as well as effects due to dead material and out-of-cone energy loss. This is corrected by applying the *Jet Numerical Inversion Correction* to the electromagnetic scale energy and momenta as a function of $p_{T,\text{jet}}^{\text{EM}}$ and $|\eta_{\text{jet}}|$; this makes use of matching the p_T and η of a measured jet to the reconstructed values of truth jets and using the response of the truth jets to estimate the actual energy scale of the jet. This new calibration at jet energy scale has been optimized using MC simulation [150].

Acceptance cuts applied to the jets are:

- $p_T > 20 \text{ GeV}$
- $|\eta| < 2.8$

After passing these selections the jets are subjected to an overlap removal scheme explained in Section 6.1.2.

Jets are considered *b-tagged* based on the output of a neural network. Jets with a neural network discriminating variable greater than 2 and $|\eta| > 2.5$ are considered *b-tagged*. This value of the discriminating variable gives an average efficiency for *b*-tagging of approximately 60% [151]. *b*-jets are used in estimating heavy flavor components for background estimation.

6.1.2 Overlap Removal

It is the nature of calorimeter objects that they can be reconstructed by multiple reconstruction algorithms. Consequently, electrons may appear in the collection of jets for an event and vice versa. In order to remove this ambiguity, objects passing the previous selections are subject to overlap removal based on their distance in terms of $\Delta R = \sqrt{(\Delta\eta)^2 + (\Delta\phi)^2}$.

If an electron and a jet are within a distance of $\Delta R < 0.2$, the electron is selected and the jet is discarded. Often, jets may contain leptonic products from *b* or *c* decays. Muons and electrons falling within $\Delta R < 0.4$ are rejected while the jet is preserved, further enhancing the quality of isolation of the leptons and reducing the contribution from these leptonic jet products, particularly in the case of muons.

A fraction of electrons are produced from muons experiencing bremsstrahlung while traversing the detector, resulting in a badly measured muon

and a spurious electron that may be the result of a mis-reconstructed photon. It is preferable to discard such leptons and to facilitate this, all electrons (muons) within $\Delta R < 0.1$ of a muon (electron) are discarded.

6.1.3 Further Object Selection Criteria

The Drell-Yan process and J/Ψ production can be considerable sources of background to multilepton supersymmetry channels, particularly when combined with leptonic fakes from the hadronic component of the event. To reduce this source of background, same-flavor opposite-sign (SFOS) lepton pairs with invariant mass below 20 GeV are discarded.

6.1.4 E_T^{miss} Definition

E_T^{miss} is a chimera, requiring the input and tuning of all other important physics objects: electrons, photons, jets, taus, muons, and any remaining energy in the calorimeter not associated with any other object. However, at this date certain object reconstruction algorithms have not been fully validated, such as τ -reconstruction. Additionally, a specialized photon term is not required for a lepton-rich analysis. Consequently, the definition of E_T^{miss} used in this analysis is a custom definition developed for ATLAS leptonic supersymmetry analyses:

$$E_{x(y)}^{\text{miss}} = E_{x(y)}^{\text{miss,e}} + E_{x(y)}^{\text{miss,jets}} + E_{x(y)}^{\text{miss,clusters}} + E_{x(y)}^{\text{miss,\mu}} \quad (6.3)$$

where each term represents the contribution to $E_{x(y)}^{\text{miss}}$ from each object. Each term is the $x(y)$ -component of the negative sum of the object contributions, i.e. $E_{x(y)}^{\text{miss,\mu}} = -\sum_{\text{muons}} p_{x(y)}$ and $E_{x(y)}^{\text{miss,e}} = -\sum_{\text{electrons}} E_{x(y)}$.

The E_T^{miss} -algorithm makes use of topological clusters as the initial input. The clusters are constructed from calorimeter cells using a 4-2-0 scheme for suppressing noise:

- Cells with $|E_{\text{cell}}| \geq 4\sigma_{\text{noise}}$ form the seed of the cluster.
- All neighboring cells with $|E_{\text{cell}}| \geq 2\sigma_{\text{noise}}$ are iteratively added to the cluster.
- The remaining neighboring cells with $|E_{\text{cell}}| \geq 0$ form the surface of the cluster.

Any cells outside of a cluster are not used. The quantity σ_{noise} is the Gaussian width measured for each cell when triggered on random events, thus giving a

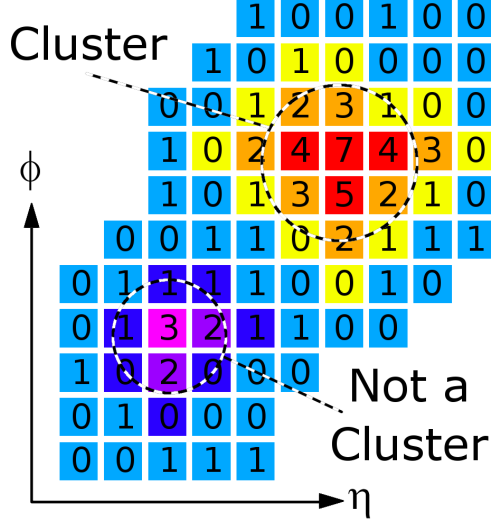


Figure 6.1: A depiction of the ATLAS clustering algorithm, showing a grouping of cells selected as a cluster and another grouping not selected. The numerical value represents the energy in the cell divided by its Gaussian width, σ_{noise} , as measured in randomly triggered events.

measure of the random noise in the cell [149, 152]. Cells known to be particularly noisy are excluded, which includes $\approx 0.1\%$ of all cells. During collisions approximately 2500 cells will be selected on average. This method was chosen over a simple threshold criteria and is optimized to suppress both electronic noise and pile-up energy, but preserve the efficiency for single pions [153]. In Figure 6.1 is a depiction of a cell grouping which would pass the 4-2-0 clustering algorithm and a depiction of a cell grouping which would not pass the algorithm.

The E_T^{miss} -algorithm associates these topological clusters to physics objects. A diagram of this process can be seen in Figure 6.2. The algorithm begins by matching the topological clusters to the electrons, though the actual cluster algorithm used in the case of electromagnetic objects is a sliding window algorithm [154, 155]. The remaining topoclusters are then matched to jets. Any remaining unmatched topological clusters are given the local calibration and make up the out-of-object cluster term of E_T^{miss} . The actual contribution from the electrons and jets is determined by calibrating the physics object, not the matched clusters [155]. Finally, the baseline muons outlined in Section 6.1.1 are added to E_T^{miss} .

The algorithm used for reconstructing E_T^{miss} has been carefully optimized on its own and not all physics objects have a one-to-one correspondence to

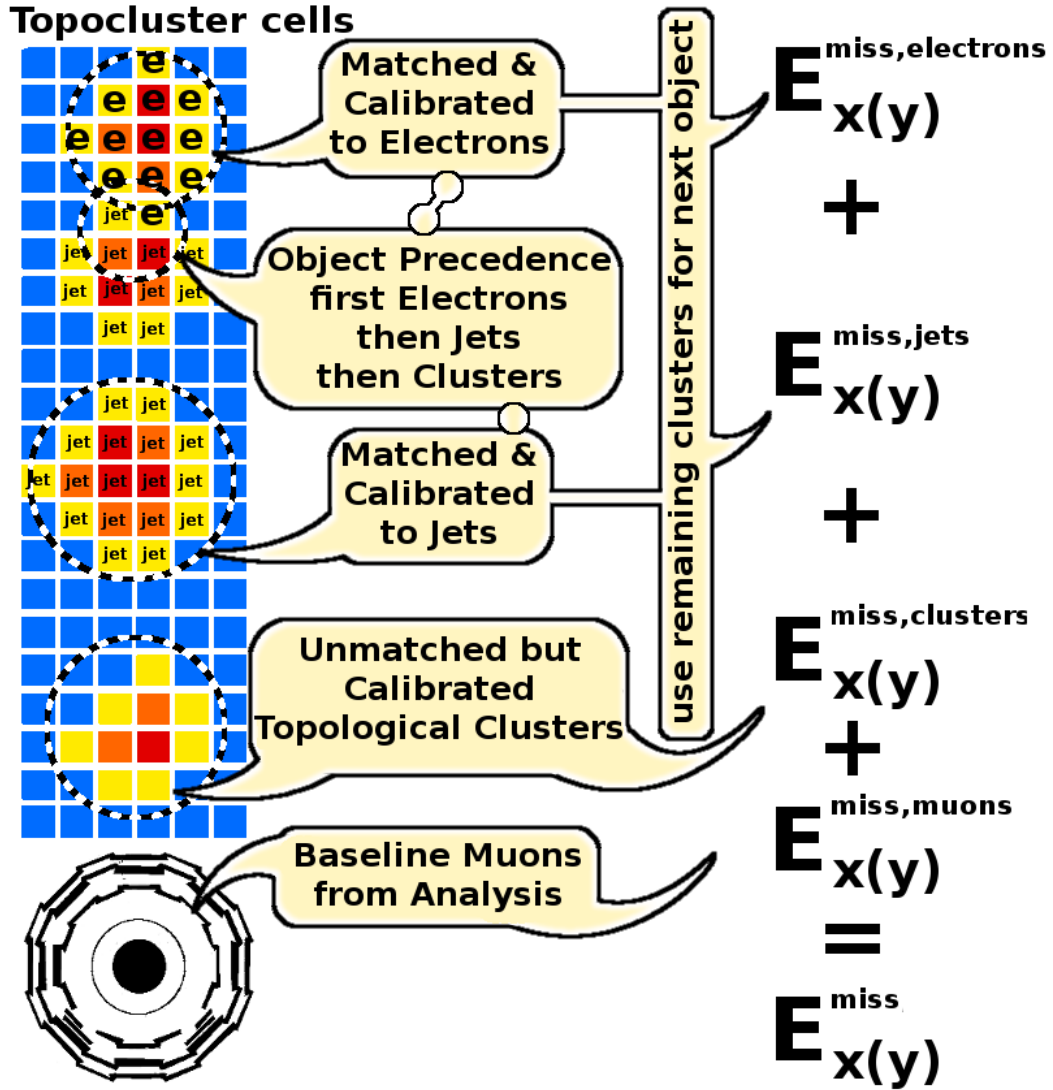


Figure 6.2: The flow of the ATLAS SUSY E_T^{miss} -algorithm.

the object selections in Section 6.1.1. For electrons the medium level selection is used and a tighter $p_T > 20$ GeV is applied. Jets are accepted up to $|\eta| < 4.5$, as are the topoclusters in the out-of-object cluster term. Out-of-object topological clusters are calibrated at the electromagnetic scale, without any hadronic correction.

However, due to an error in the algorithm calculating E_T^{miss} , topological clusters that belong to the electron term ($E_{x(y)}^{\text{miss,e}}$) may be included in the jet term ($E_{x(y)}^{\text{miss,jets}}$). This error occurs when the ΣE of the topological clusters comprising the electron object exceeds 110% of the electron E . This is done to ensure that the energy of the topological clusters used to calculate E_T^{miss} does not diverge greatly from the energy measurement of the actual object. However, this can result in an electron topological cluster being included in $E_{x(y)}^{\text{miss,jets}}$ and because this check only affects the E_T^{miss} -algorithm's overlap removal, it results in an overlapped jet surviving in $E_{x(y)}^{\text{miss,jets}}$ and causes double counting of the object energy. Events where this problem have occurred can be identified by checking for the condition:

$$\frac{|\mathbf{E}_T^{\text{miss,jets}} + \sum_{\text{jets}} \mathbf{p}_T^{\text{jet}}|}{E_T^{\text{miss,e}}} \leq 1. \quad (6.4)$$

The error is corrected by scaling $E_{x(y)}^{\text{miss,e}}$ by the expected electromagnetic to hadronic response (e/h) and subtracting all jets with $p_T > 20$ GeV to produce a new $E_{x(y)}^{\text{miss,jets}}$ term:

$$E_{x(y)}^{\text{miss,jets}} = -\frac{e}{h} \cdot E_{x(y)}^{\text{miss,e}} - \sum_{\text{jets}} \mathbf{p}_T^{\text{jet}} \quad (6.5)$$

6.2 Event Handling

In the following chapter are detailed the various selections applied to data and MC, the corrections applied to MC, and the triggering scheme used. These selections and corrections are applied after the selections and corrections applied to individual physics objects in the event, as detailed in the previous section.

6.2.1 Trigger

The following triggers are used in data:

- EF_e20_medium, which requires that an electron seeded by the calorime-

ter triggers and be reconstructed by the TDAQ event filter. The reconstruction requirement of medium is applied in addition to an E_T selection of approximately 20 GeV. The actual threshold varies by detector region but is within 10% of this value.

- EF_e22_medium, which is similar to the previous trigger, but requires approximately $E_T > 22$ as the selection.
- EF_mu18, which requires a combined muon (both ID and MS) with $p_T > 18$ GeV as the approximate cut.
- EF_mu18_medium, which has the same selection as the previous trigger but is seeded by the L1 MU11 trigger instead of L1 MU10, thus reducing the frequency.

In addition to simply requiring that the trigger fired, it is required that an offline reconstructed lepton be matched to a trigger lepton to within $\Delta R < 0.15$. Furthermore, the trigger lepton is required to be well within the trigger plateau with $p_T > 25$ (20) GeV for electrons (muons). Over the course of accelerator operations the luminosity of the LHC increased. This in turn required that additional triggers be pre-scaled. To avoid using pre-scaled triggers, this analysis makes use of the lowest threshold triggers that have not been pre-scaled. The identity of this trigger changes in later periods. The triggers used for each period are shown in Table 6.1. Note that triggers are only directly applied to data. For MC, a trigger re-weighting scheme is used, as explained in Section 6.2.3.

Period	Electron Trigger	Muon Trigger
B,D,E-I	EF_e20_medium	EF_mu18
J	EF_e20_medium	EF_mu18_medium
K	EF_e22_medium	EF_mu18_medium

Table 6.1: The triggers used for each data taking period.

6.2.2 Data Quality & Cleaning

Selections are applied to data in order to effectively deal with defects and other problems of the ATLAS detector. Careful analysis from multiple working groups has gone into identifying signatures of bad data that could potentially fake an interesting signal. The various techniques used to eliminate bad events are detailed in this chapter. In certain instances, the selections are applied to

both data and MC, to ensure agreement. Note that the integrated luminosity is not re-calculated to accomodate any event vetoes; instead these selections are considered part of the analysis' acceptance.

Vertex Track Multiplicity Selection: Any event which has a primary vertex (PV) with fewer than five tracks associated with it is vetoed, as leptonic signal events include a higher number of tracks than minimum bias events [156].

Jet Cleaning: Calorimeter effects occasionally lead to high energy deposits which fake jets. Any event with one of these “bad” jets in the acceptance region ($|\eta| < 2.8$) is vetoed. Any jet for which the following criteria are true is considered a bad jet [157]:

- Energy spikes in the Hadronic End-Cap:
 - $E_{\text{jet}}^{\text{HEC}}/E_{\text{jet}} < 0.5$ & $Q_{\text{HEC}} > 0.5$
- Limit on the negative energy cells in a jet:
 - $\sum_{E_{\text{cells}} < 0} |E| > 60 \text{ GeV}$
- Coherent Electromagnetic Noise:
 - if $|\eta| < 2.8$ & $E_{\text{jet}}^{\text{EM}}/E_{\text{jet}} < 0.95$ & $Q_{\text{LAR}} > 0.8$
- Non-collision Backgrounds and Cosmic-Rays
 - $|t_{\text{jet}}| > 25 \text{ ns}$
 - $E_{\text{jet}}^{\text{EM}}/E_{\text{jet}} < 0.05$ & $\sum_{\text{tracks in jet}} p_{\text{T}}^{\text{track}}/p_{\text{T}}^{\text{jet}} < 0.05$
 - if $|\eta| \geq 2.0$ & $E_{\text{jet}}^{\text{EM}}/E_{\text{jet}} < 0.05$
 - if $|\eta| < 2$ & $E_{\text{jet}}^{\text{max sampling}}/E_{\text{jet}} > 0.99$

The quality variables are defined as

$$Q_{\text{LAR/HEC}} = \sum_{\text{calorimeter samples}} \left(a_i^{\text{measured}} - a_i^{\text{predicted}} \right)^2 \quad (6.6)$$

where $a_i^{\text{measured(predicted)}}$ is the amplitude of the signal pulse per time sampling. An example of the pulse shape over many samplings can be seen in Figure 3.10, making $Q_{\text{LAR/HEC}}$ similar to a χ^2 measurement with the denominator fixed at one.

LAr Hole Veto: In early May 2011, a power cycling caused the failure of multiple FEBs in the LAr calorimeter. The range of the failure was $-0.1 < \eta < 1.5$ and $-0.9 < \phi < -0.5$ and affected multiple layers of the calorimeter. The problem was fixed at the end of June 2011, but affects 0.86 fb^{-1} (41.9%) of data. For events occurring during this period, if a baseline electron passes through the region of failure the event is vetoed. A more sophisticated approach was taken by using the remaining layers, which included the pre-sampler of LAr. Using the shape of the jet shower in the surviving layers, the amount of energy in dead calorimeter cells is estimated based on the fraction observed in MC. If a baseline jet passes through the affected region and the amount of energy in dead cells exceeds 40 GeV, the event is vetoed. Note that this effect is treated separately from the issue of failed optical transmitters, in which case the electron is vetoed.

LAr Error Veto: Events which exhibit excessive noise or other data quality errors in the LAr calorimeter are flagged during reconstruction and subsequently vetoed in this analysis.

Cosmic Muon Veto: To avoid letting cosmic background pollute our results, any event which contains a muon with impact parameters $|d_0^{PV}| \geq 0.2 \text{ mm}$ or $|z_0^{PV}| \geq 1.0 \text{ mm}$ is vetoed. Note that this is applied to muons that have passed object definition and overlap removal but not the isolation requirement for signal muons. This selection is also applied to MC.

Muon Cleaning: For muons, if an event contains a muon with $\frac{\sigma_{q/p}}{|q/p|} \leq 0.2$, where q/p is the charge divided by the magnitude of momentum, the event is discarded. This selection is applied before the overlap removal and is also applied to MC.

6.2.3 Data & Monte Carlo Corrections

By observing certain standard candles, disparities between MC and data can be measured, such as tag-and-probe on the Z or J/Ψ (see Appendix F.6 for the definition of tag-and-probe). Based on these measurements, corrections are applied to MC using tools provided by the combined performance groups. Note that in the cases of energy rescaling and momentum smearing, the object selections are made on the corrected energy or momentum.

Electron Efficiency Scale Factors: Scale factors are applied to the MC events multiplicatively for each electron to match the efficiency seen in

data, dependent on η and p_T . The event is weighted by a scale factor both for the efficiency of electron identification and for the efficiency of electron reconstruction [144].

Muon Efficiency Scale Factors: MC events are weighted in order to match the reconstruction efficiency for combined muons in data. This correction is also dependent on η and p_T .

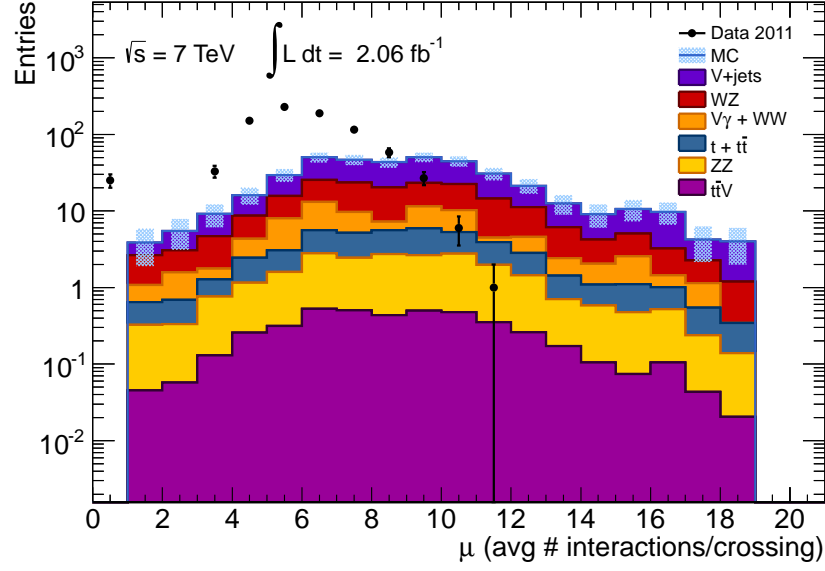
b -Tagging Efficiency A discrepancy is seen between the efficiency of b -tagging in data and MC. As b -tagging is used to estimate the contribution of heavy flavor muons to the background, this effect is corrected for in MC. MC events are weighted with a scale factor dependent p_T and η , as well as the truth flavor (b , c , or light flavor). This weight is calculated and applied multiplicatively for each selected jet within $\eta < 2.5$ and $20 < p_T < 200$ GeV. The usage conforms to the guidelines developed by the Flavor Tagging Working Group [151]

The following corrections are applied to MC for each data period. A random number is generated, seeded by the ϕ of the leading lepton. This random number is then used to assign the event to the necessary period to account for the different triggers used and the variations in accelerator conditions.

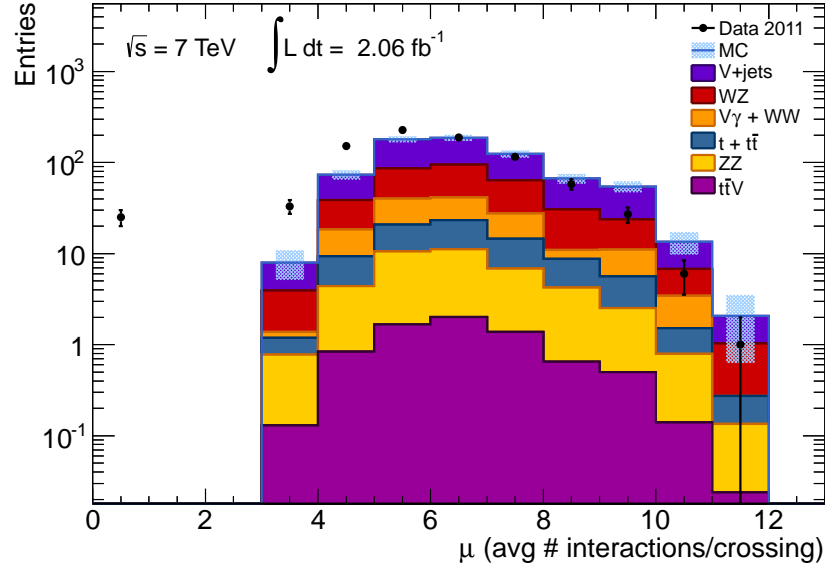
Pile-Up: ATLAS MC was generated with a bunch-spacing period of 75 ns and averaging 8 visible collision vertices per event. For each data-taking period the average number of visible interactions per bunch crossing (μ) as determined by the beam condition monitors. Each MC event is re-weighted in order to better match the μ distribution seen in the data-taking period. The effect of this re-weighting can be seen in Figure 6.3.

Trigger Efficiency: Efficiency maps for the electron and muon triggers are used to weight each MC event according to the probability of it passing the trigger hypothesis for its randomly assigned period. These maps are constructed using tag-and-probe measurements requiring SFOS lepton-pairs to be within 10 (20) GeV of the Z mass for electrons (muons). The maps are dependent on E_T , cluster η , and cluster ϕ for electrons and p_T , η , and ϕ for muons. Only the leptons on the trigger plateau are used for trigger re-weighting, requiring $p_T > 25$ (20) GeV for electrons (muons).

LAr Hole Veto: This selection is applied to data in order to avoid the LAr hole; it is only applied to MC events randomly assigned to periods E-H.



(a)



(b)

Figure 6.3: The effect of the re-weighting of MC in order to match the μ seen in data. (a) has not been re-weighted and (b) has been re-weighted. Only statistical uncertainties are shown. Note that the entries in the zero bin for data are due to non-interacting pilot bunches present in early LHC 2011 runs.

6.3 Definition of the Signal Region

After the event cleaning and quality cuts of the Section 6.2, the following signal region selections are applied:

- $N_{\text{lepton}} = 3$, for signal leptons,
- $|m_{\ell^+\ell^-} - m_Z| < 10$ GeV, for any same-flavor, opposite-charge lepton pair,
- $E_T^{\text{miss}} > 50$ GeV.

No selections are made on the multiplicity of jets or on the p_T of any jet.

The distribution of the E_T^{miss} after selecting three leptons, but before the Z -boson resonance selection, is shown in Figure 6.4 for completeness. The distribution of the invariant mass for same-flavor, opposite-charge pairs is shown in Figure 6.5. This selection improves the sensitivity to the wino co-NLSPS and higgsino Z -rich grids. The distribution of E_T^{miss} after the $|m_{\ell^+\ell^-} - m_Z| < 10$ GeV selection is shown in Figure 6.6. The selection on E_T^{miss} at 50 GeV has been shown to optimize sensitivity across a broad range of SUSY models [158, 159] and it allows the analysis to operate at a well-understood point of the E_T^{miss} distribution.

The effect of the signal region selections on each background can be seen in Table 6.2. The effect of the signal region selections on the higgsino and wino model points can be seen in Table 6.3 and Table 6.4, respectively. The acceptance and efficiency for each model point for both Higgsino and Wino can be found in Appendix ??.

6.4 Sensitivity

The sensitivity of the GGM grids to the three-lepton analysis was studied using the a log-likelihood ratio significance statistic defined as:

$$Z_{LLR} = \sqrt{2 \cdot \left((S + B) \cdot \ln \left(1 + \frac{S}{B} \right) - S \right)} \quad (6.7)$$

where S is the signal contribution and B is the expected background. Uncertainties are not included in the calculation.

Figure 6.7 shows the sensitivity of the two GGM grids in terms of the value Z_{llr} . In the case of either grid, some possibility of exclusion is expected in the region of $m_{\tilde{H}} (m_{\tilde{W}}) < 400$ GeV.

Selection	$N_{\text{leptons}} = 3$	$\ell^+ \ell^-$	$ m_{\ell^+ \ell^-} - m_Z < 10 \text{ GeV}$	$E_{\text{T}}^{\text{miss}} > 50 \text{ GeV}$
$t\bar{t}$	48.3 ± 1.6	34.2 ± 1.3	5.5 ± 0.5	3.3 ± 0.4
Single t	3.9 ± 0.7	3.6 ± 0.6	0.26 ± 0.15	0.26 ± 0.15
$t\bar{t}V$	7.37 ± 0.22	6.45 ± 0.20	4.22 ± 0.16	2.72 ± 0.13
ZZ	33.3 ± 1.0	32.9 ± 1.0	27.3 ± 0.9	3.37 ± 0.30
WZ	192 ± 5	190 ± 5	159.4 ± 4.2	58.4 ± 2.7
WW	0.24 ± 0.08	0.22 ± 0.08	0.043 ± 0.030	0.021 ± 0.021
$V\gamma$	50 ± 7	50 ± 7	15 ± 4	0 ± 1.3
$Z + \text{jets}$	364 ± 14	363 ± 14	248 ± 11	1.2 ± 0.6
$W + \text{jets}$	2.5 ± 2.5	2.5 ± 2.5	0 ± 1.4	0 ± 1.4
Drell-Yan	7.2 ± 3.2	7.2 ± 3.2	0 ± 13	0 ± 0.09
$\sum \text{SM}$	709 ± 17	690 ± 17	459 ± 18	69.3 ± 3.4

Table 6.2: The effect of the signal region selections on each Standard Model background. Yields are normalized to 2.06 fb^{-1} . All uncertainties are solely statistical.

6.5 Data-Driven Background Estimation

The SM processes that contribute to the background of the signal region fall into two categories:

Irreducible: A SM contribution is considered “irreducible” if it produces three “real” leptons. This includes diboson (WZ , ZZ) and $t\bar{t}V$ (for $V = Z, W$). The contribution of these backgrounds is estimated using the MC indicated in Section 5.1.

Reducible: A background is deemed “reducible” if it includes at least one “fake” electron or muon; either a lepton produced in a semi-leptonic decay of a heavy-flavor quark or a photon conversion mis-identified as an electron. The reducible background includes single- t , $t\bar{t}$ production, WW , and V produced with jets and photons. MC is not used to estimate the contribution of these processes; instead, a matrix method similar to the method described in [160] is used, except for internal conversions of photons mis-identified as muons, which makes use of a re-weighting technique.

Note that the usage in this case is non-standard. By reducible it is meant that the background can be “reduced” to a number of fake leptons and an irreducible background cannot.

The matrix method [159, 161] used assumes that the leading lepton is real, which MC studies verify is true 99% of the time. The matrix method is then

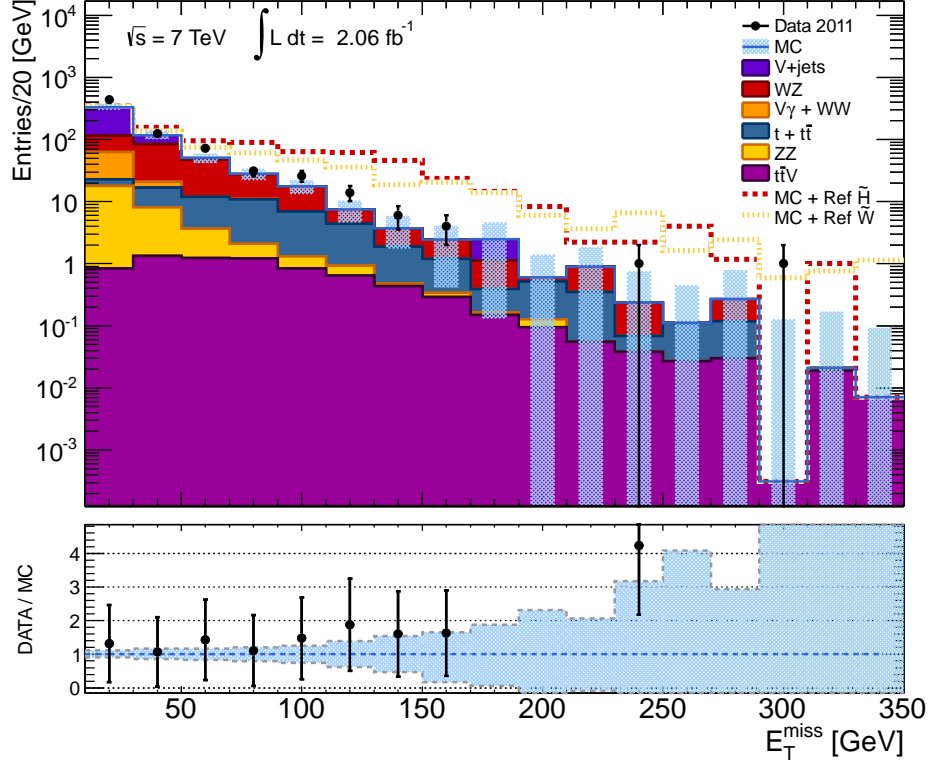


Figure 6.4: The E_T^{miss} distribution after the three-lepton event selection.

applied to the two trailing leptons in order to calculate the contribution from fakes by solving a set of linear equations that model the relationship between real or fake leptons and whether or not the lepton passed or failed the signal lepton requirements on isolation (including the tight requirement for electrons). The assumption that the leading lepton is real reduces the problem to the 4×4 matrix:

$$\begin{pmatrix} N_{SSS} \\ N_{SS\$} \\ N_{S\$S} \\ N_{S\$\$} \end{pmatrix} = \begin{pmatrix} \epsilon_1 \epsilon_2 & \epsilon_1 f_2 & f_1 \epsilon_2 & f_1 f_2 \\ \epsilon_1^c \epsilon_2^c & \epsilon_1^c f_2^c & f_1^c \epsilon_2^c & f_1^c f_2^c \\ \epsilon_1^c \epsilon_2 & \epsilon_1^c f_2 & f_1^c \epsilon_2 & f_1^c f_2 \\ \epsilon_1^c \epsilon_2^c & \epsilon_1^c f_2^c & f_1^c \epsilon_2^c & f_1^c f_2^c \end{pmatrix} \cdot \begin{pmatrix} N_{RRR} \\ N_{RRF} \\ N_{RFR} \\ N_{RFF} \end{pmatrix}, \quad (6.8)$$

Where S is a lepton which passes the signal lepton requirements and $\$$ denotes a lepton which fails the signal requirements and is thus not tight. The value ϵ_i is the efficiency of a real tagged lepton passing the signal lepton requirements. The value f_i is the fake rate, the probability that a fake tagged lepton will pass the signal

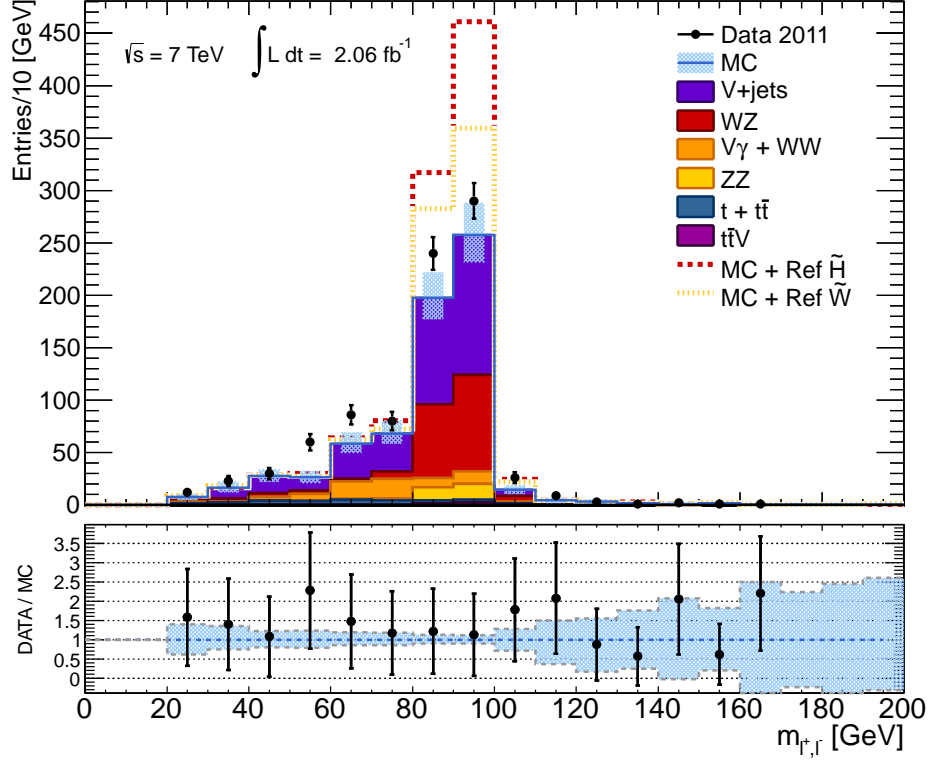


Figure 6.5: The invariant mass, $m_{\ell^+\ell^-}$, after the three-lepton event selection. In the case of more than one same-flavor, opposite-charge lepton pair, the pair closest to m_Z is plotted. The uncertainties shown are statistical and systematic.

lepton requirements. The index, i marks whether the lepton is the first or second of the two considered (actually the middle and trailing lepton in terms of p_T). The notation $\epsilon_i^c = 1 - \epsilon_i$ and $f_i^c = 1 - f_i$ are used to conserve page space. In either case, the indices mark whether the value is that of the second-leading lepton or the trailing third lepton. The left side values, N_{SSS} , $N_{SS\mathcal{S}}$, $N_{S\mathcal{S}\mathcal{S}}$, and $N_{S\mathcal{S}\mathcal{S}}$ indicates whether the two trailing leptons are signal leptons S, or failed the signal selections, \mathcal{S} . The matrix can be inverted to solve for the remaining values which cannot be measured from data, N_{RRR} , N_{RRF} , N_{RFR} , and N_{RFF} . The number of events for which one or two of the three signal leptons is a fake can then be calculated:

$$N_{RRF/RFR/RFF \rightarrow SSS} = \epsilon_1 f_2 \cdot N_{RRF} + f_1 \epsilon_2 \cdot N_{RFR} + f_1 f_2 \cdot N_{RFF} \quad (6.9)$$

In order to apply the matrix method, the efficiencies and fake rates must be known. They are measured in the following ways.

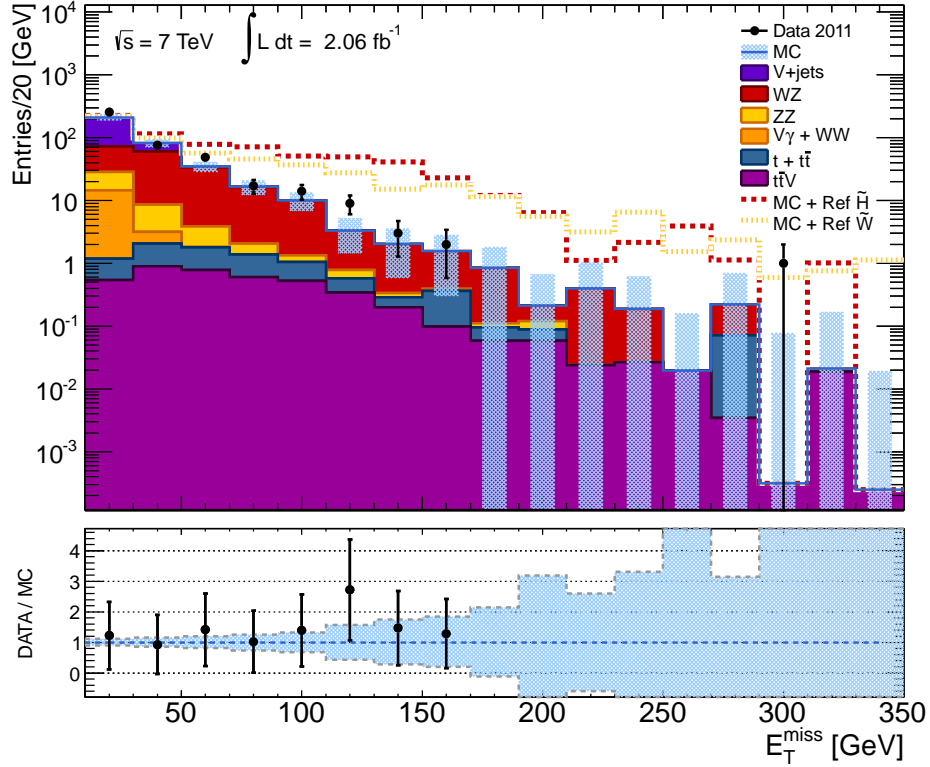
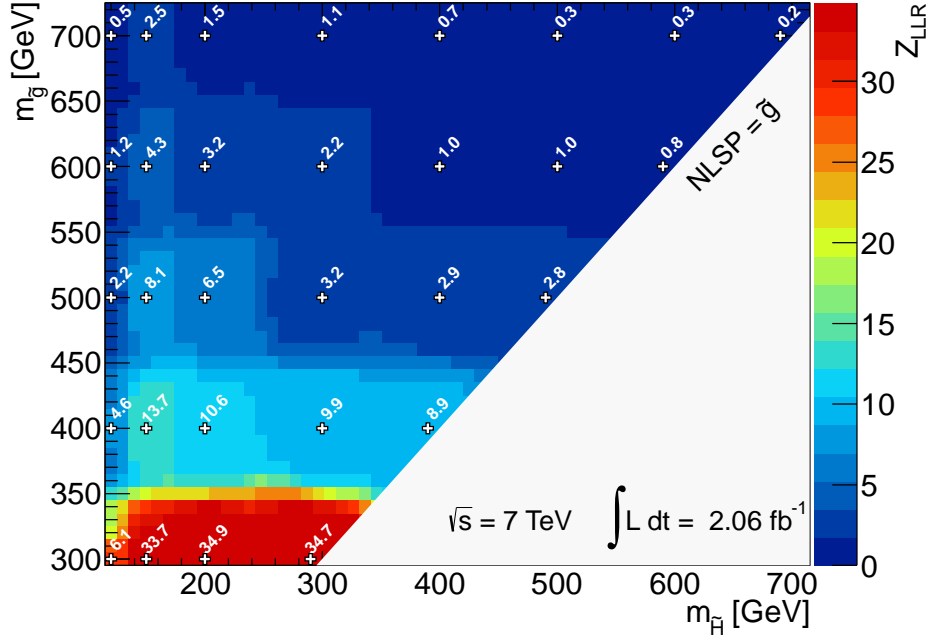
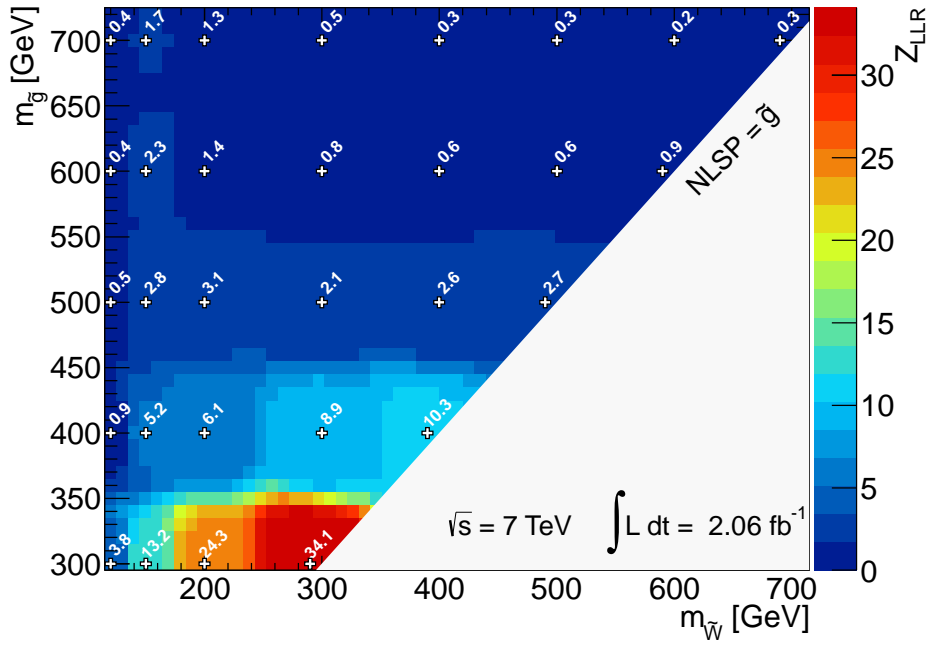


Figure 6.6: The E_T^{miss} distribution after the $|m_{\ell+\ell^-} - m_Z| < 10$ GeV event selection. The uncertainties shown are statistical and systematic.

- The efficiency of real leptons passing the signal lepton requirements was measured using tag-and-probe, requiring two baseline leptons with a same-flavor, opposite-charge pair with $|m_{\ell+\ell^-} - m_Z| < 5$ GeV. The tag lepton must pass signal requirements and match the triggering lepton. The efficiency is then calculated from the fraction of probe leptons passing the signal selections.
- The fake rate is measured in MC. Each electron or muon fake rate is specific to whether a fake lepton originated from heavy flavor or a photon conversion into an electron, as well as whether the MC used was from top backgrounds or vector boson backgrounds (W/Z). The fake rate is corrected for the proportion of top or vector boson backgrounds in the region the fake rate is applied. The difference between MC and data fake rates is measured in low- E_T^{miss} control regions and the resulting scale factor is used to correct the fake rate. For muons from heavy flavor, the MC and data fake rates are determined using take-and-probe, requiring that the tag muon be within $\delta R < 0.4$ of a b -jet and that $E_T^{\text{miss}} < 40$ GeV and $M_T < 50$ GeV in order to remove background



(a)



(b)

Figure 6.7: The signal significance Z_{LLR} for the (a) Higgsino GGM grid and (b) Wino GGM grid after all sections.

from W -decays. The fake rate is then determined from the probe muon as the fraction passing the muon isolation selection. The result in data is compared to $b\bar{b}$ MC to estimate a scale factor (the ratio of the two as a function of p_T) between MC and data, which is then applied to the MC fake rate determined in the signal region. The process for the electron heavy flavor fake rate is similar except that a muon is used for the tag (due to the requirements of b -tagging) and an electron is the probe. Electrons in the matrix method also include a fake rate due to photon conversions. This is measured by requiring two baseline SFOS muons with $m_{\mu\mu} > 20$ GeV and one baseline electron, forming a trilepton invariant mass of $m_{\mu\mu e}$ within the range 80-100 GeV. b -tagged jets are vetoed and the transverse mass of the electron is required to be less than 40 GeV, as well as requiring $E_T^{\text{miss}} < 50$ GeV. The fake rate is then determined using the number of electrons in such events which pass the isolation criteria over all such electrons. Again, the measurement in data is divided by the measurement in MC to give a scale factor.

The contribution from an internal photon conversion where the photon is misidentified as a signal muon is based on events passing all event selections, except that the three lepton cut is relaxed to two leptons. These events are used to estimate the three lepton background due to conversions by scaling them by the probability of a conversion occurring. This probability is measured in an $E_T^{\text{miss}} < 50$ GeV control region and is measured as the ratio of events with three muons with an invariant mass within 10 GeV of m_Z over the number of two muon events with an invariant mass falling within 10 GeV of m_Z . This gives an estimate of $0.7 \pm 0.1 \pm 0.7$ events in the signal region. Note that the same process for photons is included as part of the matrix method.

The background estimation methods used are validated in two control regions. The first control region is the low- E_T^{miss} region with $30 < E_T^{\text{miss}} < 50$ GeV. The second is a high- E_T^{miss} control region with $E_T^{\text{miss}} > 50$ GeV and a veto on same-flavor, opposite-charge pairs. The result for each signal region is shown in Table 6.5. The estimate from the background methods are in good agreement with the measured amount of events in data.

$m_{\tilde{g}}$ [GeV]	$m_{\tilde{t}}$ [GeV]	Selection			
		$N_{\text{leptons}} = 3$	$\ell^+\ell^-$	$ m_{\ell^+\ell^-} - m_Z < 10 \text{ GeV}$	$E_T^{\text{miss}} > 50 \text{ GeV}$
300	110	31.9 ± 4.0	28.8 ± 3.9	26.4 ± 3.7	9.5 ± 2.0
300	115	34.6 ± 10.6	34.6 ± 10.6	30.5 ± 10.4	12.3 ± 4.8
300	120	90 ± 16	85 ± 16	81 ± 16	27.5 ± 3.3
300	150	397 ± 25	392 ± 25	363 ± 23	259 ± 17
300	200	359 ± 22	358 ± 23	324 ± 22	272 ± 11
300	290	338 ± 10	336 ± 10	295 ± 10	270 ± 9
400	110	20.5 ± 2.3	19.4 ± 2.3	15.5 ± 2.0	9.7 ± 1.3
400	115	23.5 ± 2.4	22.6 ± 2.4	21.2 ± 2.3	13.6 ± 1.5
400	120	42.3 ± 3.4	40.6 ± 3.4	35.9 ± 3.2	19.8 ± 1.8
400	150	102.0 ± 4.7	101.3 ± 4.6	92.1 ± 4.4	75.1 ± 3.6
400	200	68.5 ± 3.8	67.5 ± 3.8	61.0 ± 3.8	54.3 ± 3.3
400	300	61.3 ± 4.0	60.9 ± 4.0	53.9 ± 4.0	49.7 ± 4.0
400	390	54.6 ± 5.1	54.1 ± 5.1	46.7 ± 4.7	43.8 ± 2.3
500	110	9.5 ± 1.7	8.9 ± 1.7	6.5 ± 1.4	3.6 ± 1.0
500	115	9.7 ± 1.6	9.3 ± 1.5	7.3 ± 1.4	4.7 ± 1.0
500	120	20.4 ± 2.1	19.8 ± 2.1	15.8 ± 1.9	8.7 ± 1.2
500	150	54.7 ± 2.1	52.9 ± 2.1	47.2 ± 2.0	38.7 ± 1.7
500	200	40.3 ± 1.2	38.9 ± 1.2	34.0 ± 1.1	29.9 ± 1.0
500	300	16.0 ± 0.8	15.8 ± 0.8	14.1 ± 0.7	13.2 ± 0.7
500	400	15.2 ± 0.8	15.1 ± 0.8	12.4 ± 0.8	11.9 ± 0.8
500	490	13.8 ± 0.7	13.7 ± 0.7	12.0 ± 0.7	11.5 ± 0.7
600	110	3.1 ± 1.4	2.6 ± 1.2	2.2 ± 1.1	0.5 ± 0.7
600	115	7.2 ± 2.0	6.9 ± 1.9	6.0 ± 1.8	3.2 ± 1.5
600	120	11.5 ± 2.1	11.2 ± 2.0	8.7 ± 1.7	4.8 ± 1.4
600	150	28.4 ± 1.7	27.0 ± 1.6	23.5 ± 1.5	18.4 ± 1.4
600	200	18.8 ± 0.7	17.7 ± 0.6	14.8 ± 0.6	13.0 ± 0.6
600	300	10.75 ± 0.28	10.35 ± 0.28	9.25 ± 0.26	8.74 ± 0.25
600	400	4.38 ± 0.19	4.34 ± 0.19	3.91 ± 0.17	3.78 ± 0.16
600	500	4.13 ± 0.17	4.11 ± 0.17	3.70 ± 0.17	3.60 ± 0.17
600	590	3.45 ± 0.21	3.42 ± 0.21	3.02 ± 0.21	2.97 ± 0.21
700	110	2.4 ± 0.8	2.4 ± 0.7	2.3 ± 0.7	0.14 ± 0.21
700	115	4.0 ± 2.2	3.8 ± 2.1	2.7 ± 1.4	0.7 ± 1.1
700	120	7.5 ± 1.9	7.4 ± 1.9	6.5 ± 1.7	2.1 ± 1.4
700	150	16.7 ± 1.7	16.0 ± 1.7	14.3 ± 1.6	9.9 ± 1.4
700	200	8.21 ± 0.53	7.79 ± 0.52	6.56 ± 0.47	5.88 ± 0.45
700	300	5.44 ± 0.14	5.11 ± 0.14	4.25 ± 0.13	4.04 ± 0.12
700	500	1.40 ± 0.06	1.38 ± 0.06	1.25 ± 0.06	1.22 ± 0.06
700	600	1.413 ± 0.047	1.377 ± 0.047	1.244 ± 0.045	1.22 ± 0.045
700	690	0.971 ± 0.032	0.952 ± 0.032	0.845 ± 0.030	0.83 ± 0.030
800	120	0.15 ± 0.06	0.15 ± 0.06	0.124 ± 0.040	0.025 ± 0.036
800	150	11.0 ± 1.5	10.7 ± 1.5	9.5 ± 1.4	5.2 ± 1.2
800	200	4.73 ± 0.55	4.61 ± 0.54	4.07 ± 0.50	3.60 ± 0.48
800	300	2.4 ± 0.11	2.22 ± 0.11	1.90 ± 0.10	1.80 ± 0.10
800	400	1.626 ± 0.041	1.538 ± 0.040	1.274 ± 0.037	1.222 ± 0.036
800	500	1.156 ± 0.023	1.118 ± 0.022	0.948 ± 0.021	0.927 ± 0.021
800	600	0.506 ± 0.016	0.492 ± 0.016	0.435 ± 0.015	0.421 ± 0.015
800	700	0.490 ± 0.014	0.480 ± 0.014	0.408 ± 0.012	0.404 ± 0.012
800	790	0.306 ± 0.012	0.300 ± 0.012	0.260 ± 0.012	0.257 ± 0.012
900	120	6.2 ± 2.8	6.2 ± 2.8	5.2 ± 2.8	1.2 ± 2.6
900	150	10.5 ± 1.8	10.4 ± 1.8	9.7 ± 1.7	5.1 ± 1.5
900	200	3.6 ± 0.6	3.5 ± 0.5	3.1 ± 0.4	2.6 ± 0.4
900	300	1.11 ± 0.10	1.04 ± 0.09	0.89 ± 0.09	0.85 ± 0.08
900	400	0.726 ± 0.029	0.675 ± 0.028	0.577 ± 0.026	0.557 ± 0.026
900	500	0.582 ± 0.013	0.550 ± 0.013	0.477 ± 0.012	0.470 ± 0.012
900	600	0.361 ± 0.007	0.348 ± 0.007	0.301 ± 0.007	0.295 ± 0.007
900	700	0.183 ± 0.005	0.180 ± 0.005	0.162 ± 0.006	0.160 ± 0.005
900	800	0.183 ± 0.004	0.175 ± 0.004	0.149 ± 0.004	0.148 ± 0.004
900	890	0.191 ± 0.005	0.190 ± 0.005	0.161 ± 0.005	0.161 ± 0.005

Table 6.3: The effect of the signal region selections on each of the Higgsino model points. Yields are normalized to 2.06 fb^{-1} . All uncertainties are solely statistical.

$m_{\tilde{g}}$ [GeV]	$m_{\tilde{W}}$ [GeV]	Selection			
		$N_{\text{leptons}} = 3$	$\ell^+\ell^-$	$ m_{\ell^+\ell^-} - m_Z < 10 \text{ GeV}$	$E_T^{\text{miss}} > 50 \text{ GeV}$
300	120	45 \pm 29	45 \pm 28	39 \pm 27	28 \pm 23
300	150	113 \pm 20	112 \pm 20	98 \pm 20	72 \pm 15
300	200	214 \pm 18	209 \pm 18	190 \pm 18	163 \pm 17
300	290	327 \pm 19	325 \pm 19	286 \pm 18	264 \pm 18
400	120	45 \pm 8	44 \pm 8	36 \pm 7	17.4 \pm 5.0
400	150	39.3 \pm 4.8	37.9 \pm 4.8	33.3 \pm 4.4	23.9 \pm 3.6
400	200	36.1 \pm 3.1	35.6 \pm 3.0	32.7 \pm 3.0	27.2 \pm 2.6
400	300	54.1 \pm 3.5	53.4 \pm 3.5	47.1 \pm 3.5	43.9 \pm 3.5
400	390	61.2 \pm 2.2	60.8 \pm 2.2	53.8 \pm 2.1	52.1 \pm 2.1
500	120	20.2 \pm 2.3	19.9 \pm 2.3	17.6 \pm 2.2	10.0 \pm 1.6
500	150	17.8 \pm 1.3	17.6 \pm 1.3	15.6 \pm 1.2	11.4 \pm 1.1
500	200	17.9 \pm 1.3	17.5 \pm 1.3	15.5 \pm 1.2	12.9 \pm 1.09
500	300	10.2 \pm 0.8	10.1 \pm 0.8	8.9 \pm 0.8	8.3 \pm 0.7
500	400	12.4 \pm 0.6	12.3 \pm 0.6	11.3 \pm 0.6	10.7 \pm 0.6
500	490	12.41 \pm 0.28	12.26 \pm 0.28	11.22 \pm 0.27	10.92 \pm 0.25
600	120	18.3 \pm 1.6	18.2 \pm 1.6	16.8 \pm 1.6	9.0 \pm 1.2
600	150	15.7 \pm 0.8	15.4 \pm 0.8	13.5 \pm 0.8	9.2 \pm 0.6
600	200	7.99 \pm 0.43	7.83 \pm 0.43	6.76 \pm 0.40	5.46 \pm 0.36
600	300	3.76 \pm 0.27	3.62 \pm 0.27	3.07 \pm 0.26	2.93 \pm 0.25
600	400	2.84 \pm 0.21	2.79 \pm 0.21	2.44 \pm 0.19	2.36 \pm 0.19
600	500	2.84 \pm 0.16	2.82 \pm 0.16	2.40 \pm 0.15	2.35 \pm 0.15
600	590	3.84 \pm 0.09	3.78 \pm 0.09	3.24 \pm 0.09	3.19 \pm 0.09
700	120	15.9 \pm 1.3	15.7 \pm 1.2	13.6 \pm 1.2	7.2 \pm 0.8
700	150	11.63 \pm 0.55	11.57 \pm 0.55	10.4 \pm 0.51	6.64 \pm 0.41
700	200	6.82 \pm 0.30	6.76 \pm 0.30	6.01 \pm 0.29	5.09 \pm 0.26
700	300	2.29 \pm 0.12	2.23 \pm 0.12	1.95 \pm 0.12	1.81 \pm 0.11
700	400	1.25 \pm 0.07	1.20 \pm 0.07	1.01 \pm 0.07	0.95 \pm 0.07
700	500	1.12 \pm 0.06	1.11 \pm 0.06	0.94 \pm 0.06	0.93 \pm 0.06
700	600	0.982 \pm 0.047	0.968 \pm 0.047	0.824 \pm 0.043	0.805 \pm 0.043
700	690	1.394 \pm 0.051	1.379 \pm 0.051	1.191 \pm 0.050	1.168 \pm 0.049
800	120	14.2 \pm 1.2	13.9 \pm 1.2	12.2 \pm 1.1	6.1 \pm 0.8
800	150	12.3 \pm 0.6	12.2 \pm 0.6	10.93 \pm 0.53	7.48 \pm 0.44
800	200	6.64 \pm 0.26	6.59 \pm 0.26	5.94 \pm 0.24	4.77 \pm 0.22
800	300	1.22 \pm 0.06	1.20 \pm 0.06	1.052 \pm 0.052	0.969 \pm 0.050
800	400	0.487 \pm 0.027	0.469 \pm 0.027	0.398 \pm 0.025	0.389 \pm 0.025
800	500	0.357 \pm 0.022	0.339 \pm 0.021	0.275 \pm 0.020	0.270 \pm 0.020
800	600	0.275 \pm 0.014	0.269 \pm 0.014	0.237 \pm 0.013	0.230 \pm 0.013
800	700	0.252 \pm 0.009	0.246 \pm 0.009	0.213 \pm 0.008	0.211 \pm 0.008
800	790	0.378 \pm 0.009	0.371 \pm 0.009	0.332 \pm 0.009	0.329 \pm 0.009
900	120	15.6 \pm 1.3	15.4 \pm 1.3	14.1 \pm 1.3	6.3 \pm 0.9
900	150	11.73 \pm 0.51	11.67 \pm 0.51	10.44 \pm 0.48	7.08 \pm 0.39
900	200	4.97 \pm 0.19	4.93 \pm 0.19	4.49 \pm 0.18	3.63 \pm 0.16
900	300	1.047 \pm 0.041	1.037 \pm 0.041	0.931 \pm 0.040	0.860 \pm 0.037
900	400	0.380 \pm 0.017	0.377 \pm 0.017	0.317 \pm 0.016	0.309 \pm 0.016
900	500	0.181 \pm 0.010	0.172 \pm 0.010	0.145 \pm 0.009	0.140 \pm 0.009
900	600	0.117 \pm 0.006	0.112 \pm 0.006	0.092 \pm 0.005	0.09 \pm 0.005
900	700	0.097 \pm 0.005	0.095 \pm 0.005	0.083 \pm 0.004	0.081 \pm 0.004
1000	120	12.0 \pm 0.9	11.9 \pm 0.9	10.8 \pm 0.9	5.5 \pm 0.6
1000	150	10.34 \pm 0.46	10.28 \pm 0.46	9.27 \pm 0.43	6.14 \pm 0.35
1000	300	0.844 \pm 0.033	0.836 \pm 0.033	0.746 \pm 0.031	0.702 \pm 0.030
1000	400	0.288 \pm 0.012	0.284 \pm 0.012	0.243 \pm 0.011	0.235 \pm 0.011
1000	500	0.121 \pm 0.005	0.114 \pm 0.005	0.094 \pm 0.004	0.095 \pm 0.004

Table 6.4: The effect of the signal region selections on each of the Wino model points. Yields are normalized to 2.06 fb^{-1} . All uncertainties are solely statistical.

Control Region	$t\bar{t}V$	ZZ	WZ	Reducible Background	Total Background	Data
Low- $E_{\text{T}}^{\text{miss}}$	1.4 ± 0.6	6.7 ± 1.8	61.2 ± 15.0	55.9 ± 35.2	125.2 ± 38.3	122
high- $E_{\text{T}}^{\text{miss}}$	0.7 ± 0.6	0.03 ± 0.04	0.4 ± 0.2	13.5 ± 8.7	14.7 ± 8.7	12

Table 6.5: The result of the background estimation test in the low- $E_{\text{T}}^{\text{miss}}$ and high- $E_{\text{T}}^{\text{miss}}$ control regions for 2.06 fb^{-1} . Uncertainties include statistical and systematic uncertainties [159, 161].

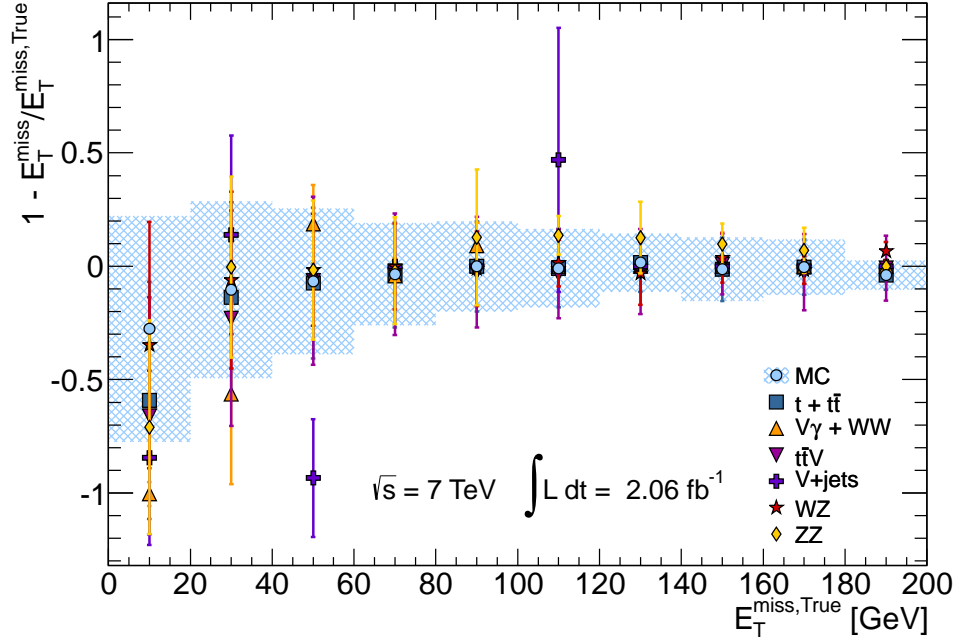


Figure 6.8: The linearity of the E_T^{miss} calculation binned in terms of $E_T^{\text{miss, True}}$ after requiring $N_{\text{leptons}} = 3$. The linearity of the principal contributing backgrounds are shown separately in addition to the overall value for all MC backgrounds. The shaded band represents the root-mean square for all MC backgrounds.

6.6 E_T^{miss} -Performance

Due to the importance of E_T^{miss} to this analysis, it is vital to achieve a full understanding of its behavior. A principal measure of the success of the E_T^{miss} algorithm is its linearity in MC with respect to the true E_T^{miss} , $E_T^{\text{miss, True}}$, calculated from all non-interacting particles in an event. Linearity is defined as $(E_T^{\text{miss, True}} - E_T^{\text{miss}})/E_T^{\text{miss, True}}$. A profile of E_T^{miss} -linearity for the combined MC background can be seen in Figure 6.8 after requiring $N_{\text{leptons}} = 3$. The linearity is also shown for principal contributing backgrounds. Errors shown are simply the root-mean square deviation from the mean. The shaded band is the root-mean square deviation for the combined MC backgrounds. The linearity of E_T^{miss} is seen to be well-behaved from low- E_T^{miss} to well beyond the value of the E_T^{miss} selection in this analysis.

The resolution of E_T^{miss} versus ΣE_T^{EM} is shown for the $N_{\text{leptons}} = 3$ selection level in Figure 6.9. Again, the ΣE_T is calculated with EM-scale clusters and then scaled scaled by the ratio of $\Sigma E_T^{\text{EM}}/\Sigma E_T$. In general we see agreement between data and MC, but examination of this performance metric is limited by the statistics available

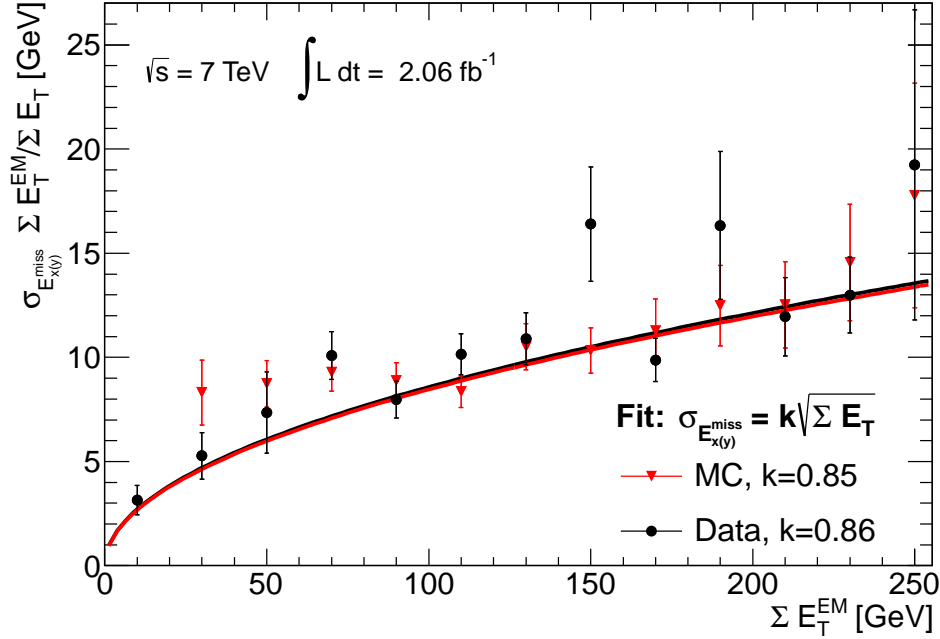


Figure 6.9: The E_T^{miss} resolution versus $\sum E_T^{\text{EM}}$ after requiring 3 leptons, shown for both data and background MC. In general, good agreement is seen between data and MC.

after requiring three leptons.

The E_T^{miss} -algorithm divides E_T^{miss} into four terms, $E_{x(y)}^{\text{miss},e}$ for electrons, $E_{x(y)}^{\text{miss},\text{jets}}$ for jets, $E_{x(y)}^{\text{miss},\text{clusters}}$ for clusters not associated with an electron or jet, and $E_{x(y)}^{\text{miss},\mu}$, constructed from all baseline muons. It is important that we understand E_T^{miss} performance on a term-by-term basis. Plotted in Figure 6.10 is $E_{x(y)}^{\text{miss},e}$, in Figure 6.11 is $E_{x(y)}^{\text{miss},\text{jets}}$, in Figure 6.12 is $E_{x(y)}^{\text{miss},\text{clusters}}$, and in Figure 6.13 is $E_{x(y)}^{\text{miss},\mu}$. For each term it can be seen that the MC and data are in acceptable agreement.

6.7 Systematic Uncertainties

The following methods are used to account for the various systematic uncertainties. For the irreducible systematic uncertainties and the signal systematic uncertainties, please note that the uncertainties for jets and leptons are propagated to E_T^{miss} using the techniques explained in Appendix E.3.

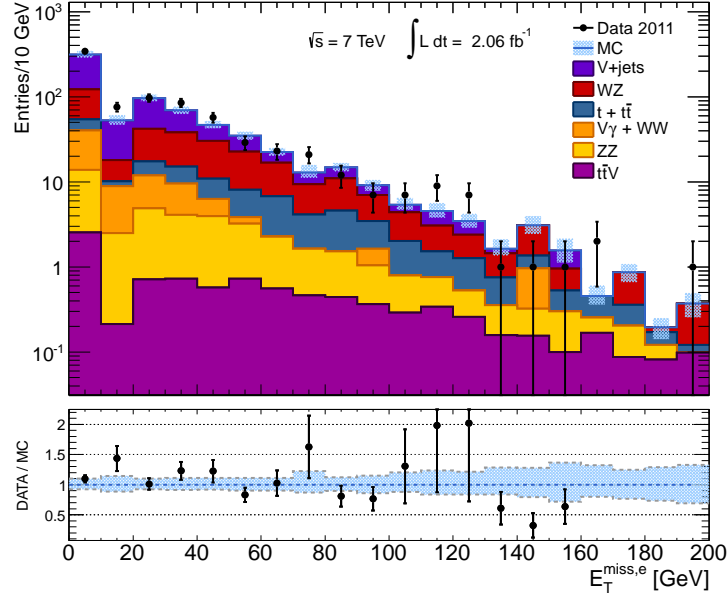


Figure 6.10: The distribution of $E_{x(y)}^{\text{miss,e}}$, the E_T^{miss} term for electrons.

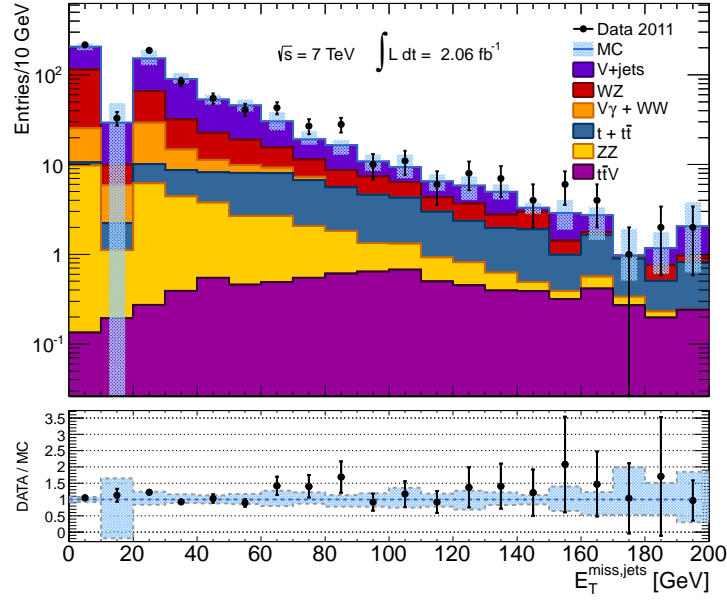


Figure 6.11: The distribution of $E_{x(y)}^{\text{miss,jets}}$, the E_T^{miss} term for electrons.

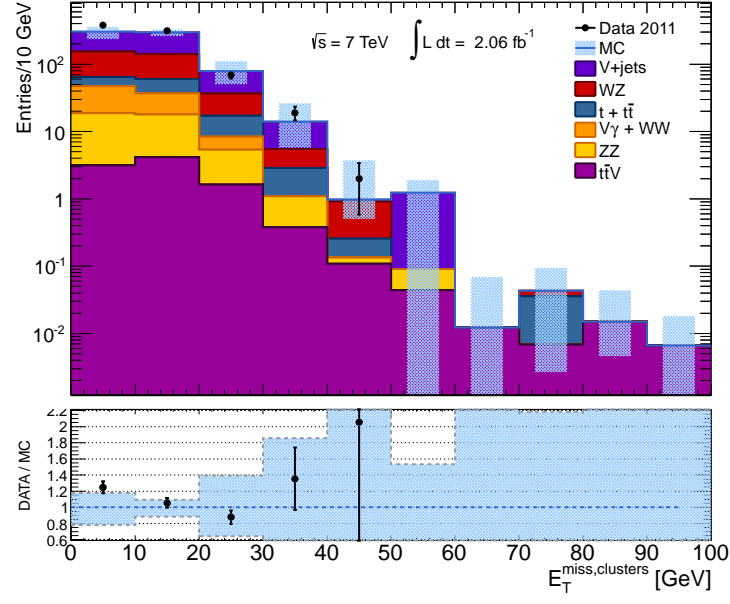


Figure 6.12: The distribution of $E_{x(y)}^{\text{miss,clusters}}$, the E_T^{miss} term for electrons.

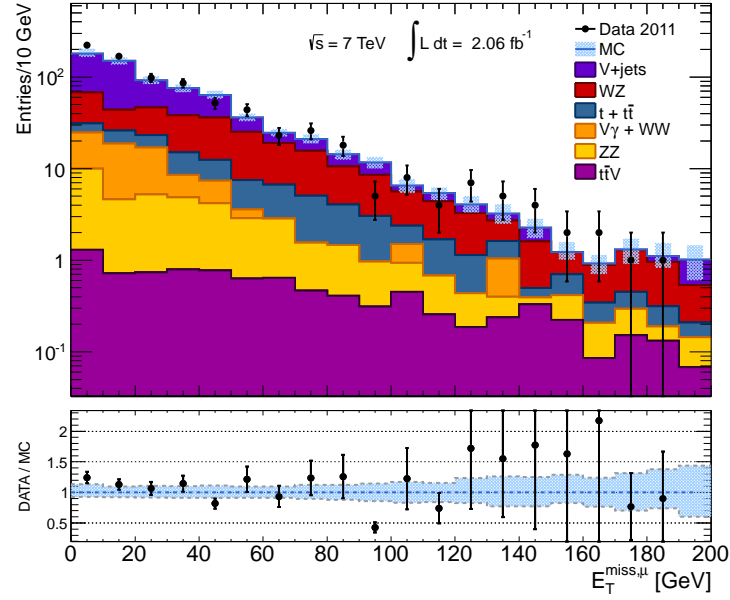


Figure 6.13: The distribution of $E_{x(y)}^{\text{miss},\mu}$, the E_T^{miss} term for electrons.

6.7.1 Irreducible Backgrounds

The following uncertainties are estimated for the irreducible background:

Electron Energy Scale, Resolution, & Scale Factor: The uncertainty in electron energy scale (EES) and electron energy resolution (EER) is estimated using tools provided by the ATLAS egamma performance group. The estimate is based on studies performed using the standard candles of $Z \rightarrow e^+e^-$ and $J/\Psi \rightarrow e^+e^-$ events, with additional checks performed using the ratio of E/p , comparing the calorimeter to the inner detector. This gives access to the much larger statistics of the $W \rightarrow e\bar{\nu}_e$ sample but requires knowledge of the inner detector alignment [144]. The results are applied both to the energy re-scaling of data electrons and the resolution smearing of MC electrons (see Section 6.1.1). The EES uncertainty has a 1.3% effect on the irreducible background and the EER has a 0.2% effect.

As mentioned in Section 6.2.3, MC is re-weighted event-by-event with electron scale factors (ESF) in order to match data, and the uncertainty in these scale factors is accounted for and has a 3.1% effect on the event yield of the irreducible background.

Muon Energy Resolution & Muon Efficiency Scale Factors: As mentioned in Section 6.1.1, the p_T of muons in MC are smeared in order to match the resolution observed in data. The same tools that provide the smearing also provide for the uncertainties on the part of the inner detector (MERID) and uncertainty on the part of the muon spectrometer (MERMS). Also included are uncertainties due to curvature offset and biases in the momentum. Like electrons, muon scale factors (MSF) are provided in order to match MC to the muon reconstruction efficiencies seen in data [146]. The effect on the irreducible background estimate due to MERID was 1.7% and for MERMS was 2.0%. The effect due to uncertainty in MSF was found to be 0.8%.

Jet Energy Scale & Resolution: The uncertainty in jet energy scale (JES) is based on results present in [150, 162] for jets with $|\eta| < 4.5$ and $15 < p_T < 7000$ GeV. An estimate of the out-of-time pile-up contribution (energy deposits originating from interactions from later bunch crossings) is added in quadrature to the JES uncertainty. The value of this estimate is:

- 5% if $20 < p_T < 50$ GeV and $|\eta| < 2.1$
- 7% if $20 < p_T < 50$ GeV and $2.1 < |\eta| < 4.5$
- 2% if $50 < p_T < 100$ GeV and $|\eta| < 2.1$
- 3% if $50 < p_T < 100$ GeV and $2.1 < |\eta| < 4.5$

The effect of the JES uncertainty on the irreducible background is 0.4%. Also accounted for is the effect of the uncertainty on jet energy resolution

(JER). The p_T of each jet is smeared by Gaussian distribution with parameters determined by the jet's p_T and η [163]. The effect of JER on the irreducible background was found to be 0.8%.

E_T^{miss} Cluster Term Energy Scale: The uncertainty of the topocluster energy scale is applied to the cluster term of the E_T^{miss} -calculation following the procedure outlined in [164]. The effect is found to be negligible.

LAr-Hole Veto: The uncertainty due to the effect of the LAr-hole veto on MC is estimated by varying the p_T -threshold of the veto by 20% up and down. This is seen to have a 0.1% effect on the irreducible background.

Pile-Up Uncertainty: An uncertainty on the effect due to the pile-up re-weighting is estimated by using a different μ distribution for data in the re-weighting of MC. Nominally, the MC is divided among the different data periods and then re-weighted to match the μ estimated for that period. For an estimate on the uncertainty of pile-up re-weighting, a μ estimated from the entire data taking period is used instead. This produces an 0.3% effect on the irreducible background due to pile-up re-weighting.

Trigger Re-Weighting: The effect of the uncertainty due to trigger re-weighting is estimated based on the statistic uncertainty of the trigger re-weighting maps. The efficiencies from the maps are varied by $\pm\sigma$ and the effect is seen to be small at 0.2%.

Monte Carlo Cross Section: The uncertainty in the cross sections for the MC used in the irreducible background is:

$t\bar{t}V$ has an uncertainty of 78% on its cross section, including 55% from factorization and re-normalization of the production energy scale, 25% from PDF uncertainty, and 50% uncertainty in the k-factor [165, 166].

ZZ has an uncertainty of 5% on its cross section [126].

WZ has a cross section uncertainty of 7% [126].

The total effect on these MC cross section uncertainties is 7.2% on the irreducible background.

Particle Distribution Functions: For the ZZ and WZ samples the PDF uncertainties (including uncertainty on α_S) are estimated using MSTW08LO [135]. the PDF uncertainty is found to have a 13.9% impact on the irreducible background. Note that the PDF uncertainty of the $t\bar{t}V$ sample is included in its cross section uncertainty.

b -tagging Efficiency Uncertainties in the b -tagging weight used to correct MC to data are used to estimate the systematic uncertainty of this correction [151]. The effect on the irreducible background is found to be negligible.

Luminosity Uncertainty: The uncertainty in the luminosity measurement for data taking periods B-K is 3.7% [167].

	$t\bar{t}V$	ZZ	WZ	Total
Nominal	2.7	3.4	58.4	64.5
Statistical	± 0.1	± 0.4	± 2.7	± 2.7
JES	± 0.1	± 0.2	± 0.2	± 0.3
JER	± 0.1	± 0.0	± 0.5	± 0.5
EES	± 0.0	± 0.0	± 0.8	± 0.8
EER	± 0.0	± 0.0	± 0.1	± 0.1
MID	± 0.1	± 0.0	± 1.1	± 1.1
MMS	± 0.1	± 0.0	± 1.3	± 1.3
ESF	± 0.1	± 0.1	± 2.0	± 2.0
MSF	± 0.0	± 0.0	± 0.5	± 0.5
Trigger	± 0.0	± 0.0	± 0.2	± 0.2
Btag	± 0.0	± 0.0	± 0.0	± 0.0
Pileup	± 0.0	± 0.1	± 0.2	± 0.2
LArhole	± 0.0	± 0.1	± 0.0	± 0.1
PDF	—	± 0.6	± 8.9	± 9.0
Cross Section	± 2.1	± 0.2	± 4.090	± 4.6
TOTAL	± 2.1	± 0.8	± 10.5	± 11.0

Table 6.6: The effect of the systematics on the irreducible backgrounds, normalized to 2.06 fb^{-1} . The expected value for each SM background is labeled *nominal*. The uncertainties follow in absolute number of events. The total includes the 3.7% luminosity uncertainty. The $E_{\text{T}}^{\text{miss}}$ cluster energy systematic is not included as it has no effect on event yields.

The above uncertainties are also applied to the GGM signal grids.

6.7.2 Reducible Backgrounds

The systematic uncertainties on the matrix method can be divided into [159]:

Fake Rate: The uncertainty of the fake rates in the matrix method is estimated by taking the relative difference between the low- and high- $E_{\text{T}}^{\text{miss}}$ regions. For most types of fakes the uncertainties range over 0.4—35%, but are as high as 82% for heavy flavor electrons from $V + \text{jets}$.

Fake-Rate Scale Factors: For conversions the scale factor uncertainties are estimated by varying the selections, such as changing the Z -mass window to

± 5 GeV or ± 20 GeV, giving an uncertainty of 30—50%.

For the heavy flavor scale factors a fit to a constant is performed; the p_T -fit is used as the central value and the η -variation is used to set a systematic uncertainty of 10%. An additional uncertainty of 10% covers the difference between hadronic shower simulation in different MC generators.

Process Fraction: The relative contribution of the processes that make up the reducible background in the signal region is unknown, including the top-production and Z/γ^* -production used for estimating the weighted fake rate. To estimate the contribution the MC used to calculate the fake rates is varied by $\pm\sigma$ in the same manner as the reducible backgrounds are (see Section 6.7.1). This gives an uncertainty of 50% in the low- E_T^{miss} region and 50—200% in the high- E_T^{miss} region.

A systematic uncertainty is set on the internal conversion of a photon to a muon probability by varying the Z -mass window. It gives an uncertainty of 46%, though the systematic uncertainty includes a 100% uncertainty due to radiation off of quark lines [159].

6.7.3 Systematic Uncertainties on the Signal Grids

The largest contributions to the GGM systematic uncertainties are in the cross section due to the uncertainties in the PDFs, factorization and normalization scale, and on α_s .

As stated previously, the signal process cross-sections are calculated using PROSPINO/NLLFAST; the calculations follow the PDF4LHC recommendations [168], using MSTW2008NLO [169, 170] for PDF and scale uncertainties and CTEQ6.6M [134] for scale, PDF, and α_s uncertainties. The re-normalization and factorization scales are set to the sum of the masses of the initial particles produced. An uncertainty on this scale is obtained by taking twice and half this values and re-calculating the cross section. The PDF and α_s uncertainties are derived from data and consequently have errors owing to the measurements used. This produces 44 (40) PDF sets covering the range of these uncertainties for CTEQ (MSTW). The value of α_s is varied by its uncertainty up and down. The extrema of the cross-section estimates from the variations over these uncertainties are used to set an envelope, such that $\sigma_{\text{max}} = \max(\text{CTEQ}, \text{MSTW})$ and $\sigma_{\text{min}} = \min(\text{CTEQ}, \text{MSTW})$. The cross section value and its uncertainty is then:

$$\sigma_{\text{NLO}} = \frac{1}{2} \cdot (\sigma_{\text{max}} + \sigma_{\text{min}}) \quad (6.10)$$

and

$$\delta\sigma_{\text{NLO}} = \left| \frac{1}{2} \cdot (\sigma_{\text{max}} - \sigma_{\text{min}}) \right| \quad (6.11)$$

For the higgsino grid the mean uncertainty is 10% with some regions of the parameter space having an uncertainty as high as 35%. In the wino grid the mean uncertainty is 15% with some regions reaching as high as 44%. The systematic uncertainties estimated for the irreducible background in Section 6.7.1 are also applied to the signal processes and produce similar results.

6.8 Observed Data in the Signal Region

After applying the event selections for the signal region to the 2.06 fb^{-1} dataset, 95 events are observed with an expected background of 72 ± 12 events. A comparison of the expected number of background events compared to data can be found in Table 6.7. The details for each event in the dataset can be found in Table 6.8 through Table 6.11. Each table is dedicated to a different combination of leptonic flavors. Event displays of selected events are available in Appendix A; events were chosen if they contain notably large momenta or event level quantities, such as E_T^{miss} .

The estimate of E_T^{miss} uncertainty, δE_T^{miss} is estimated by summing in quadrature the contributions of the systematic uncertainties affecting the energy of scales of the leptons and jets, such as the JES uncertainty, the EES uncertainty, or the cluster energy scale uncertainty. In general, the δE_T^{miss} is on the order of 10%, though there are events with larger uncertainty, such as run number 184022, event number 21785917, which has 24.3% error.

The distribution of the leading, second, and third lepton E_T^e (p_T^μ) can be seen in Figure 6.14, Figure 6.15, and Figure 6.16, respectively. The distribution of E_T^{miss} after the event selections can be seen in Figure 6.14.

While no cuts are made on the jets in the event, the jet multiplicity is shown in Figure 6.18 and the spectrum of jet p_T is shown in Figure 6.19. Neither shows any significant disagreement overall between data and prediction.

Additionally, shown in Figure 6.20 is the effective mass, m_{eff} . The effective mass is defined as:

$$m_{\text{eff}} \equiv E_T^{\text{miss}} + \sum_{\text{leptons}} p_T + \sum_{\text{jets}}^{p_T > 40 \text{ GeV}} p_T \quad (6.12)$$

The m_{eff} distribution shares the excess seen in data, but it is not significant. Shown in Figure 6.21 is the invariant mass constructed from the three leptons. In the case of these two plots an estimate from the reducible background was not available, so the MC is used to illustrate the distribution. Again, a non-significant excess is seen.

$t\bar{t}V$	ZZ	WZ	Reducible Background	Total Background	Data
2.7 ± 2.1	3.4 ± 0.8	58 ± 11	7.5 ± 3.9	72 ± 12	95

Table 6.7: The expected number of events in the signal region for the SM background MC and the number of events observed in data for 2.06 fb^{-1} . Both statistical and systematic uncertainties are included.

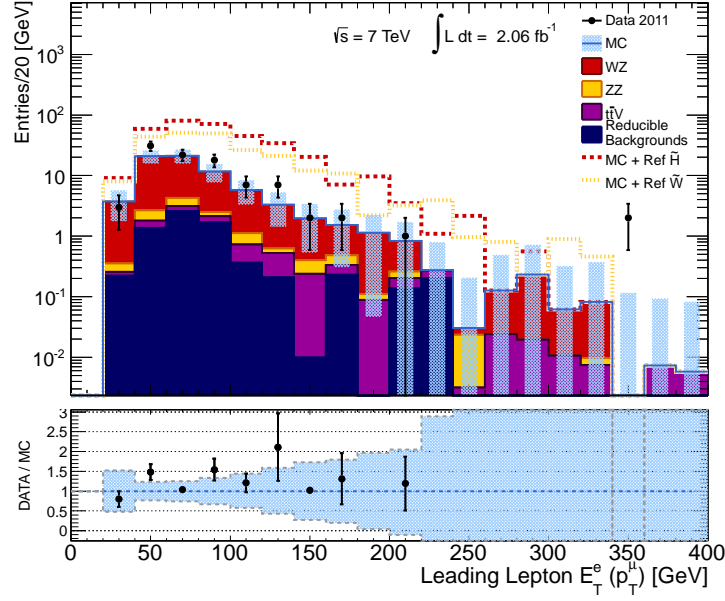


Figure 6.14: The $E_T^e(p_T^\mu)$ distribution for the leading lepton in the signal region. The uncertainties shown are statistical and systematic.

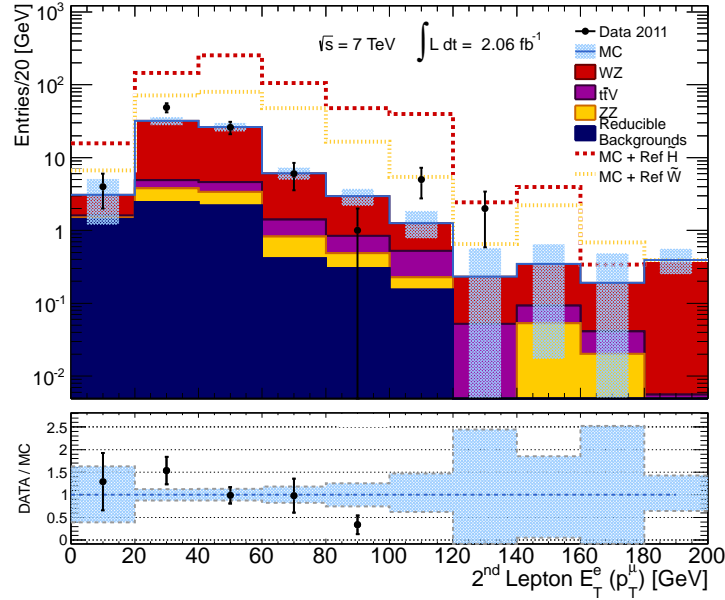


Figure 6.15: The $E_T^e(p_T^\mu)$ distribution for the second leading lepton in the signal region. The uncertainties shown are statistical and systematic.

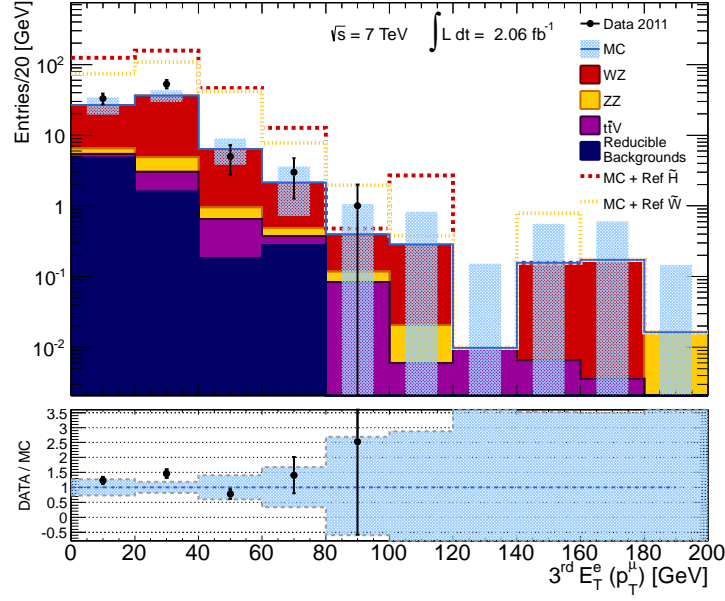


Figure 6.16: The $E_T^e(p_T^\mu)$ distribution for the third leading lepton in the signal region. The uncertainties shown are statistical and systematic.

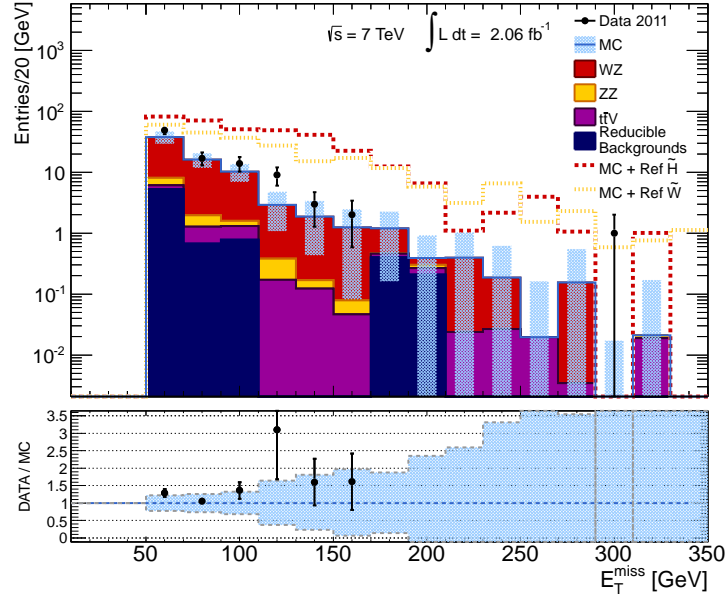


Figure 6.17: The E_T^{miss} distribution in the signal region. The uncertainties shown are statistical and systematic.

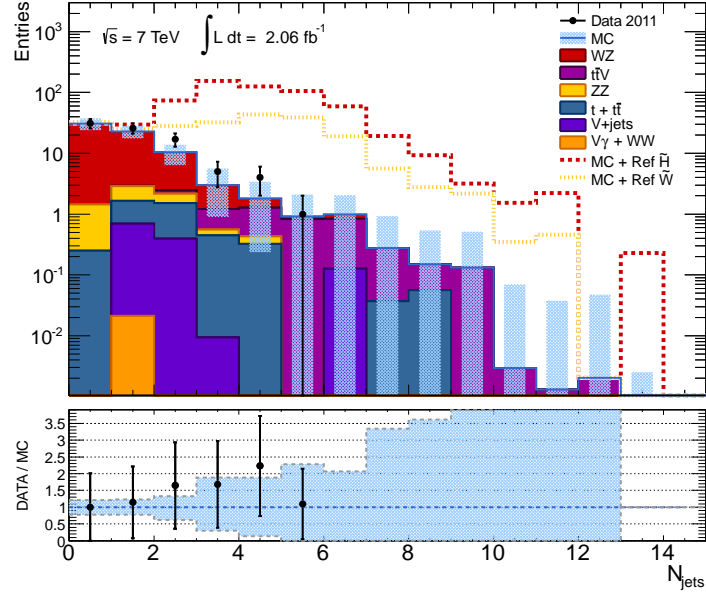


Figure 6.18: The jet multiplicity after the $E_T^{\text{miss}} > 50$ GeV event selection. The uncertainties shown are statistical and systematic.

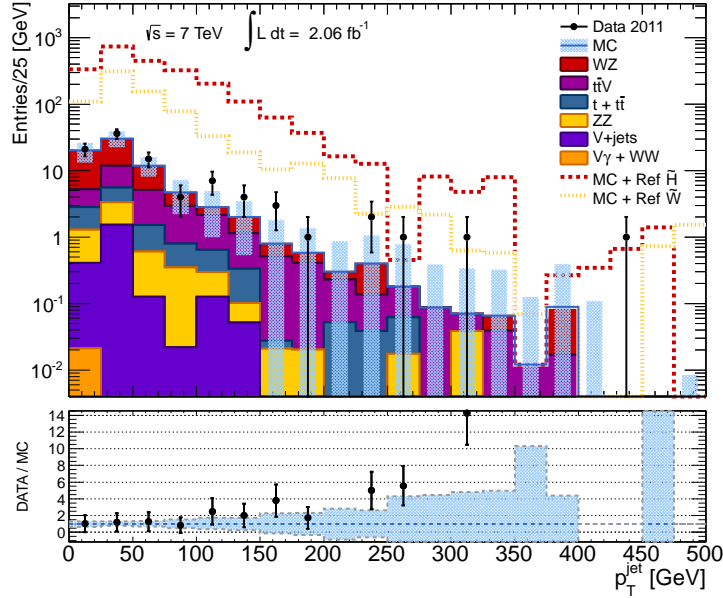


Figure 6.19: The jet p_T distribution after the $E_T^{\text{miss}} > 50$ GeV event selection. The uncertainties shown are statistical and systematic.

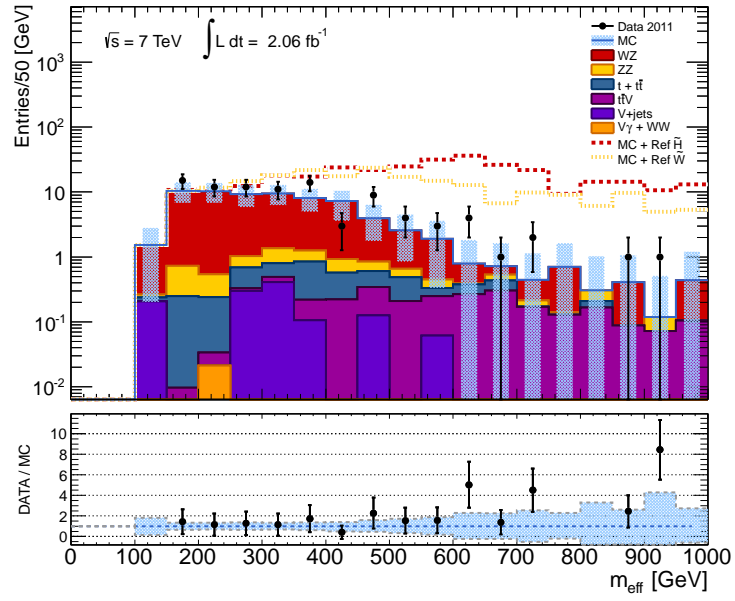


Figure 6.20: The effective mass distribution in the signal region. The uncertainties shown are statistical and systematic.

$e^+e^-e^\pm$											
Run #	Event #	Flavor	p_T^e [GeV]	m_T [GeV]	m_{l+l-1} [GeV]	m_{l+l-1,l^\pm} [GeV]	N_{jets}	Jet p_T [GeV]	m_{eff} [GeV]	E_T^{miss} [GeV]	δE_T^{miss} (%)
180164	98593931	$e^-e^+e^+$	71.7, 54.0, 33.4	132.0, 77.3, 56.6	203.3, 86.8	247.0	0		222.0	60.8	1.9
180225	38923591	$e^+e^-e^-$	37.3, 36.1, 15.8	89.5, 1.1, 63.7	89.2, 37.8	108.1	1	56.9	152.1	64.3	9.5
180309	14077706	$e^-e^+e^-$	46.7, 29.1, 16.1	26.2, 89.3, 69.9	102.6, 89.6	150.7	2	46.4, 39.7	175.8	83.9	12.6
182787	56439353	$e^+e^-e^-$	94.8, 22.0, 11.2	129.6, 13.3, 64.8	90.7, 55.5	113.3	1	109.7	223.3	96.4	7.8
183003	5466177	$e^+e^-e^-$	84.7, 27.3, 19.6	64.0, 19.9, 75.2	32.5, 91.9	108.6	1	162.5	206.4	74.6	16.8
183003	61556406	$e^-e^+e^-$	51.5, 44.9, 12.4	52.9, 70.9, 52.6	95.0, 51.0	121.7	2	47.6, 23.4	166.3	57.5	14.8
183129	16288174	$e^-e^+e^-$	80.6, 21.1, 13.2	196.4, 63.6, 80.1	96.9, 23.7	107.5	1	44.8	239.9	124.9	4.9
183426	10151435	$e^-e^+e^+$	63.2, 31.7, 25.6	109.5, 67.7, 78.2	87.1, 65.8	122.9	0		182.9	61.7	0.8
184022	21785917	$e^-e^+e^+$	56.7, 56.4, 12.6	56.0, 7.0, 50.9	86.7, 58.4	116.8	3	71.6, 47.1, 39.1	177.7	52.6	24.3
184022	128414499	$e^-e^+e^+$	89.7, 22.3, 20.7	146.4, 59.2, 13.0	89.5, 84.6	128.5	1	37.6	204.5	71.5	4.3
185644	25257494	$e^+e^-e^-$	139.9, 124.8, 14.7	118.4, 36.7, 92.2	85.6, 101.3	163.0	2	236.1, 125.6	426.0	146.7	14.4
186049	1958828	$e^+e^-e^-$	52.2, 43.9, 43.7	103.5, 87.6, 35.4	159.6, 89.2	264.2	0		193.2	51.3	7.0
186729	243498369	$e^-e^-e^+$	48.9, 34.5, 29.5	133.7, 67.0, 34.7	91.2, 112.1	352.9	4	59.2, 41.1, 29.8, 25.8	215.6	102.6	8.4
186753	3683826	$e^+e^-e^-$	110.4, 62.0, 41.9	73.8, 65.0, 94.6	201.1, 87.4	248.3	2	139.6, 35.0	287.4	72.4	12.4
187219	31582796	$e^-e^+e^+$	41.1, 28.0, 27.9	89.2, 64.9, 83.5	85.7, 65.8	111.6	2	42.7, 33.2	162.0	65.1	3.1
187811	62120095	$e^-e^+e^-$	71.7, 34.6, 29.0	33.4, 62.7, 95.3	256.3, 91.3	290.3	2	107.5, 54.7	236.3	101.0	9.0
186965	28815719	$e^+e^-e^-$	131.0, 42.2, 21.5	257.4, 48.6, 102.4	161.9, 96.3	196.0	0		322.9	128.3	3.5
186965	120508399	$e^+e^-e^-$	83.9, 18.5, 15.5	161.9, 92.4, 6.2	88.1, 33.8	120.2	2	80.3, 31.4	242.1	124.2	6.3
186965	155446128	$e^-e^-e^+$	45.9, 38.0, 36.2	61.8, 89.6, 25.4	84.4, 82.8	126.8	3	154.2, 41.5, 20.4	181.8	62.1	2.5

Table 6.8: A summary of the data events containing an electron-positron pair with an invariant mass within 10 GeV of m_Z and an additional electron. Shown are the transverse momenta of the electrons, their transverse mass with E_T^{miss} , the invariant mass of an same-flavor, opposite-charge combination, the invariant mass of all three electrons, the jet multiplicity and momenta, the effective mass, and the E_T^{miss} and its uncertainty.

$e^+e^-\mu^\pm$											
Run #	Event #	Flavor	p_T^l [GeV]	m_T [GeV]	m_{l+l-1} [GeV]	m_{l+l-1,l^\pm} [GeV]	N_{jets}	Jet p_T [GeV]	m_{eff} [GeV]	E_T^{miss} [GeV]	δE_T^{miss} (%)
182456	55533226	$e^-e^+\mu^+$	96.7, 30.4, 18.3	184.8, 103.0, 85.4	85.1	172.0	1	41.4	249.2	102.7	1.6
182486	16677615	$e^-\mu^-e^+$	107.2, 39.7, 38.8	200.6, 38.9, 104.6	88.2	171.7	0		279.8	94.1	6.1
182486	21528951	$e^-\mu^-e^+$	120.8, 17.4, 16.1	202.1, 58.9, 14.2	90.0	113.4	0		239.2	84.6	3.7
182879	19439981	$e^-e^+\mu^-$	52.3, 50.1, 19.0	89.1, 90.0, 52.8	89.8	113.6	0		172.0	50.7	5.1
183021	69425573	$e^-e^+\mu^+$	50.3, 28.6, 26.5	97.2, 43.3, 72.5	90.8	179.7	0		155.6	50.2	3.2
183286	97150217	$e^-\mu^+e^+$	66.5, 39.6, 15.5	40.3, 64.8, 49.0	89.2	139.3	2	124.2, 21.6	189.1	68.2	11.4
183780	108727692	$e^-\mu^-e^+$	89.7, 38.5, 23.4	129.0, 46.7, 45.2	86.9	154.7	0		204.2	52.7	3.0
186169	16345995	$e^-e^+\mu^-$	41.5, 27.2, 11.4	18.9, 74.4, 26.9	82.3	95.0	1	20.3	131.1	51.0	10.5
186216	27680559	$e^-\mu^-e^+$	58.8, 45.5, 22.4	110.4, 95.5, 27.8	90.0	208.6	0		187.0	60.8	2.8
185761	18433702	$e^+\mu^-e^-$	67.0, 20.3, 11.8	129.4, 71.1, 6.4	90.7	105.2	0		162.3	63.2	4.5
185998	4354615	$e^+e^-\mu^+$	83.7, 38.9, 34.2	149.5, 101.9, 1.5	94.3	294.0	2	21.1, 20.6	225.8	66.8	4.3
186729	81190803	$e^-e^+\mu^+$	213.4, 105.5, 35.5	359.0, 254.2, 10.1	91.5	329.5	2	73.9, 64.6	508.8	154.0	4.7
186729	159856729	$e^-\mu^+e^+$	98.0, 19.9, 18.4	145.3, 48.8, 43.5	88.4	108.9	2	39.0, 27.9	195.6	59.3	5.0
186877	21782291	$\mu^-e^+e^-$	51.0, 37.2, 33.0	103.5, 84.8, 30.9	92.4	154.5	4	116.7, 41.4, 22.2, 20.3	174.8	53.4	11.6
186923	59240008	$e^+\mu^-e^-$	110.3, 46.6, 29.6	177.4, 111.6, 34.7	86.4	173.9	1	49.2	271.5	85.2	3.0

Table 6.9: A summary of the data events containing an electron-positron pair with an invariant mass within 10 GeV of m_Z and an additional muon. Shown are the transverse momenta of the leptons, their transverse mass with E_T^{miss} , the invariant mass of an same-flavor, opposite-charge combination, the invariant mass of all leptons, the jet multiplicity and momenta, the effective mass, and the E_T^{miss} and its uncertainty.

$\mu^+\mu^-e^\pm$											
Run #	Event #	Flavor	p_T^ℓ [GeV]	m_T [GeV]	m_{l^+,l^-} [GeV]	m_{l^+,l^-,l^\pm} [GeV]	N_{jets}	Jet p_T [GeV]	m_{eff} [GeV]	E_T^{miss} [GeV]	δE_T^{miss} (%)
180448	1483181	$\mu^-e^-\mu^+$	46.8, 43.0, 39.6	111.5, 65.6, 70.0	91.1	147.7	5	80.1, 55.9, 46.8, 37.8, 27.4	209.8	80.4	5.8
180139	47529321	$\mu^+\mu^-e^+$	91.6, 30.8, 15.7	151.6, 69.4, 14.7	85.8	119.8	0		203.8	65.7	4.3
180400	1649049	$\mu^+e^+\mu^-$	112.7, 103.6, 67.0	202.9, 55.7, 159.2	93.0	305.6	0		378.1	94.6	1.4
182787	18945920	$\mu^+\mu^-e^-$	46.0, 43.1, 29.6	74.1, 91.8, 65.1	93.2	135.7	0		173.4	54.7	2.6
182787	117824417	$\mu^-e^-\mu^+$	122.1, 37.1, 35.0	223.0, 21.3, 102.9	95.9	192.0	0		297.3	103.2	0.4
183054	25255214	$e^-\mu^+\mu^-$	128.6, 104.6, 83.4	12.3, 189.1, 167.5	82.3	358.6	2	52.8, 20.6	403.4	86.9	2.9
183081	160821752	$\mu^+e^-\mu^-$	179.2, 128.6, 24.7	256.1, 73.6, 96.7	97.6	397.5	0		427.0	94.7	2.5
183407	36412879	$\mu^+\mu^-e^-$	59.0, 36.2, 31.0	110.4, 50.1, 59.5	88.1	135.4	0		178.4	52.1	1.3
183462	137952124	$\mu^-e^-\mu^+$	87.6, 35.5, 31.3	155.8, 78.5, 39.8	91.6	141.7	0		224.2	69.8	1.1
183462	149168776	$\mu^+\mu^-e^-$	52.8, 32.9, 26.0	106.4, 46.8, 75.6	90.9	132.7	0		166.9	55.2	2.2
184130	43351005	$\mu^+\mu^-e^+$	65.7, 28.8, 27.3	113.4, 72.1, 28.8	92.8	158.8	0		176.4	55.5	2.2
183780	40559312	$\mu^+\mu^-e^-$	50.3, 45.5, 33.2	92.9, 83.2, 82.1	90.6	166.4	1	31.0	182.6	53.3	6.9
184169	35750750	$e^+\mu^+\mu^-$	87.8, 77.5, 67.0	141.3, 196.7, 156.5	90.9	335.7	1	21.5	357.7	125.3	1.9
184169	105464632	$\mu^-\mu^+e^-$	54.3, 33.9, 33.7	62.1, 91.0, 92.1	92.1	159.6	3	39.4, 28.8, 21.0	185.3	63.4	6.4
184130	44517484	$\mu^+e^-\mu^-$	59.6, 24.9, 20.9	21.2, 9.2, 65.7	99.1	152.3	1	138.2	157.5	52.5	16.1
183780	49478936	$\mu^+\mu^-e^-$	66.2, 25.8, 23.9	130.7, 0.6, 76.1	87.2	109.4	0		180.7	64.7	1.2
183780	62734339	$\mu^+e^+\mu^-$	81.5, 24.5, 14.9	152.1, 75.6, 70.1	94.1	127.8	2	74.9, 22.0	204.9	84.1	1.5
184072	10617609	$e^+\mu^+\mu^-$	23.1, 20.1, 20.0	75.6, 89.1, 43.2	86.5	117.7	1	91.0	177.1	113.9	6.4
186182	7407118	$\mu^-e^+\mu^+$	140.6, 30.3, 17.5	258.0, 42.1, 14.1	99.1	280.1	0		308.9	120.5	3.3
186169	17499798	$\mu^-\mu^+e^-$	53.4, 35.8, 30.1	47.2, 79.0, 77.6	88.8	136.0	2	44.0, 21.9	171.0	51.8	4.9
186169	60145885	$\mu^+\mu^-e^+$	72.8, 46.2, 31.9	157.5, 96.9, 92.4	89.3	184.9	0		238.7	87.8	1.1
186361	18855850	$\mu^+e^-\mu^-$	346.4, 45.9, 36.8	380.9, 65.7, 120.6	94.1	305.0	1	248.2	534.7	105.9	11.8
186721	30840259	$e^+\mu^-\mu^+$	128.1, 108.1, 60.0	88.7, 213.1, 173.4	91.0	304.8	2	25.3, 23.0	421.3	125.3	7.3
186669	42109584	$\mu^-\mu^+e^-$	54.6, 48.3, 13.7	83.1, 100.5, 53.2	94.4	124.7	0		176.4	59.7	3.9
186934	75059135	$\mu^-e^-\mu^+$	66.2, 40.7, 22.7	111.2, 54.4, 66.3	87.3	153.3	0		185.3	55.7	2.2
187763	61044675	$\mu^+e^+\mu^-$	128.4, 30.3, 23.2	232.9, 48.6, 59.3	91.5	155.5	0		287.2	105.7	0.5
187811	15210356	$\mu^+\mu^-e^-$	72.2, 45.7, 32.6	139.7, 133.7, 14.7	87.5	142.7	1	74.1	253.0	102.5	3.9
186877	126711223	$\mu^-e^-\mu^+$	95.4, 75.9, 30.6	59.2, 86.8, 139.5	100.0	135.9	3	251.5, 26.8, 24.0	365.3	163.4	9.6
186923	10398981	$e^-\mu^-\mu^+$	36.0, 28.8, 18.6	89.7, 39.0, 43.0	89.9	233.7	2	94.4, 20.6	167.3	84.0	8.8
187219	43654572	$\mu^-\mu^+e^-$	46.5, 33.6, 14.8	67.3, 67.8, 52.3	91.1	110.9	3	22.1, 21.5, 21.0	145.9	51.0	9.1

Table 6.10: A summary of the data events containing a same-flavor, opposite-charge muon pair with an invariant mass within 10 GeV of m_Z and an additional electron. Shown are the transverse momenta of the leptons, their transverse mass with E_T^{miss} , the invariant mass of an same-flavor, opposite-charge combination, the invariant mass of all three leptons, the jet multiplicity and momenta, the effective mass, and the E_T^{miss} and its uncertainty.

$\mu^+\mu^-\mu^\pm$											
Run #	Event #	Flavor	p_T^ℓ [GeV]	m_T [GeV]	$m_{l+l^{-1}}$ [GeV]	m_{l+l^{-1},l^\pm} [GeV]	N_{jets}	Jet p_T [GeV]	m_{eff} [GeV]	E_T^{miss} [GeV]	δE_T^{miss} (%)
179739	23068430	$\mu^+\mu^+\mu^-$	73.0, 44.8, 30.6	112.4, 85.6, 36.1	95.0, 41.5	141.3	1	30.0	202.5	54.0	4.6
180124	68526315	$\mu^+\mu^+\mu^-$	62.7, 43.0, 34.5	90.2, 92.3, 54.0	93.7, 73.2	154.7	0		192.0	51.7	1.1
180164	73825441	$\mu^-\mu^+\mu^+$	67.0, 24.6, 13.2	117.2, 7.7, 41.6	90.7, 78.1	124.7	1	20.9	156.7	51.8	6.6
180309	31818991	$\mu^+\mu^-\mu^-$	52.6, 33.8, 27.7	80.3, 36.5, 71.9	81.4, 85.7	123.4	1	73.1	182.2	68.1	7.8
182454	4702311	$\mu^+\mu^-\mu^-$	109.2, 100.5, 53.8	128.5, 88.4, 2.8	57.6, 91.1	131.0	1	315.3	377.3	113.8	12.3
182456	37283247	$\mu^-\mu^+\mu^-$	86.4, 76.2, 30.1	129.3, 130.0, 61.5	88.6, 65.5	120.6	1	145.6	248.2	55.5	13.9
182796	41972295	$\mu^+\mu^+\mu^-$	94.4, 70.9, 34.4	101.5, 66.8, 66.8	113.9, 94.3	248.3	2	67.1, 21.6	251.7	51.9	11.8
183054	21026988	$\mu^+\mu^-\mu^+$	62.4, 36.8, 36.8	137.6, 119.2, 51.0	90.2, 78.1	155.3	1	159.1	271.3	135.4	5.6
183286	53451031	$\mu^+\mu^+\mu^-$	83.5, 29.5, 19.9	115.7, 64.0, 24.4	83.7, 73.7	233.5	1	22.8	183.5	50.5	5.5
183412	2242543	$\mu^-\mu^+\mu^-$	163.8, 29.2, 19.5	251.7, 69.3, 40.2	101.9, 86.7	234.7	1	56.0	309.2	96.8	3.8
182747	112682971	$\mu^+\mu^-\mu^-$	60.1, 53.6, 29.2	111.9, 106.5, 14.5	84.3, 83.6	153.4	1	28.5	195.8	52.9	5.8
182787	34276063	$\mu^-\mu^+\mu^-$	55.0, 41.9, 14.9	158.9, 27.7, 69.1	90.9, 50.7	113.6	1	111.8	234.8	123.0	4.7
182787	103600363	$\mu^-\mu^+\mu^+$	104.2, 31.7, 29.7	7.8, 6.2, 97.3	88.4, 93.5	139.2	4	116.1, 110.6, 34.5, 22.0	299.1	133.5	12.3
184130	35410477	$\mu^+\mu^+\mu^-$	40.4, 25.6, 11.1	106.0, 55.9, 56.4	53.2, 98.6	134.8	1	22.4	150.0	73.0	3.7
184022	43591184	$\mu^-\mu^+\mu^+$	45.0, 18.7, 13.7	115.8, 65.1, 61.5	91.9, 58.5	109.4	0		151.9	74.6	2.1
186049	70818458	$\mu^-\mu^+\mu^-$	94.8, 80.3, 21.3	157.9, 105.2, 65.7	82.3, 100.8	164.1	3	48.0, 30.4, 25.2	269.8	73.4	0.8
186179	5228295	$\mu^-\mu^+\mu^-$	79.2, 41.1, 32.7	119.8, 35.6, 95.4	93.1, 51.7	141.6	4	441.4, 193.0, 58.4, 25.5	245.6	92.6	8.2
186169	47351357	$\mu^-\mu^+\mu^-$	56.3, 32.8, 32.3	101.2, 40.6, 83.8	90.5, 89.1	141.4	0		175.7	54.4	0.6
186216	11067182	$\mu^-\mu^+\mu^-$	57.4, 31.7, 31.2	101.4, 68.6, 79.8	89.1, 27.2	137.9	0		185.2	64.9	5.8
186729	54074612	$\mu^-\mu^+\mu^+$	58.8, 36.4, 11.8	131.5, 85.2, 59.1	90.5, 42.5	124.9	0		186.8	79.8	2.7
186729	175034387	$\mu^-\mu^+\mu^-$	61.4, 43.8, 15.6	94.8, 120.8, 24.8	91.9, 53.7	131.6	1	69.6	205.3	84.6	4.3
186923	146860679	$\mu^-\mu^+\mu^+$	77.4, 37.5, 20.9	128.2, 73.2, 3.1	110.2, 92.6	150.1	0		193.5	57.7	1.5
186965	15778260	$\mu^-\mu^+\mu^+$	63.3, 57.8, 28.4	99.1, 134.1, 69.3	92.2, 102.7	169.9	1	31.4	227.4	77.9	2.1
186965	63620161	$\mu^-\mu^+\mu^-$	45.5, 41.1, 35.6	56.2, 81.6, 85.4	91.4, 40.7	128.8	0		173.5	51.2	2.6
186965	155056482	$\mu^-\mu^-\mu^+$	100.3, 40.6, 14.5	56.7, 90.0, 53.4	92.2, 41.0	322.5	1	92.2	205.6	50.2	7.6
186965	180209937	$\mu^+\mu^-\mu^-$	141.2, 46.1, 18.1	112.6, 97.4, 59.7	280.6, 88.7	297.0	4	56.4, 53.0, 25.3, 23.8	257.0	51.5	3.8
187219	68267656	$\mu^-\mu^-\mu^+$	347.8, 77.3, 36.0	607.8, 23.3, 149.2	95.8, 102.2	423.8	1	286.7	758.3	297.2	1.9
187811	67845541	$\mu^-\mu^+\mu^-$	71.9, 37.6, 37.3	135.4, 91.5, 52.4	88.7, 77.0	182.4	1	23.3	211.5	64.6	2.3
187811	68065554	$\mu^-\mu^+\mu^-$	50.7, 27.6, 17.0	107.2, 38.0, 61.2	87.3, 60.6	170.5	0		152.7	57.4	2.4
187812	11122323	$\mu^-\mu^+\mu^-$	70.9, 59.6, 40.1	107.7, 113.6, 44.1	93.7, 92.2	176.9	0		227.9	57.3	0.9
187763	79698027	$\mu^-\mu^+\mu^+$	73.0, 52.2, 46.9	151.7, 135.9, 70.9	95.5, 168.2	290.2	0		263.0	90.9	1.6

Table 6.11: A summary of the data events containing a same-flavor, opposite-charge muon pair with an invariant mass within 10 GeV of m_Z and an additional muon. Shown are the transverse momenta of the muons, their transverse mass with E_T^{miss} , the invariant mass of an same-flavor, opposite-charge combination, the invariant mass of all three muons, the jet multiplicity and momenta, the effective mass, and the E_T^{miss} and its uncertainty.

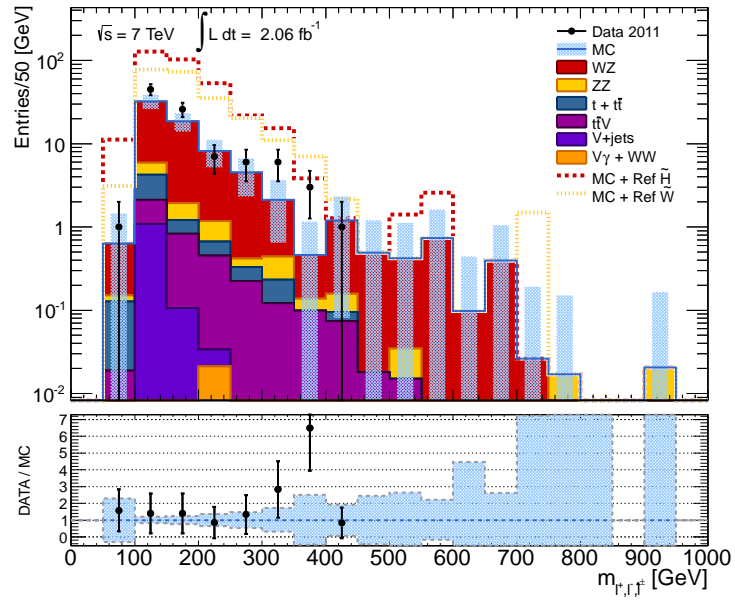


Figure 6.21: The distribution of the invariant mass calculated from all three leptons in the signal region. The uncertainties shown are statistical and systematic.

“We ain’t found shit!”

Mel Brooks [171]

7

Interpretations of Results

The results of this analysis are interpreted with a modified frequentist approach using the CL_s method, whereby the confidence level of the signal+background hypothesis is normalized to the background-only hypothesis, $\text{CL}_s = \text{CL}_{s+b}/\text{CL}_b$ [172]. The confidence levels were calculated using the standard limit-setting tools of the ATLAS SUSY Working Group.

The test statistic derives from a profile log likelihood (LLR), with the likelihood function defined as:

$$L(n, \theta^0 | \mu, b, \theta) = P(n | \lambda_S(\mu, b, \theta)) \cdot P_{Syst}(\theta^0, \theta) \quad (7.1)$$

where

- n is the number of events observed in data,
- μ is the predicted SUSY signal strength for each test, normalized to the expected background,
- b is the estimate of the background contribution,
- θ represents the systematic uncertainties in the form of nuisance parameters,
- θ^0 represents the nominal values about which θ is varied.

$P(n | \lambda_S(\mu, b, \theta))$ is a Poisson distribution describing the probability of observing n given an expectation generated by $\lambda_S(\mu, b, \theta)$ based on the signal estimate, the background estimate, and systematic uncertainties. $P_{Syst}(\theta^0, \theta)$ is a probability density function composed of the product of unit normal distributions, $G(\theta^0 - \theta)$, for each of the systematic uncertainties accounted for. The profile LLR is then:

$$\Lambda(\mu) \equiv \Lambda(\mu, n, \theta^0) \equiv -2 \ln \left(\frac{L(n, \theta^0 | \mu, \hat{b}, \hat{\theta})}{L(n, \theta^0 | \hat{\mu}, \hat{b}, \hat{\theta})} \right), \quad (7.2)$$

where the maximum of the likelihood occurs at $\hat{\mu}$, \hat{b} , $\hat{\theta}$. For a fixed signal strength, μ , the maximum likelihood is given by \hat{b} and $\hat{\theta}$. We use $\Lambda(\mu)$ as an abbreviation since n and θ^0 are fixed. It is assumed that the signal can only increase the number of events, so that for $\hat{\mu} < 0$, $\hat{\mu} = 0$ is substituted. At this point it could be suitable to make an approximation for calculating the test statistic, such as using the χ^2 probability distribution function. This would be warranted under Wilks' theorem [173, 174], however to more accurately determine the p -value, pseudo-experiments are used. The likelihood function $L(n, \theta^0 | \mu, b, \theta)$ is used to make pseudo-measurements to obtain new values of n and θ^0 , and then calculate a new value of the profile LLR, q . The p -value is calculated by integrating over all $q' < q_{\text{nominal}}$. This is done for both the signal case, $q_{\text{nominal}} = q_{\mu}$, and the SM case, $q_{\text{nominal}} = q_0$ and CL_s is taken as the ratio. Values of less than 0.05 are excluded [173–175]. For this analysis, 50000 pseudo-experiments are required for each point, though 100000 are run to ensure redundancy in the case of computing failures.

For the signal region we find a p -value of 0.06 (1.6σ). Any model which contributes more than 49.1 events in excess of the SM background is excluded at the 95% confidence level (CL) with an expected limit of 29.0 events. Based on the number of events and predicted background, the limit at 95% CL for the visible cross section (cross section \times acceptance \times branching ratio) for non-SM processes is 23.8 fb for the signal region selections. The expected value based on background estimates was 14.1 fb.

The results are applied to the GGM grids using the CL_s method. The resulting 95% CL exclusion intervals are shown for the higgsino grid in Figure 7.1 and for the wino grid in Figure 7.2. p -values are calculated for each point of the grid, marked with crosses in Figures 7.1 and 7.2. The exclusion interval is determined using linear interpolation between neighbors, using a simple linear slope between excluded and non-excluded points to find the boundary of 95% confidence. Unfortunately, the excess in the signal region seriously deteriorates the exclusion reach. A stronger limit on the Higgsino grid can be found in the ATLAS $Z + E_{\text{T}}^{\text{miss}}$ result [176]. In the case of the Wino grid, this analysis represents the first interpretation based on a direct measurement. If theoretical interpretations [61] of other LHC results are accepted, including assumptions made by the theorists responsible, other LHC results have a broader reach than the measurement presented here.

The efficiency and acceptance of the analysis on the GGM model grids can be found in Appendix B.

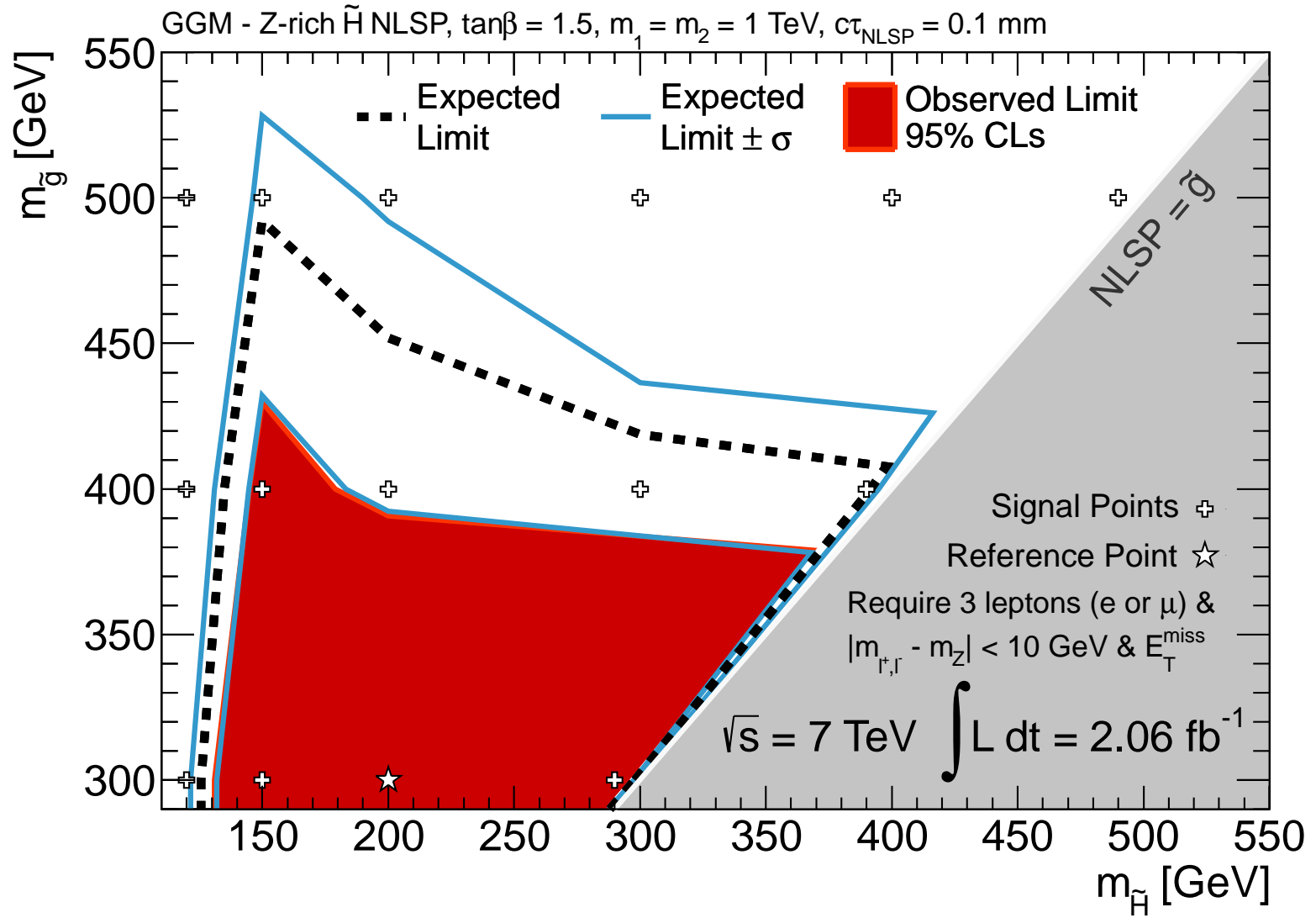


Figure 7.1: The 95% CL exclusion limit for the GGM higgsino grid using CL_s; the exclusion interval is determined by calculating the p -values at the model points marked with crosses and then linearly interpolating between excluded and non-excluded neighbors to find the boundary of 95% confidence.

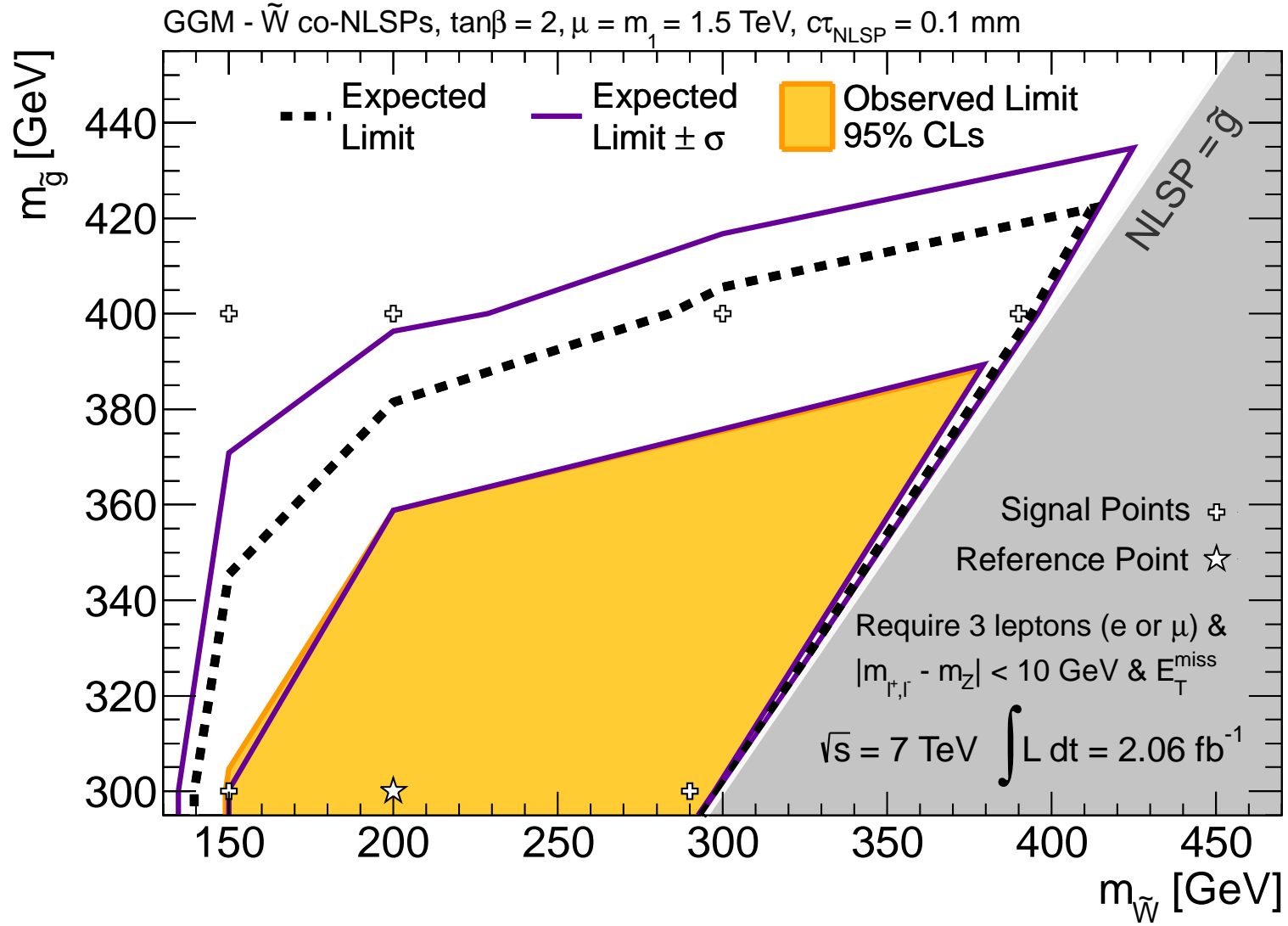


Figure 7.2: The 95% CL exclusion limit for the GGM wino grid using CL_s ; the exclusion interval is determined by calculating the p -values at the model points marked with crosses and then linearly interpolating between excluded and non-excluded neighbors to find the boundary of 95% confidence.

My interest is in the future because I am going to spend the rest of my life there

Charles. F. Kettering [177]

8

Future Studies

8.1 Alternative Analysis Scenarios

For the total 2011 running period ATLAS has collected an integrated luminosity of over 5 fb^{-1} , as shown in Figure 2.2(b). The three-lepton analysis is being updated to that dataset, as is a four-lepton analysis. The obvious question is how the increase in integrated luminosity will improve the exclusion interval against the GGM grids? Shown in Figure 8.1 and Figure 8.2 are the expected limits for an increase in luminosity, as well as other potential signal regions, compared to the current results for the Higgsino and Wino grid. The new scenarios include:

- The expected 5 fb^{-1} limit after requiring three leptons, with a reconstructed Z -boson from the leptons, and $E_{\text{T}}^{\text{miss}} > 50 \text{ GeV}$,
- The expected 5 fb^{-1} limit with the $E_{\text{T}}^{\text{miss}}$ selection increased to 100 GeV ,
- The expected 5 fb^{-1} limit with an additional requirement on the transverse mass of the third lepton not forming the best Z -pair. The best Z -pair is considered the one closest to $m_Z = 91.2 \text{ GeV}$. The transverse mass selection is $m_{\text{T}} > 90 \text{ GeV}$. The $E_{\text{T}}^{\text{miss}}$ selection is 50 GeV for this scenario.
- The expected 5 fb^{-1} limit for an analysis requiring four or more leptons, with a reconstructed Z -boson from the leptons, and $E_{\text{T}}^{\text{miss}} > 50 \text{ GeV}$,

For the Higgsino grid the increased integrated luminosity leads to an increased exclusion interval, while the increase of the $E_{\text{T}}^{\text{miss}}$ selection to 100 GeV offers additional improvement. Requiring a transverse mass cut on the non- Z lepton also shows promise for increasing total exclusion area. The four-lepton analysis would also offer a rather large increase in the exclusion interval. Also examined was requiring two Z resonances from the four leptons, though this did not improve on the exclusion potential. A four-lepton selection along with a requirement of $E_{\text{T}}^{\text{miss}} > 100 \text{ GeV}$ was also examined, but such a selection reduces the signal event yield to nothing.

The Wino grid also shows improvement in the extended, 5 fb^{-1} scenario and with the $E_{\text{T}}^{\text{miss}}$ selection increased to 100 GeV the exclusion interval is increased greatly, much like the Higgsino grid. And again, the inclusion of a transverse mass requirement on the lepton outside of the best Z -resonance has mixed results, though overall an increase in exclusion area is shown. Requiring four or more leptons does not improve upon the three lepton analysis at 5 fb^{-1} . Not shown is a requirement for four or more leptons and two leptonic Z -resonances, but the exclusion potential is similar to that of the four lepton with one Z requirement.

8.2 Outstanding Issues

One of the systematic uncertainties not well understood in this analysis is the shape of the $E_{\text{T}}^{\text{miss}}$ distribution for the ZZ and WZ contributions, as well as other principle contributions. No straightforward idea for dealing with this uncertainty was available for this analysis. In connection with this is a method for deriving a data-driven background estimate of the ZZ , WZ , and $t\bar{t}V$ backgrounds.

Potential avenues for exploring this uncertainty are a fit in a low- $E_{\text{T}}^{\text{miss}}$ region with extrapolation into the high- $E_{\text{T}}^{\text{miss}}$ signal region. This could be motivated by a template provided in another orthogonal region, perhaps a region with non-isolated leptons.

Another potential method is to base the template off of similar events with photons, as performed in [176]. However, signal pollution could potentially be an issue with such a method in combination with a GGM search, as the Higgsino model has a large branching fraction to photons.

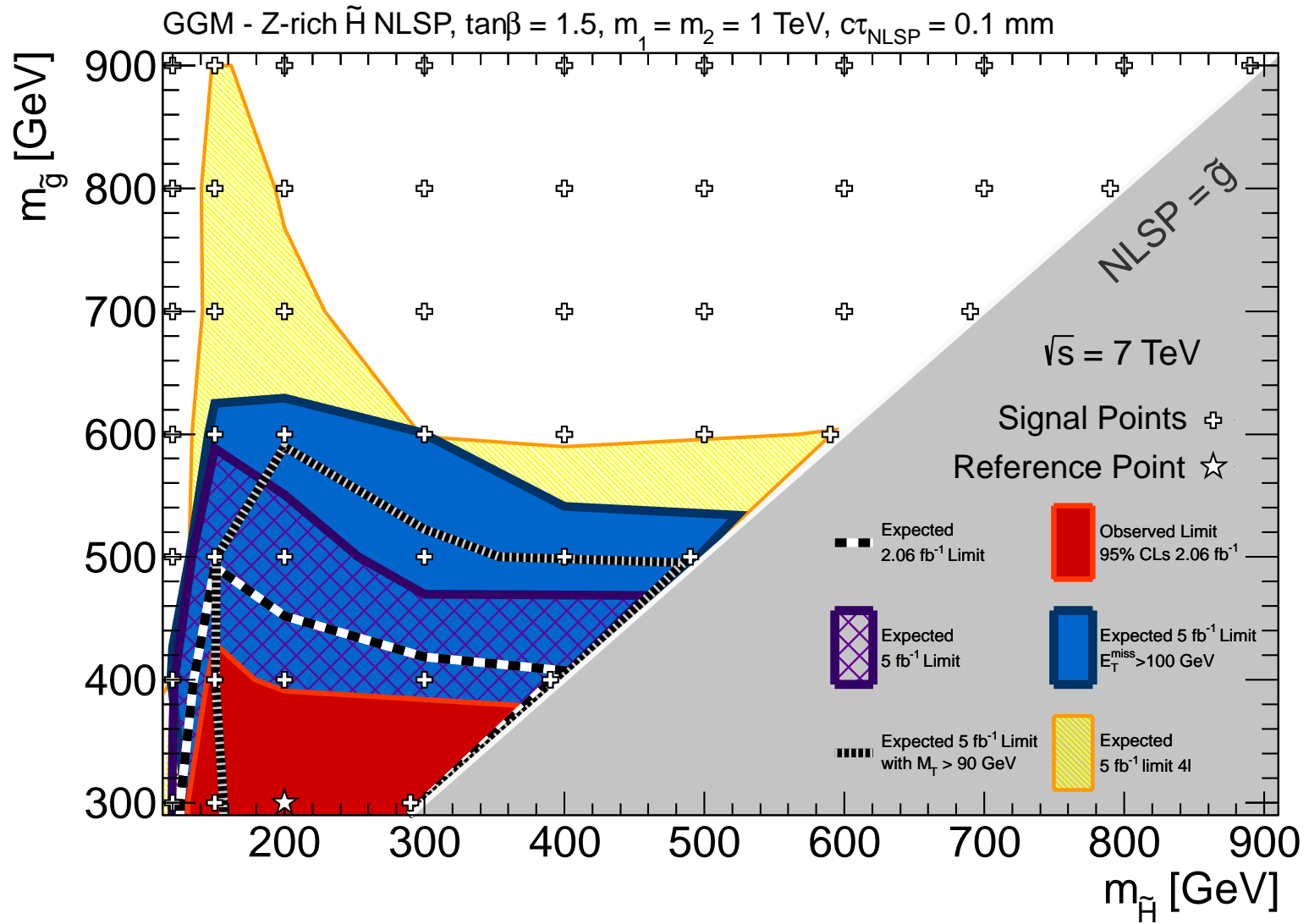


Figure 8.1: The current Higgsino grid exclusion interval, observed and expected, compared to potential 5 fb⁻¹ studies. This includes the same analysis extended to 5 fb⁻¹, an increase of the E_T^{miss} selection to 100 GeV, a requirement on the third lepton transverse mass, $m_T > 90$ GeV. Also examined is changing the N_{lepton} requirement to four or more leptons.

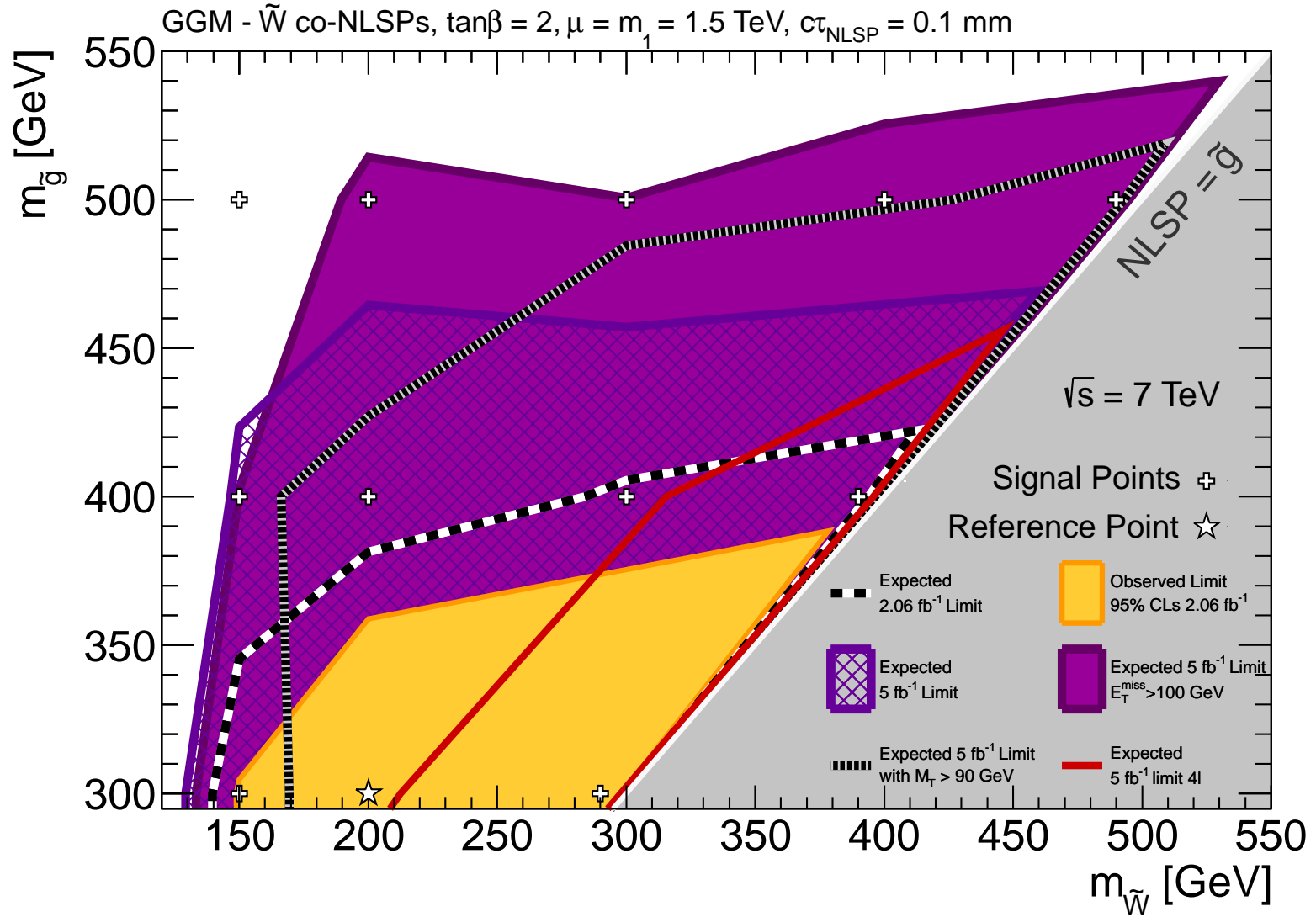


Figure 8.2: The current Wino grid exclusion interval, observed and expected, compared to potential 5 fb^{-1} studies. This includes the same analysis extended to 5 fb^{-1} , an increase of the E_T^{miss} selection to 100 GeV, a requirement on the third lepton transverse mass, $m_T > 90$ GeV. Also examined is changing the N_{lepton} requirement to four or more leptons.

“The trouble with being educated is that it takes a long time; it uses up the better part of your life and when you are finished what you know is that you would have benefited more by going into banking.”

Philip K. Dick [178]

9

Conclusion

I presented a supersymmetric search for events with large values of E_T^{miss} and three leptons, further requiring that two of the leptons form a same-flavor, opposite-sign pair with an invariant mass within 10 GeV of the Z mass. After all selections, there were 95 events observed in data and 72 ± 12 were expected. An upper limit of 23.8 fb was set at 95% confidence level on the visible cross section for processes beyond the standard model which result in this signature.

An interpretation of this upper limit was performed using two models from GGM supersymmetry; one model in which the NLSP is a Z -rich higgsino and another model featuring wino co-NLSPs. The exclusion intervals presented are among the first interpretations of the two GGM models made from direct measurement.

Bibliography

- [1] J.B.S. Haldane. Book reviews: Darwinism and the staphylococci. *J. Genetics*, 58(3):450–464, Dec 1963.
- [2] H. Baer & X. Tata. *Weak Scale Supersymmetry*, pages 6–8. Cambridge University Press, New York, 2006.
- [3] K. Nakamura *et al.* Review of particle physics. *J. Phys. G*, 37:101,405–418, 2010.
- [4] D.J. Griffiths. *Introduction to Elementary Particles*, pages 26–31. Wiley, New York, NY, 1987.
- [5] D.J. Griffiths. *Introduction to Elementary Particles*, pages 55–65. Wiley, New York, NY, 1987.
- [6] M.E. Peskin & D.V. Schroeder. *An Introduction to Quantum Field Theory*, pages 13–33. Westview, Boulder, CO, 1995.
- [7] M.E. Peskin & D.V. Schroeder. *An Introduction to Quantum Field Theory*, page 487. Westview, Boulder, CO, 1995.
- [8] C.S. Quigg. *Gauge Theories of the Strong, Weak, and Electromagnetic Interactions*, page 59. Addison-Wesley, Reading, MA, 1983.
- [9] M.E. Peskin & D.V. Schroeder. *An Introduction to Quantum Field Theory*, pages 196–198. Westview, Boulder, CO, 1995.
- [10] D.J. Griffiths. *Introduction to Elementary Particles*, pages 37–44. Wiley, New York, NY, 1987.
- [11] F. Halzen & A.D. Martin. *Quarks and Leptons: An Introductory Course in Modern Particle Physics*, pages 169–171,. Wiley, New York, NY, 1984.
- [12] M.E. Peskin & D.V. Schroeder. *An Introduction to Quantum Field Theory*, pages 545–548. Westview, Boulder, CO, 1995.

- [13] A. Zee. *Quantum Field Theory in a Nutshell*, pages 359–360. Princeton University Press, second edition, 2010.
- [14] C.S. Quigg. *Gauge Theories of the Strong, Weak, and Electromagnetic Interactions*, pages 73–78. Addison-Wesley, Reading, MA, 1983.
- [15] M.E. Peskin & D.V. Schroeder. *An Introduction to Quantum Field Theory*, pages 700–719. Westview, Boulder, CO, 1995.
- [16] M.E. Peskin & D.V. Schroeder. *An Introduction to Quantum Field Theory*, pages 351–352. Westview, Boulder, CO, 1995.
- [17] S.P. Martin. A supersymmetry primer, Sep 2011. hep-ph/9709356v6.
- [18] M.E. Peskin & D.V. Schroeder. *An Introduction to Quantum Field Theory*, pages 690–700. Westview, Boulder, CO, 1995.
- [19] C.S. Quigg. *Gauge Theories of the Strong, Weak, and Electromagnetic Interactions*, pages 106–115. Addison-Wesley, Reading, MA, 1983.
- [20] D.J. Griffiths. *Introduction to Elementary Particles*, page 46. Wiley, New York, NY, 1987.
- [21] CDF & D0 Collaborations. 2012 update of the combination of cdf and d0 results for the mass of the w boson. Technical Report arXiv:1204.0042v2 [hep-ex], FermiLab, Batavia, IL, Mar 2012.
- [22] S. Schael *et al.* Precision electroweak measurements on the Z resonance. *Phys. Rep.*, 427(hep-ex/0509008):257–302, Sep 2005.
- [23] G. Aad *et al.* Combination of Higgs boson searches with up to 4.9 fb⁻¹ of pp collisions data taken at a center-of-mass energy of 7 TeV with the ATLAS experiment at the LHC. Technical Report ATLAS-CONF-2011-163, CERN, Geneva, Dec 2011.
- [24] CMS Collaboration. Combination of CMS searches for a standard model Higgs boson. Technical Report CMS-PAS-HIG-11-032, CERN, Geneva, Dec 2011.
- [25] D.J. Griffiths. *Introduction to Elementary Particles*, page 55. Wiley, New York, NY, 1987.
- [26] M.E. Peskin & D.V. Schroeder. *An Introduction to Quantum Field Theory*, pages 786–791. Westview, Boulder, CO, 1995.

- [27] A. Zee. *Quantum Field Theory in a Nutshell*, pages 403–404. Princeton University Press, second edition, 2010.
- [28] H. Baer & X. Tata. *Weak Scale Supersymmetry*, pages 14–16. Cambridge University Press, New York, 2006.
- [29] M.E. Peskin & D.V. Schroeder. *An Introduction to Quantum Field Theory*, pages 795–796. Westview, Boulder, CO, 1995.
- [30] S. Dawson. Susy and such. *NATO Adv. Study Inst. Ser. B Phys.*, 365:33–80, 1997.
- [31] I. Aitchison. *Supersymmetry in Particle Physics: An Elementary Introduction*, pages 4–10, 165–166. Cambridge Univ. Press, Cambridge, 2007.
- [32] I. Aitchison. *Supersymmetry in Particle Physics: An Elementary Introduction*, page 135. Cambridge Univ. Press, Cambridge, 2007.
- [33] H. Baer & X. Tata. *Weak Scale Supersymmetry*, pages 463–464. Cambridge University Press, New York, 2006.
- [34] A.D. Sakharov. Violation of CP invariance, C asymmetry, and baryon asymmetry of the universe. *Sov. Phys. Usp*, 34(5):392–393, May 1991.
- [35] A. Riotto & M. Trodden. Recent progress in baryogenesis. *Annu. Rev. Nucl. Part. S.*, 49(hep-ph/9901362):35–75, Jan 1999.
- [36] J. Ellis. Searching for particle physics beyond the standard model at the LHC and elsewhere. Technical Report arXiv:1102.5009, CERN, Feb 2011.
- [37] T.K. Hemmick. *A search for anomalously heavy isotopes of low Z nuclei*. PhD thesis, University of Rochester, Rochester, NY, 1988. Presented on Oct 1988.
- [38] F. Zwicky. Die rotverschiebung von extragalaktischen nebeln. *Helvetica Physica Acta*, 6:110–127, 1933.
- [39] F. Zwicky. On the masses of nebulae and of clusters of nebulae. *Astrophys. J.*, 86(3):217–246, Oct 1937.
- [40] B.W. Carroll, D.A. Ostlie, & A. Black. *An Introduction to Modern Galactic Astrophysics and Cosmology*, page 452. Addison-Wesley, San Francisco, CA, second edition, 2007.

- [41] V.C. Rubin, W.K. Ford, & N. Thonnard. Rotation properties of 21 sc galaxies with a large range of luminosities and radii from NGC 4605 ($r = 4$ kpc) to UGC 2885 ($r = 122$ kpc). *Astrophys. J.*, 238:471–487, Jun 1980.
- [42] D. Clowe *et al.* A direct empirical proof of the existence of dark matter. *Astrophys. J. Lett.*, 648(2):109–113, Aug 2006.
- [43] B.D. Sherwin *et al.* Evidence for dark energy from the cosmic microwave background alone using the atacam cosmology telescope lensing measurements. *Phys. Rev. Lett.*, 107(2):021302, Jul 2011.
- [44] H. Baer & X. Tata. *Weak Scale Supersymmetry*, page 130. Cambridge University Press, New York, 2006.
- [45] I. Aitchison. *Supersymmetry in Particle Physics: An Elementary Introduction*, page 49. Cambridge Univ. Press, Cambridge, 2007.
- [46] H. Baer & X. Tata. *Weak Scale Supersymmetry*, pages 134–138. Cambridge University Press, New York, 2006.
- [47] H.E. Haber. The status of the minimal supersymmetric standard model and beyond. *Nucl. Phys. B, Proc. Suppl.*, 62(hep-ph/9709450):469–484, Sep 1997.
- [48] H. Baer & X. Tata. *Weak Scale Supersymmetry*, pages 199–204. Cambridge University Press, New York, 2006.
- [49] C. Kolda. Gauge-mediated supersymmetry breaking: Introduction, review and update. *Nucl. Phys. Suppl.*, 62:266–275, 1997.
- [50] H. Baer & X. Tata. *Weak Scale Supersymmetry*, pages 264–272. Cambridge University Press, New York, 2006.
- [51] H. Baer & X. Tata. *Weak Scale Supersymmetry*, pages 285–286. Cambridge University Press, New York, 2006.
- [52] G.F. Giudice & R. Rattazzi. Theories with gauge-mediated supersymmetry breaking. *Phys. Rept.*, 322(CERN-TH/97-380):419–499, Jan 1998.
- [53] M. Drees, R. Godbole, & P. Roy. *Theory and Phenomenology of Sparticles: an Account of Four-Dimensional $N=1$ Supersymmetry in High-Energy Physics*, pages 323–325. World Scientific, Singapore, 2004.

- [54] L.M. Carpenter. Surveying the phenomenology of general gauge mediation. arXiv:0812.2051v1 [hep-ph].
- [55] H. Baer & X. Tata. *Weak Scale Supersymmetry*, pages 289–290. Cambridge University Press, New York, 2006.
- [56] M. Drees, R. Godbole, & P. Roy. *Theory and Phenomenology of Sparticles: an Account of Four-Dimensional $N=1$ Supersymmetry in High-Energy Physics*, pages 202–206. World Scientific, Singapore, 2004.
- [57] H. Baer & X. Tata. *Weak Scale Supersymmetry*, page 111. Cambridge University Press, New York, 2006.
- [58] M. Drees, R. Godbole, & P. Roy. *Theory and Phenomenology of Sparticles: an Account of Four-Dimensional $N=1$ Supersymmetry in High-Energy Physics*, pages 326–327. World Scientific, Singapore, 2004.
- [59] P. Meade, N. Sieberg, D. Shih. General gauge mediation. *Prog. Theor. Phys Suppl.*, 177:143–158, 2009.
- [60] M. Buican et al. Exploring general gauge mediation. *JHEP*, 16:0903, 2009.
- [61] Y. Kats et al. The status of GMSB after 1/fb at the LHC. arXiv:1110.6444v2 [hep-ph], Nov 2011.
- [62] P. Meade, M. Reece, and D. Shih. Prompt decays of general neutralino NLSPs at the Tevatron. arXiv:0911.4130v2 [hep-ph].
- [63] G. Lucas et al. Star Wars, Episode VI: Return of the Jedi. film, May 1983. Lucasfilm.
- [64] K. Schindl. The injector chain for the LHC. In *9th LEP-SPS Performance Workshop*, pages 47–52, Mar 1999.
- [65] M. Benedikt *et al.* Performance of the LHC pre-injectors. Technical Report CERN-PS-2001-011-DR, CERN, Geneva, Apr 2001.
- [66] P. Belochitskii *et al.* LEIR commissioning. In *10th European Particle Accelerator Conference*, pages 1876–1880, Edinburgh, UK, Jul 2006.
- [67] S. Myers. LHC commissioning and first operation. In *1st International Particle Accelerator Conference*, pages 1–6, Kyoto, Japan, Jun 2010.
- [68] L. Evans & P. Bryant. LHC Machine. *JINST*, 3(1):1–5, 2008.

- [69] F. Herbert. *Dune*. Chilton Books, 1965.
- [70] G. Aad *et al.* *Expected performance of the ATLAS experiment: detector, trigger and physics*, pages 17–38,162–183. CERN, Geneva, 2009. CERN-OPEN-2008-020.
- [71] G. Aad *et al.* The ATLAS experiment at the CERN large hadron collider. *JINST*, 3(3):19–320, 2008.
- [72] G. Aad *et al.* Alignment of the ATLAS inner detector tracking system with 2010 LHC proton-proton collisions at $\sqrt{s} = 7$ TeV. Technical Report ATLAS-CONF-2011-012, CERN, Geneva, Mar 2011.
- [73] G. Alimonti *et al.* A study of charge trapping in irradiated silicon with test beam data. Technical Report ATL-INDET-2003-014, CERN, Geneva, Aug 2003.
- [74] F. Huegging. The ATLAS pixel insertable B-layer (IBL). Technical Report ATL-INDET-PROC-2010-034, CERN, Geneva, Oct 2010.
- [75] M. Capeans *et al.* ATLAS insertable B-layer technical design report. Technical Report ATLAS-TDR-019, CERN, Geneva, Sep 2010.
- [76] P. Vankov. ATLAS silicon microstrip tracker operation and performance. Technical Report ATL-INDET-PROC-2010-041, CERN, Geneva, Nov 2010.
- [77] M. Brice. Dplacement du sub-detector silicon tracker de l’exprience ATLAS dans l’axe du barrel silicon tracker. Photo album, Sep 2005.
- [78] R. Mashinistov. Performance of the ATLAS Transition Radiation Tracker with cosmic rays and first high energy collisions at LHC. Technical Report ATL-INDET-PROC-2010-043, CERN, Geneva, Dec 2010.
- [79] G. Aad *et al.* Calibration of the ATLAS Transition Radiation Tracker. Technical Report ATLAS-CONF-2011-006, CERN, Geneva, Feb 2011.
- [80] M. Aharrouche. The ATLAS liquid argon calorimeter: Construction, integration, commissioning and combined test beam results. In *Nucl. Instrum. Meth. A*, volume 581, pages 373–376, February 2007.
- [81] P. Krieger. The ATLAS liquid argon calorimeter. In *IEEE NSS/MIC*, pages 1029–1033, October 2005.

- [82] G. Aad *et al.* Construction of the ATLAS hadronic end-cap pre-prototype module. Photo Album, Nov 1996.
- [83] J.P. Archambault *et al.* Energy calibration of the ATLAS liquid argon forward calorimeter. *JINST*, 3(P02002):1–31, February 2008.
- [84] B. Trocmé. The ATLAS liquid argon calorimeter: Commissioning with cosmic muons and first LHC beams. In *11th Topical Seminar on Innovative Particle and Radiation Detectors*, number ATL-COM-LARG-2008-011, page 4, Sienna, Italy, Nov 2008.
- [85] G. Aad *et al.* Liquid argon calorimeter technical design report. Technical report, CERN, December 1996.
- [86] S. Majewski. Electronic readout of the ATLAS liquid argon calorimeter: Calibration and performance. In *17th IEEE NPSS Real Time Conference*, pages 1–4, Lisbon, Portugal, Jun 2010.
- [87] I. Koletsou. The ATLAS liquid argon calorimeter at the LHC. Technical Report ATL-LARG-PROC-2010-001, CERN, Geneva, Mar 2010.
- [88] K. Copic. LAr: 2009 status and plans. ATLAS Week February 2009, February 2009. Internal Pres. 4 pages.
- [89] A. Bazan *et al.* Atlas liquid argon calorimeter back end electronics. *JINST*, 2(P06002):3–12, June 2007.
- [90] C. Collard. Electronic calibration of the ATLAS lar calorimeter. In *1st International Conference on Technology and Instrumentation in Particle Physics*, pages 246–238, Tsukuba, Japan, April 2009.
- [91] T. Zenis. Tile calorimeter at work in the collision era. Technical Report ATL-TILECAL-PROC-2010-007, CERN, Geneva, Jul 2010.
- [92] V. Rossetti. Commissioning of the ATLAS tile hadronic calorimeter with cosmic muons, single beams and first collisions. In *14th International Conference on Calorimetry in High Energy Physics*, pages 1–6, Beijing, China, Aug 2010.
- [93] R. Alves *et al.* The distribution of laser light for the calibration and monitoring system of the ATLAS hadronic calorimeter. In *IEEE Medical Imaging Conference 1999*, pages 230–232, Seattle, WA, Oct 1999.

- [94] J. Wotschack. Atlas muon chamber construction parameters for CSC, MDT, and RPC chambers. Technical Report ATL-MUON-PUB-2008-006, CERN, Geneva, Apr 2008.
- [95] G. Aad *et al.* Monitored drift tubes chambers for muon spectroscopy in ATLAS. Technical Report ATL-MUON-94-044, CERN, Geneva, Jun 1994.
- [96] G. Aad *et al.* *ATLAS muon spectrometer: Technical Design Report*. Technical Design Report ATLAS. CERN, Geneva, 1997. distribution.
- [97] J. Ying *et al.* Study of an avalanche-mode resistive plate chamber. *J. Phys. G: Nucl. Part. Phys.*, 26(1291-1298), 2000.
- [98] A. Aloisio *et al.* The muon spectrometer barrel level-1 trigger of the ATLAS experiment at LHC. Technical Report ATL-DAQ-CONF-2006-014, CERN, Geneva, May 2006.
- [99] J. Shank. The ATLAS detector: Status and results from cosmic rays. Technical Report ATL-GEN-PROC-2009-013, CERN, Geneva, Oct 2009.
- [100] T. Hayakawa. Detailed performance study of ATLAS end-cap muon trigger with beam collision. Technical Report ATL-DAQ-PROC-2010-035, CERN, Geneva, Oct 2010.
- [101] H. Pernegger. First test results of a high-speed beam conditions monitor for the ATLAS experiment. In *51st Nuclear Science Symposium and Medical Imaging Conference*, pages 2248–2257, Rome, Italy, Oct 2004.
- [102] G. Aad *et al.* Performance of the minimum bias trigger in p-p collisions at $\sqrt{s} = 900$ GeV. Technical Report ATLAS-CONF-2010-025, CERN, Geneva, Jul 2010.
- [103] M. Villa. The luminosity monitor of the ATLAS experiment. Technical Report ATL-LUM-PROC-2009-004, CERN, Geneva, Nov 2009.
- [104] P. Jenni, M. Nessi, & M. Nordberg. Zero degree calorimeters for atlas. Technical Report LHCC-I-016. CERN-LHCC-2007-001, CERN, Geneva, Jan 2007.
- [105] P. Jenni *et al.* ATLAS forward detectors for measurement of elastic scattering and luminosity. Technical report, CERN, Geneva, 2008.

- [106] D.Dobos & H. Pernegger. Diamond pixel modules and the ATLAS beam conditions monitor. Technical Report ATL-INDET-PROC-2010-007, CERN, Geneva, Mar 2010.
- [107] A.G. Brandt. Atlas forward detectors. Technical Report ATL-LUM-PROC-2010-003, CERN, Geneva, Jul 2010.
- [108] R.E. Kwee. Minimum bias trigger in ATLAS. Technical Report ATL-DAQ-PROC-2010-055, CERN, Geneva, Dec 2010.
- [109] J.D. Jackson. *Classical Electrodynamics*. Wiley, third edition, 1999.
- [110] P. Miele & H.H.J. ten Kate. The superconducting magnet system for the ATLAS detector at CERN. *Fusion Eng. Des.*, 58-59(CERN-OPEN-2001-064):195–203, Jun 2001.
- [111] ATLAS Collaborator. ATLAS magnet system: Technical design report, 1. Technical Report ATLAS-TDR-006, CERN, Geneva, 1997.
- [112] R. Ruber *et al.* Ultimate performance of the ATLAS superconducting solenoid. *IEEE Trans. Appl. Supercond.*, 17:2, 2007.
- [113] P. Védérine *et al.* Manufacturing and integration progress of the ATLAS barrel toroid magnet at cern. *IEEE Trans. Appl. Supercond.*, 14(2):491–494. 4 p, 2004.
- [114] E. Dobson. Performance of the ATLAS trigger and data acquisition system. slides, Jul 2011.
- [115] C. Haeberli *et al.* The ATLAS-TDAQ DataCollection software. Technical Report ATL-DAQ-2004-003, CERN, Geneva, May 2003.
- [116] G. Aad et al. Performance of the ATLAS trigger system in 2010. *Eur. Phys. J. C*, 72:1849, Oct 2011.
- [117] N. Stephenson. *Anathem*. William Morrow and Company, 2008.
- [118] P. Waller. ATLAS data quality monitoring: Experience with first collision data. Technical Report ATL-DAPR-PROC-2010-001, CERN, Geneva, Nov 2010.
- [119] J.A. Frost. Commissioning of ATLAS data quality infrastructure with first collision data. Technical Report ATL-SOFT-PROC-2011-005, CERN, Geneva, Jan 2011.

- [120] R.A. Heinlein. *Time Enough for Love*. G.P Putnam's Sons, 1973.
- [121] ATLAS collaboration. First tuning of herwig/jimmy to atlas data. ATL-PHYS-PUB-2010-014, 2010.
- [122] S. Agostinelli *et al.* GEANT4: A simulation toolkit. *Nucl. Instrum. Meth.*, A506:250–303, 2003.
- [123] T. Sjostrand, S. Mrenna, & P. Skands. PYTHIA 6.4 physics and manual. *JHEP*, 05:026, 2006.
- [124] G. Corcella *et al.* HERWIG 6: An event generator for hadron emission reactions with interfering gluons (including supersymmetric processes). *JHEP*, 01(010):1–93, 2001.
- [125] J.M. Campbell & R.K. Ellis. Update on vector boson pair production at hadron colliders. *Phys. Rev.*, D60:113006, Nov 1999.
- [126] J. Butterworth *et al.* Single boson and diboson production cross sections in pp collisions at $\sqrt{s} = 7$ TeV. Technical Report ATL-COM-PHYS-2010-695, CERN, Geneva, Aug 2010.
- [127] J. Alwall *et al.* Madgraph/madevent, 2007.
- [128] A. Lazopoulos *et al.* Next-to-leading order QCD corrections to $t\bar{t}z$ production at the LHC. *Phys. Lett.*, B(666):62–65, 2008.
- [129] S. Frixione and B.R. Webber. The MC@NLO 3.2 event generator, hep-ph/0601192, 2006.
- [130] S. Moch & P. Uwer. Theoretical status and prospects for top-quark pair production at hadron colliders. *Phys. Rev.*, D(78):034003, 2008.
- [131] J. Forshaw J. Butterworth and M. Seymour. Multiparton interactions in photoproduction at hera. *Z. Phys.*, C72:637–646, 1996.
- [132] M. Mangano *et al.* Alpgen, a generator for hard multiparton processes in hadronic collisions. *JHEP*, 07(001):1–35, 2003.
- [133] P. Nadolski *et al.* Implications of CTEQ global analysis for collider observables. *Phys. Rev.*, D(78):013004, 2008.
- [134] J. Pumplin *et al.* New generation of parton distributions with uncertainties from global QCD analysis. *JHEP*, 0207:012, 2002.

- [135] A. Sherstnev and R. S. Thorne. Parton distributions for LO generators. *Eur. Phys. J.*, C55:553–575, 2008.
- [136] A. Djouadi, J.-L. Kneur, & G. Moultaka. Suspect: a fortran code for the supersymmetric and higgs particle spectrum in the mssm. *Compute. Phys. Comm.*, 176:426–455, 2007.
- [137] M. Muhlleitner, A. Djouadi, & Y. Mambrini. Sdecay: A fortran code for the decays of the supersymmetric particles in the mssm. *Compute. Phys. Comm.*, 168:46–70, 2005.
- [138] W. Beenakker, R. Hopker, & M. Spira. Prospino: A program for the production of supersymmetric particles in next-to-leading order qcd, Nov 1996.
- [139] W. Beenakker et al. *Nucl.Phys.B*, 492:51–103, 1997.
- [140] W. Beenakker et al. *Phys.Rev.Lett.*, 83:3780–3783, 1999.
- [141] W. Beenakker et al. Squark and gluino hadroproduction. *Int. J. Mod. Phys*, A26:2637–2664, 2011.
- [142] L. Niven. *Niven’s Laws*. Owlswick Press, 1984.
- [143] G. Aad *et al.* Expected electron performance in the ATLAS experiment. Technical Report ATL-PHYS-PUB-2011-006, CERN, Geneva, Apr 2011.
- [144] G. Aad *et al.* Electron performance measurements with the ATLAS detector using the 2010 LHC proton-proton collision data. Technical Report CERN-PH-EP-2011-117, CERN, Geneva, Oct 2011.
- [145] A. Ahmad *et al.* Measurement of the cross-section for jets produced in association with a w-boson in pp collisions at $\sqrt{s} = 7$ TeV. Technical Report ATL-COM-PHYS-2010-756, CERN, Geneva, Sep 2010.
- [146] F. Cerutti *et al.* Muon momentum resolution in first pass reconstruction of pp collision data recorded by ATLAS in 2010. Technical Report ATLAS-COM-CONF-2011-003, CERN, Geneva, Jan 2011.
- [147] G. Aad et al. Search for supersymmetry in final states with jets, missing transverse momentum and one isolated lepton in $\sqrt{s} = 7$ tev pp collisions using 1 fb⁻¹ of atlas data. Technical Report CERN-PH-EP-2011-153, CERN, Geneva, Sep 2011.

- [148] M. Cacciari, G.P. Salam, & G. Soyez. The anti- k_t jet clustering algorithm. *JHEP*, 04(063):1–15, 2008.
- [149] W. Lampl *et al.* Calorimeter clustering algorithms: Description and performance. Technical Report ATL-LARG-PUB-2008-002, CERN, Geneva, Apr 2008.
- [150] G. Aad *et al.* Jet energy scale and its systematic uncertainty in proton-proton collisions at $\sqrt{s}=7$ tev in ATLAS 2010 data. Technical Report ATLAS-CONF-2011-032, CERN, Geneva, Mar 2011.
- [151] ATLAS Collaboration. Commissioning of the ATLAS high-performance b-tagging algorithms in the 7 TeV collision data. Technical Report ATLAS-CONF-2011-102, CERN, Geneva, Jul 2011.
- [152] G. Aad *et al.* Performance of the missing transverse energy reconstruction and calibration in proton-proton collisions at a center-of-mass energy of 7 tev with the ATLAS detector. Technical Report ATLAS-CONF-2010-057, CERN, Geneva, Jul 2010.
- [153] Measurement of missing tranverse energy. Technical Report ATL-PHYS-PUB-2009-016; ATL-COM-PHYS-2009-118, CERN, Geneva, Mar 2009.
- [154] G. Aad *et al.* Electron and photon reconstruction and identification in ATLAS: expected performance at high energy and results at 900 GeV. Technical Report ATLAS-CONF-2010-005, CERN, Geneva, Jun 2010.
- [155] G. Aad *et al.* Performance of missing transverse momentum reconstruction in proton-proton collisions at $\sqrt{s} = 7$ tev with atlas. *Eur. Phys. J. C*, 72(DOI 10.1140/epjc/s10052-011-1844-6):1844–1879, 2012.
- [156] G. Piacquadio, K. Prokofiev & A. Wildauer. Primary vertex reconstruction in the ATLAS Experiment at LHC. *J. Physics: Conf. Series (CHEP07)*, 119(032033):1–8, 2008.
- [157] M. Baak, M. Petteni, & N. Makovec. Data-quality requirements and event cleaning for jets and missing transverse energy reconstruction with the atlas detector in proton-proton collisions at a center-of-mass energy of $\sqrt{s} = 7$ tev. Technical Report ATLAS-COM-CONF-2010-038, CERN, Geneva, May 2010.
- [158] Susy searches at ATLAS in multilepton final states with jets and missing transverse energy. Technical Report ATLAS-CONF-2011-039, CERN, Geneva, Mar 2011.

- [159] ATLAS Collaboration. Search for supersymmetry in events with three leptons and missing transverse momentum in $\sqrt{s} = 7$ TeV pp collisions with the ATLAS detector. Technical Report ATLAS-CONF-2012-023, CERN, Geneva, Mar 2012.
- [160] ATLAS Collaboration. Measurement of the top quark-pair production cross section with ATLAS in pp collisions at $\sqrt{s} = 7$ TeV. *Eur. Phys. J.*, C71:1577, 2011.
- [161] ATLAS Collaboration. Search for supersymmetry in events with three leptons and missing transverse momentum in 7 TeV *pp* collisions with the ATLAS detector. Technical Report ATL-COM-PHYS-2012-091, CERN, Geneva, Jan 2012.
- [162] G. Aad *et al.* Jet energy measurement with the ATLAS detector in proton-proton collisions at $\sqrt{s} = 7$ tev. Technical Report CERN-PH-EP-2011-191, CERN, Geneva, Dec 2011. submitted to *Eur. Phys. J. C*.
- [163] G. Aad *et al.* Jet energy resolution and selection efficiency relative to track jets from in-situ techniques with the ATLAS detector using proton-proton collisions at a center of mass energy $\sqrt{s} = 7$ tev. Technical Report ATLAS-CONF-2010-054, CERN, Geneva, Jul 2010.
- [164] G. Aad *et al.* Reconstruction and calibration of missing transverse energy and performance in Z and W events in ATLAS proton-proton collisions at 7 tev. Technical Report ATLAS-CONF-2011-080, CERN, Geneva, Jun 2011.
- [165] A. Lazopoulos et al. Next-to-leading order QCD corrections to $t\bar{t}z$ production at the LHC. *Phys. Lett. B.*, 666:62–65, 2008.
- [166] Search for gluinos in events with two same-sign leptons, jets and missing transverse momentum with the ATLAS detector in *pp* collisions at $\sqrt{s} = 7$ TeV. Technical Report ATLAS-CONF-2012-004, CERN, Geneva, Feb 2012.
- [167] E. Torrence. Preliminary 2011 lumi uncertainty. Email on behalf of ATLAS Luminosity Working Group, Nov 2011.
- [168] M. Botje et al. The PDF4LHC working group interim recommendations. arXiv:1101.0538 [hep-ph], Jan 2011.
- [169] A.D. Martin et al. Parton distributions for the LHC. *Eur. Phys. J.*, C63:189–285, 2009.

- [170] A.D. Martin et al. Uncertainties on α_S in global PDF analyses and implications for predicted hadronic cross sections. *Eur. Phys. J.*, C64:653–680.
- [171] M. Brooks et al. Spaceballs. film, June 1987. Brooksfilm.
- [172] A.L. Read. Modified frequentist analysis of search results (the CL_S method). Technical Report CERN-OPEN-2000-205, CERN, Aug 2000.
- [173] M. Baak et. al. Setting exclusion limits in atlas supersymmetry searches with a likelihood ratio based method. Technical report, CERN, Feb 2011.
- [174] G. Cowan et. al. Asymptotic formulae for likelihood-based tests of new physics. *Eur. Phys. J.*, C71:1554, 2011.
- [175] T. Junk. Confidence level computation for combining searches with small statistics. *Nucl. Instrum. Methods Phys. Res. A*, 434(2-3):435–443, 1999.
- [176] Search for physics beyond the Standard Model in events with a z boson and large missing transverse momentum with the ATLAS detector. Technical Report ATLAS-CONF-2012-047, CERN, Geneva, Apr 2012.
- [177] C. Kettering. Thoughts on the business of life. *Forbes*, 62(34), 1948.
- [178] P.K. Dick. *The Transmigration of Timothy Archer*. Timescape Books, 1982.
- [179] Z. Maxa. Event visualization for the ATLAS experiment - the technologies involved. In S. Banerjee, editor, *CHEP06*, pages 167–169, February 2006.
- [180] D. Shepard. A two-dimensional interpolation function for irregularly-spaced data. In *Proceedings of the 1968 23rd ACM national conference*, pages 517–524, New York, NY, USA, 1968.
- [181] B. Resende. Muon identification algorithms in ATLAS. Technical Report ATL-PHYS-PROC-2009-113, CERN, Geneva, Sep 2009.
- [182] G. Aad *et al.* *ATLAS detector and physics performance: Technical Design Report, 1*. Technical Design Report ATLAS. CERN, Geneva, 1999.
- [183] M. Schott, G. Duckeck, & M. Obermaier. Study of the sagitta resolution of mdt-chambers. Technical Report ATL-MUON-PUB-2006-010, CERN, Geneva, Mar 2006.

- [184] O. Kortner *et al.* New methods for the alignment of the ATLAS muon spectrometer. In *Nuclear Science Symposium Conference Record*, volume 1, pages 666–668, Nov 2007.
- [185] P. Bagnaia *et al.* Calibration model for the MDT chambers of the ATLAS muon spectrometer. Technical Report ATL-MUON-PUB-2008-004, CERN, Geneva, Feb 2008.
- [186] S.D. Ellis and D.E. Soper. Successive combination jet algorithm for hadron collisions. *Phys. Rev.*, D48:3160–3166, May 1993.
- [187] K.S. Grogg. *Jets produced in association with W-bosons in CMS at the LHC*. PhD thesis, University of Wisconsin - Madison, Madison, 2011. Presented 20 Jul 2011.

A

Displays of Selected Events

Event displays for events of particular note are presented here. The events chosen are those that stand out due to high values of lepton p_T , jet p_T , E_T^{miss} , or $m_{\ell+\ell-,\ell'\pm}$. Leptons in the event displays are indexed by the order of lepton p_T so as to facilitate matching to table of data events. These event displays were produced using ATLANTIS-09-15-51 [179].

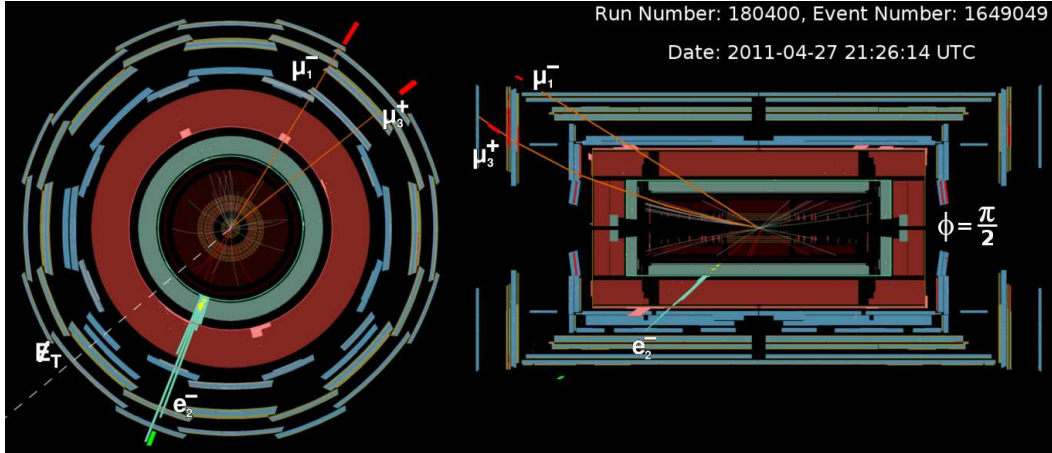


Figure A.1: Event display for Event 1649049 from run 180400. The indices are indicative of lepton p_T order. This event is notable for having two leading muons with $p_T > 100$ GeV, 112.7 GeV and 103.6 GeV.

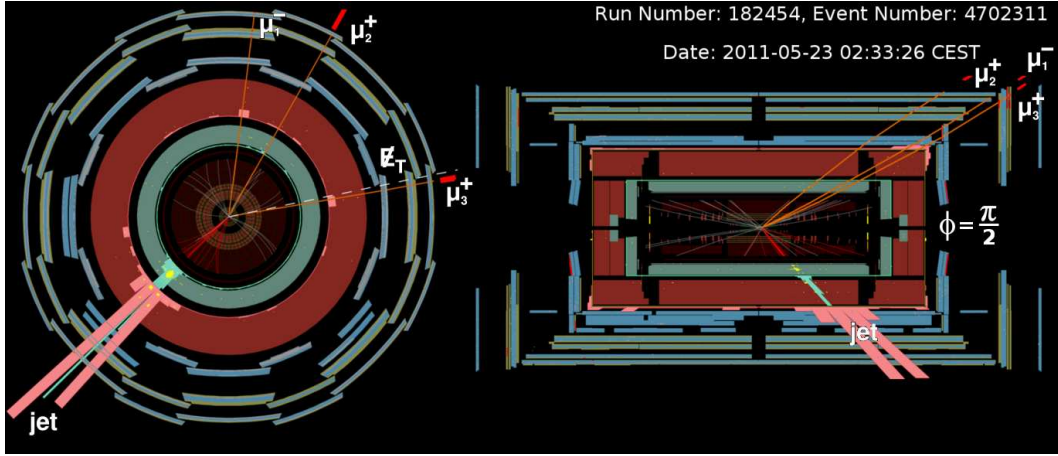


Figure A.2: Event display for Event 4702311 from run 182454. The indices are indicative of lepton p_T order. This event is notable for having muons with $p_T = 109.2$ GeV and 100.5 GeV and a jet with $p_T = 315.3$ GeV, as well as $E_T^{\text{miss}} = 113.8$ GeV.

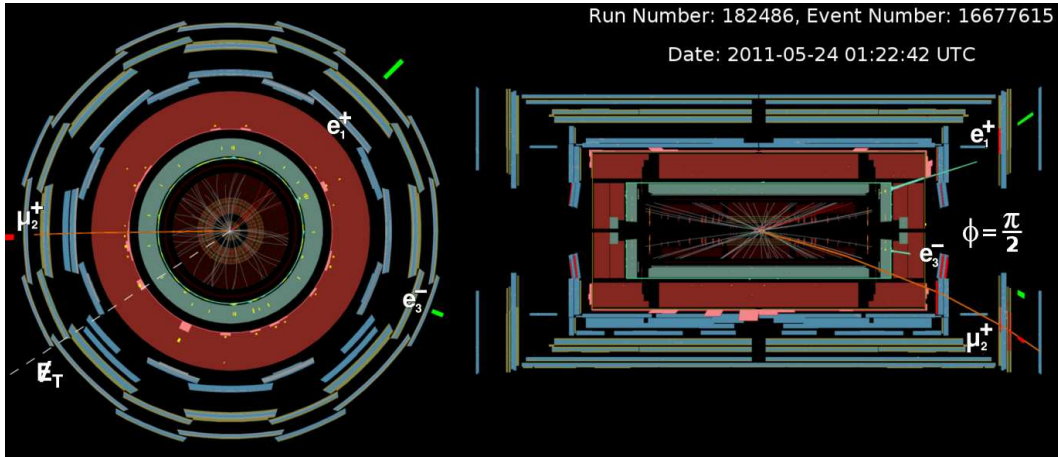


Figure A.3: Event display for Event 16677615 from run 182486. The indices are indicative of lepton p_T order. This event is notable for a $p_T = 107.2$ GeV lead-electron and a high transverse mass, $m_T = 200.6$ GeV.

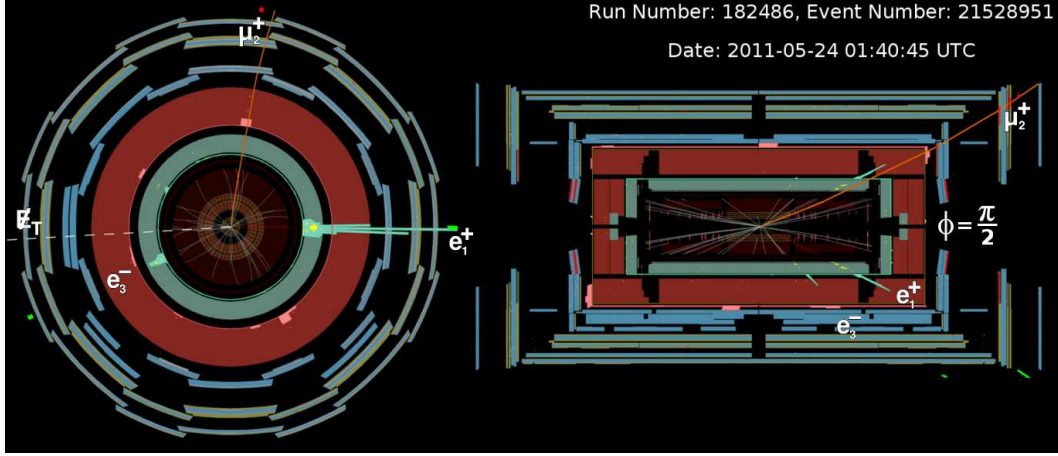


Figure A.4: Event display for Event 21528951 from run 182486. The indices are indicative of lepton p_T order. This event is notable for a high- p_T lead-electron, $p_T = 120.8$ GeV, and a high transverse mass, $m_T = 202.1$ GeV.

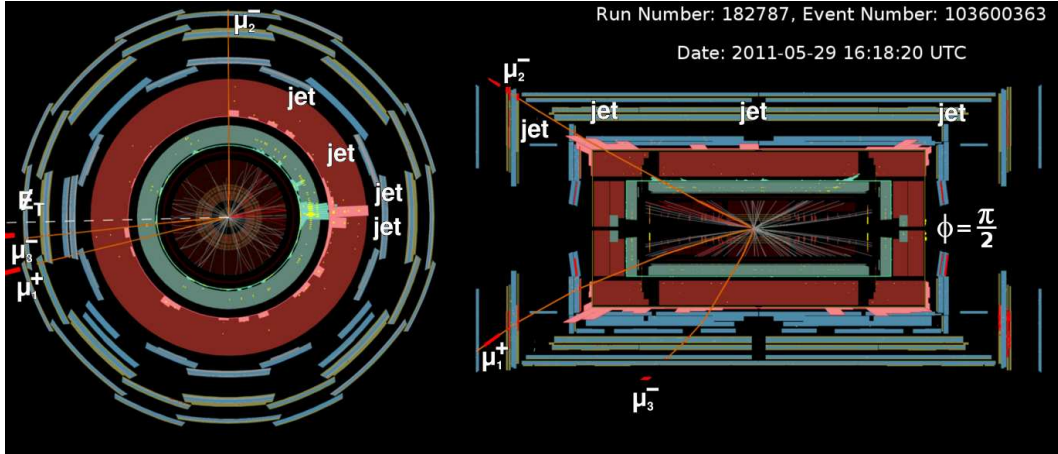


Figure A.5: Event display for Event 103600363 from run 182787. The indices are indicative of lepton p_T order. Notable features of this event are the $p_T = 104.2$ GeV muon, as well as the large E_T^{miss} value of 133.5 GeV. This event also has a relatively high jet multiplicity, with four jets.

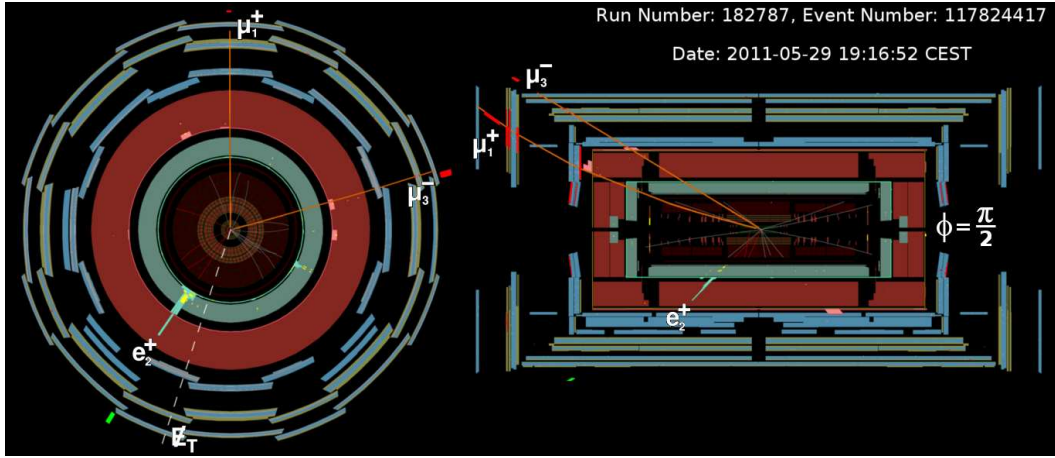


Figure A.6: Event display for Event 117824417 from run 182787. The indices are indicative of lepton p_T order. This event is notable for the $p_T = 122.1$ GeV muon and $E_T^{\text{miss}} = 103.2$ GeV.

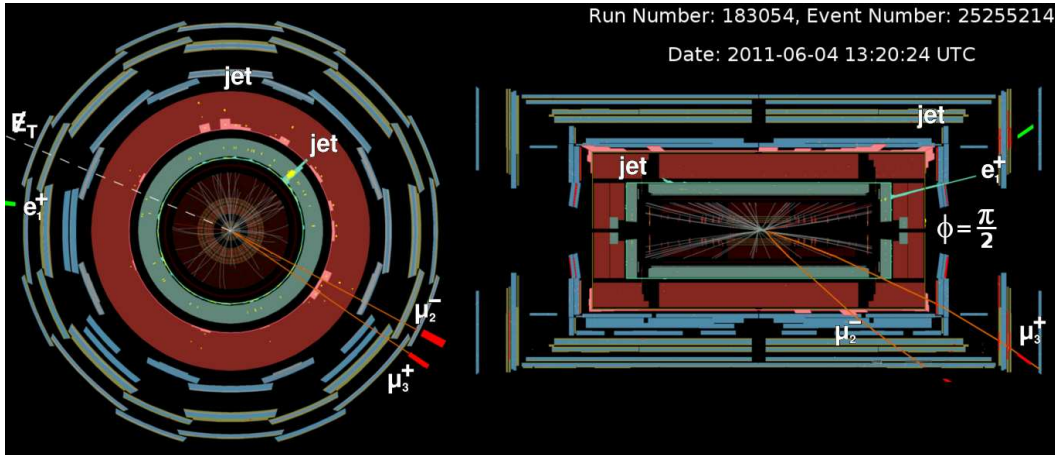


Figure A.7: Event display for Event 25255214 from run 183054. The indices are indicative of lepton p_T order. The $p_T = 128.6$ GeV electron and $p_T = 104.6$ GeV muon make this event notable. Additionally, it has a trilepton invariant mass of 358.6 GeV.

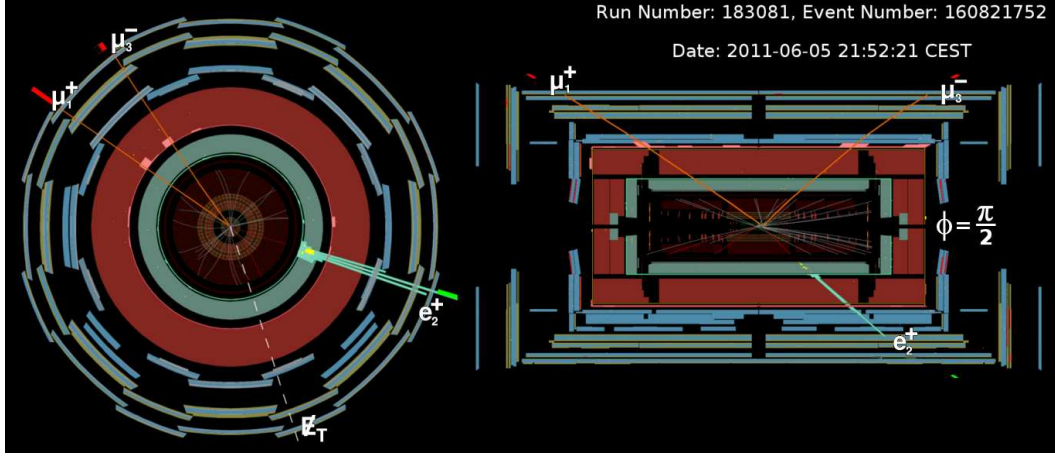


Figure A.8: Event display for Event 160821752 from run 183081. The indices are indicative of lepton p_T order. This event is notable for featuring a $p_T = 179.2$ GeV muon, a $p_T = 128.6$ GeV electron, and a tripleton mass of 397.5 GeV.

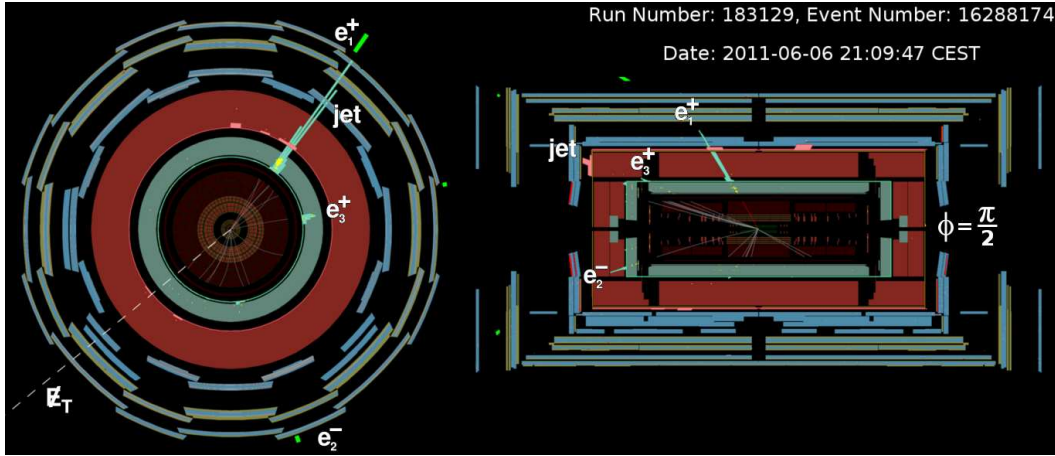


Figure A.9: Event display for Event 16288174 from run 183129. The indices are indicative of lepton p_T order. This event has 124.9 GeV of E_T^{miss} .

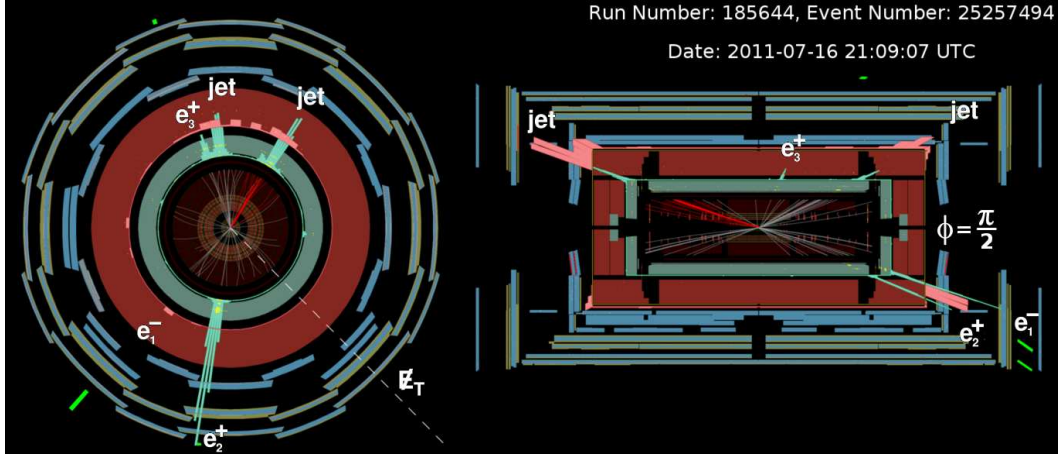


Figure A.12: Event display for Event 25257494 from run 185644. The indices are indicative of lepton p_T order. This event has a sizable amount of E_T^{miss} , 146.7 GeV, and leading electrons with $p_T = 139.9$ and 124.8 GeV.

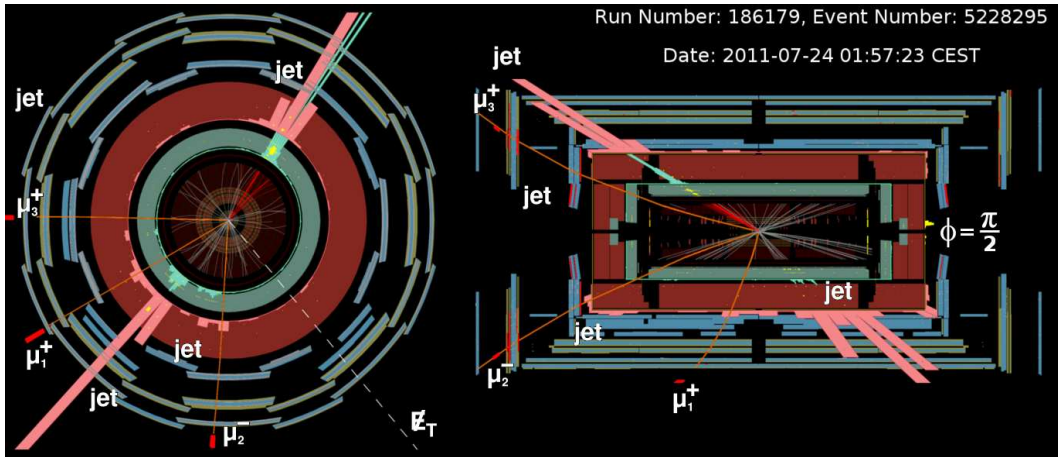


Figure A.13: Event display for Event 5228295 from run 186179. The indices are indicative of lepton p_T order. This event is notable for having a jet with $p_T = 441.4$ GeV, on top of a relatively large jet multiplicity.

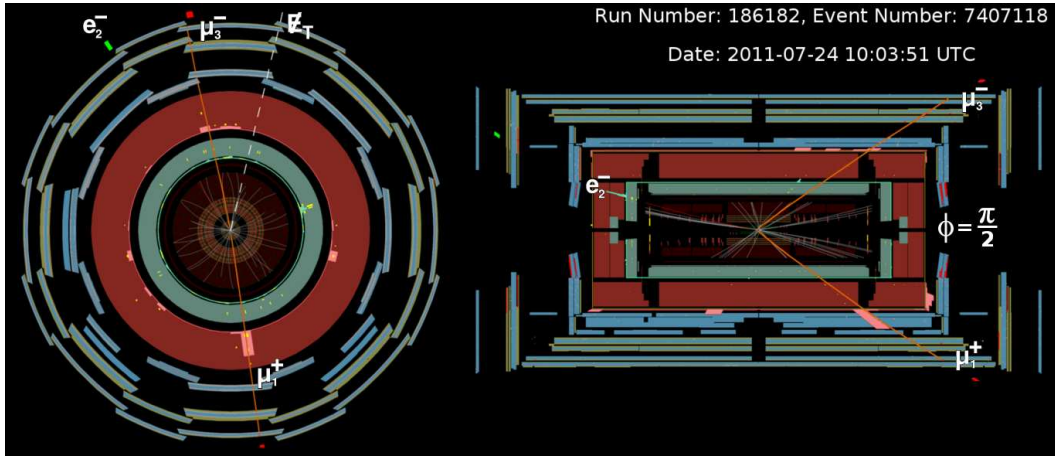


Figure A.14: Event display for Event 7407118 from run 186182. The indices are indicative of lepton p_T order. This event is notable for having a $p_T = 140.6$ GeV muon and a trilepton mass of 280.1 GeV.

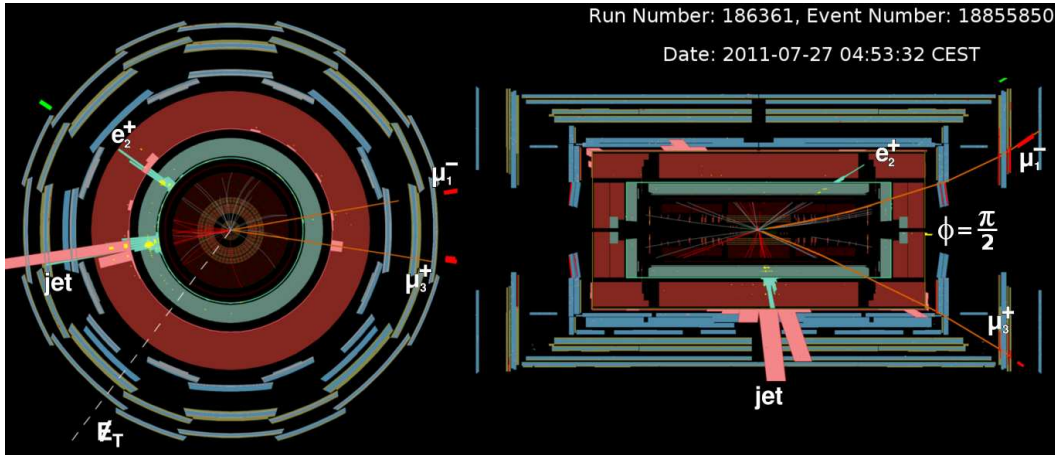


Figure A.15: Event display for Event 18855850 from run 186361. The indices are indicative of lepton p_T order. This event is remarkable by virtue of including a $p_T = 346.4$ GeV muon and having a trilepton mass of 305.0 GeV.

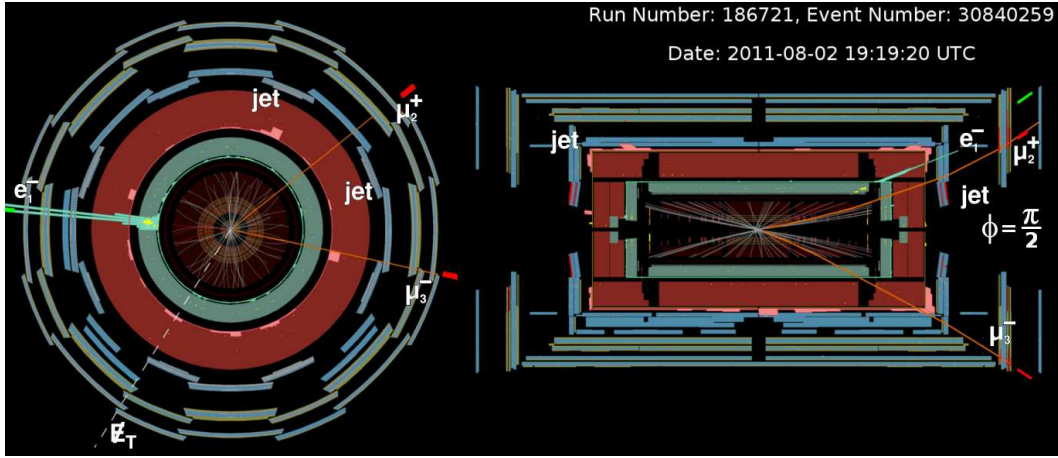


Figure A.16: Event display for Event 30840259 from run 186721. The indices are indicative of lepton p_T order. This event is notable for having a $p_T = 128.1$ GeV electron and a $p_T = 108.1$ GeV muon. It also has a 304.8 GeV tripletonic mass and 125.3 GeV of E_T^{miss} .

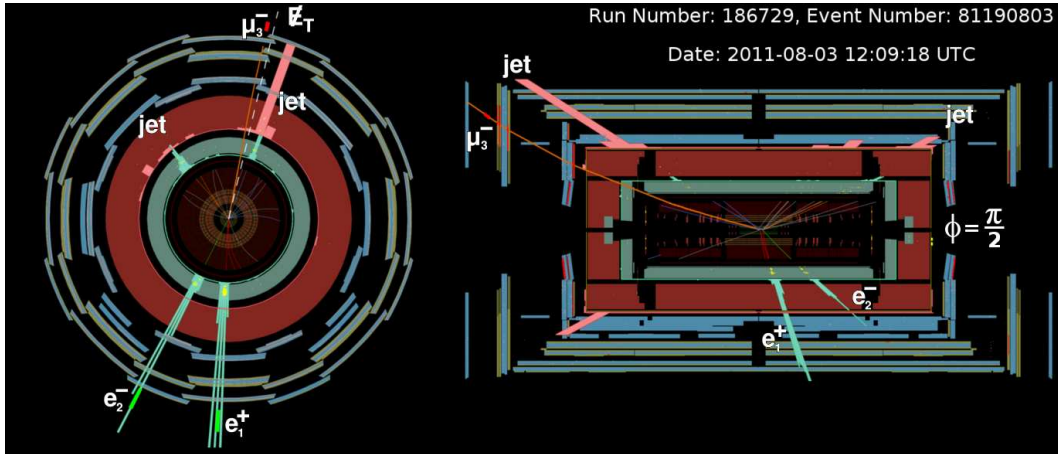


Figure A.17: Event display for Event 81190803 from run 186729. The indices are indicative of lepton p_T order. This event is notable for its $p_T = 213.4$ GeV lead electron and $E_T^{\text{miss}} = 154.0$ GeV. It also has $m_{\ell^+\ell^-, \ell^\pm} = 329.5$ GeV.

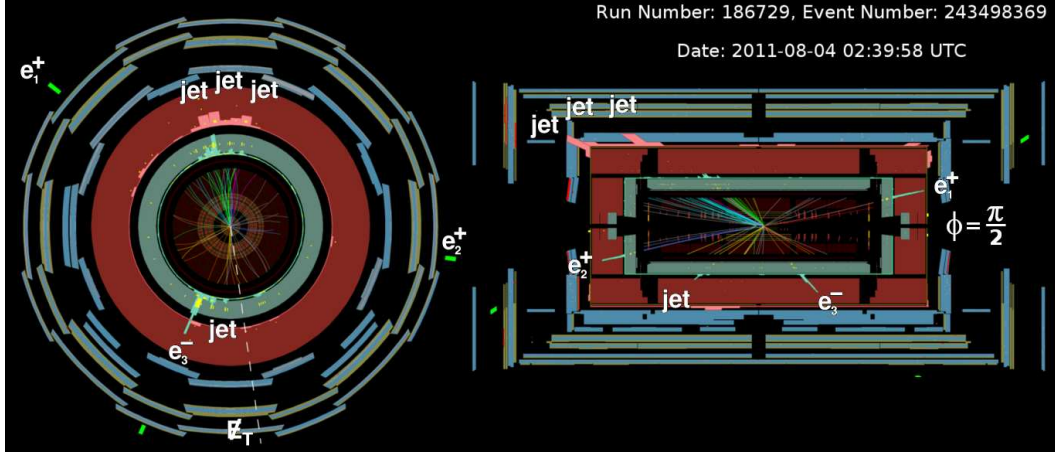


Figure A.18: Event display for Event 243498369 from run 186729. The indices are indicative of lepton p_T order. This event features a large trilepton mass, $m_{\ell^+\ell^-\ell^\pm} = 352.9$ GeV and large E_T^{miss} , 102.6 GeV.

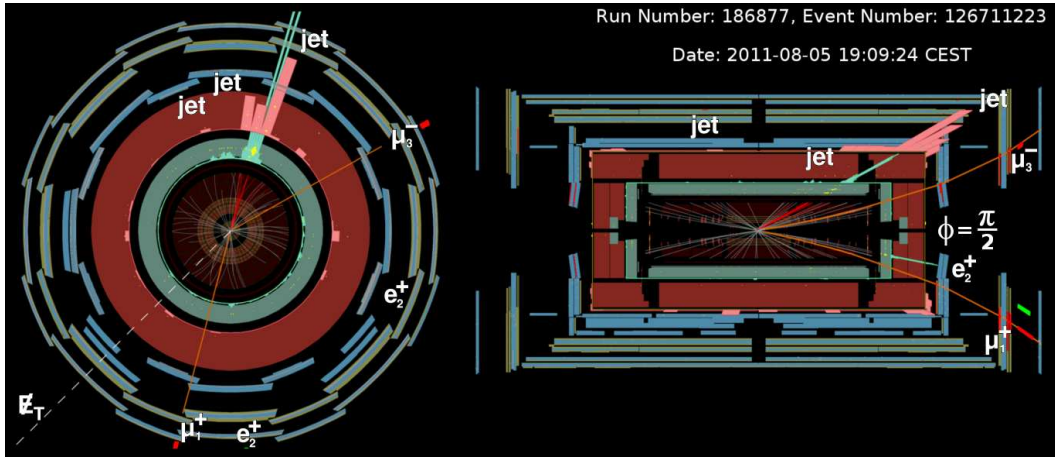


Figure A.19: Event display for Event 126711223 from run 186877. The indices are indicative of lepton p_T order. This event has a jet with $p_T = 251.5$ GeV and $E_T^{\text{miss}} = 163.4$ GeV.

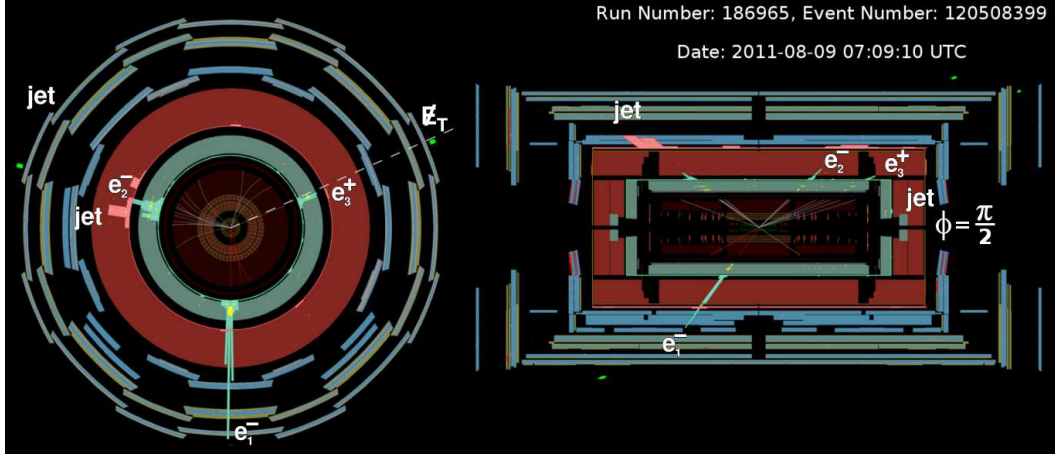


Figure A.20: Event display for Event 120508399 from run 186965. The indices are indicative of lepton p_T order. This event contains 124.2 GeV of E_T^{miss} .

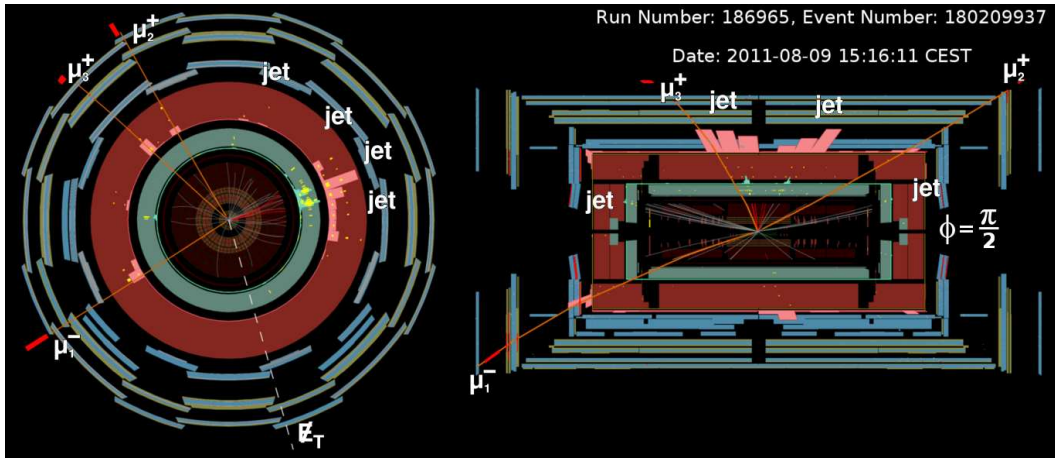


Figure A.21: Event display for Event 180209937 from run 186965. The indices are indicative of lepton p_T order. This event is notable for having a $p_T = 141.2$ GeV muon and $m_{\ell^+\ell^-,\ell'\pm} = 297.0$ GeV.

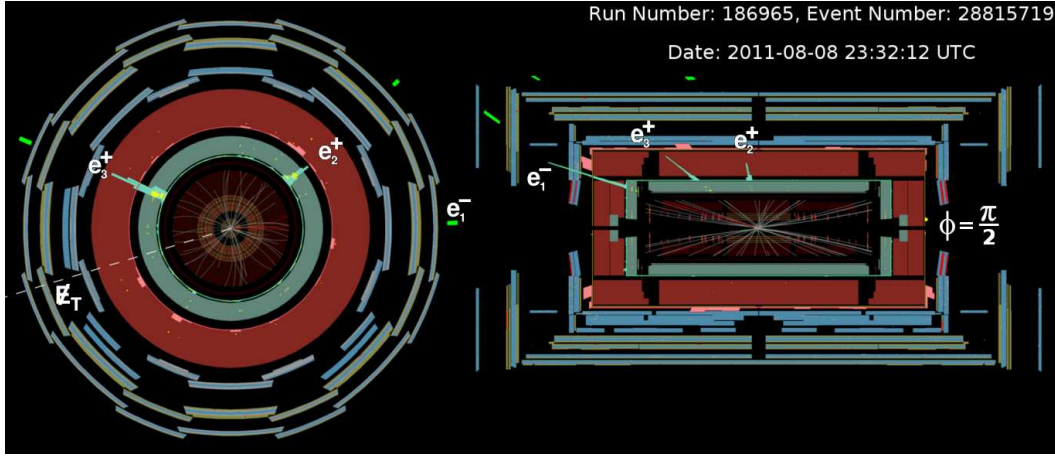


Figure A.22: Event display for Event 28815719 from run 186965. The indices are indicative of lepton p_T order. This is another event with a large amount of E_T^{miss} , $E_T^{\text{miss}} = 128.3$ GeV and an electron with $p_T = 131.0$ GeV.

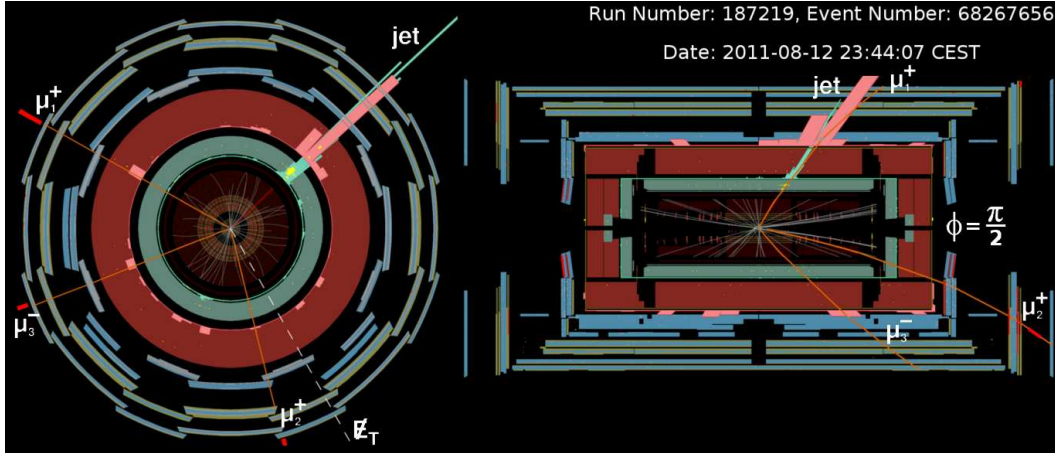


Figure A.23: Event display for Event 68267656 from run 187219. The indices are indicative of lepton p_T order. This event is notable for having a $p_T = 347.8$ GeV muon, as well as a $p_T = 286.7$ GeV jet and $E_T^{\text{miss}} = 297.2$ GeV. The trilepton mass is 423.8 GeV. This event has been super-sized.

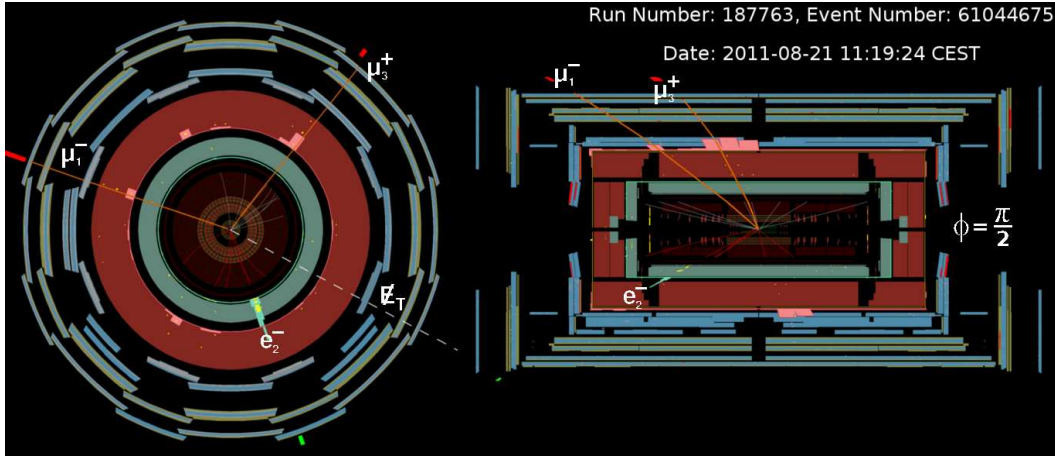


Figure A.24: Event display for Event 61044675 from run 187763. The indices are indicative of lepton p_T order. This event is notable for having a $p_T = 128.4$ GeV muon.

B

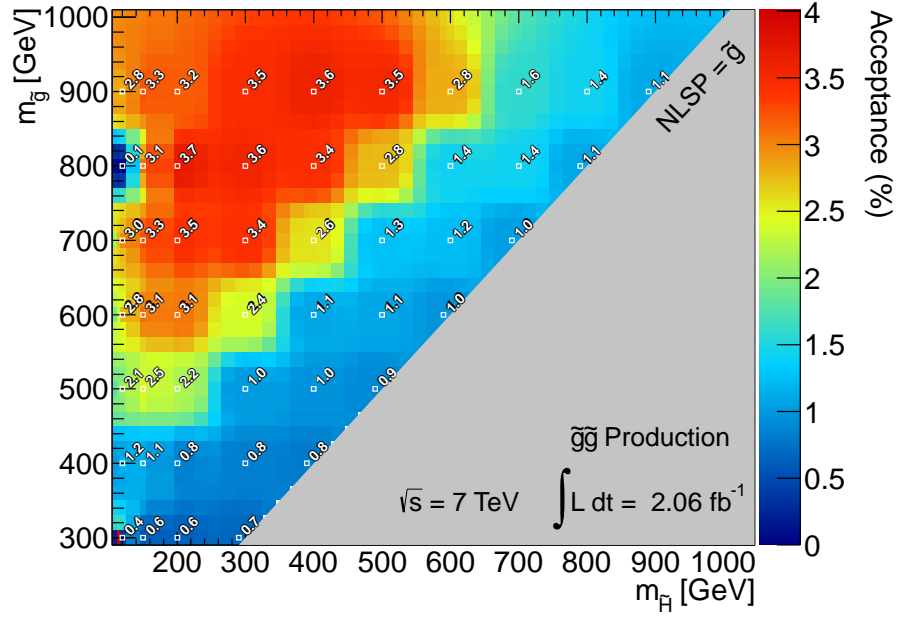
Acceptance and Efficiency of the GGM Grids

The acceptance for the GGM grids is determined by applying the p_T and η selections and overlap removal listed in Section 6.1.1 to generator-level objects, electrons, muons, jets, and E_T^{miss} . The jets are constructed by applying the anti- k_T clustering algorithm to the generator level objects. The generator-level E_T^{miss} is constructed by summing the transverse momenta of non-interacting particles such as neutrinos or any potential LSP. The event level selections are also applied, requiring three leptons, a leptonic Z -resonance, and more than 50 GeV of E_T^{miss} . The acceptance is specifically the number of events passing these generator levels selections divided by the cross section times the integrated luminosity (2.06 fb^{-1}). This includes the efficiencies of the two-lepton and $Z \rightarrow \ell^+ \ell^-$ event filters. The acceptance is shown for both $\tilde{g}\tilde{g}$ -production and gaugino-production for the higgsino (wino) grid in Figure B.1 (Figure B.4).

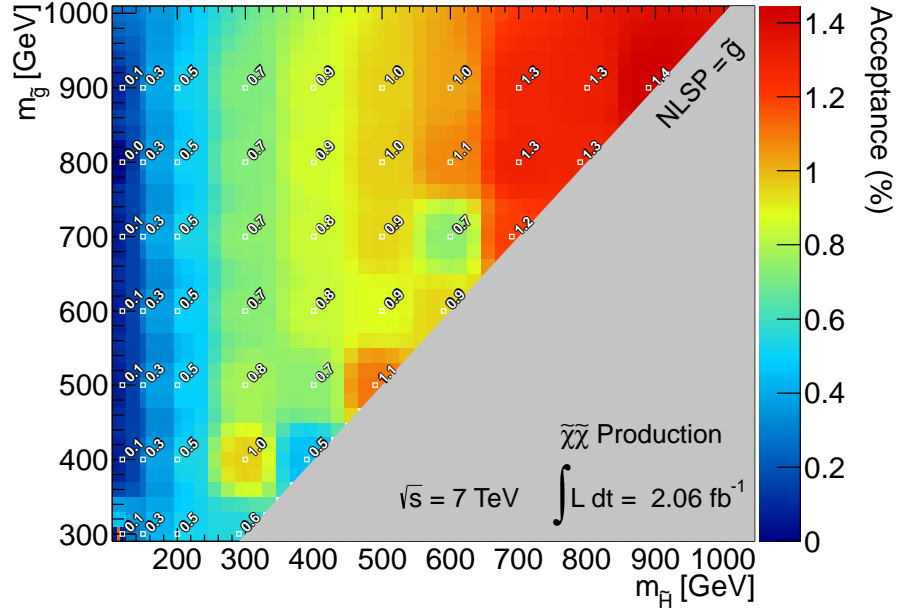
The efficiency is calculated as the event yield after applying the object selections from Section 6.1.1 and the signal region event selections to the GGM grids. The ratio over the cross section times the integrated luminosity (with event filters). The efficiency is shown for both $\tilde{g}\tilde{g}$ -production and gaugino-production for the higgsino (wino) grid in Figure B.2 (Figure B.5).

Also shown is the acceptance \times cross section for both $\tilde{g}\tilde{g}$ -production and gaugino-production for the higgsino (wino) grid in Figure B.3 (Figure B.6).

Note that the actual generated points are labeled with the relevant values. The color-coding is interpolated using Shepard's Method [180].

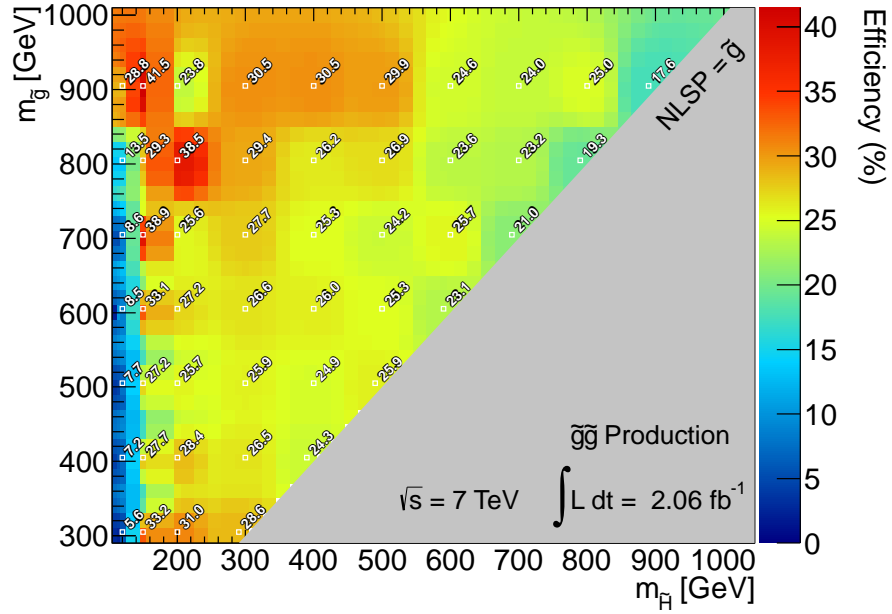


(a)

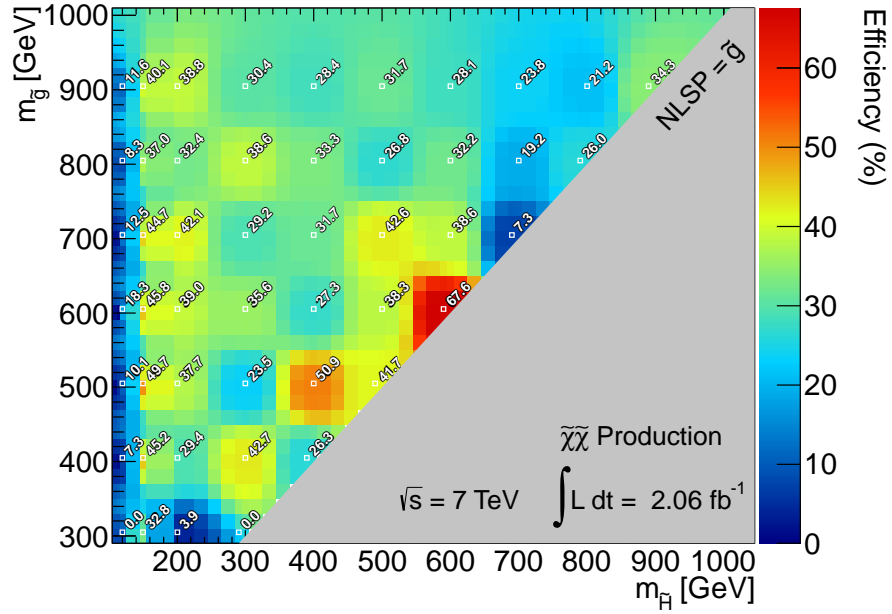


(b)

Figure B.1: The acceptance of the higgsino grid for (a) $\tilde{g}\tilde{g}$ -production and (b) gaugino-production.

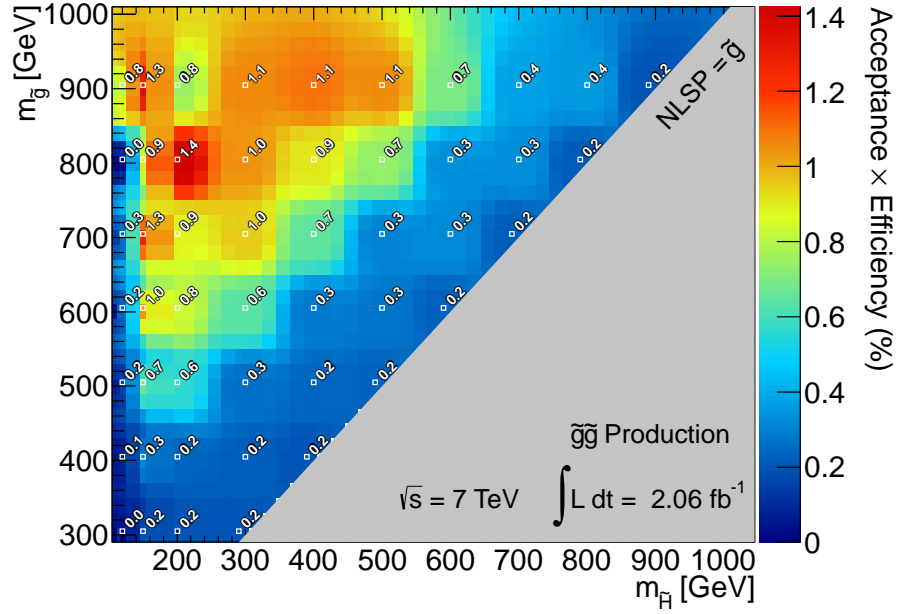


(a)

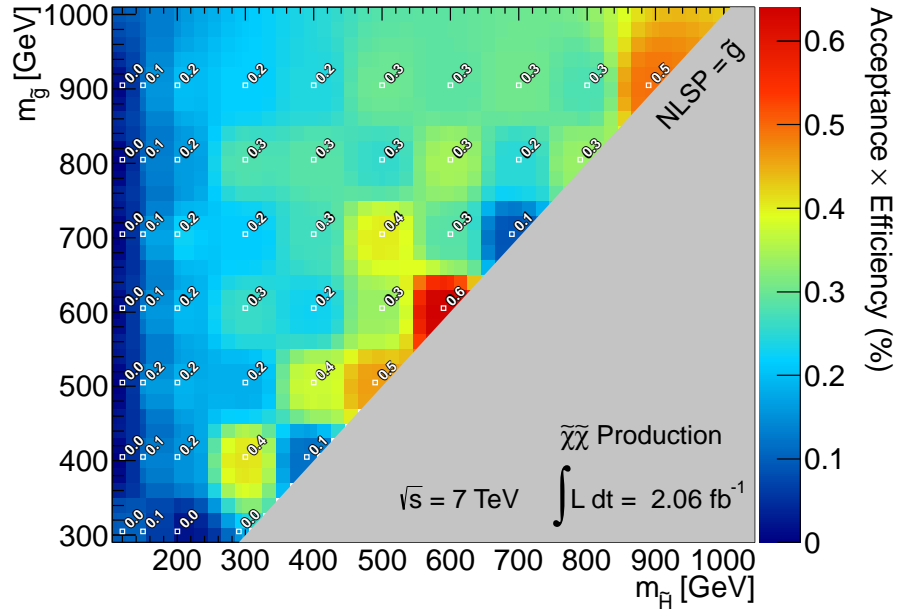


(b)

Figure B.2: The efficiency of the higgsino grid for (a) $\tilde{g}\tilde{g}$ -production and (b) gaugino-production.

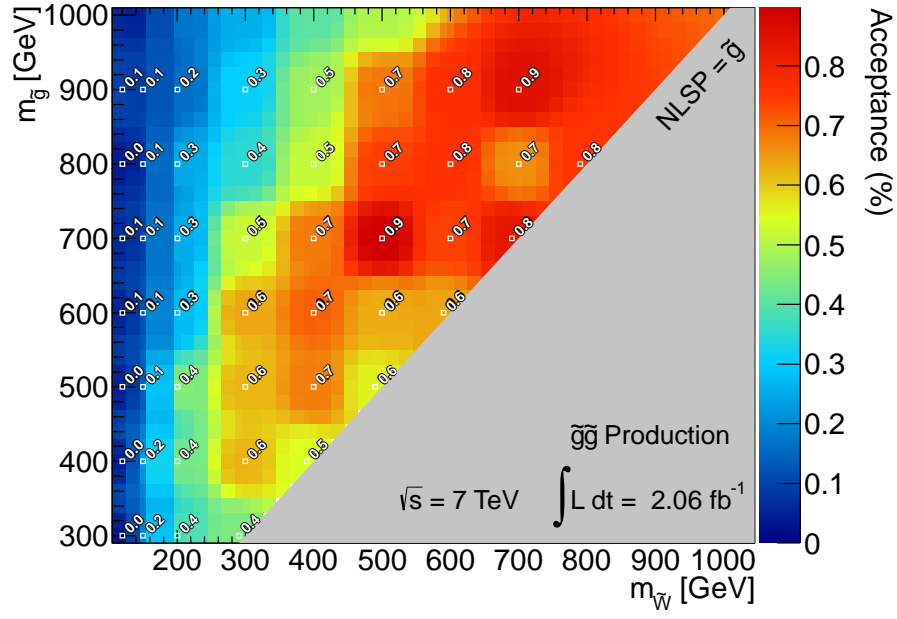


(a)

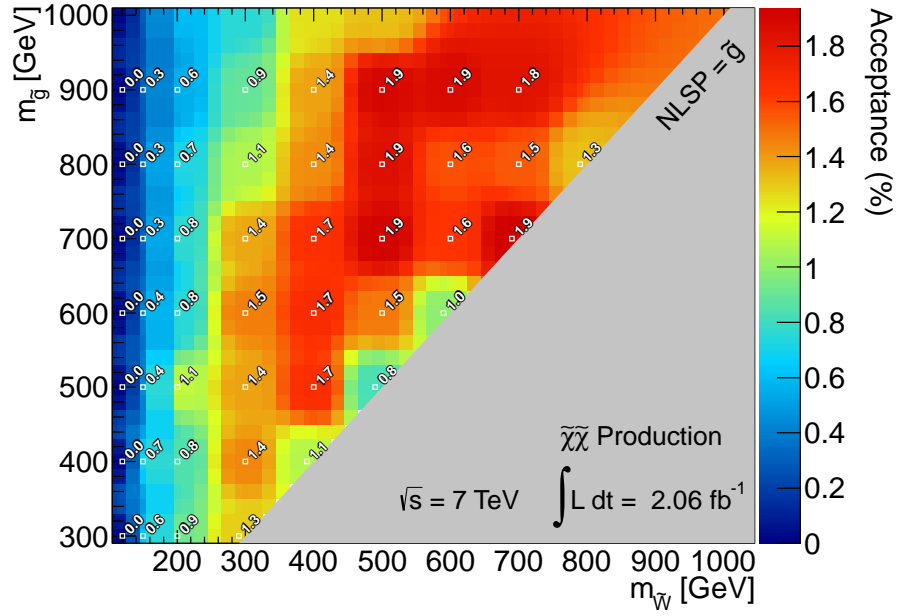


(b)

Figure B.3: The acceptance \times efficiency of the higgsino grid for (a) $\tilde{g}\tilde{g}$ -production and (b) gaugino-production.

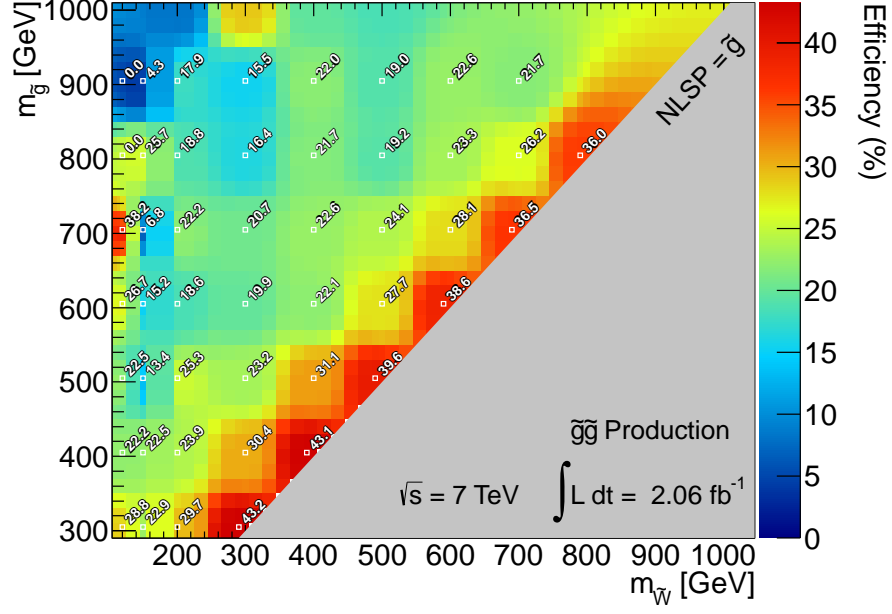


(a)

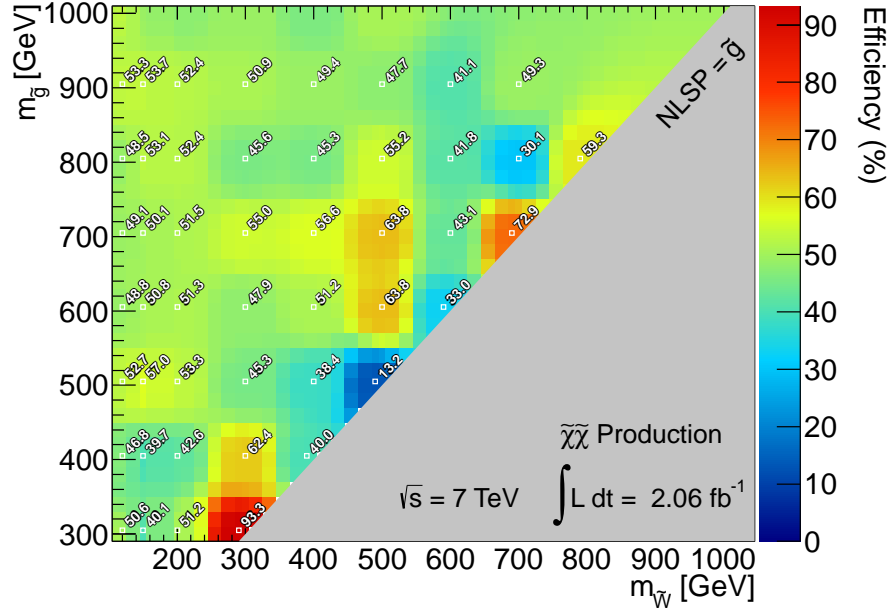


(b)

Figure B.4: The acceptance of the wino grid for (a) $\tilde{g}\tilde{g}$ -production and (b) gaugino-production.

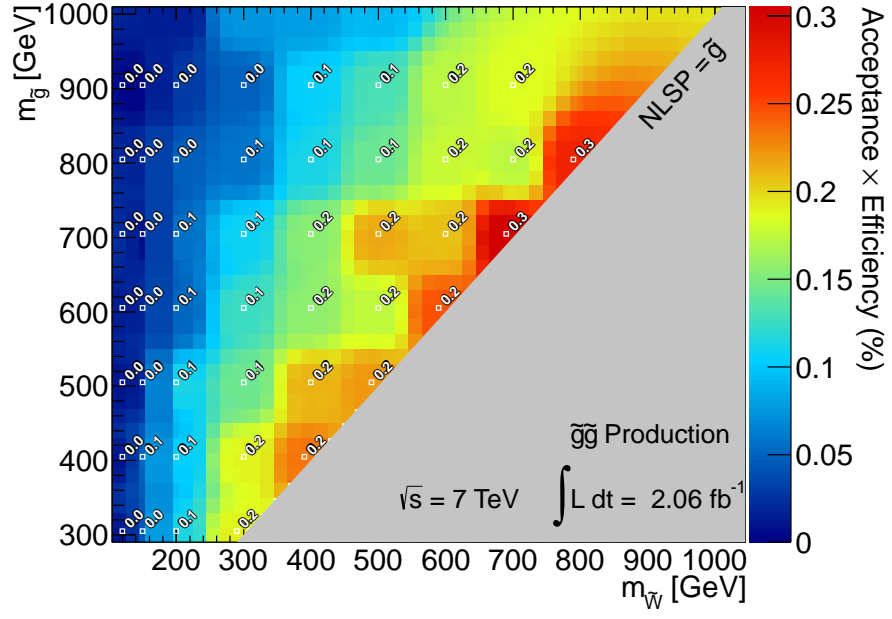


(a)

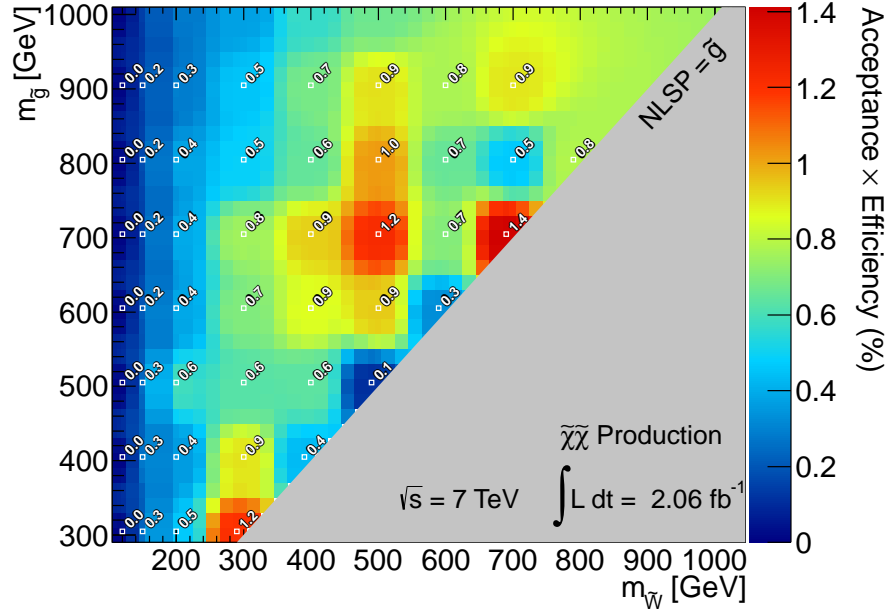


(b)

Figure B.5: The efficiency of the wino grid for (a) $\tilde{g}\tilde{g}$ -production and (b) gaugino-production.



(a)



(b)

Figure B.6: The acceptance × efficiency of the wino grid for (a) $\tilde{g}\tilde{g}$ -production and (b) gaugino-production.

C

Monitoring of the Liquid Argon Read-Out Drivers

RodMonitoring is a software package that is part of the LArgOnline software used to operate, monitor, and maintain the Liquid Argon sub-detector. RodMonitoring specifically monitors the status of the LAr Read-Out Drivers (RODs), and the Processing Units (PUs) and Digital Signal Processors (DSPs) that compose the RODs. The RodMonitoring software provides LAr shifters with information on:

- The current and maximum temperature of the g-link chips that receive data from the Front-End Boards and are not allowed to exceed 35° Celsius.
- The number of Timing/Trigger Control (TTC) events recieved.
- The number events input, output, with errors, and discarded.
- For each channel a pulse energy calculation is performed and the statistics, mean, variance, overflow, and overflow are recorded.

The codebase for RodMonitoring is available to ATLAS users at <https://svnweb.cern.ch/track/largonline/browser/RodMonitoring>.

Starting in 2009, the RODs were frequently producing busy signals, where the ROD ceased to pass data. In order to monitor this problem and quickly deal with it, busy monitoring was added to the RodMonitoring software.

During operations the run controller would notice that LAr had gone busy and inform the LAr shifters. From the detector level busy monitor, the run controller and LAr shifters would know which partition of LAr was busy, allowing them to winnow the information down to which end of LAr, and whether

it was the barrel, end-cap, hadronic end-cap, or forward calorimeter. The shifters would then be required to open the LAr hardware control in the run manager as shown in Figure C.1, telling them that the third ROD has a busy signal. The shifters would then have to navigate to the panel for that ROD, shown in Figure C.2, where they would see which DSPs were busy (in this example, the second and third as noted by the green lights). It was decided to make this information more accessible via the RodMonitoring package.

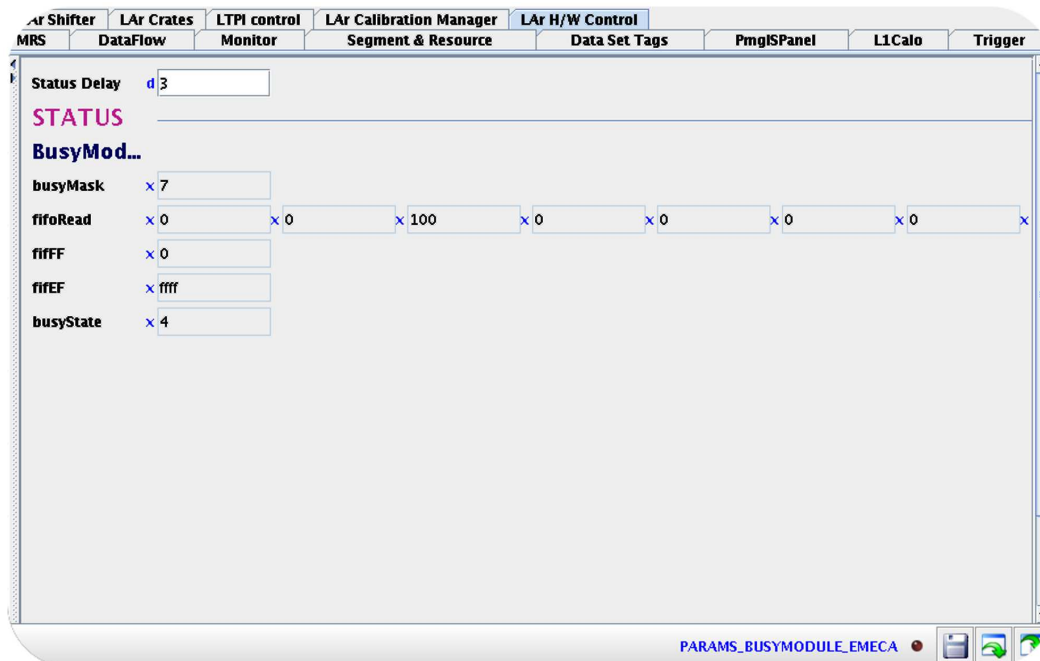


Figure C.1: Shown here is an example of the Run Manager panel that a LAr shifter must use to determine which ROD in a partition is the source of the busy signal. In this example the third ROD is 100% busy.

Modifying the RodMonitoring to enable busy monitoring required modification to the busy tools in the lower-level Rod package, available at <https://svnweb.cern.ch/track/largonline/browser/Rod>. In Rod, the tools Busy.cpp and Busy.h provide a Virtual Machine Environment (VME) to exchange information with the underlying busy hardware. In order to monitor the fraction of time a DSP was busy, Busy.cpp was modified to sample the busy state of each DSP over a fixed fraction of time and report the fraction of busy time. This information was then used to provide a warning to the TDAQ if a particular ROD went 100% busy.

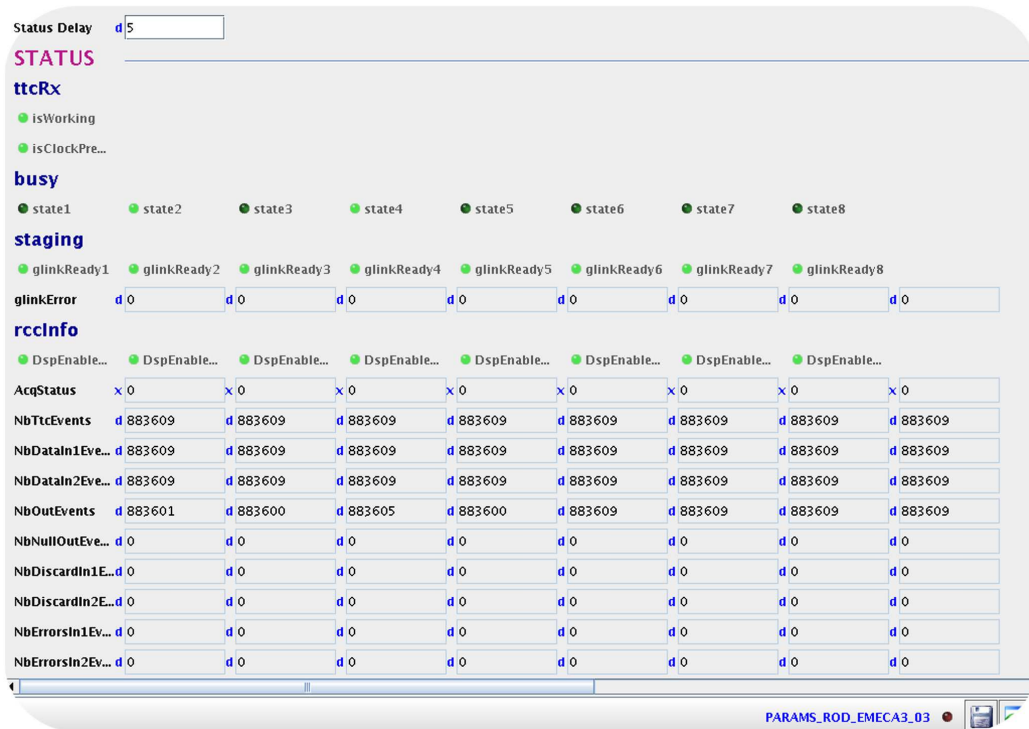


Figure C.2: The Run Manager panel for a busy ROD, showing which of the RODs DSPs is responsible for the busy signal. In this example the second and fourth DSPs are returning a busy signal.

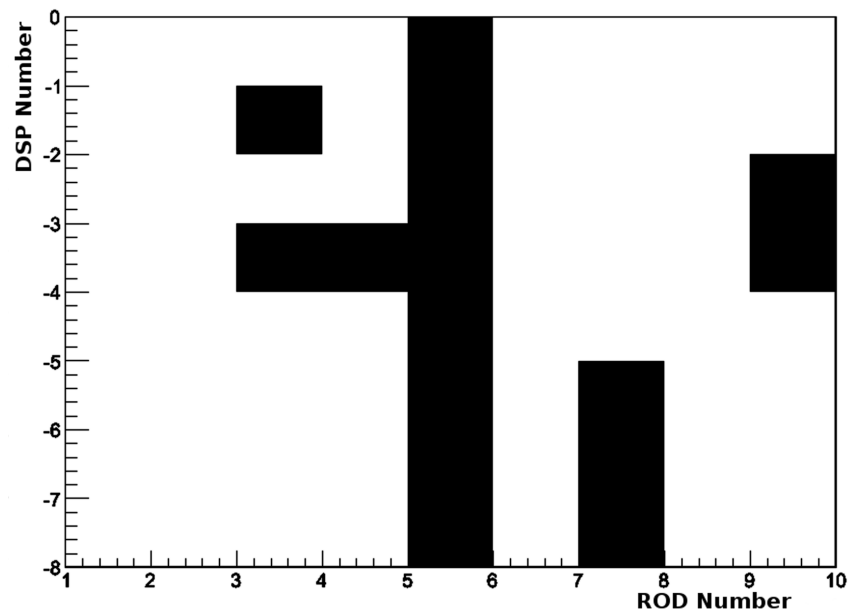


Figure C.3: An example of the ROD busy plot provided in OHP to LAr shifters, allowing a shifter to determine more quickly which DSP of a ROD is busy.

RodMonitoring was then modified to pick the busy fraction information up and provide a two-dimensional histogram via the Online Histogram Provider (OHP) to LAr shifters to quickly examine which ROD and DSP was busy, with a histogram provided for each crate of the LAr sub-detector. An example of this can be seen in Figure C.3. This allows shifters to quickly look over the histograms in a partition of LAr and determine where the problematic DSP is and cycle it to fix the problem. In addition, the busy fraction for each ROD is also provided, as shown in Figure C.4 so that shifters can monitor problematic RODs, such as noting RODs that frequently show a high occupancy. Also included in RodMonitoring is a warning message to users, immediately informing them which ROD and DSP is busy. An example would be:

Rod EMBA2 07 PU: 0 DSP: 1 > 99% busy

Which tells the user that in the LAr electromagnetic barrel's second crate, the seventh ROD, zeroeth PU, the first DSP is busy.

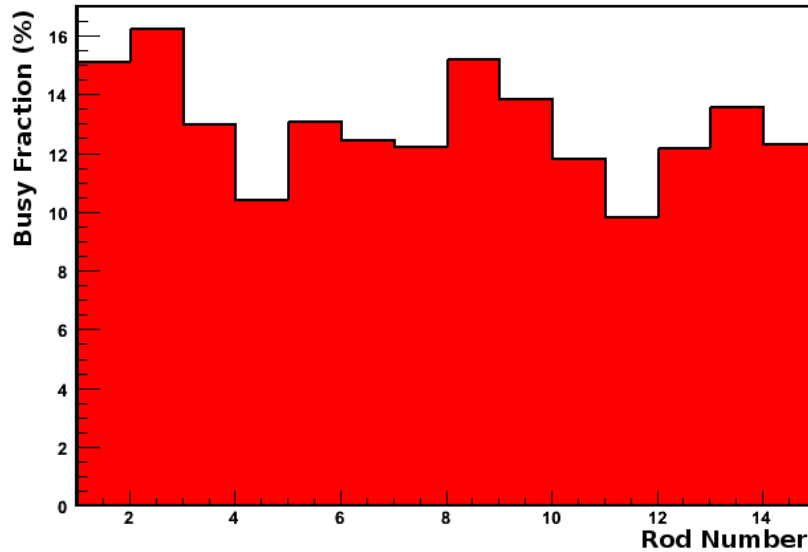


Figure C.4: An example of the ROD busy fraction plot provided in the OHP for users to monitor ROD occupancy.

D

Muons in MET

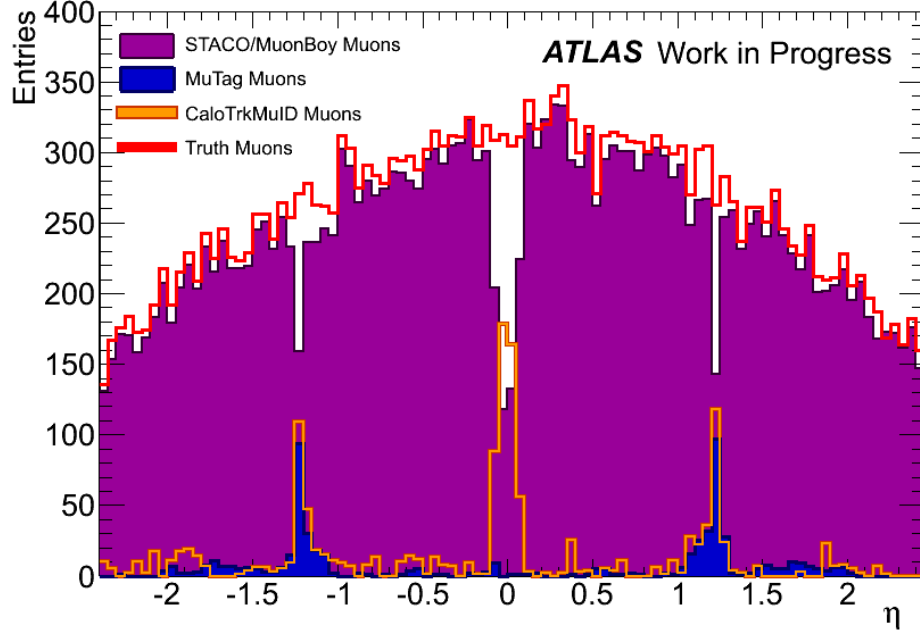
Originally the muon term of the RefFinal algorithm of E_T^{miss} consisted of two sub-components, a term calculated from the momenta of muons in the muon spectrometer and a correction due to small minimal ionizing particle contributions in the calorimeter. The work in this appendix motivated changes toward a more sophisticated muon E_T^{miss} algorithm.

The algorithm used by E_T^{miss} for muons is the STACO/Muonboy combination. Muonboy provides for the standalone reconstruction of a track in the muon spectrometer and STACO stitches the Muonboy tracks to inner detector tracks [181].

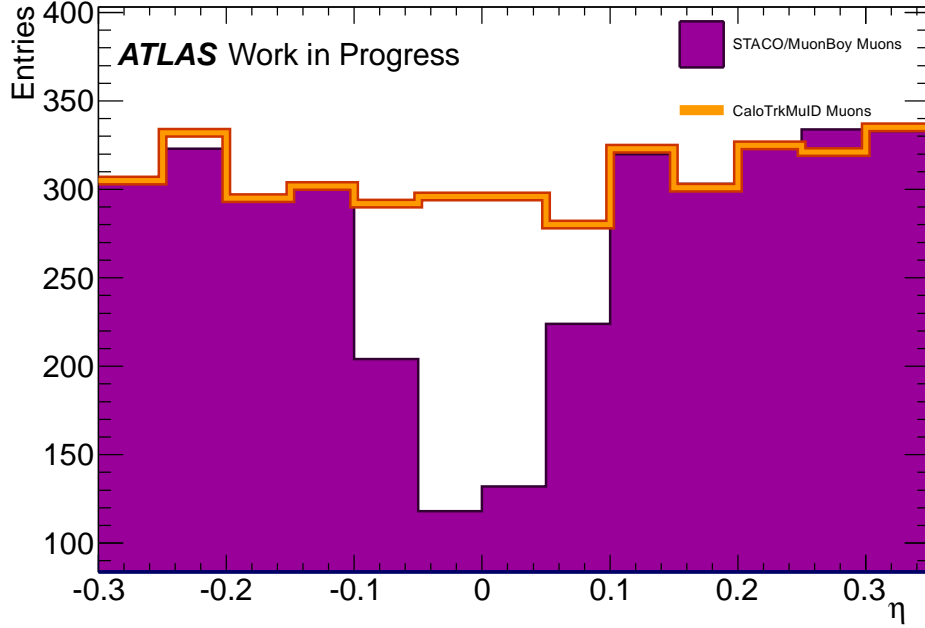
One of the drawbacks of using the muon spectrometer alone is that some regions of the spectrometer have a lower efficiency due to gaps between the individual detector modules. Gaps are found in the regions of $|\eta| < 0.05$ and $|\eta| \sim 1.3$. These defects can be overcome through the use of supplementary muon algorithms, such as CaloTrkMuID and MuTag.

CaloTrkMuID is a muon algorithm that extrapolates and matches inner detector tracks to energy deposits in the outer layer of the Tile Calorimeter. Due to its use of inner detector and calorimeter information it is not affected by the muon spectrometer gap around $\eta \sim 0$ and can be used to fill in over this region. Figure D.1(a) shows the distribution of CaloTrkMuID muons with their overlap with STACO/Muonboy muons removed. Figure D.1(b) shows a close-up of the distributions in the $\eta \sim 0$ region without the overlap between CaloTrkMuID and STACO/Muonboy removed, clearly demonstrating the capability of CaloTrkMuID to help recover missing muons.

However, one would like to avoid including fake muons in the E_T^{miss} calculation when these muons are recovered. In order to facilitate this, selections against fake muons have been examined. Ultimately, the variables that clearly differentiated between true and fake muons in Monte Carlo were a comparison



(a)



(b)

Figure D.1: (a) shows the η distribution for the STACO/MuonBoy, CaloTrkMuID, and MuTag muons compared to truth muons; CaloTrkMuID and MuTag muons are only shown if they do not correspond to a STACO/MuonBoy muon. (b) shows the STACO/MuonBoy and CaloTrkMuID collections in detail in the region of $|\eta| < 0.3$, and the CaloTrkMuID collection is shown including muons which correspond to a STACO/MuonBoy collection in order to show the utility in using CaloTrkMuID muons in that region.

of the muon p_T with the isolation of the muon, calculated by summing the E_T in a cone of $\Delta R < 0.3$ around the muon. A scatter plot of this relationship for CaloTrkMuID muons in a mixture of $Z \rightarrow \mu^+\mu^-$ and dijet samples can be seen in Figure D.2(a), and the population of fake muons stands out rather starkly. Based on this, it was decided to cut fake muons by requiring that CaloTrkMuID muons in the region $|\eta| < 0.1$ be added to the E_T^{miss} algorithm if they meet the criteria of:

$$\log_{10}(p_T[\text{GeV}]) - \log_{10}(E_T^{\Delta R < 0.3}[\text{GeV}]) - \log_{10}(3) > 0 \quad (\text{D.1})$$

The use of these selection criteria gave the results shown in Table D.1, which shows that the effect was quite strong on reducing fakes in both the $Z \rightarrow \mu^+\mu^-$ and DiJet samples. Note that fake muons in this instance are those that do not correspond to a truth muon.

Effect of Isolation- p_T Selection on CaloTrkMuID Muons				
Sample	Before Cuts		After Cuts	
	Real	Fake	Real	Fake
$Z \rightarrow \mu^+\mu^-$	15018	1930	14759	235
DiJet	3	315	0	24

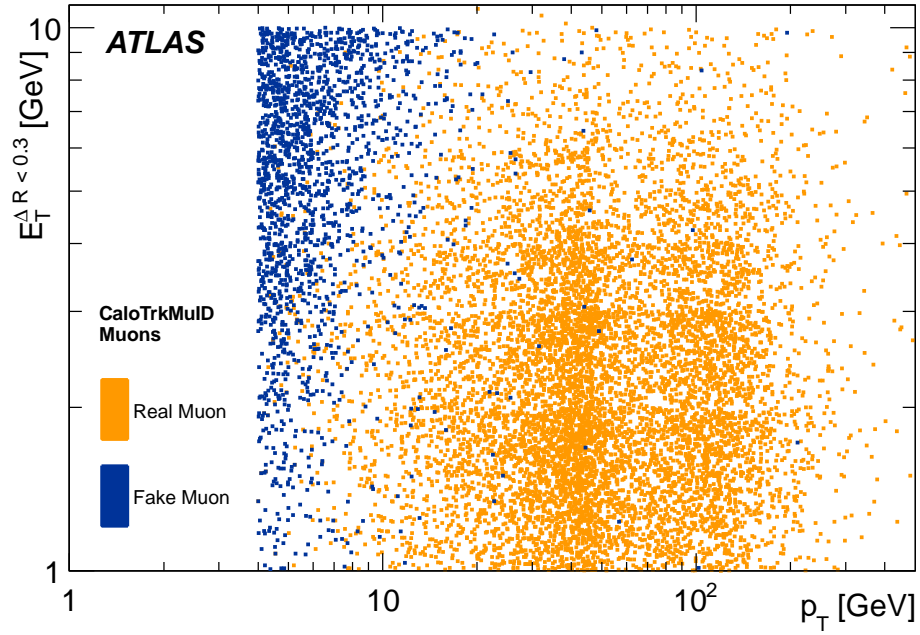
Table D.1: The result of the isolation- p_T selection on CaloTrkMuID muons in selected samples.

In addition, one can make use of muons from the MuTag algorithm. MuTag functions by matching inner detector tracks to segments in the muon spectrometer that were not incorporated into a complete muon track, which allows it to recover muons lost in the $|\eta| \sim 1.3$ gap, as shown in Figure D.1. It is optimized for finding low p_T muons. As with the CaloTrkMuID collection, it is preferable to minimize the contribution from fake muons. It was decided to cut fake muons by requiring that MuTag muons in the region $1.0 < |\eta| < 1.3$ be added to the E_T^{miss} algorithm if they meet the criteria of:

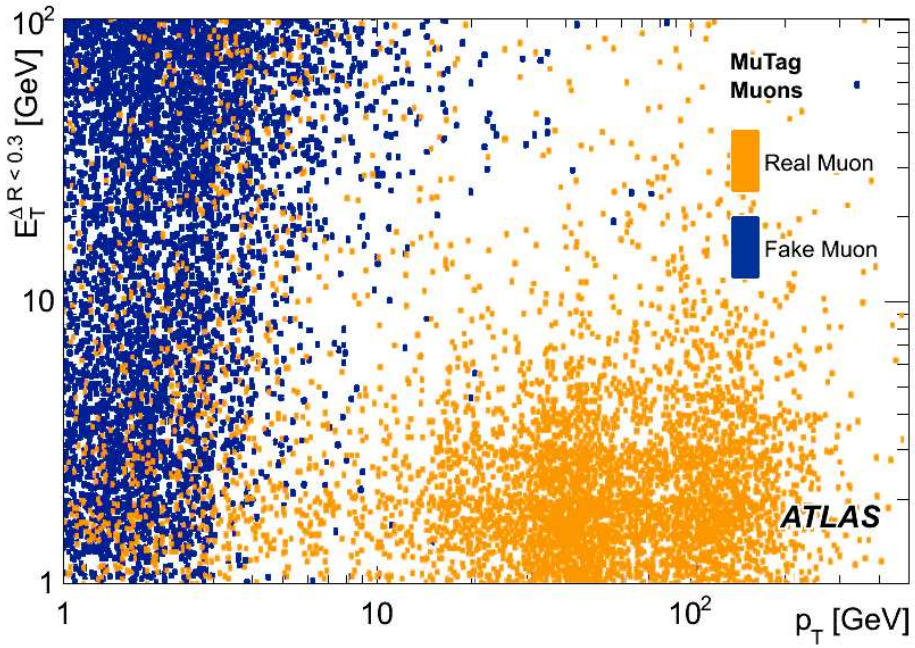
$$2 \cdot \log_{10}(p_T[\text{GeV}]) - \log_{10}(E_T^{\Delta R < 0.3}[\text{GeV}]) - 10^{3/7} > 0 \quad (\text{D.2})$$

This selection was based on the relationship seen in Figure D.2(b), showing the distribution of real and fake muons from a mixture of $Z \rightarrow \mu^+\mu^-$, DiJet, and $t\bar{t}$ samples. This selection gave the results in Table D.2. The case for cleaning the MuTag collection is not as clear cut as that for the CaloTrkMuID collections and the selections errs toward eliminating more fake muons.

A third change examined for the muon component of the E_T^{miss} calculation



(a)



(b)

Figure D.2: (a) The muon isolation, $E_T^{\Delta R < 0.3}$, versus muon p_T for real and fake muons in the CaloTrkMuID collection in a mixture of $Z \rightarrow \mu^+\mu^-$ and DiJet events. (b) The muon isolation, $E_T^{\Delta R < 0.3}$, versus muon p_T for real and fake muons in the MuTag collection in a mixture of $Z \rightarrow \mu^+\mu^-$, DiJet, and $t\bar{t}$ events.

Effect of Isolation- p_T Selection on MuTag Muons				
Sample	Before Cuts		After Cuts	
	Real	Fake	Real	Fake
$Z \rightarrow \mu^+ \mu^-$	7512	5668	5028	9
DiJet	305	10788	4	4
$t\bar{t}$	1789	4268	327	4

Table D.2: The result of the isolation- p_T selection on MuTag muons in selected samples.

was the use of combined muons instead of only using the muon spectrometer. Prior to this, the muon spectrometer was used to avoid double counting energy found in the calorimeter, which is measured using cells in the calorimeter. A combined muon gives a better estimate of the muon energy though and the effect was examined of using the combined muon energy and merely omitting the energy found in the calorimeter for the muon, as well as giving muons priority in the E_T^{miss} -algorithm over jets.

The effect on the E_T^{miss} distribution for the change to combined muons, as well as supplementing with CaloTrkMuID and MuTag muons, is shown in Figure D.3, which is the distribution of $E_{x(y)}^{\text{miss,truth}} - E_{x(y)}^{\text{miss,reco}}$ in $Z \rightarrow \mu^+ \mu^-$ events. The resolution, σ , is determined by fitting with a normal distribution. Note that $Z \rightarrow \mu^+ \mu^-$ are expected to have very little real E_T^{miss} , and thus make a good candidate events for diagnosing causes of fake E_T^{miss} . The E_T^{miss} “tails” are defined as the number of events outside of $|3\sigma|$ divided by the total number of events. The distributions in Figure D.3 clearly show that using combined muons is an improvement over using the muon spectrometer alone, in terms of both resolution and tails. The addition of CaloTrkMuID and MuTag muons similarly show clear improvements in the calculation of E_T^{miss} .

Additionally, E_T^{miss} performance can be parameterized in terms of ΣE_T . We expect the E_T^{miss} resolution to follow the relationship $\sigma_{E_{x(y)}^{\text{miss}}} = k \cdot \sqrt{\Sigma E_T}$ and the ATLAS Technical Design Report predicts a value of 0.46 for the parameter k [182], though this is only under optimal conditions. Figure D.4 shows the relationship of E_T^{miss} resolution versus the true ΣE_T for the changes to the E_T^{miss} -algorithm examined here for the $Z \rightarrow \mu^+ \mu^-$ sample. Again, we see marked improvement in using combined muons instead of spectrometer muons, and smaller improvements from adding the CaloTrkMuID and MuTag muons.

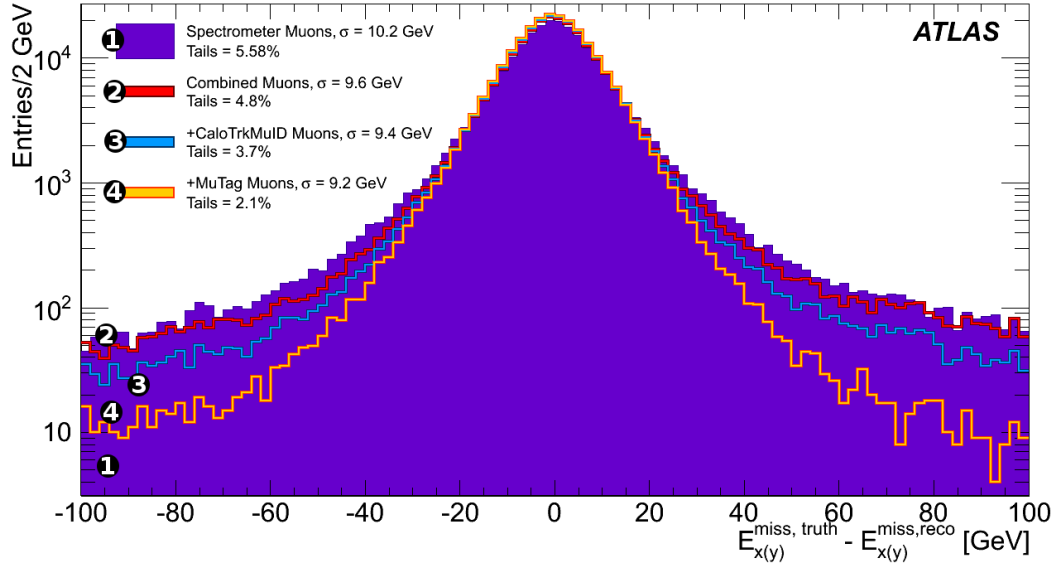


Figure D.3: The E_T^{miss} distribution for $Z \rightarrow \mu^+\mu^-$ events for each of the changes to the muons used in the E_T^{miss} algorithm. The move from spectrometer-only muons to combined muons shows clear improvement in both resolution and tails, as does the inclusion of CaloTrkMuID and MuTag muons.

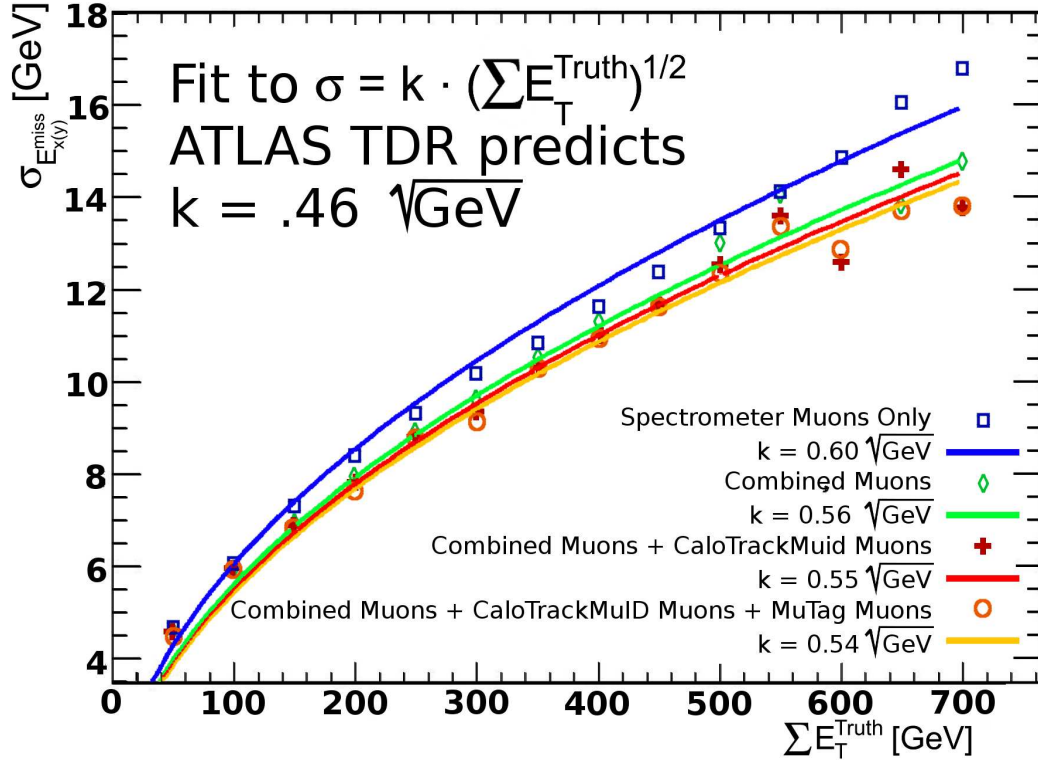


Figure D.4: A comparison of $\sigma_{E_{x(y)}^{\text{miss}}} = k \cdot \sqrt{\sum E_T}$ for $Z \rightarrow \mu^+ \mu^-$ events after changes to the muons used in the E_T^{miss} -algorithm. The improvement in performance after switching to combined muons from spectrometer muons is quite stark; the inclusion of CaloTrkMuID and MuTag muons produce smaller improvements in performance.

E

Offline Software Development

In 2009 effort was intensified in ATLAS for providing a common framework to produce flat n-tuples derived from the higher level datasets. At the time, users general came into contact with data and Monte Carlo in one of two formats derived from the raw data: Event Summary Data (ESD) and Analysis Object Data (AOD). Each containing data that has been refined and streamlined. For instance, ESDs often contain the information for every cell of a calorimeter, while AODs usually only contain the topoclusters constructed from the cells. Both of these formats relied extensively on object classes inside of the ATHENA framework, which is the framework used by ATLAS for event reconstruction, including tools for analysis. Usually a user would either analyze directly on the AOD, or have their own routines to transfer the AOD and ESD information to their own custom n-tuples.

It was desired that there be a common framework for producing n-tuples, to economize the work of doing so and provide for commonality among the different n-tuples produced by the physics and performance groups. It was also felt that the n-tuples produced by the framework should be flat, defined by not requiring libraries outside of ROOT to be readable and thus ruling out any object more complicated than a standard C++ library vector.

The framework arrived at was developed by Scott Snyder of Brookhaven National Laboratory and is called D3PDMaker, where D3PD refers to the n-tuples being the **D**erived **3rd**-level **P**hysics **D**ata. For ATLAS users the D3PDMaker software can be found at <https://svnweb.cern.ch/trac/atlasoff/browser/PhysicsAnalysis/D3PDMaker>. It provides a common framework for translating ATHENA physics objects into a flat, ROOT-readable n-tuple, allowing for both event level variables, such as E_T^{miss} -components, or collections of physics objects, such as electrons or muons.

Once the desired framework was developed, it was necessary to adapt the

tools to specific objects as dictated by each performance group (such as for E_T^{miss}), and customize the usage of the objects to produce n-tuples that meet the needs of each physics group (such as the supersymmetry analysis group). In addition, common tools were developed to run on the n-tuples, such as the MissingETUtility, which allows users to rebuild E_T^{miss} and take into account systematic errors and changes in energy scale.

E.1 MissingETD3PDMaker

From the beginning E_T^{miss} provided unique challenges to adapting the D3PDMaker framework to it. A general overview of the up-to-date structure of MissingETD3PDMaker can be seen in the block diagram presented in Figure E.1, showing the flow of information from higher-level objects in an AOD or ESD to the flat architecture of the E_T^{miss} n-tuple information. In ATHENA there are three classes of E_T^{miss} .

MissingEtCalo, a calorimeter-based E_T^{miss} , holding unsophisticated E_T^{miss} calculations made simply by summing the cells or clusters in the calorimeters.

MissingET, which holds more refined E_T^{miss} calculations or individual sub-terms of the calculation, such as RefFinal E_T^{miss} or its terms.

MissingEtTruth, which exists only in Monte Carlo and holds the E_T^{miss} calculated from truth variables using either interacting or non-interacting particles.

Each of these three types has its own class, but in general each is composed of five main variables for each type of E_T^{miss} : E_T^{miss} , E_x^{miss} , E_y^{miss} , SET , and $\phi_{E_T^{\text{miss}}}$. Though one should note that either $E_T^{\text{miss}}, \phi_{E_T^{\text{miss}}}$ or $E_x^{\text{miss}}, E_y^{\text{miss}}$ are redundant. Additionally, MissingEtCalo and MissingET include E_T^{miss} calculated from the different η regions of the detector. In order to provide customizability to the user, a different tool for each different class of E_T^{miss} was necessary. On top of this, the D3PDMaker tools are oriented around the storage of physics objects in the ATHENA memory pool, referred to as StoreGate. Each different E_T^{miss} is stored separately in StoreGate and requires a new iteration of the MissingETD3PDMaker tool to recover it from StoreGate. In preliminary versions of MissingETD3PDMaker the performance group tools were required to call it dozens of times to get the different E_T^{miss} -terms they might require. In contrast, users wanting muons would call on the MuonD3PDMaker in one command and get all the muon variables they needed, depending on the preset detail level parameter they provide it.

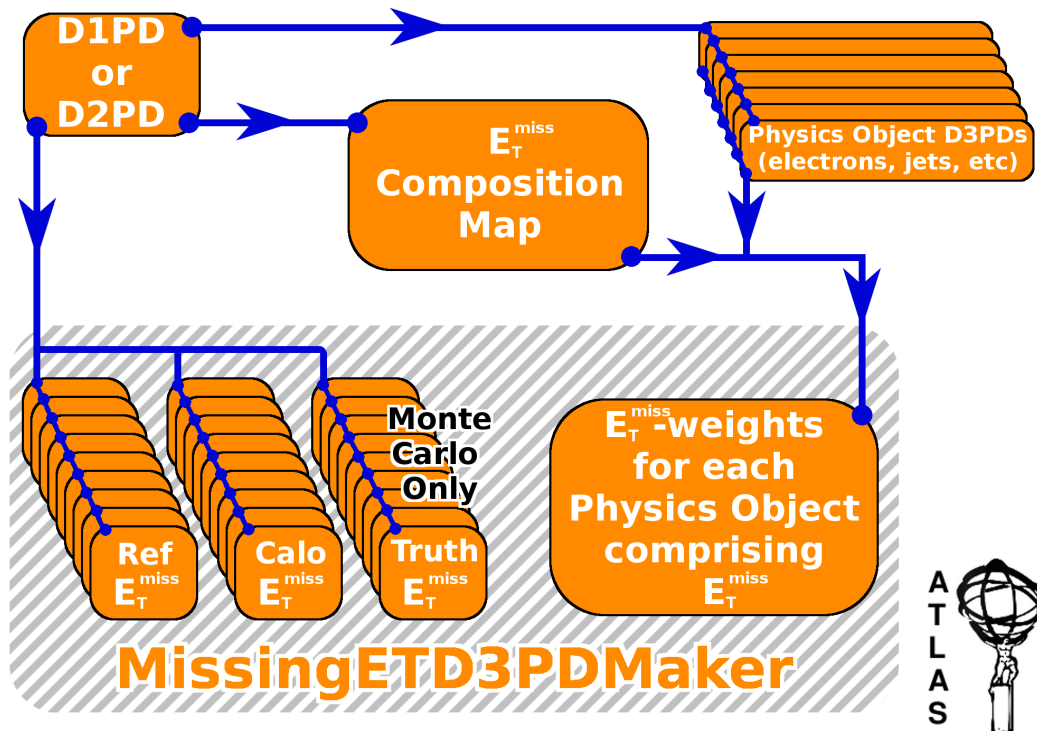


Figure E.1: Block diagram showing the flow of data from the ATHENA-based physics objects contained in StoreGate to the flat n-tuple structure used by MissingETD3PDMaker.

The solution to this problem was to put the MissingETD3PDMaker tools into a wrapper. The tools remain disparate, but a user can call one function and provide a preset detail level parameter or list of E_T^{miss} terms to include or exclude, thus handling all the messy details of customizability behind the scenes in the mechanics of the package itself. Additionally, users can also give the MissingETD3PDMaker the names of custom E_T^{miss} calculations they have committed to StoreGate.

The MissingETD3PDMaker also calls on the other D3PDMaker packages, such as those for electrons, photons, muons, jets, clusters, and tracks, in order to provide details of the physics objects used in the E_T^{miss} . Information about how the objects were used and weighted by the E_T^{miss} -algorithm is provided by the RefComposition object that is in StoreGate. This information is matched to the objects that have been committed to the n-tuple by tools in the MissingETD3PDMaker algorithm. This information is the weight applied to the $p_{x(y)}$ to calculate E_T^{miss} , the weight applied to E_T to calculate ΣE_T , and a StatusWord providing information on how the object was used in the E_T^{miss} calculation (such as whether the spectrometer or combined momentum measurement was used in the case of muons). Provided with this information and the 4-momenta given by the other physics objects D3PDMakers, a user can reconstruct E_T^{miss} from the n-tuple and make corrections to it or examine the effects of systematics on the E_T^{miss} calculation.

E.2 SUSYD3PDMaker

No single D3PDMaker configuration can meet the needs of every performance group on ATLAS without ballooning the size of the n-tuples to a similar size as the AOD format. Consequently, each performance group must choose a D3PDMaker configuration or maintain their own. To meet the needs of the supersymmetry analysis groups, considerable customization must be utilized, requiring a supersymmetry-specific D3PDMaker configuration. That configuration is developed and maintained in the SUSYD3PDMaker package. An outline of the structure of information flow in SUSYD3PDMaker can be seen in the block diagram shown in Figure E.2.

The SUSYD3PDMaker package is a mixture of pre-existing D3PDMaker tools configured to the detail level needed by the supersymmetry working group, as well as custom tools and reconstruction algorithms developed by the supersymmetry working group. Generally, the following objects are passed by the D3PDMaker tools with only the level of detail customized by the SUSYD3PDMaker:

Photons are customized to include kinematics as well as information about

the shape of the shower in the calorimeter.

Muons actually refers to two different muon collections. The ATLAS experiment has two competing muon algorithms, STACO and MuID. While STACO is considered the default for supersymmetry analysis, MuID is also included in the n-tuple for comparisons and cross checks. Information about the muons includes kinematics, isolation variables, and information about the provenance and quality of muon tracks.

Event Level Variables included such information as the run number and event number, as well as the number of vertices in the event, or the μ -value of the event, which is a measure of the pile-up.

Trigger Objects is information about the corresponding objects built by the trigger hypothesis, such as electrons or jets. These objects are not necessarily 1-to-1 to reconstruction objects and matching to them can help analyses minimize trigger bias.

Trigger Decisions are the boolean information on whether a trigger fired in an event or not. Upstream of the n-tuple dumper they are used to divide data into different streams (JetTauEtMiss, Muons, and Egamma) and are also used by the supersymmetry group to slim data entering the n-tuple.

The other n-tuple tools that SUSYD3PDMaker calls on are preceded by numerous custom algorithms for rebuilding objects or modifying them. This has included:

Electrons in early data taking required modification of certain quality flags used by the E_T^{miss} algorithms. While unmodified electrons were passed to the n-tuple, a custom electron collection was made that contained only those electrons to be used by E_T^{miss} , thus ensuring the quality of electron desired by the supersymmetry group.

Jets have at various times required special algorithms to add necessary variables, such as track information for cleaning. At times the jet collections have been completely rebuilt to guarantee the desired calibration scales and variables.

Taus represent one of the physics objects most difficult to analyze and the tau reconstruction algorithms undergo constant development. Consequently, it is often necessary for the SUSYD3PDMaker to adjust the tau collections available in AODs to the state-of-the-art of tau reconstruction, to ensure that users receive the best information about the taus.

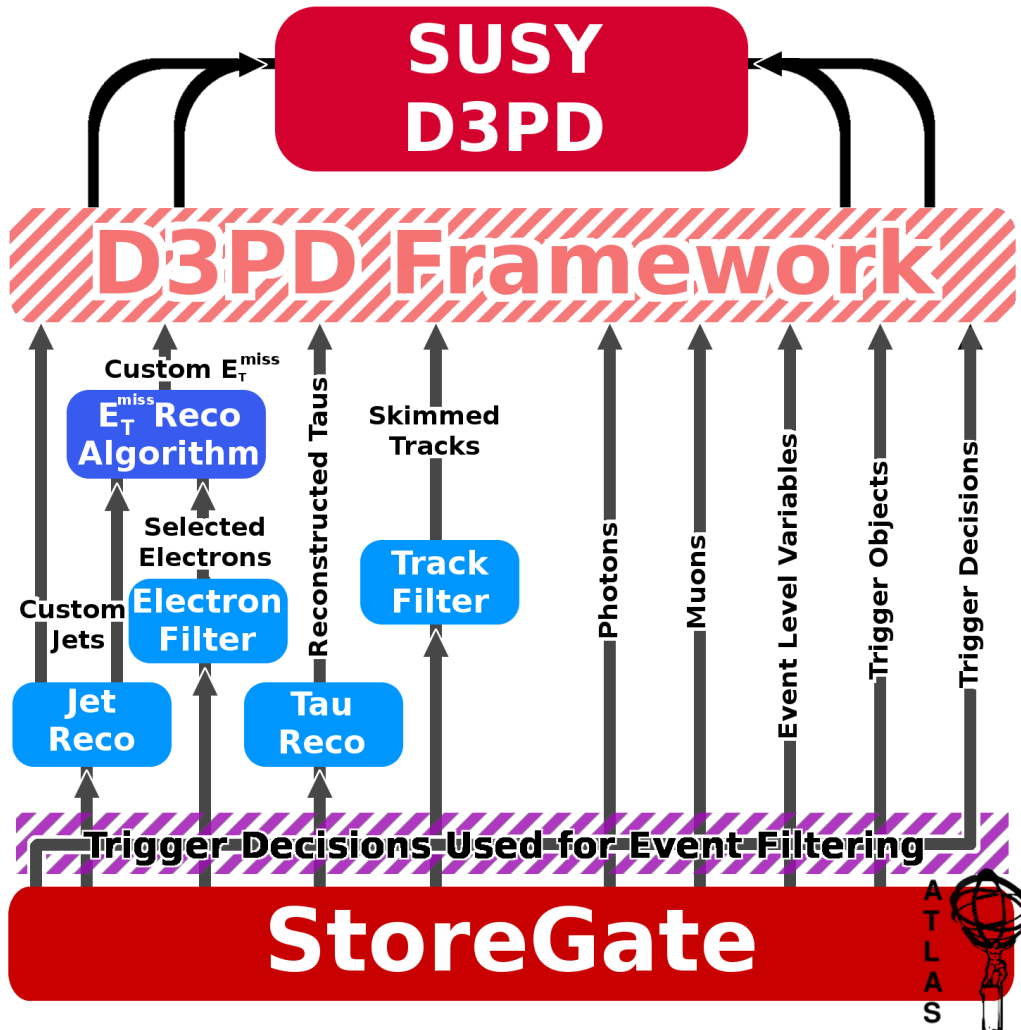


Figure E.2: Block diagram showing the flow of data from higher

Tracks are provided to a limited extent by the SUSYD3PDMaker. Filters are included prior to writing the tracks to strike a balance between the necessary track information and the large amount of memory that tracks require. These operate by producing special track collections with selection criteria applied, which are then fed to the D3PDMaker tools for tracks.

E_T^{miss} is a principle signature of R-parity preserving supersymmetry and receives considerable attention in the design of the n-tuple software. At times this has required the use of customized electron and jet classes in order to reconstruct E_T^{miss} as desired. For the 2010 and 2011 analyses, the default algorithm used by the supersymmetry group is the so-called “Simplified20” algorithm, which includes an electron term with a $p_T > 20$ GeV requirement, a hadronic jet term using Anti- k_T jets with a characteristic size of $\Delta R = 0.4$ and $p_T > 20$ GeV, and a cluster term for all remaining calorimeter activity calibrated at electromagnetic-scale, as well as a muon term. An additional customized E_T^{miss} is also provided which provides for a photon term. Also, the standard E_T^{miss} algorithm terms are provided, as well as composition maps for all the E_T^{miss} algorithms in question.

The results of these custom algorithms are then fed into the standard D3PDMaker tools provided by the performance groups and together produce the n-tuple used by the supersymmetry group, with SUSYD3PDMaker forming the nucleus of the supersymmetry n-tuple production machine.

E.3 METUtility

The complexity of the E_T^{miss} -algorithm is detailed in Section 6.1.4. When dealing with systematic uncertainties and corrections to these objects, it is necessary to re-calculate the E_T^{miss} -object. METUtility is provided to allow users to do this from the objects available in n-tuples. A block diagram of METUtility is provided in Figure E.3.

The functionality of METUtility is dependent on the E_T^{miss} -composition map that is made available at n-tuple and AOD level. The composition map provides status words for each physics object providing information on whether the object requires special handling. For most objects the status word is provided with a default value but unneeded for proper reconstruction. The status word is vital in the case of muons, where it indicates whether to use the muon spectrometer momentum measurement alone in the case of non-isolated muons or to use the combined inner detector and muon spectrometer

measurement for isolated or badly measured muons; muons may also have additional status words to indicate the energy they left in the calorimeter in the case of non-isolated muons. The status word is also used to re-construct the out-of-object energy from clusters and tracks, providing information on how the various tracks and topological clusters are used. For each object (and status word) a set of three weights are provided, $w_{E_x}, w_{E_y}, w_{E_T}$, which can then be used to re-calculate $E_x^{\text{miss}}, E_y^{\text{miss}}$, and ΣE_T . If an object is not used or identified as another physics object the weights are equal to zero.

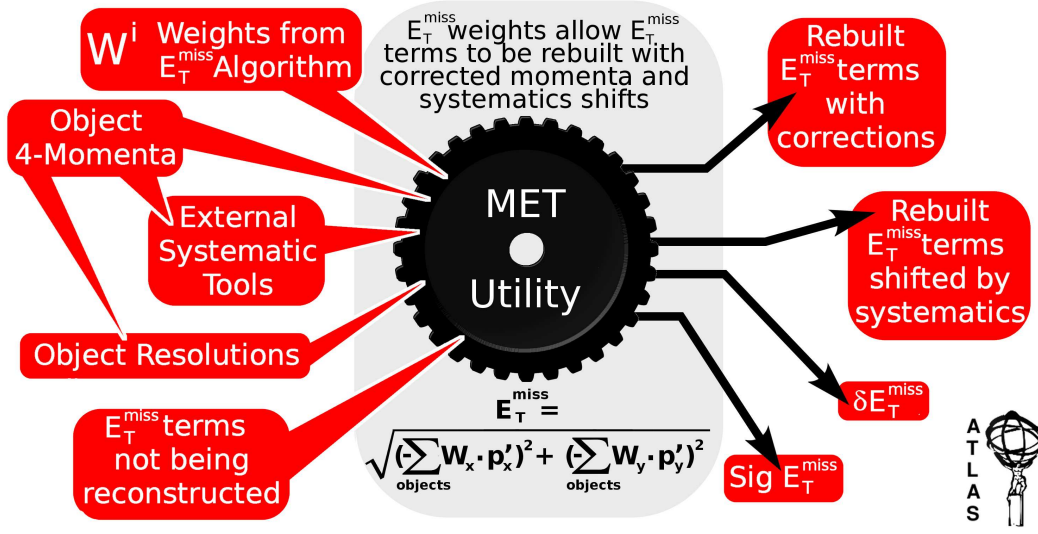


Figure E.3: Block diagram showing the functionality of the METUtility software

A user provides the momenta of the physics objects and the associated E_T^{miss} -weights and status words to METUtility, which in turn applies the necessary recipe for the E_T^{miss} algorithm. If corrections are not being applied to the physics objects (or the physics objects are unavailable to the user), the original E_T^{miss} sub-terms can be provided to METUtility. Users can apply corrections to the energy-scale and resolution of the physics objects prior to supplying them to METUtility. In addition, users can supply uncertainties for energy-scale and resolution to METUtility and it will provided the resulting value of E_T^{miss} from shifting the central value up or down one value of the uncertainty. These uncertainties and corrections to energy-scale and resolution are expected to be provided by external tools supplied by the experts in other performance groups. By requiring the user to provide these values, we provide the user with the maximum leeway in customizing the external tools to their

own analysis.

It is common for analyses making use of n-tuples to not have the reconstructed clusters or tracks at their disposal. Additionally, energy scale uncertainties are not provided for jets with energies $7 < E_T < 20$ GeV, which are used for the soft jet term in some versions of E_T^{miss} . For the portion of E_T^{miss} due to these objects a systematic uncertainty is provided, which shifts the value of these portions of E_T^{miss} based on the value of ΣE_T for the portion. The parameterization of ΣE_T was derived in [164].

When all the necessary systematic errors for an analyses are provided, a final uncertainty for E_T^{miss} can be provided by taking the sum in quadrature of the difference between the assumed central value of E_T^{miss} and the value obtained from the variation resulting from each systematic error. A user can also provide the resolution for each physics object and have a value of $\text{Sig}_{E_T^{\text{miss}}}$ returned.

F

Miscellaneous

F.1 Coordinate Frame

The coordinate system used by the ATLAS detector is right-handed spherical co-ordinates. The x -axis is defined as the axis point from the center of the detector to the center of the LHC ring. The y -axis is vertical and the z -axis is along the beam line. ϕ is the azimuth from the x -axis in the xy -plane. θ is the inclination angle from the z -axis.

For a hadronic collider it is more natural to forego using θ and instead use pseudo-rapidity:

$$\eta = -\ln \left(\tan \left(\frac{\theta}{2} \right) \right) \quad (\text{F.1})$$

As the mass of an object becomes negligible compared to its energy (as is the case for the protons colliding in ATLAS), η approaches the value of the rapidity:

$$y = \frac{1}{2} \cdot \ln \left(\frac{E + p_z c}{E - p_z c} \right) \quad (\text{F.2})$$

Rapidity is useful in the relativistic domain of particle collisions as it is a quantity that is additive under boosts in the z -direction.

F.2 Calorimeter Resolution

The resolution of a calorimeter can be parameterized by the equation [3]:

$$\frac{\Delta E}{E} = \frac{a}{\sqrt{E}} \oplus b \oplus \frac{c}{E} \quad (\text{F.3})$$

where a is a stochastic term determined by statistical issues such as shower fluctuations, photoelectron conversions, dead material, and fluctuations of the samplings. b is the systematic term and is usually the result of uncertainty in the detector material and calibrations. For high-luminosity experiments such as ATLAS, radiation damage to the active medium is also parameterized by this term. In non-compensating calorimeters the lack of compensation for hadronic showers also contributes to the systematic term. The final term, c , is the noise term. The primary contributions to this term are from electronic noise and pile-up events [3].

F.3 Sagitta

Muon spectrometer performance can be parameterized through the sagitta, which is the divergence of the muon track due to the magnetic field and multiple scattering in the detector material. Approximating the track trajectory as a segment of a circle and assuming the angle of the segment is small enough to merit truncating the Maclaurin series of cosine gives an equation for the sagitta, which is the displacement of the path of the track from a straight line (see Figure F.1).

$$s = r(1 - \cos \frac{\alpha}{2}) \approx r \frac{\alpha^2}{8} \quad (\text{F.4})$$

Solving the angle, α , for the chord of the circle segment and applying the equations of motion for a charged particle in a magnetic field gives:

$$p_T \approx \frac{1}{8} \frac{L^2 B}{s} \quad (\text{F.5})$$

Consequently, the measurement of the momentum of a track is dependent on the chord of the track, the magnetic field strength, and the sagitta [183]. The inner detector also makes use of the sagitta method and provides a concrete example: the decay of a W -boson into a lepton with 40 GeV of transverse momentum gives a sagitta of ~ 1 mm for the 2 Tesla magnetic field of the solenoid [71].

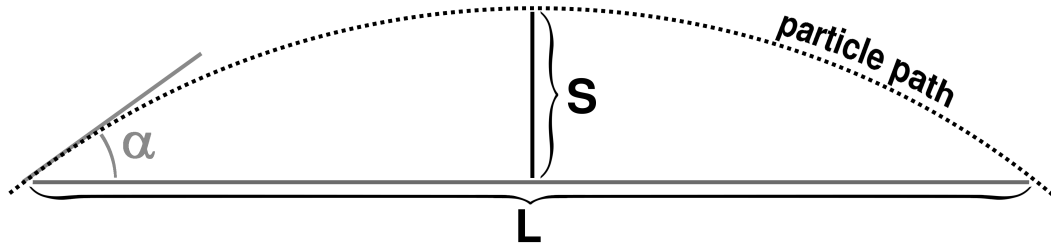


Figure F.1: The sagitta, S , and chord, L , of a circle.

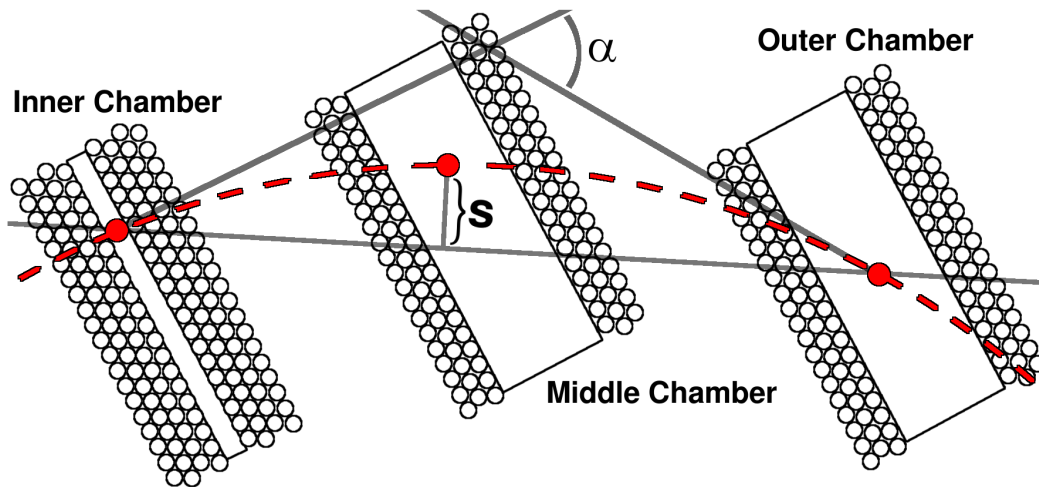


Figure F.2: The method used to measure the sagitta in the ATLAS muon spectrometer [184].

In the ATLAS muon spectrometer the sagitta is measured as shown in Figure F.2, by measuring the track displacement in the middle MDT module compared to an inside and outside MDT module [184]. In order to achieve the desired uncertainty of 10% on the p_T resolution of a 1 TeV track, the resulting 500 μm sagitta must be known to a resolution of 50 μm , the alignment of the muon spectrometer components be known to 30 μm and the uncertainty on the bending power of the magnetic field is targeted for $\sim 10^{-4}$ T to keep its effect on muon momentum scale at a minimum [71, 185]

F.4 Anti- k_T Jet Clustering Algorithm

Clustering algorithms are used to aid our understanding of hadronic collisions by simplifying the structure in a coherent manner. ATLAS makes use of the anti- k_T clustering algorithm. In general, particle clustering algorithms begin by defining two distances:

$$d_{ij} = \min(k_{T,i}^{2p}, k_{T,j}^{2p}) \frac{\Delta R_{ij}^2}{R_c^2} \quad (\text{F.6})$$

$$d_{i,beam} = k_{T,i}^{2p} \quad (\text{F.7})$$

where $\Delta R_{ij}^2 = (\eta_i - \eta_j)^2 + (\phi_i - \phi_j)^2$ and R_c is the characteristic radius. $k_{T,i}$, η_i , and ϕ_i are the transverse momentum, pseudo-rapidity, and azimuthal coordinate of the i th particle. The anti- k_T is the implementation where one takes $p = -1$. To perform the clustering, one iterates over all objects, i , starting with the leading- p_T object. One then iterates again over all other objects, j , and calculates d_{ij} and $d_{i,beam}$. If $d_{ij} < d_{i,beam}$ the j object is merged into i . If $d_{i,beam} < d_{ij}$, the object i is a final state jet and no longer included in the iterations [148, 186, 187].

The use of $p = -1$ versus $p > 0$ in the clustering algorithm has the affect of forcing softer objects to cluster to harder objects instead of clustering with other soft objects and producing a new jet. This produces well-shaped, conical jets which are *infrared safe*. Jets that overlap, such that $R_c < \Delta R_{12} < 2R_c$ for jets 1,2 will share the softer particles between them. For $\Delta R_{12} < 2R_c$ the jets will simply merge to form one jet, ensuring jets which are *collinear safe*. This is an important point, as showering is a statistical process. The parent parton could randomly produce one large shower or two smaller showers and it is important that both cases produce the same jet topology in order to make strong prediction [148].

F.5 Missing Transverse Momentum

In experiments at hadronic colliders, it is not possible to precisely know the actual center-of-mass energy with which a collision occurs, owing to the composite nature of that particles used. However, as all but a negligible portion of the particles' momentum is longitudinal, the momentum in the transverse plane for all particles should sum to zero. When the transverse momentum does not sum to zero, this can be indicator that a weakly-interacting particle was present in the collision. This measurement is heavily dependent on the calorimeters measurement of energy and is referred to as E_T^{miss} , missing transverse momentum. The notation uses an E , reflective of the fact that the instrument primarily used to measure E_T^{miss} is the calorimeter; the term missing transverse energy is often used interchangeably.

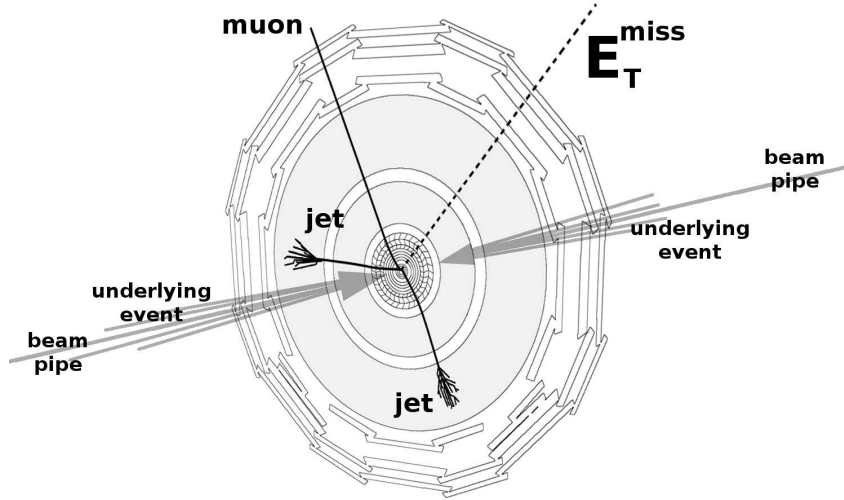


Figure F.3: The relationship of E_T^{miss} to physics objects and the beam in collisions. This diagram is modeled on a hypothetical $W \rightarrow \mu\bar{\nu}_\mu$ event, where the W is balanced against jets.

A diagram of E_T^{miss} is shown in Figure F.3. This is modeled on a $W \rightarrow \mu\bar{\nu}_\mu$ event, where the W is balanced against jets. The $\bar{\nu}_\mu$ is responsible for the E_T^{miss} . Leptonic decays of the W will always involve a neutrino and consequently an accurate measurement of E_T^{miss} is vital to accurate measurements of the W , in particular its mass, which can be reconstructed via its transverse mass using E_T^{miss} and the lepton p_T .

E_T^{miss} can be faked by mis-measured physics objects. In the hadronic-rich environment of pp -collisions the most common source of fake E_T^{miss} is mis-measured jets. However, any poorly reconstructed object can be a source and thus considerable care has been taken at ATLAS to make sure that the object selections for E_T^{miss} give robust and accurate results.

F.6 Tag-and-Probe

Tag-and-probe is a method for measuring efficiencies or fake rates for physics objects. The tag and the probe are each the same type of physics object, such as jets or muons. They are selected from some type of process which forces a relationship between the two objects, such as a decay. The tag object is then required to pass the criteria of interest. The other physics object can then be used to “probe” the efficiency of the criteria. A standard example of this is the measurement of the isolation efficiency of electrons. In this scenario two electrons are required to form a same-flavor, opposite-sign pair within some mass-window of the Z -mass. The tag electron is then required to be isolated. The efficiency of the isolation can then be measured by taking the ratio of the number of isolated probe electrons to the total number of probe electrons. Beyond this example, the method finds use in measuring numerous types of efficiencies, such as reconstruction or trigger efficiencies for leptons, or b -tagging efficiencies for jets.

F.7 Glossary

ALFA — Absolute Luminosity for ATLAS, a luminosity monitor.

AOD — Analysis Object Data, the second level of derived physics data but still in an ATHENA-compatible format.

ATHENA — ATHENA is the ATLAS framework for event reconstruction and analysis, making use of C++ tools in a python wrapper. It is derived from the GAUDI framework developed for LHCb.

ATLANTIS — an ATLAS event display program.

Baryogenesis — A generic term for the origin of the asymmetry in the number of baryons and anti-baryons observed in the universe.

BCM — Beam Conditions Monitor, a low-rapidity system for monitor beam and collision status.

CaloTrkMuId — A muon identification algorithm which associates an inner detector track with a deposit in the calorimeter consistent with a muon.

CL — Confidence Limit.

CSC — Cathode-Strip Chamber, part of the Muon Spectrometer.

CMSSM — Constrained Minimal Supersymmetric Standard Model, another name for mSUGRA.

CTP — Central Trigger Processor, part of the L1 trigger.

D3PD — Derived 3rd-level Physics Data, a common name for the n-tuples in ATLAS produced by D3PDMaker.

DAQ — Data Acquisition.

DCN — DataCollection Network, part of the DAQ.

DCS — Detector Control System.

DFM — DataFlow Manager, part of the DAQ.

DSP — Digital Signal Processor.

EF — Event Filter, part of the High-Level Trigger.

ESD — Event Summary Data, the first level of derived physics data containing virtually all information from the event as well as reconstructed physics objects.

E_T^{miss} — Missing E_T , a measurement of the imbalance of momentum in the transverse-plane of the detector due to non-interacting particles, mis-measured objects, and detector effects.

FCNC — Flavor Changing Neutral Currents,

FEB — Front-End Board.

GGM — General Gauge Mediation

GMSB — Gauge-Mediated Supersymmetry Breaking, a family of models of SUSY in which SUSY is broken in a hidden sector and then communicated to the MSSM via the SM gauge bosons.

GRL — Good Runs List, an XML file detailing which luminosity blocks of a run were free of detector problems so severe as to render the run unusable.

GWS — Glashow-Weinberg-Salam, an eponymous name for the electroweak theory unifying the weak-nuclear force and quantum electrodynamics.

HLT — High-Level Trigger.

L1 — Level-1 trigger

L2 — Level-2 trigger, part of the High-Level Trigger.

LAr — The Liquid Argon calorimeter.

Leptogenesis — A generic term for the origin of the asymmetry in the number of leptons and anti-leptons observed in the universe.

LO — Leading order, referring to the lowest order term in a perturbative calculation of cross-section.

LUCID — LUMinosity measurment using Cerenkov Integrating Detector, a sub-detector for measuring luminosity.

Luminosity Block — An approximately two minute interval of beam collisions, a period of time for which it is expected that beam conditions should be approximately constant. Principally used for logging detector problems and estimating luminosity.

MBTS — Minimum Bias Trigger Scintillators, which provide Minimum Bias trigger in early data-taking.

MDT — Monitored Drift Tube, part of the Muon Spectrometer.

MSSM — The Minimal Supersymmetric Standard Model, a supersymmetric formulation with minimal changes to the standard model, such as the Higgs boson being a quintet.

mSUGRA — Minimal Supergravity, a supersymmetric model with supersymmetry broken in the gravity sector.

μ — The average number of visible collision vertices per bunch crossing; used as a measure of pile-up.

MuTag — A muon identification algorithm which matches tracks in the inner detector to track segments or hits in the muon spectrometer to recover lost tracks.

Muonboy — An algorithm used in ATLAS for standalone muon reconstruction in the muon spectrometer. Muonboy is paired with STACO for combined muons.

NLO — Next-to-Leading-Order, referring to terms other than the leading order (LO) in the calculation of a cross-section.

OHP — Online Histogram Provider, a service that collects and publishes histograms to be used by ATLAS control room shifters.

PDF — Parton Distribution Function.

PU — Processing Unit, a sub-component of a Liquid Argon ROD.

PV — Primary vertex. The vertex with the greatest number of associated tracks.

ROB — Read-Out Buffer.

ROD — Read-Out Driver.

ROI — Region-of-Interest.

ROOT — ROOT is a family of analysis libraries developed for particle physics analysis paired with a C++ interpreter for command line analysis.

ROS — Read-Out System.

RPC — Resistive Plate Chambers, part of the Muon Spectrometer.

SCT — Semi-Conductor Tracker, part of the inner tracker.

SFI — SubFarm Input, part of the DAQ.

SFO — SubFarm Output, part of the DAQ.

SFOS — Same-Flavor Opposite Sign, referring to leptons of the same flavor type and opposite charge, such as those produced in Z -boson decays.

Signal Lepton — A tagged lepton that passes the isolation requirement (and the “tight” requirement in the case of electrons) is considered a signal lepton.

STACO — **S**tatistical **C**ombination is the algorithm used in this analysis for combining inner detector and muon spectrometer tracks to form a single muon. It is paired with Muonboy as a source for standalone tracks.

SUSY — Supersymmetry.

Tagged Lepton — A tagged lepton is a lepton that has passed all lepton selections and overlap removal except for the selection on isolation and the “tight” selection in the case of electrons.

TDAQ — Trigger and Data Acquisition.

TGC — Thin-Gap Chambers, part of the Muon Spectrometer.

TileCal — The Tile Calorimeter.

TRT — Transition Radiation Tracker, part of the inner tracker.

TTC — Timing/Trigger Control.

VME — Virtual Machine Environment.

XML — Extensible Mark-up Language.

ZDC — Zero Degree Calorimeter, part of the forward physics systems.